Centre for Hydrogeology of the University of Neuchâtel
Stochastic Hydrogeology Group

Deterministic and probabilistic numerical modelling towards sustainable groundwater management

Application to seawater intrusion in the Korba aquifer (Tunisia)

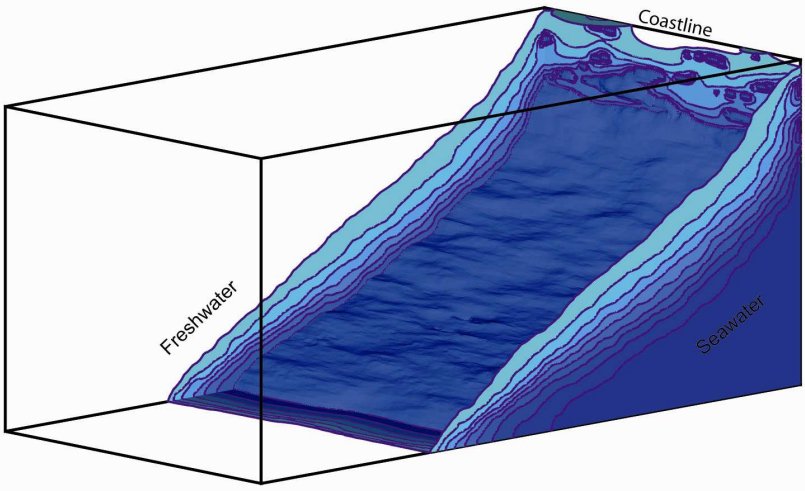

Jaouher Kerrou

PhD Thesis

Thesis defence date: 30 September 2008

Prof. Renard Ph., University of Neuchâtel, Switzerland	Thesis director
Prof. Ababou R., National Institute of Polytechnics, Toulouse, France	Jury member
Prof. Carrera J., Earth Sciences Institute, Barcelona, Spain	Jury member
Prof. de Marsily G., University Paris VI, France	Jury member
Prof. Perrochet P., University of Neuchâtel, Switzerland	Jury member
Prof. Tarhouni J., National Institute of Agronomy, Tunis, Tunisia	Jury member

Université de Neuchâtel

FACULTE DES SCIENCES
Secrétariat-Décanat de la faculté
- Rue Emile-Argand 11
- CP 158
- CH-2009 Neuchâtel

IMPRIMATUR POUR LA THESE

Deterministic and probabilistic numerical modelling towards sustainable groundwater management – Application to seawater intrusion in the Korba aquifer (Tunisia)

Jaouher KERROU

UNIVERSITE DE NEUCHATEL

FACULTE DES SCIENCES

La Faculté des sciences de l'Université de Neuchâtel,
sur le rapport des membres du jury

P. Renard (directeur de thèse),
P. Perrochet, G. de Marsily (Paris), R. Ababou (Toulouse),
J. Carrera (Barcelone) et J. Tarhouni (Tunis)

autorise l'impression de la présente thèse.

Neuchâtel, le 28 novembre 2008

Le doyen :
F. Kessler

UNIVERSITE DE NEUCHATEL
FACULTE DES SCIENCES
Secrétariat - décanat de la faculté
Rue Emile-Argand 11 - CP 158
CH-2009 Neuchâtel
Felix Kessler

This PhD Thesis was funded by the Swiss National Science Foundation (SNSF) within the framework of the *CAPBON* Joint Research Project (Grants: 207020-110017/1). Additional funds were provided by the Swiss Agency for Development and Cooperation (SDC) under the program “Jeunes chercheurs 2004-2006”. Contributions were also provided by the Centre for Hydrogeology of the University of Neuchâtel (CHYN) and by the Institut National Agronomique de Tunisie (INAT).

A mes parents, Mohammed Sghaïer et Farida

Remerciements

Durant mes quatre ans et demi de thèse, j’ai eu le plaisir de collaborer avec plusieurs personnes de différentes institutions de part et d’autre de la Méditerranée, principalement Neuchâtel et Tunis. Dans ces pays, j’ai aussi tissé des liens d’amitiés qui m’ont autant aidé pour mener à bien mon projet de doctorat. C’est le moment de remercier toutes ces personnes, amis et collègues, de leur soutien.

Je commence tout naturellement par Philippe Renard, mon directeur de thèse qui est à la source de la réussite de ce travail. Je le remercie vivement pour m'avoir encouragé et conseillé en permanence, du début à la fin, tout en me laissant une grande liberté. Je le remercie pour m’avoir fait partager ses grandes qualités de chercheur avec un enthousiasme et un humain remarquables. C’était une chance de travailler sous sa direction.

Ensuite, je tiens à exprimer mes sincères remerciements et mon admiration a Pierre Perrochet pour sa disponibilité et pour ses précieux conseils en hydrogéologie quantitative qui m’ont guidé au cours de ma thèse.

Je suis reconnaissant à Jamila Tarhouni de l’Institut National Agronomique de Tunisie (INAT, mon école d’origine) qui a su trouver un financement pour les premiers mois de ma thèse et qui a mis à ma disposition tous les moyens nécessaires pour l’acquisition de données sur le site d’étude. Je remercie également Rachida Bouhlila de l’Ecole National d’Ingénieur de Tunis (ENIT) pour sa contribution au montage et la réussite du projet FNS CAPBON qui a financé ma recherche doctorale.

Un grand merci à tous les membres du Jury de ma thèse, les Professeurs: Rachid Ababou de l’Institut de Mécanique des Fluides de Toulouse, Jesus Carrera de l’Institut des Sciences de la Terre, Barcelone, Ghislain de Marsily de l’Université Pierre et Marie Curie, Pierre Perrochet du Centre d’Hydrogéologie de l’Université de Neuchâtel, et Jamila Tarhouni de l’Institut National Agronomique de Tunisie.

Cette thèse ne serait pas ce qu'elle est sans la contribution de Harrie-Jan Hendricks Franssen de l'Ecole Polytechnique de Zurich et Ivan Lunati de l'Ecole Polytechnique de Lausanne. Je les remercie de leur aide dans mon étude sur les milieux « non-multiGaussian ». Également, je remercie Giuditta Lecca de m'avoir accueilli deux mois au Centre d' Etudes Avancées, Recherche et Développement en Sardaigne (CRS4) et de m'avoir aidé dans mon expérience avec la technologie GRID.

Je remercie Fabien Cornaton pour m'avoir fait partager son expérience de modélisateur et aussi pour son aide à l'utilisation de son code *GroundWater*. Je remercie aussi tous mes collègues du CHYN qui m'ont écouté, conseillé et aidé avec amabilité dans mon quotidien de doctorant : Pierre Schnegg, Daniel Hunkeler, Heinz Surbeck, Ray Flyn, Hélène Demougeot-Renard, Stéphane Cattin, Elisabeth Kuster, Corinne Carraux, Carine Erard et François Zwahlen le directeur du CHYN. Certainement, sans mes collègues et amis de bureau : Michiel Pronk, Alexandro Comunian, Antoine Bailleux et Denis Blanc, les années de ma thèse aurait pu être nettement plus longues. Je remercie également Yumico Abe, Grégoire Mariethoz, Ducommun Romain, Vincent Badoux, Ludovic Savoy, Alain Pochon, Pascale Ducommun, Julien Straubhaar. Je les remercie tous pour l'ambiance agréable qu'ils ont su instaurer, jour pour jour et même le soir… Un merci tout particulier à Rob de Rooij et Andres Alcolea pour les soirées scientifiques au Gibraltar...

Pour la mise à disposition, l'acquisition et la saisie de données sur le site de Korba, j'adresse mes remerciements à : Emna Trabelsi et Dafer Mannaî de l'INAT, Daniel Käser du CHYN, Fethi Ben Hammouda du CNSTN, Naceur Oueslati, Ridha Hadj Salem, Hédi Ferjani du CRDA Nabeul, Brinsi Monia, Abdelhak Amri et Youssef Bouazizi de l'ETAP, Habib Bensalme et Kamel Mahjoub de l'ONM et Mohamed Salah Chagour de l'EGTH. Je remercie particulièrement Faïrouz Slama, ma compagne du projet CAPBON pour sa collaboration constructive.

Je remercie aussi mes amis qui ont rendu le quotidien de ma vie de thésard plus agréable: Nico, Gil, Virginie, Stefan, Fairouz, Naceur, Bouchra et Zied. Je remercie également Adeline pour le soutien qu'elle m'a fourni durant les premières années de ma thèse et ces parents pour leur accueil familial.

Mes plus profonds remerciements vont à Ellen Milnes pour m'avoir fait profiter de ses compétences en matière de modélisation d'aquifères côtiers, mais surtout pour sa chaleureuse amitié et sa sympathie.

Enfin, mes parents, ma sœur Dorra et mes frères Bader et Naïm, je ne saurais jamais les remercier assez pour leur amour et leur soutien inestimable, à qui je dédie affectueusement cette thèse.

Abstract

Mots clés: Intrusion marine; Caractérisation hydrogéologique; Modélisation numérique; Trois dimensions; Hétérogénéité; Incertitude; Modélisation inverse; Géostatistique; Simulations de Monte Carlo; Grilles informatiques; L'aquifère de Korba

Key words: Seawater intrusion; Aquifer characterization; Numerical modelling; Three-dimension; Heterogeneity; Uncertainty; Inverse modelling; Geostatistics; Monte Carlo simulations; Grid computing; The Korba aquifer

This PhD endeavours numerical groundwater modelling considering heterogeneous and uncertain hydraulic parameters. It is made of three parts.

First, we investigated the effects of dimensionality and heterogeneity of the hydraulic conductivity on dispersive seawater intrusion (SWI) processes. Multiple 2D and 3D unconditional simulations of hydraulic conductivity fields sharing the same statistics were generated then used to solve density-dependent flow and solute transport equations with a finite element code. Monte Carlo simulations were analysed in terms of dimensionless criteria including the penetration length and width of the saltwater wedge. Results showed that the 2D heterogeneity is affecting more strongly the SWI processes than the 3D heterogeneity. The saltwater wedge length in the 2D models is smaller than in the 3D ones while there is more mixing in 2D models. Most important, results showed that there is a critical ratio between advection and dispersion processes which is controlling the behaviour of SWI in heterogeneous porous medium.

The second part of the thesis dealt with deterministic and probabilistic modelling and long term forecasts of SWI in the Korba aquifer (Tunisia). The study started by the development of a 3D density-dependent flow and solute transport model of the regional Korba aquifer. Then, two geostatistical models of the exploitation rates and of the hydraulic conductivities within the aquifer were built by combining incomplete direct data and secondary information including aquifer

physical parameters. The effects of the uncertainty on the spatial distribution of the pumping rates and the uncertainty on the hydraulic conductivity field on the 3D density-dependent model were analysed separately and then jointly. To circumvent the large computing time required to run hundreds of 44-years transient models, the simulations were made in a parallel fashion on the EGEE Grid infrastructure as well as on a local Linux cluster. The deterministic numerical model allowed to estimate the current over-exploitation of the Korba aquifer to 135%. It also allowed to estimate the time lapse needed to turn back the initial head and slat distributions (before exploitation start) to about 150 years. The results of the stochastic simulations showed that both uncertainties led to a zone representing 12 % of the aquifer area, where the groundwater heads and salt concentrations are not known with accuracy. Most important, results showed that reducing the pumping rates progressively by 50% until 2048 will not result in a recession of the saltwater wedge; instead an additional 9.5 % of the surface of the aquifer will be contaminated in 2048.

In the third part of the thesis, the performances of kriging, stochastic simulations and sequential self-calibration inversion are assessed when characterizing a non-multi-Gaussian synthetic 2D braided channel aquifer. In a first step, the performance of the three methods was compared in terms of reproducing the original reference transmissivity or head fields. In a second step, the methods were compared in terms of accuracy of flow and transport (capture zone) forecasts. Results showed that the errors remain large even for a dense data network. In addition, some unexpected behaviours are observed when large transmissivity datasets are used. We also observed an increase of the bias with the number of transmissivity data and an increasing uncertainty with the number of head data. This was interpreted as a consequence of the use of an inadequate multi-Gaussian stochastic model.

Table of contents

Chapter 3

Status of the Korba groundwater resources (Tunisia): Observations and 3D modelling of seawater intrusion

Chapter 4

A Grid-enabled Monte-Carlo analysis of the impact of uncertain discharge rates distribution on seawater intrusion in the Korba aquifer (Tunisia)

Chapter 5

Stochastic forecasts of seawater intrusion in the Korba aquifer (Tunisia) towards a sustainable groundwater management

Chapter 1

Introduction

1. Motivations

Scientists and groundwater resources managers are involved in numerical modelling studies of environmental problems, such as contaminant migration prediction, aquifer remediation, seawater intrusion, etc. From a methodological point of view, numerical modelling of such phenomena faces challenges such as characterizing and accounting for complex geological settings. Other challenges are specific to the applications themselves, such as accounting for complex flow and solute transport processes like density effects or reactive solute transport. Those issues affect the accuracy of the forecasts made by numerical models and consequently may affect decisions about groundwater management policies.

This PhD endeavours modelling flow and solute transport considering uncertain hydraulic parameters. It deals with tools that groundwater managers may use to design sustainable groundwater resources management. Those general objectives are addressed through particular applications including seawater intrusion.

Socioeconomical and environmental impacts caused by seawater intrusion (SWI) have claimed the attention of the scientific community worldwide during the last decades. Different approaches have been developed to assess the problem (Bear et al. 1999; Cheng and Ouazar 2003). The validity and the interest of using numerical models for simulating the dynamics of SWI and as tool for optimal management of coastal aquifers have been extensively illustrated in numerous case studies. In the Mediterranean region, many studies have used groundwater numerical models to assess SWI problems (Galeati et al. 1992; Iribar et al. 1997; Yakirevich et al. 1998; Paniconi et al. 2001; Sadeg and Karahanoglu 2001; Aharmouch et al. 2002;

Arfib et al. 2002; Milnes and Renard 2004) and to design schemes for the optimal management of groundwater resources (Mantoglou et al. 2004; Abarca et al. 2006).

Even if saltwater is a conservative solute, and SWI represents a stable configuration of density-driven flow and solute transport, modelling such phenomenon remains a challenge due to difficulties such as: handling large-scale models with sufficiently detailed resolution, accounting for heterogeneity of hydraulic parameters, estimating effective hydraulic parameters, solving the inverse problem while accounting for all available information, etc. Most often, simplifying assumptions (e.g., use of a sharp interface model, use of a broad zonation, reducing the dimension of the problem, fixing parameter values based on numerical mesh resolution, etc.) facilitate the development of a solution. This alleviates partly the intensive calculation demanded for solving the highly nonlinear equations defining SWI processes. At the same time, due to these practical considerations, many questions on the reliability of those simplified models arise as discussed by Diersch and Kolditz (2002).

Moreover, real-word aquifers are four-dimensional and naturally heterogeneous. The heterogeneity patterns include a whole range of scales and features (that include discontinuities). As for uniform density flow and solute transport, it has been shown that heterogeneity controls density-dependent flow and solute transport (Dagan and Zeitoun 1998; Schwarz 1999; Simmons et al. 2001; Darvini et al. 2002; Al-Bitar and Ababou 2005; Held et al. 2005; Abarca 2006). It has also been shown that modelling uniform density flow and solute transport (controlled by 3D properties) in 1D or 2D might lead to considerable differences in the model outputs (Gelhar and Axness 1983). In the context of SWI, the study of the effects of 3D heterogeneity has not been yet carried out. An objective of this Thesis is therefore to investigate the effects of dimensionality (2D and 3D) and the degree of heterogeneity of hydraulic conductivity on SWI (Chapter 2). This is important not only because it allows a better understanding of the phenomenon of SWI, but also because it allows pointing out limitations of those modelling simplifications.

Moreover, in most of groundwater modelling applications, the lack of sufficient data to estimate model input parameters as well as their distributions in space and time will lead to uncertain model predictions. In the context of SWI, a few studies coupled deterministic and probabilistic modelling approaches to evaluate the uncertainties on real-world model parameters and their effects on model predictions (e.g. Pohlmann et al. 2002). At the same time, uncertainties associated with model predictions justify the need for stochastic models as a tool to help decision-makers in the design of robust management policies (Watkins and McKinney 1997). A main

objective of this Thesis is therefore to couple deterministic (Chapter 3) and stochastic modelling techniques (Chapter 4 and 5) to analyse and forecast the behaviour of an important regional coastal aquifer in Tunisia towards a sustainable management of the groundwater resources.

Furthermore, a large number of techniques has been developed during the last decades with the aim of characterizing the spatial variability of aquifer parameters and their uncertainty (Carrera 1993; Koltermann and Gorelick 1996; de Marsily et al. 2005). Most of groundwater studies adopt a multiGaussian model. However, it is known already that multiGaussian models have severe limitations with a high impact on flow and transport predictions (Journel and Deutsch 1993; Wen and Gómez-Hernández 1998; Zinn and Harvey 2003). This is why another objective of this Thesis (Chapter 6) is to explore what happens if widely used direct and inverse multiGaussian techniques are applied to characterize non-multiGaussian fields exhibiting preferential flow paths.

2. Structure of the Thesis

This dissertation consists of five self-contained chapters followed by a general synthesis and conclusions chapter. Additional materials are presented in the Appendixes (A, B, C and D). The chapters were partially presented in international conferences (Kerrou et al. 2007a; Kerrou et al. 2007b) and submitted for publication in international journals (Kerrou et al. 2008).

Chapter 2: Dimensionality effects on seawater intrusion in heterogeneous porous media, addresses the aforementioned problems of modelling SWI in 3D heterogeneous porous media. It presents a comparison between SWI in homogenous and heterogeneous media, as well as a comparison between SWI in 2D and in 3D. The stochastic framework consists in generating (multiGaussian) heterogeneous hydraulic conductivity fields, in 2D and 3D, calculating their effective parameters, and then solving density-dependent flow and solute transport for each realisation. Most importantly, an analytical stochastic model of effective hydraulic conductivities was used to transform a 2D model enabling it to reproduce 3D model predictions.

Chapter 3: Status of the Korba groundwater resources (Tunisia): Observations and 3D modelling of seawater intrusion. This is the first out of three chapters focusing on the Korba aquifer. Chapter 3 presents a review of the previous studies on the site as well as a detailed description of the regional hydrogeological settings

and the status of the groundwater resources in 2004. A major part of Chapter 3 was devoted to the development of a 3D density-dependent flow and solute transport model. This part starts with an estimation of model input parameters, especially, the spatial distribution of the pumping rates distribution. The latter was estimated using a multivariate linear regression model combining secondary variables, including aquifer properties and distributed data from remote sensing analysis. The gathered knowledge at this stage was then used to build and calibrate a 3D numerical model, which is used further to discuss some issues on the management of the regional groundwater resources.

Chapter 4: A Grid-enabled Monte Carlo analysis of the impact of uncertain discharge rates distribution on seawater intrusion in the Korba aquifer (Tunisia). This Chapter focuses mainly on the uncertainty associated with the predictions of the numerical model developed in Chapter 3. In this chapter, only uncertainty on the spatial distribution of the pumping rates in the Korba aquifer is considered. Firstly, a geostatistical model of the pumping rates was built based on the regression model of the pumping rates developed in Chapter 3. Second, density-dependent flow and solute transport Monte Carlo simulations were performed to propagate the input uncertainty and to evaluate its effects on SWI. An important question in Chapter 4 was the use of the Grid technology to run Monte Carlo simulations and the interest of that emerging technology on hydrological applications.

Chapter 5: Stochastic forecasts of seawater intrusion in the Korba aquifer (Tunisia) towards a sustainable groundwater management. This Chapter deals with the uncertainty related to SWI model predictions, resulting from combined uncertainties on the input parameters. The effects of the uncertainty on the spatial distribution of the pumping rates and the uncertainty on the hydraulic conductivity field were analysed separately and then jointly. In Chapter 5, forecasts of the impacts of two different management scenarios on seawater intrusion in 2048 were performed in a stochastic framework and accounting for uncertainties in the input parameters as well as eventual changes on the boundary conditions of the Korba aquifer.

Chapter 6 corresponds to the paper: Issues in characterizing heterogeneity and connectivity in non-multiGaussian media, published in Advances in Water Resources Journal (Kerrou et al. 2008). The paper dealt with three methods commonly used to characterize heterogeneity of subsurface properties, including two direct methods (kriging and stochastic simulations) and one stochastic inverse

method (Sequential Self-Calibration Method). The study consisted in comparing the performance of the three methods when characterizing a non-multiGaussian synthetic 2D braided channel aquifer. In a first step, the comparison was based on the performance of the three methods reproducing the original reference transmissivity or head fields. In a second step, the methods were compared in terms of accuracy of flow and transport (capture zone) forecasts. Note that further research on the subject is presented in Appendix C.

The **Chapter 7** summarizes the main conclusions from the foregoing chapters.

References

Abarca E (2006) Seawater intrusion in complex geological environments. PhD Thesis, Technical University of Catalonia, Barcelona

Abarca E, Vazquez-Sune E, Carrera J, Capino B, Gamez D, Batlle F (2006) Optimal design of measures to correct seawater intrusion. Water Resources Research 42

Aharmouch A, Larabi A, Hilali M (2002) A 3D model for groundwater flow and seawater intrusion interface: Application to the Martil coastal aquifer system. Developments in Water Science 47: 539-546

Al-Bitar A, Ababou R (2005) Random field approach to seawater intrusion in heterogeneous coastal aquifers: unconditional simulations and statistical analysis. In: Geostatistics for Environmental Applications Renard P, Demougeot-Renard H, Froidevaux R Eds Springer

Arfib B, de Marsily G, Ganoulis J (2002) Coastal karst springs in the Mediterranean basin: study of the mechanisms of saline pollution at the Almyros spring (Crete), observations and modelling. Bulletin De La Societe Geologique De France 173: 245-253

Bear J, Cheng AH-D, Sorek S, Ouazar D, Herrera I (1999) Seawater intrusion in coastal aquifers- concepts, methods and practices. Kluwer academic publishers, Dordrecht

Carrera J (1993) An Overview of Uncertainties in Modeling Groundwater Solute Transport. Journal of Contaminant Hydrology 13: 23-48

Cheng AHD, Ouazar D (2003) Coastal Aquifer Management: Monitoring, Modeling, and Case Studies. Lewis Publishers

Dagan G, Zeitoun DG (1998) Seawater-freshwater interface in a stratified aquifer of random permeability distribution. Journal of Contaminant Hydrology 29: 185-203

Darvini G, Spendolini L, Salandin P (2002) Saltwater intrusion for finite Peclet numbers in random permeability aquifersDevelopments in Water Science. Elsevier: 523-530

de Marsily G, Delay F, Goncalves J, Renard P, Teles V, Violette S (2005) Dealing with spatial heterogeneity. Hydrogeology Journal 13: 161-183

Diersch H-JG, Kolditz O (2002) Variable-density flow and transport in porous media: approaches and challenges. Advances in Water Resources 25: 899–944

Galeati G, Gambolati G, Neuman SP (1992) Coupled and Partially Coupled Eulerian-Lagrangian Model of Fresh-Water-Seawater Mixing. Water Resources Research 28: 149-165

Gelhar LW, Axness CL (1983) 3-Dimensional Stochastic-Analysis of Macrodispersion in Aquifers. Water Resources Research 19: 161-180

Held R, Attinger S, Kinzelbach W (2005) Homogenization and effective parameters for the Henry problem in heterogeneous formations. Water Resouces Research 41: 1-14. doi:doi:10.1029/2004WR003674

Iribar V, Carrera J, Custodio E, Medina A (1997) Inverse modelling of seawater intrusion in the Llobregat delta deep aquifer. Journal of Hydrology 198: 226-244

Journel AG, Deutsch CV (1993) Entropy and spatial disorder. Mathematical Geology 25: 329-355

Kerrou J, Lecca G, Murgia F, Renard P (2007a) Grid-enabled simulation of the impact of exploitation uncertainty on the seawater intrusion of the Korba aquifer, Tunisia. Paper presented at the Regional Impact of Information Society Technologies in Africa, IST-Africa 2007, Mozambique2007

Kerrou J, Renard P, Hendricks Franssen H-J, Lunati I (2008) Issues in characterizing heterogeneity and connectivity in non-multiGaussian media. Advances in Water Resources 31: 147-159

Kerrou J, Renard P, Perrochet P (2007b) Seawater intrusion in 3D heterogeneous formation. Paper presented at the Calibration and Reliability in Groundwater Modelling, Credibility of Modelling, ModelCare 2007, Denmark2007

Koltermann CE, Gorelick SM (1996) Heterogeneity in sedimentary deposits: A review of structure-imitating, process-imitating, and descriptive approaches. Water Resources Management 32: 2617-2658

Mantoglou A, Papantoniou M, Giannoulopoulos P (2004) Management of coastal aquifers based on nonlinear optimization and evolutionary algorithms. Journal of Hydrology 297: 209-228

Milnes E, Renard P (2004) The problem of salt recycling and seawater intrusion in coastal irrigated plains: an example from the Kiti aquifer (Southern Cyprus). Journal of Hydrology 288: 327-343

Paniconi C, Khlaifi I, Lecca G, Giacomelli A, Tarhouni J (2001) Modeling and analysis of seawater intrusion in the coastal aquifer of eastern Cap-Bon, Tunisia. Transport in Porous Media 43: 3-28

Pohlmann KF, Hassan AE, Chapman JB (2002) Modeling density-driven flow and radionuclide transport at an underground nuclear test: Uncertainty analysis and effect of parameter correlation. Water Resources Research 38

Sadeg SA, Karahanoglu N (2001) Numerical assessment of seawater intrusion in the Tripoli region, Libya. Environmental Geology 40: 1151-1168

Schwarz C (1999) Dichteabhängige strömungen in homogenen und heterogenen porösen medie. PhD Thesis, Swiss Federal Institute of Technology, Zurich

Simmons CT, Fenstemaker TR, Sharp JM (2001) Variable-density groundwater flow and solute transport in heterogeneous porous media: approaches, resolutions and future challenges. Journal of Contaminant Hydrology 52: 245-275

Watkins DW, Jr , McKinney DC (1997) Finding robust solutions to water resources problems. Journal of Water Resources Planning and Management ASCE 123: 49-58

Wen X-H, Gómez-Hernández JJ (1998) Numerical modeling of macrodispersion in heterogeneous media: A comparison of multiGaussian and non-multiGaussian models. Journal of Contaminant Hydrology 30: 129-156

Yakirevich A, Melloul A, Sorek S, Shaath S, Borisov V (1998) Simulation of seawater intrusion into the Khan Yunis area of the Gaza Strip coastal aquifer. Hydrogeology Journal 6: 549-559

Zinn B, Harvey CF (2003) When good statistical models of aquifer heterogeneity go bad: A comparison of flow, dispersion, and mass transfer in connected and multivariate Gaussian hydraulic conductivity fields. Water Resources Research 39: 1051. doi:doi:10.1029/2001WR001146

Chapter 2

Dimensionality and heterogeneity effects on advective dispersive seawater intrusion processes*

Abstract This chapter presents a study of the effects of model dimensionality and heterogeneity of the hydraulic conductivity on dispersive seawater intrusion (SWI) processes. Multiple 2D and 3D unconditional simulations of multiGaussian hydraulic conductivity fields were generated then used to solve density-dependent flow and solute transport equations with a finite element code. Basing on effective hydraulic parameters, a comparison of SWI in homogenous and in heterogeneous media in both 2D vertical cross-sections and 3D configurations was carried out. After, a comparison of SWI in heterogeneous 2D and fully 3D models sharing the same statistics of the log-permeability distribution was performed for increasing level of heterogeneity. Monte Carlo simulations were analysed in terms of dimensionless criteria including the toe penetration length and width of the saltwater wedge. Results showed that the 2D heterogeneity is affecting more strongly the SWI processes than the 3D heterogeneity. The saltwater wedge length in the 2D models is smaller than in the 3D ones while there is more mixing in 2D models. Results also showed that there is a critical ratio between advection and dispersion processes which is controlling the behaviour of SWI in heterogeneous porous medium. Most important, a simple method allowing the transformation of 2D field in order to better approximate 3D SWI was developed.

* This chapter is based on the papers:
Kerrou J., Renard P. and Perrochet P. (2007) Seawater intrusion in 3D heterogeneous formation. (Poster and paper) Calibration and Reliability in Groundwater Modelling, Credibility of Modelling. ModelCare 2007, Copenhagen, Denmark
Kerrou J. and Renard P. (2008) Dimensionality and heterogeneity effects on advective dispersive seawater intrusion processes. Submitted to Hydrogeology Journal

1. Introduction

Excess of freshwater in coastal aquifers generally flows toward the sea. However, near the shoreline, heavier seawater penetrates inland underneath freshwater due to density-driven flows and forms a mixing zone or an interface between the two miscible fluids in the aquifer. Under natural conditions of equilibrium, it has been demonstrated that the geometry of the salt wedge depends on several parameters such as aquifer hydraulic and water physical properties (e.g. Glover, 1959; Henry, 1964; Voss and Souza, 1987; Croucher and O'Sullivan, 1995), aquifer geometry (e.g. Abarca et al., 2007b), or tidal patterns (e.g. Brovelli et al., 2007). It is also known that the geometry and extension of the salt wedge depends on the degree of heterogeneity of the aquifer (e.g. Dagan and Zeitoun, 1998; Held et al., 2005). But to our knowledge, the studies related to the impact of heterogeneity on seawater intrusion (SWI) were all conducted in 2D. In this work, the aim is to investigate how heterogeneity controls the behaviour of SWI in 3D.

To conduct such an analysis, one can either adopt a sharp interface or a density-dependent dispersive model (Bear, 2005). The sharp interface approach was introduced by Badon-Ghyben (1888) and Herzberg (1901). The freshwater and saltwater are considered immiscible. This technique allows developing analytical solutions of the geometry of the interface based on Darcy's law, Dupuit approximation, fluid mass conservation and pressure continuity on the interface. Depending on the other assumptions, such as stationary interface and simple boundary conditions, a broad range of analytical solutions were published (Glover, 1959; Dagan and Bear, 1968; Fetter, 1972; Strack, 1976). Other authors developed numerical models based on the sharp interface concept (Huyakorn et al., 1996). Reviews of this approach can be found in Reilly and Goodman (1985) and Bear (1999). Despite the fact that assuming a sharp interface significantly simplifies the problem of SWI and allows the development of solutions that are useful for the understanding of the phenomenon and for the direct application in real-world cases, this approach does not take into account the hydrodynamic dispersion. Indeed, it is well known that instead of a sharp interface between freshwater and saltwater there is a transition zone since both fluids are miscible (Henry, 1964). Therefore several methods have been developed to solve the coupled variable-density flow and advective-dispersive solute transport. Simmons et al. (2001) and Diersch and Kolditz (2002) reviewed recent advances in modelling stable or unstable configurations of variable-density flow and solute transport. One of the major

challenges that groundwater modellers confront in that domain for both concepts (sharp interface and dispersive transport) is to account for the spatial heterogeneities.

Yet, the knowledge of the spatial heterogeneity of hydraulic properties especially hydraulic conductivity, or at least the knowledge of its effect on groundwater processes is of prime importance when dealing not only with variable fluid density, but also with other groundwater modelling applications (e.g. Gelhar, 1993; de Marsily et al., 2005). In the case of variable density flow and transport, Simmons et al. (2001) have shown for unstable situations that heterogeneity can affect transport over many length scales. In the stable case of SWI, only a few studies were conducted. Dagan and Zeitoun (1998) studied analytically in a 2D vertical section the effect of a layered heterogeneity with a sharp interface model. Al-Bitar and Ababou (2005) use a sharp interface model too but in an horizontal plane. They developed an analytical expression of the first two moments of the position of the interface and compare it with the results of a sharp interface numerical model. An other group of authors (Schwarz, 1999; Darvini et al., 2002; Held et al., 2005; Abarca, 2006) investigated the effects of heterogeneity of hydraulic conductivity on 2D vertical sections inspired by the Henry's problem. One of the questions raised by these authors is whether it is possible to represent the mean behaviour of SWI in heterogeneous aquifers by using adequate equivalent parameters. This is a classical idea often used to represent spatial heterogeneity (de Marsily et al., 2005). Detailed reviews of various methods and concepts used to estimate equivalent hydraulic parameters have been published by Renard and de Marsily (1997) and by Sanchez-Vila et al. (2006). The use of effective or equivalent parameters in SWI models can be of high interest because it could allow sidestepping difficulties in numerical modelling but at the same time, it could insure the respect of average hydrodynamic properties at a relevant scale. In that perspective, Held et al. (2005) used homogenization theory to derive expressions for the effective flow and transport parameters for SWI in 2D isotropic and anisotropic heterogeneous permeability fields. They showed that for an isotropic heterogeneous medium, the effective permeability corresponds to the geometric mean of the local permeabilities like under standard uniform flow conditions without fluid density contrast (Matheron, 1967). For an anisotropic medium, the expression derived by Held et al. (2005) is identical to that of Gelhar (1993) for the case without density effects. They also showed that the dispersion coefficients that should be used to model SWI in an equivalent homogeneous medium correspond to the local dispersion coefficients, rather than the macroscopic coefficients.

Although modelling a naturally 3D problem such as groundwater flow and transport (controlled by 3D properties) in 1D or 2D might lead to considerable differences in the model outputs (Gelhar and Axness, 1983), reducing problem dimension is a common practice in hydrogeology. Burnett and Frind (1987) pointed out the effects of such a practice on transport model predictions (without density variation) when reducing a 3D system to a 2D one. They showed numerically that the high-concentration core of a contaminant plume stabilizes later and further in a 2D vertical cross-section than in the equivalent 3D simulation. They also showed that vertical averaging of a 3D system would not give sufficiently correct predictions in case of large vertical distribution of contaminants. Shapiro and Cvetkovic (1990) also compared 2D and 3D stochastic interpretations of solute transport in porous media without density effects. They showed that the longitudinal and transversal evolution of solute plume is underestimated in the case of a 2D simulation (vertical averaging of 3D hydraulic conductivity field). Pohll et al. (2000) investigated the error associated with a 2D model in the simulation of solute breakthrough. They found that the removal of the vertical dimension and its hydraulic conductivity variability introduces 5-10% error in model predictions. All these studies indicate that the results of density-dependent flow and transport models should be affected by the dimension of the problem. However, such research has not yet been carried out.

The present work consists of two parts. The first aims at numerically investigate the effects of small to medium-scale hydraulic conductivity heterogeneity and problem dimensionality on modelling SWI under coupled variable-density flow and advective-dispersive solute transport in steady state conditions. To this end, a comparison of SWI in homogenous and in heterogeneous media sharing the same effective parameters in both 2D vertical cross-sections and 3D configurations was carried out, as well as a comparison between heterogeneous 2D and fully 3D models sharing the same statistics of the log-permeability distribution and the same correlation lengths in the common directions. A main question in this part is: what is the effect of increasing the level of heterogeneity on SWI in both 2D and 3D configurations. The aim of the second part is to propose a simple method to allow representing a 3D heterogeneous field by an equivalent 2D heterogeneous field that approximate the behaviour of SWI in 3D field.

The study starts by introducing the 2D anisotropic dispersive Henry problem which is the conceptual model adopted in this research (Section 2.1). The model is extended to 3D (Section 2.2) and to an heterogeneous case (Section 2.3). Then, the chapter describes how the Monte Carlo analysis was conducted. This includes a

description of the geostatistical unconditional simulations of 2D and 3D hydraulic conductivity fields (Section 3.1), the estimation of the effective hydraulic parameters (Section 3.2), as well as the density-dependent flow and solute transport simulations (Section 3.3). The numerical results are presented in Section 4. The section begins with a test of the ergodicity assumption used in the rest of the analysis (Section 4.1) and by presenting some preliminary observations (Section 4.2). Next, the effects of 2D and 3D heterogeneity (comparison between homogeneous and heterogeneous models outputs), and the effect of dimensionality (comparison between 2D and 3D models outputs) are presented in Sections 4.3 and 4.4, respectively. The effects of increasing the level of 2D and 3D heterogeneities on SWI are detailed in Section 4.5. In Section 5, a simple method allowing to approximate 3D model prediction by transformation of a 2D one is proposed and tested in Sections 5.1 and 5.2, respectively. Discussion and conclusions are presented in Section 6.

2. Problem setup

2.1 The 2D anisotropic dispersive Henry problem

Abarca et al. (2007a) modified the Henry problem (1964) to set up an anisotropic dispersive version of it. The fundamental modification is the assumption that mixing between freshwater and saltwater results from advection and velocity-dependent dispersion processes rather than advection and pure diffusion. The second modification is the use of an anisotropic hydraulic conductivity tensor instead of an isotropic one. These modifications lead to a more realistic description of seawater intrusion phenomena especially more realistic salinity profiles. Abarca et al. (2007a) tested the sensitivity of the mixing zone (length and width) as well as inflowing seawater to the new model parameters (including dispersion and anisotropy of hydraulic conductivity) and showed that in this dispersive version of the Henry problem, the penetration length depends basically on the horizontal hydraulic conductivity and the geometric mean of the local horizontal and vertical dispersivities and that the width of the mixing zone is controlled by the geometric mean of the horizontal and vertical dispersivities. Furthermore, the flux of inflowing seawater is controlled by the transverse dispersivity and the geometric mean of the directional hydraulic conductivities.

Note that flow boundary conditions are the same for both versions of the Henry problem and consist of no flow boundary conditions on top and bottom of the (assumed) confined aquifer, a constant flux is assumed along the inland boundary

and a hydrostatic pressure distribution along the seaside boundary. In both versions, a concentration equal to 0 is prescribed along the inland boundary. However, the maximum concentration along the seaside boundary in the original Henry problem was modified and imposed only for the entering fluxes in the dispersive version.

2.2 Extension to the 3D case

The model setup chosen for the purposes of the research is a direct extension of the 2D anisotropic dispersive Henry problem (Abarca et al., 2007a). The geometry of the domain is a rectangular parallelepiped whose longest edges are perpendicular to the coastline (Fig. 1).

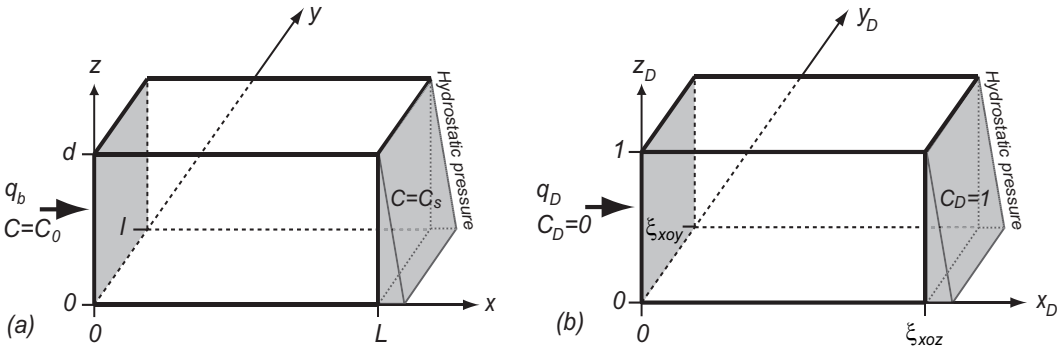

Fig. 1 Model geometry and boundary conditions. (a) real dimensions, (b) dimensionless. Boundary conditions for flow are: no flow conditions on top, bottom and lateral faces of the block, a prescribed flux (q_b) along the inland boundary and a constant hydrostatic head on the seaside boundary. Boundary conditions for transport are: C=0 prescribed along inland boundary fluxes and $C=C_s$ for the inflowing seawater along seaside boundary.

As the mathematical dimensionless formulation was already presented in 2D in Abarca et al. (2007a), we will only present its 3D extension in dimensionless form. First, the dimensionless coordinates and the longitudinal and lateral shape ratios ξ_{xoz} and ξ_{xoy} are defined (Fig. 1):

$$x_D = \frac{x}{d},\ y_D = \frac{y}{d},\ z_D = \frac{z}{d}, \text{ and } \xi_{xoz} = \frac{L}{d} \text{ and } \xi_{xoy} = \frac{l}{d} \qquad (1)$$

where d is the width and thickness of the aquifer, L is the distance between the coast and the inland boundary and l is the lateral extension. The freshwater inland boundary is located at x_D=0 and the sea is at $x_D=\xi_{xoz}$.

Following previous works, we define the dimensionless head h_D, Darcy velocity q_D, and salt concentration C_D as:

$$q_D = \frac{q}{q_b},\ h_D = \frac{hK_{xx}}{q_b d},\ \text{and}\ c_D = \frac{c}{c_s} \tag{2}$$

where q_b represents the prescribed Darcy velocity of the freshwater flux at the inland boundary, q the Darcy velocity in the domain, h the equivalent freshwater head, K_{xx} the xx component of the hydraulic conductivity tensor, C the salt concentration, and C_s the salt concentration of the seawater. Note that the hydraulic conductivity is assumed to be anisotropic but its main axis is aligned with the coordinate axis. Therefore, $\boldsymbol{K}$ is a diagonal tensor. The anisotropy ratios are defined as $r_{YX} = \frac{K_Y}{K_X}$ and $r_{ZX} = \frac{K_Z}{K_X}$. With those definitions, the flow equation in 3D homogenous medium is expressed as:

$$\frac{\partial^2 h_D}{\partial {x_D}^2} + r_{YX}\frac{\partial^2 h_D}{\partial {y_D}^2} + r_{ZX}\frac{\partial^2 h_D}{\partial {z_D}^2} + \frac{1}{a}\frac{\partial c_D}{\partial z_D} = \frac{\varepsilon}{1+\varepsilon c_D}\mathbf{q}_D \cdot \nabla' c_D \tag{3}$$

where $a = \frac{q_b}{\varepsilon K_{zz}}$ and $\varepsilon = (\rho_s - \rho_0)/\rho_0$ with ρ_s being the fluid density of the seawater and ρ_0 is the fresh water density and ∇' means that the operator is written in the dimensionless coordinates. As for the standard Henry's problem, the boundary conditions are no-flow conditions on the top, bottom and lateral faces of the block, and a prescribed flux (q_b) along the inland boundary:

$$\left.\frac{\partial h_D}{\partial y_D}\right|_{y_D=0,1} = 0,\ \left.\frac{\partial h_D}{\partial z_D}\right|_{z_D=0,1} = 0,\ \left.\frac{\partial h_D}{\partial x_D}\right|_{x_D=0} = -1 \tag{4}$$

A hydrostatic pressure distribution is prescribed along the seaside boundary:

$$h_D(x_D = \xi_{xoz}, y_D, z_D) = \frac{1}{r_{ZX}\,a}\left(\frac{1}{\varepsilon} + 1 - z_D\right) \tag{5}$$

The advective-dispersive salt transport equation is then written as:

$$\mathbf{q}_D \cdot \nabla' c_D - \nabla' \cdot \left[b_L \mathbf{D}_\mathbf{D} + b_m \mathbf{I}\right] \nabla' c_D = 0 \tag{6}$$

with $D_\mathbf{D}$ the dimensionless dispersion tensor, b_m is the (reverse) Peclet number corresponding to the molecular diffusion and b_L is the dimensionless longitudinal dispersivity:

$$b_m = \frac{D_m \phi}{q_b d},\ b_L = \frac{\alpha_L}{d}. \tag{7}$$

The ratio of transverse to longitudinal dispersivities is defined by

$$r_\alpha = \frac{\alpha_T}{\alpha_L}, \tag{8}$$

and the components of the dimensionless dispersivity tensor are:

$$D_D^{ij} = r_\alpha \left\| \mathbf{q}_D \right\| \delta^{ij} + (1 - r_\alpha) \frac{q_D{}^i q_D{}^j}{\left\| \mathbf{q}_D \right\|} \tag{9}$$

The transport boundary conditions are the classical ones (Fig. 1). A dimensionless concentration of 0 is prescribed along the inland side of the domain (x_D=0), a zero mass flux is prescribed on the top, bottom and lateral boundaries, while the boundary condition along the seaside is:

$$\mathbf{q}_D c_D\big|_{x_D=0} - \left[b_L \mathbf{D_D} + b_m \mathbf{I} \right] \nabla' c_D\big|_{x_D=0} . \phi = \begin{cases} q_D c_D\big|_{x_D=0} & \text{if} \quad q_D > 0 \\ q_D & \text{if} \quad q_D < 0 \end{cases} \tag{10}$$

In comparison with the 2D problem (Abarca et al., 2007a), we needed to accommodate one additional spatial coordinate (z_D). This leads to the addition of a new hydraulic conductivity anisotropy ratio $r_{YX}=K_y/K_x$. All the rest remains unchanged. Therefore, the dynamic of this problem is controlled by six parameters:

$$a,\ b_m,\ b_L,\ r_\alpha,\ r_{YX} = \frac{K_{yy}}{K_{xx}}, \text{ and } r_{ZX} = \frac{K_{zz}}{K_{xx}} \tag{11}$$

For the numerical model, we used the parameter values shown in Table 1. Note that only statistical anisotropy (due to heterogeneity) was considered.

2.3 Extension to the heterogeneous case

The deterministic mathematical models described in the previous section can also be applied to solve numerically SWI in heterogeneous media or to perform stochastic modelling. In heterogeneous medium, the tensor of the hydraulic conductivity can be written as:

$$\mathbf{K}(x,y,z) = \frac{K_g}{K_g} k(x,y,z) \mathbf{I} \tag{12}$$

where K_g is the geometric mean hydraulic conductivity. In this case, Darcy's law can be express in dimensionless form as following:

$$q_D^x = -k_D \frac{\partial h_D}{\partial x_D},\ q_D^y = -k_D \frac{\partial h_D}{\partial y_D} \text{ and } q_D^z = -k_D \frac{\partial h_D}{\partial z_D} - k_D \frac{c_D}{a} \tag{13}$$

Where $k_D = \frac{k(x,y,z)}{K_g}$ is the dimensionless hydraulic conductivity.

In this framework, the spatial heterogeneity of the hydraulic conductivity has been modelled using a multiGaussian random function model. A Gaussian distribution and a spherical variogram model of the natural logarithm of the hydraulic conductivities $Y=ln(K)$ were assumed for both 2D and 3D configurations. Note that μ_Y (equal to the geometric mean hydraulic conductivity) and σ_Y are the mean and the standard deviation of Y respectively. Very often, the horizontal correlation lengths (λ_x and λ_y) are one order of magnitude larger than in the vertical direction (Gelhar, 1986). In this study, this concept is respected. For the case of identical correlation lengths in the three directions ($\lambda_x=\lambda_y=\lambda_z$), the medium is considered statistically isotropic while it is considered statistically anisotropic if not.

The dimensionless directional correlation lengths are: $l_x=\lambda_x/d$, $l_y=\lambda_y/d$ and $l_z=\lambda_z/d$ where d is the thickness of the considered aquifer. It is worth noting that the level of the heterogeneity of the medium depends on the variance ($\sigma_Y{}^2$) of the random variable.

3. Stochastic framework

The 2D configurations previously studied by Dagan and Zeitoun (1998), Held et al. (2005), Abarca et al. (2006) or Al-Bitar and Ababou (2005) can be considered as some particular cases of 3D fields if we consider infinite correlations in the horizontal and lateral directions as in Dagan and Zeitoun (1998), infinite correlation along the coastline as in Abarca et al. (2006) and Held et al. (2005), or infinite correlation lengths in the vertical direction as in Al-Bitar and Ababou (2005). Here, a more general case is investigated. The complete transition from a 2D vertical cross-section to a full 3D case is considered.

3.1 Hydraulic conductivity fields

In the following, we define the sets of hydraulic conductivity fields which will be used to investigate the effects of heterogeneity (comparison between homogeneous and heterogeneous fields) as well as the effects of dimensionality (comparison between 2D and 3D fields).

3.1.1 2D and 3D heterogeneity

The 2D models have a shape ratio $\xi_{xoz} = 2$, and the 3D models have in addition a value of $\xi_{xoy} = 1$. All 2D and 3D random correlated hydraulic conductivity fields used in this study were generated using the Turning Band method (Matheron, 1973;

Tompson et al., 1989). Firstly, an isotropic 3D hydraulic conductivity field with equal directional correlation lengths (l_x=l_y=l_z=*0.04*), μ_Y =0.01 [m/s] and σ_Y=1 was generated. Then, the correlation length in the *y* direction (l_y) is increased in 6 steps until it largely exceeds the size of the domain in that direction while keeping unchanged the other parameters (l_z, μ_Y and σ_Y). Figure 2 shows the isotropic 3D field (Fig. 2a), one 3D field with intermediate l_y (Fig. 2b) and the 3D field with infinite l_y, equivalent to the 2D isotropic fields used by Abarca et al. (2006) and Held et al. (2005). Increasing l_y led to seven 3D *ln(K)* fields sharing the same statistics in the *xoz* plane, all statistically equivalent to an isotropic 2D field with l_x=l_z=*0.04,* μ_Y =0.01 [m/s] and σ_Y =1. Then, 100 2D fields were generated with the same statistics, and will be compared to each of the 3D models. In order to allow the comparison between the 100 2D fields and a single 3D field, the hypothesis of ergodicity was assumed and will be tested further (section 4). For the sake of brevity, this set of 2D and 3D fields will be called *isotropic*.

Secondly, an anisotropic 3D hydraulic conductivity field with l_x=*0.12,* l_y=*0.04, and* l_z=*0.04,* μ_Y =0.01 [m/s] and σ_Y =1 was generated. Then l_y was increased as for the isotropic set in 6 steps leading to 7 3D *ln(K)* fields sharing the same statistics in the *xoz* plane. The anisotropic 3D *ln(K)* fields will be compared to 100 anisotropic 2D *ln(K)* fields (sharing the same statistics).

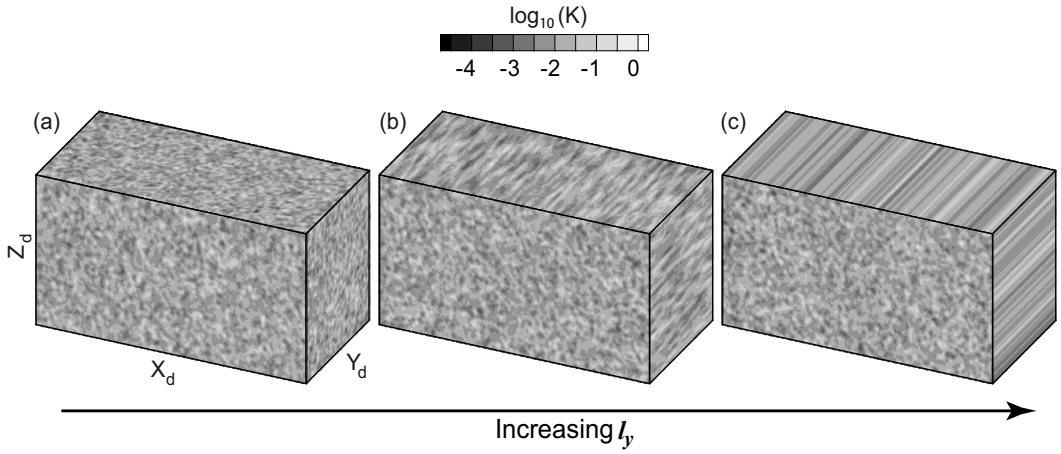

Fig. 2 View of the 3D hydraulic conductivity fields. For all cases l_z=0.04, μ_g =0.01 [m/s] and σ_Y =1 are constant: (a) l_x=l_y=0.04 (statistically isotropic case); (b) l_x=0.04, l_y=0.5; (c) l_x=0.04, l_y=+∞. Note that (c) is equivalent to Abarca et al. (2006) and Held et al. (2005) cases.

To ensure statistically meaningful solutions of the flow and transport equations which will be solved in next step, the 3D models were discretized into 256x128x128 grid cells (more than 4.27 millions nodes) while the 2D models were discretized into 256 x 128 grid cells. The shortest correlation length for the isotropic case corresponds to 5.16 times the grid cell size and to 2 % of the size of the domain in the *x* direction and 4 % of the size of the domain in the *y* and *z* directions.

3.1.2 Increasing the level of heterogeneity

To investigate the effect of increasing the level of heterogeneity on SWI, the *ln(K)* distributions of the reference cases described above (2D and 3D models) were transformed as follows:

$$Y(\mu_Y, \sigma_Y) = (Y_0 - \mu_Y).\frac{\sigma_Y}{\sigma_{Y0}} + \mu_Y \qquad (14)$$

where Y_0 is the initial distribution with μ_Y mean and σ_{Y0} standard deviation, and $Y(\mu_Y, \sigma_Y)$ is the target distribution. For the isotropic case, four levels of σ_Y^2: 0.5, 1, 2 and 3 were studied while only three level of σ_Y^2: 0.5, 1, and 2 were studied for the anisotropic case. This led to four sets of 100 2D simulations which will be compared depending on the *ln(K)* variance to four sets of seven 3D simulations in the isotropic case; and three sets of 100 2D simulations which will be compared to three sets of seven 3D simulations in the anisotropic case. Note that in all cases, the geometric mean of the hydraulic conductivity (μ_g) is equal to μ_Y= 0.01 [m/s].

Table 1 Dimensions and statistics of the hydraulic conductivity fields

Parameter	**Value**
Domain size ξ_{xoz} & ξ_{xoy} [-]	2 & 1
Domain discretization Δx_D, Δy_D & Δz_D [-]	0.0078125
$ln(k_D$ [-]) distribution	Gaussian
Variogram type	Spherical
Geometric mean (k_D [-])	0.01
Cases of $ln(k_D$ [-]) variance	0.5, 1, 2, 3*
Cases of range along *x* (l_x) [-]	0.04, 0.12
Cases of range along *y* (l_y) [-]	0.04, 0.06, 0.1, 0.2, 0.5, 1 & $+\infty$
Range along *z* (l_z) [-]	0.04
Total number of 2D simulations	700
Total number of 3D simulations	49

* Only for the isotropic set.

3.2 Effective hydraulic parameters

3.2.1 Effective hydraulic conductivity

For each configuration, the effective directional hydraulic conductivities of the heterogeneous fields were estimated with Ababou (1996) formula:

$$K_{ef,ii} = \mu_g \exp\left(\sigma_Y^2\left[\frac{1}{2} - \frac{1}{N}\frac{\lambda_h}{\lambda_i}\right]\right) \tag{15}$$

where μ_g is the geometric mean of the hydraulic conductivity [m/s]; σ^2_Y is the *ln(K)* distribution variance; N is the number of dimensions; λ_i is the correlation length [m] in the direction i and λ_h is the harmonic mean of the correlation lengths [m]. This formula is a generalization of Matheron's conjecture (Matheron, 1967) applicable for the 3D anisotropic multiGaussian media. An advantage of this method is that it is not limited to small variances (Ababou, 1996). It is worth noting that this formula does not account for density variations.

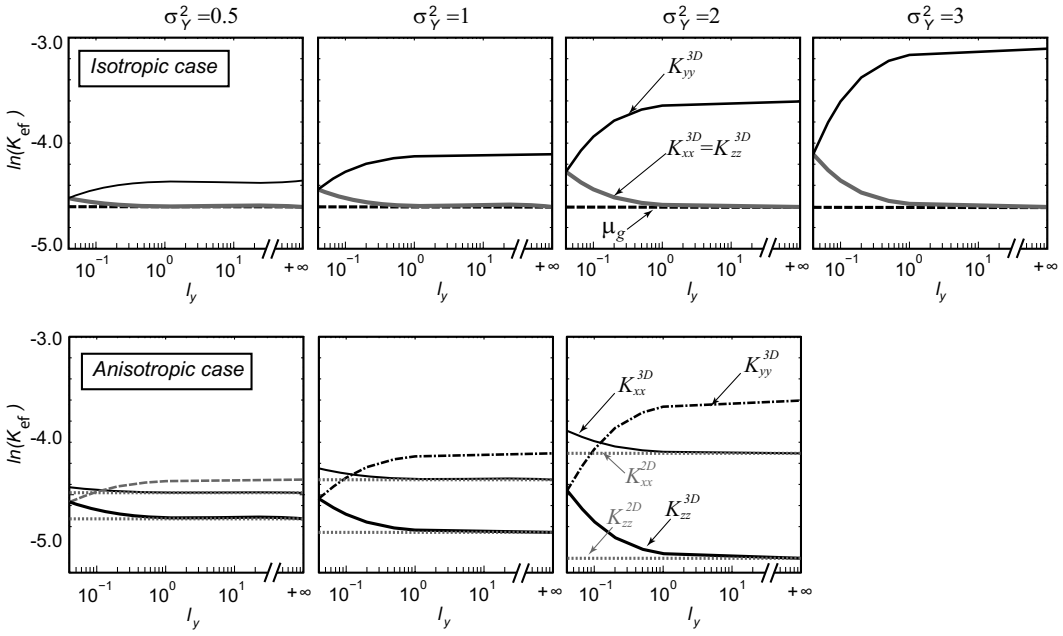

Fig. 3 Evolution of the effective directional hydraulic conductivities K_{ef} as a function of increasing l_y for different levels of *ln(K)* variances in the 3D and 2D models.

The resulting effective hydraulic conductivities are shown in figure 3. It is worth noting that the maximum anisotropy ratio r_{YX} was 4.48 for the case of

l_x=l_z=0.04 and l_y=+∞. (σ_Y^2 =3) and r_{ZX}=0.36 for the case of l_x=3·l_z=0.12 and l_y=+∞ (σ_Y^2 =2).

Theoretically, in a 2D multiGaussian isotropic medium, the effective horizontal and vertical hydraulic conductivities are equal to the geometric mean and independent of *ln(K)* variance. In statistically anisotropic media, the effective hydraulic conductivity in the direction parallel to the stratification (longest correlation length) tends toward the arithmetic mean which is also its upper bound, while it tends to the harmonic mean in the perpendicular direction. Note that for comparison and validation reasons, equivalent hydraulic conductivities were also calculated numerically by solving steady state flow with constant hydraulic gradients. Note that for comparison and validation reasons, equivalent hydraulic conductivities were also calculated numerically by solving steady state flow with constant hydraulic gradients (Appendix A).

3.2.2 Effective dispersivities

An important question was whether effective dispersivities should be used or not; and if they needed to be use, how to estimate them in a simple manner? As a starting point, it was decided to use the same values for the longitudinal and transversal dispersivities for both the heterogeneous and homogenous media (2D and 3D). This was motivated by the fact that at the scale and the level of heterogeneity that are investigated in our numerical simulations, there was not an appropriate model to compute effective dispersivities. Indeed, the results obtained by spectral perturbation techniques to calculate effective dispersivities as in Welty (1991; 2003) and Dentz (2000) are valid for weakly heterogeneous media. In addition, the dispersive Henry problem is characterized by high local dispersivity coefficients as compared to the correlation length of the heterogeneity (α_L=0.1 and l_x=0.04 or 0.12), while the expressions of effective dispersivity usually assume α_L << l_x, e.g. Welty (1991, 2003). Finally, Held et al. (2005) used the homogenization theory to derive expressions for the heterogeneous Henry problem. They found that the effective longitudinal and transversal dispersivities correspond closely to the local values. However, in their numerical analysis Held et al. (2005) considered high molecular diffusion even in the dispersive case they investigated. The latter implies that dispersion is not velocity-dependent only. In addition, they considered low *ln(K)* field variance (equal to 1).

3.3 Density-dependent flow and transport Monte Carlo simulations

The coupled variable-density flow and advective-dispersive solute transport equations were solved with the finite element code *GroundWater* (Cornaton, 2007) for both the 2D and 3D configurations. The *Boussinesq* approximation and constant fluid viscosity are used due to the small density contrast between fresh and saltwater. The model geometry and the boundary conditions (Fig. 1) are described in section 2.1.2. The hydraulic parameters used in the numerical simulation are provided in Table 2. The 3D models were discretized into 256 x 128 x 128 elements while the 2D models were discretized into 256 x 128 elements (the same as for the hydraulic conductivity fields). For all simulations, the parameters are kept unchanged. Only the hydraulic conductivity fields are modified. A series of simulations have shown that the steady state transport regime was reached in less than 0.75 day which is the fixed time for 2D and 3D simulations.

Table 2 Used model parameters.

Symbol	Parameter	Value	Units
K	Geometric mean conductivity	$1.00\ 10^{-2}$	m/s
ϕ	Porosity	0.35	[-]
D_m	Molecular diffusion coefficient	0.00	m^2/s
α_{LH}	Horizontal longitudinal dispersion	0.10	m
α_{TH*}	Horizontal transversal dispersion	0.10	m
α_{TV}	Vertical transversal dispersion	0.01	m
q_b	Inland freshwater flux	$6.60\ 10^{-5}$	m/s
ρ	Freshwater density	$1.0\ 10^{3}$	kg/m^3
ρ_S	Seawater density	$1.025\ 10^{3}$	kg/m^3
μ	Fluid viscosity	$1.00\ 10^{-3}$	kg/ms

* Only in three-dimensional models.

The results of the flow simulations are characterized by three parameters adapted from Abarca et al. (2007a). Two parameters describe the geometry of the freshwater/seawater interface (length and width), and the third measures the amount of saltwater entering the system (Fig. 4). In order to avoid scale-dependent analysis, all parameters are dimensionless and defined as follows:

- Dimensionless penetration length of the saltwater wedge $L_D=L_{toe}/d$: the distance L_{toe} between the seaside boundary and the point where the relative iso-concentration C_D=0.5 intersects the bottom of the aquifer normalized by the aquifer thickness d.
- Dimensionless width of the mixing zone $W_D=w_{mz}/d$: the average vertical width w_{mz} of the area between the relative iso-concentrations C_D=0.25 and C_D=0.75 and between 0.2 L_{toe} and 0.8 L_{toe} normalized by the aquifer thickness d.

- Dimensionless saltwater inflowing flux $R_D=q_s/q_b$: the saltwater inflowing flux q_s normalised by the inflowing freshwater flux q_b.

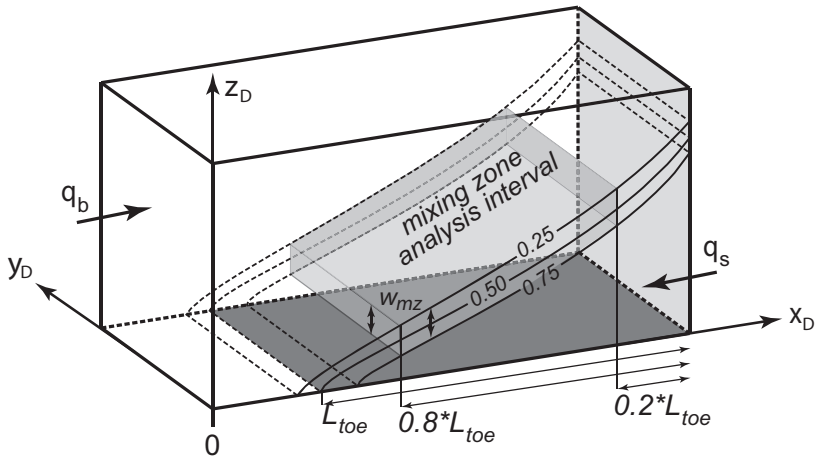

Fig. 4 Evaluation criteria. L_{toe} represents the toe penetration length, q_s the seawater inflowing flux and w_{mz} the width of the mixing zone.

For the heterogeneous 2D cases, ensemble averages of the criteria over 100 simulations were calculated as follows:

$$L_D^{2DHet.}=\frac{1}{n}\sum_{sim=1}^{n}L_D^{sim},\ W_D^{2DHet.}=\frac{1}{n}\sum_{sim=1}^{n}W_D^{sim}\ \text{and}\ R_D^{2DHet.}=\frac{1}{n}\sum_{sim=1}^{n}R_D^{sim} \qquad (16)$$

where n is the number of 2D simulations, and *sim* refer to one 2D simulation.
In 3D, the CPU time required to run the complete set of 3D simulations needed for all the configurations investigated in this study would have required about 500 days (on a linux AMD Opteron 64 bit machine) if we would have run 100 simulations per configuration. To reduce the computing time, we have used spatial averages on single 3D simulations instead of ensemble averages on many simulations. In other words, it is assumed that for one 3D realisation, the spatial averaging of flow and transport solutions along the y direction (parallel to the shoreline) will give the same ensemble statistics (average and variance) than multiple 3D realisations (ergodicity assumption):

$$L_D^{3DHet.}=\frac{1}{ns}\sum_{slice=1}^{ns}L_D^{slice},\ W_D^{3DHet.}=\frac{1}{ns}\sum_{slice=1}^{ns}W_D^{slice}\ \text{and}\ R_D^{3DHet.}=R_D^{sim} \qquad (17)$$

where ns is the number of 2D vertical slices in a 3D model, and *slice* refer to one slice of a 3D model (128 slices). A similar assumption was used by Al-Bitar and Ababou (2005). In the following, the ergodicity assumption is tested numerically for three configurations.

4. Numerical results

4.1 Ergodicity hypothesis

We compared the ensemble statistics of the 3D salt concentration distribution along the central slice of the model (y_D=*0.5*) calculated over 100 3D realisations with the spatial statistics calculated on a single realization with equation (17). The 3D hydraulic conductivity fields have the following correlation length l_x=*0.12,* l_y=*0.12,* l_z=0.04. The numerical test has been conducted for three levels of *ln(K)* variance: 1, 2 and 3.

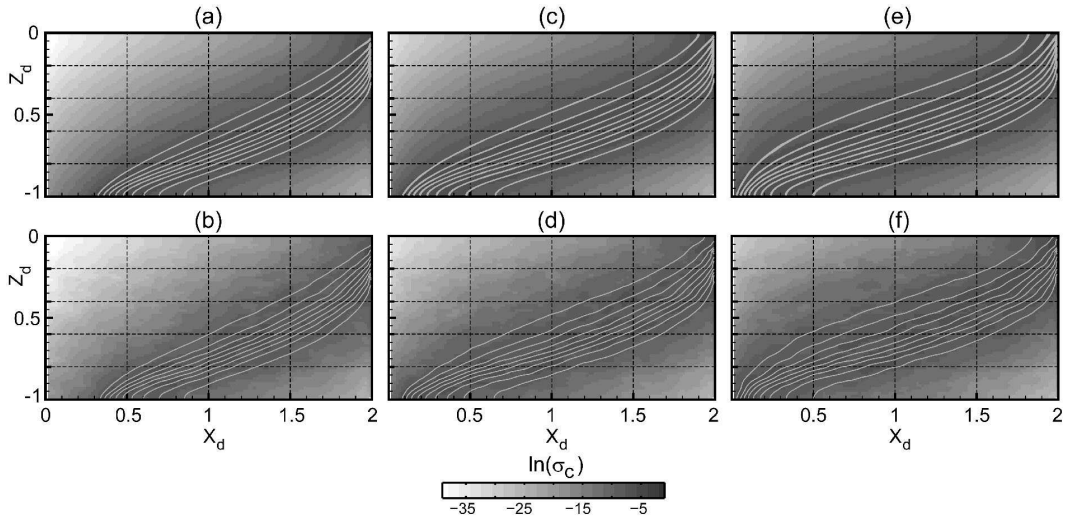

Fig. 5 Ergodicity test: Upper row: 2D vertical cross-section (y=0.5) of the Ensemble average relative salt concentration [-] isolines (0.1 to 0.9) and the ensemble variance (background grayscale map) calculated on 100 3D simulations. Lower row: 2D view of the spatial average relative salt concentration [-] isolines (0.1 to 0.9) and the spatial variance calculated on a single 3D simulation. Grayscale maps represent the natural logarithm of the variance. The results are presented for l_x=l_y=0.12 l_z=0.4 and the 3 cases of *ln(k)* variance (a-b σ_Y^2=1, c-d σ_Y^2=2, e-f σ_Y^2=3).

It was found that the ensemble average concentrations (gray lines on Figs. 5a,c,e) are well approximated by the spatial mean (gray lines on Figs. 5b,d,f). Similarly, the ensemble concentration variance (background graymaps in Figs. 5a,c,e) are well approximated by the spatial concentration variance (Figs. 5b,d,f) even for a large *ln(K)* variance (σ_Y^2=3). Figure 5 shows also that the ensemble estimates are smoother and more regular than the spatial estimates. In terms of

estimation of the mean position of the toe, the test shows that the spatial average performs very well (Table 3), the width of the mixing zone is estimated reasonably well, but the variances are much less accurate both for the position of the toe and the width of the mixing zone (Table 3). Therefore, the ergodicity assumption can be accepted, but results concerning the estimated variances must be interpreted with care. In addition, for large correlation lengths in the *y* direction, the ergodicity assumption is certainly not reasonable any more.

Table 3 Comparison between ensemble and spatial statistics (EA refers to ensemble average, SA refers to spatial average).

σ_Y^2	$\frac{L_D^{EA}}{L_D^{SA}}$	$\frac{\sigma_{LD}^{EA}}{\sigma_{LD}^{SA}}$	$\frac{W_D^{EA}}{W_D^{SA}}$	$\frac{\sigma_{WD}^{EA}}{\sigma_{WD}^{SA}}$
1	1.01	1.34	0.96	0.56
2	1.00	1.55	1.02	0.63
3	1.00	0.71	1.02	0.83

4.2 Preliminary results

To start the analysis of the effect of heterogeneity, let us consider a single realisation in 2D and another one in 3D sharing the same parameters and the same distribution of hydraulic conductivity. Figure 6 shows the 2D vertical cross-sections of the relative salt concentration isolines calculated considering a heterogeneous medium (solid line) and those calculated considering a homogenous medium (dashed line) whose equivalent hydraulic conductivity was calculated with Ababou (1996) formula. Note that for the 2D case, only one realisation is shown whereas for the 3D case the lateral average (in the *Y* direction) of salt concentrations is shown. By visual comparison, it is clear that in all cases there is a difference in the concentration distributions between the homogenous and heterogeneous cases. The difference increases as σ_Y^2 increases (compare 6b and 6d and compare 6c and 6e), and the magnitude of the difference is larger in 2D than in 3D (compare 6b and 6c and compare 6d and 6e).

Moreover, the comparison of the iso-concentration contours in figures 6a and 6d allows to characterise the behaviour of the saltwater wedge as:

- In 2D as well as in 3D, concentration gradients are higher in the low permeable zones as compared to the gradient in the high permeable zones.

- The organization of heterogeneity, especially isolated high permeability zones along the sea boundary, might lead to the apparition of convection cells depending on the *ln(k)* variance.
- There is a rotation (seaward and upward shift of the saltwater wedge) of freshwater/saltwater interface in 2D heterogeneous models as compared to the ones in 2D homogenous models. The same behaviour is less visible in the 3D configuration.

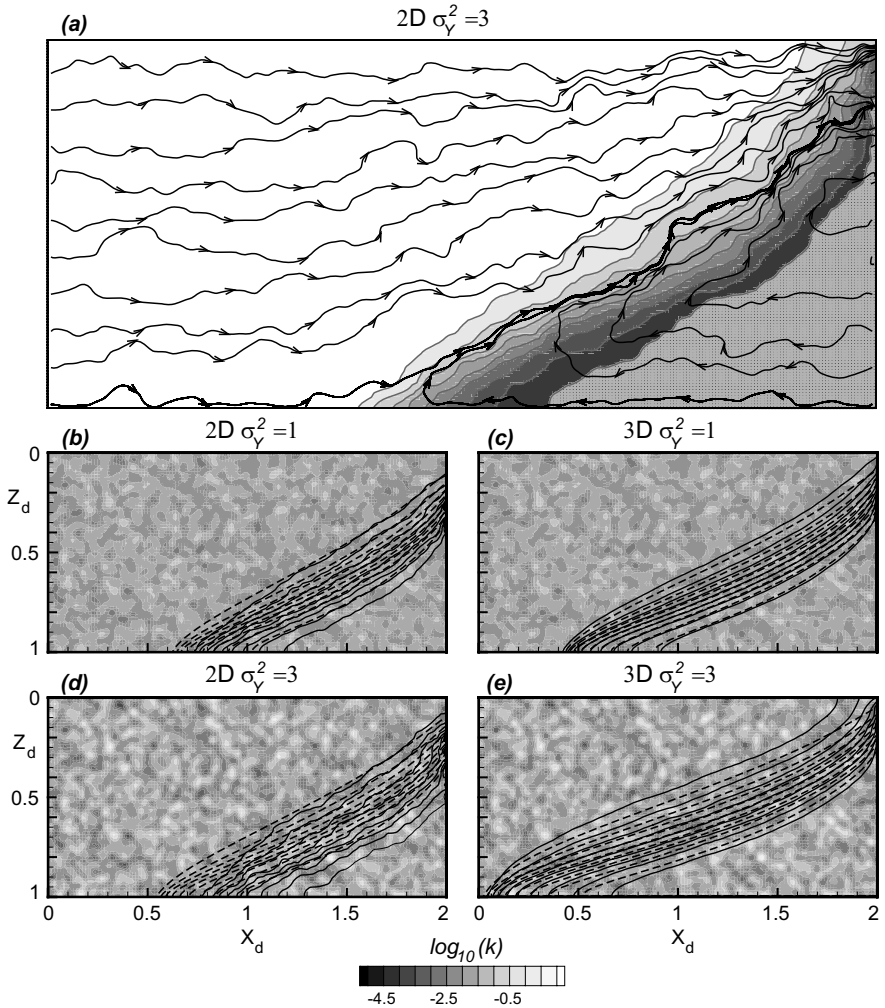

Fig. 6 (a) Streamlines and dimensionless concentration contours for a single 2D isotropic realisation of variance of 3; 2D vertical cross-section views of concentrations [-] isolines (0.1 to 0.9): (b) for the 2D heterogeneous isotropic case (solid line) and homogenous case (dashed line); (c) for the 3D heterogeneous isotropic case (solid line) and homogenous (dashed line). For both cases σ_Y^2=1. (d) and (e) same as (b) and (c) but for σ_Y^2=3.

Those effects of 2D heterogeneity are in agreement with previous findings (Held et al., 2005; Abarca, 2006). Yet, these studies investigated the effects of 2D heterogeneity with hydraulic conductivity variance up to 2.

4.3 2D and 3D heterogeneity effects

This section is focused only on the description of the effects of hydraulic conductivity heterogeneity on steady state SWI, and not on dimensionality effects which will be studied in detail in the next sections. Heterogeneity effects are investigated by comparing the ratios of the dimensionless characteristic parameters (i.e. dimensionless toe penetration L_D, dimensionless width of the mixing zone W_D and dimensionless steady saltwater inflow R_D) obtained for heterogeneous media and the corresponding parameters obtained for the effective homogenous medium (both are sharing the same effective directional hydraulic conductivities). This comparison is carried out separately for both 2D and 3D isotropic and anisotropic configurations and for increased levels of *ln(K)* variances. Monte Carlo simulation results are presented in Table 4.

Table 4 Comparison between heterogeneous (characteristic norms with *Het.* subscript) versus homogenous (norms with *Hom.* subscript) media.

	2D Isotropic				**2D Anisotropic**		
σ_Y^2	0.5	1	2	3	0.5	1	2
$L_D^{Het.} / L_D^{Hom.}$ [-]	0.97	0.95	0.92	0.89	0.94	0.89	0.82
$W_D^{Het.} / W_D^{Hom.}$ [-]	1.12	1.24	1.42	1.53	1.15	1.25	1.31
$R_D^{Het.} / R_D^{Hom.}$ [-]	3.35	5.98	14.03	28.08	3.46	6.15	14.14

	3D Isotropic				**3D Anisotropic**		
σ_Y^2	0.5	1	2	3	0.5	1	2
$L_D^{Het.} / L_D^{Hom.}$ [-]	1.02	1.01	0.99	0.97	0.99	0.97	0.95
$W_D^{Het.} / W_D^{Hom.}$ [-]	1.04	1.07	1.18	1.21	1.05	1.11	1.17
$R_D^{Het.} / R_D^{Hom.}$ [-]	2.38	3.84	7.72	13.35	2.65	4.43	9.22

The analysis is based on the ensemble average of 100 simulations for the 2D cases and the spatial average (averaging following the *Y* direction parallel to the sea) for the 3D cases.

The first observation that can be made in Table 4 is that globally all the ratios deviates more significantly from 1.00 in the 2D case than in the 3D cases. This shows that the difference between heterogeneous and their equivalent homogeneous media is higher in 2D than in 3D. One can also note that the difference increases when increasing the *ln(K)* variance. Another important observation is that the steady inflowing saltwater flux is the parameter which is most affected by the hydraulic conductivity heterogeneity since it can be more than 20 times larger in heterogeneous models as compared to homogenous models with equal effective directional hydraulic conductivity (σ_Y^2=3). The magnitude of the saltwater flux is always much lager in the heterogeneous cases than in the homogenous ones, and increases almost exponentially when increasing σ_Y^2. According to Abarca (2007a), the entering saltwater flux (in 2D) is controlled by the geometric mean hydraulic conductivity and the transversal dispersion. Our numerical results imply that the difference between heterogeneous and their equivalent homogeneous media is due to an inadequacy of the local dispersivities. An increase of the transversal dispersion due to vertical velocity variation implies a decrease of the density effects (more mixing), therefore the entering saltwater flux (R_D) increases to compensate it. This difference between the heterogeneous and homogenous models might also be explained by the absence of simulation of the local convection cells which appear when high permeability zones are less connected close to the sea boundary and become more disconnected by increasing *ln(K)* variance. The role of the convection cells should be more determinant in 2D configurations. In 3D, highly permeable zones are better connected hence reducing the possible mixing of entering saltwater, which results in reducing the difference between heterogeneous and homogenous models.

With regard to the others parameters L_D and W_D, one can see that in all cases, the saltwater wedge tends to recede seaward when considering heterogeneous models instead of homogenous ones and at the same time the width of the mixing zone tends to increase. Those two effects are expected and linked. Indeed, the heterogeneity increases both longitudinal and transversal dispersivities. Transversal dispersivity normal to the concentration gradients will cause mass spreading (larger mixing zone) which reduces density effect leading to a seaward horizontal and upward vertical shifts (rotation) of the interface as shown in figure 6. For both parameters, the contrast increases when increasing the level of heterogeneity and more significantly in 2D than in 3D models. In 3D, the connection of preferential mass path reduces salt spreading and thus the contrast between heterogeneous and homogenous models.

When comparing the effects of isotropic and anisotropic heterogeneity in 2D and 3D configurations, one can see that the trends are similar but slightly more pronounced for the anisotropic media (compare isotropic versus anisotropic values in table 4). In fact, it is a consequence of velocity increases in the horizontal direction as well as horizontal and transversal dispersion increases.

The calculation of the relative salt concentration variance over 100 2D and 100 3D Monte Carlo simulations showed (Fig. 7) that the two extremities of the saltwater wedge (near the bottom and freshwater outlet zones) are most affected by the spatial variability of the hydraulic conductivities. Indeed this uncertainty increases with increasing σ_Y^2. The uncertainty on the toe is amplified by particular velocities in this zone (existence of a stagnation point). The freshwater output zone (outflow face) is conditioned by the organization of the heterogeneity. Yet, in those zones, average velocities are parallel to concentration gradients, therefore, longitudinal and transversal dispersivities affect more salt transport as explained in Held (2005).

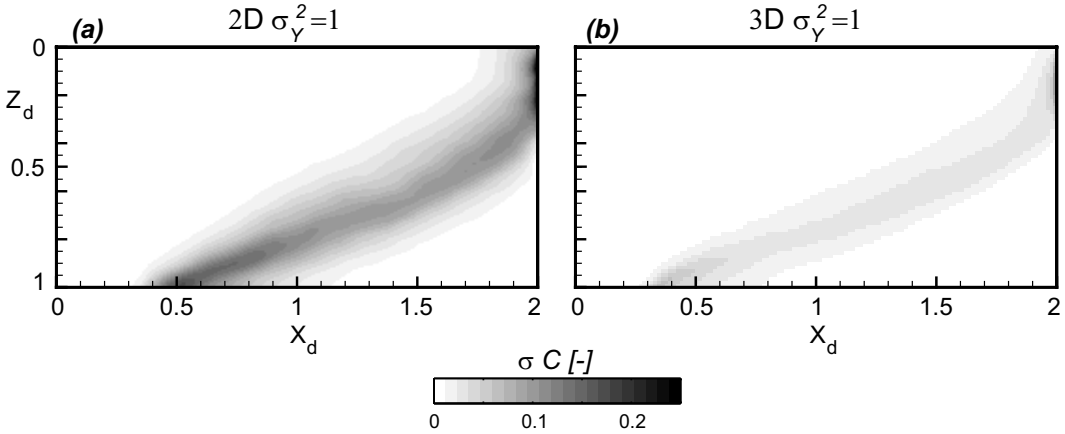

Fig. 7 Ensemble standard deviation of the relative concentrations calculated over: (a) 100 2D simulations with l_x=0.12 and l_z=0.04; (b) 100 3D simulations with l_x=l_y=0.12 and l_z=0.04. For both cases σ_Y^2=1.

An important point which arises from this analysis is the effects of dispersivities. According to Held et al. (2005), in steady state, macrodispersion has a negligible effect on saltwater wedge. At the same time, in strongly heterogeneous media with high σ_Y^2 and anisotropic ratios, local dispersivities are not sufficient and effective ones are needed to model correctly SWI in the equivalent homogenous medium even in steady state.

4.4 Dimensionality effects

This section focuses on dimensionality on steady SWI behaviour, especially on the geometry of the interface. We compared in a first case, a set of seven 3D models (for which l_y increases in 6 stages until exceeding the size of the domain in that direction) with a set of 100 2D simulations, all sharing the same mean and variance of *ln(K)* as well as the same directional correlation lengths l_x and l_z. Note that in the first case, the starting 3D model (before increasing l_y) as well as the set of 2D simulations is statistically isotropic with l_x=l_y=l_z=0.04. However, the second case differs from the first only by the fact that the starting 3D model (before increasing l_y) as well as the set of 2D simulations are statistically anisotropic with l_x=l_y=3·l_z=0.12. The comparison is made in terms of the characteristic parameters L_D, W_D, and R_D.

One result of this study is illustrated in Figure 8. It shows in a set of 3 single realizations that the seawater intrusion moves further inland when a full 3D heterogeneity (Fig. 8a) is considered as compared to a 2D heterogeneous model (equivalent to Fig. 8c). Figure 8 also shows that the mixing zone is wider and much more irregular in 2D than in 3D models.

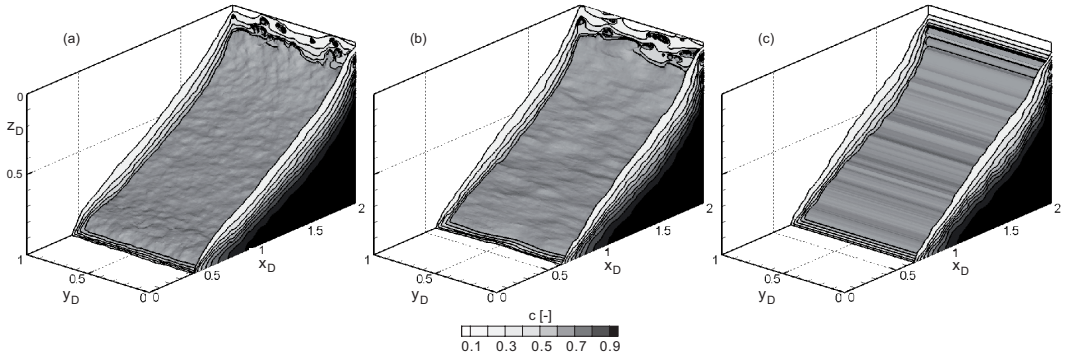

Fig. 8 3D view of the relative salt concentration [-] isolines (0.1 to 0.9); (a) for the isotropic case with l_x= l_y=l_z=0.04, (b) for the case where l_x=l_z=0.04 and l_y=0.1, (c) for the case with l_x=l_z=0.04 and l_y=+∞. Note that (c) is equivalent to a 2D model. For the 3 cases, the *ln(k)* variance is equal to 1.

Figure 9 shows the first moment of dimensionless norms L_D, W_D, and R_D obtained for 3D models normalised by those obtained in 2D as a function of increasing l_y. In other words, figure 9 shows the behaviour of the SWI through the transition from a fully 3D model (small l_y) to a 2D model (3D model with l_y=+∞) with different levels of heterogeneity. The position of the toe is the parameter that is the most affected by model dimensionality. The salt wedge penetrates further

landward in 3D as compared to 2D configurations for both isotropic and anisotropic cases. Even for small *ln(K)* variances, the landward shift is around 10%. This effect increases when increasing σ_Y^2, and the (relative error) difference between 2D and 3D reaches 38% for σ_Y^2=3.

This is not surprising, because the saltwater wedge penetration is highly dependent on the horizontal hydraulic conductivity (Abarca, 2007), and increasing the dimension of the problem increases the effective hydraulic conductivity in the main flow direction (*x* direction). For example, the effective hydraulic conductivity of a statistically isotropic heterogeneous 2D field is the geometric mean. However, for a 3D field with equal geometric mean, variance and correlation lengths, the effective hydraulic conductivity is $\exp(\sigma_Y^2/6)$ times larger than in 2D. As a consequence of an increase of the effective hydraulic conductivity, the global pressure gradient between the freshwater flux landside and the seawater hydrostatic pressure decreases, inducing thus, a landward movement of the saltwater interface. That is why saltwater wedge penetrates further landward in 3D than in 2D configurations.

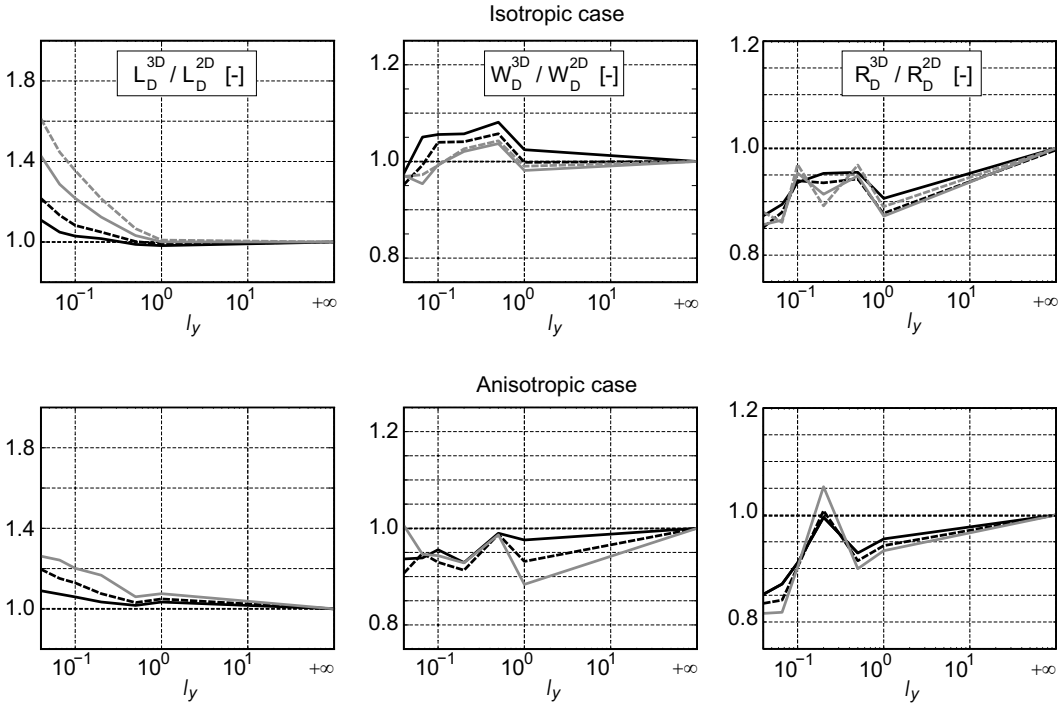

Fig. 9 Dimensionless norms comparison between 2D and 3D for different level on *ln(K)* variance (solid black line for σ_Y^2=0.5, dashed black line for σ_Y^2=1, solid gray line for σ_Y^2=2 and dashed gray line for σ_Y^2=3).

Furthermore, it has already been shown analytically that the ratio of directional velocity variations ($\sigma_{qV}^2 / \sigma_{qH}^2$, where σ_{qV}^2 is the variation of vertical velocity and σ_{qH}^2 is the variation of horizontal velocity) is larger in 2D than in 3D. Indeed, according to *Gelhar* (1993), for a 2D statistically isotropic medium, the ratio of transverse to longitudinal velocity variation is 1/3, whereas, it is 8/3 times smaller in 3D. That point implies that there is more vertical mixing in 2D and thus less density effects which causes a rotation of the saltwater wedge (seaward horizontal and upward vertical shifts) as explained in the previous section. At the same time, even if the geometric mean of longitudinal and transversal dispersivities increases when hydraulic conductivity increases (from 2D to 3D), the dispersion-advection ratio decreases and becomes an advection dominant transport process leading to a convergence to a sharp interface (longer penetration and thin mixing zone).The effective hydraulic conductivity is higher in 3D than in 2D which implies a reduction of the dimensionless parameter $a=q_b/\varepsilon K_{zz}$ (with respect to Peclet condition) which compares viscosity and buoyancy forces, hence more density effects as discussed by Simpson and Clement (2004).

The width of the mixing zone W_D is also affected by model dimensionality (Fig. 9). The results are not as clear as for the position of the toe probably because of the limits of the ergodicity assumption. Yet, some tendencies can be observed. In all cases, the difference between 2D and 3D does not exceed 10 %. In the isotropic case, for small correlation length l_y, W_D in 3D models is smaller than those in 2D, while the reverse for higher correlations lengths. For the statistically anisotropic cases, the width of the mixing zone in 3D models is always smaller than those in 2D even for a σ_Y^2. The width of the mixing zone (in homogenous media) depends mostly on the geometric mean of the longitudinal and transversal dispersivities (Abarca et al., 2007a). This suggests that (mechanical) dispersion due to heterogeneity, especially the transversal dispersivity, increases as a function of velocity variance more significantly in 2D than in 3D models.

With regard to the inflowing saltwater, the flux in 2D models is larger than in 3D models. This confirms that the dispersion due to the heterogeneity is larger in 2D than in 3D models because R_D is highly controlled by dispersion (Abarca et al., 2007a).

Another difference between the 2D and 3D models is the estimation of the uncertainty of the outputs (variances of L_D, W_D and R_D). Table 5 shows that the 2D models predict a higher uncertainty (up to 5 times) than 3D models. However, the relative variability of L_D ($\sigma L_D^{3D}/L_D^{3D}$ *or* $\sigma L_D^{2D}/L_D^{2D}$) is slightly larger in 2D but does

not exceed 0.03. The same is true for W_D with a maximal value of 0.05. This is attributed to less saltwater spreading in 3D models due to less velocity variability.

An analysis of the effects of the anisotropy of 3D hydraulic conductivity fields on SWI (Appendix B) showed that there are negative correlations between the horizontal anisotropy ratio (r_{YX}) and the penetration of saltwater wedge and a negative correlation between the vertical anisotropy ratio (r_{ZX}) and the width of the mixing zone.

Table 5 Comparison between 2D and 3D uncertainty, σ represents the standard deviation.

	Isotropic		**Anisotropic**	
σ_Y^2	$\sigma L_D^{3D}/\sigma L_D^{2D}$	$\sigma W_D^{3D}/\sigma W_D^{2D}$	$\sigma L_D^{3D}/\sigma L_D^{2D}$	$\sigma W_D^{3D}/\sigma W_D^{2D}$
0.5	0.17	0.29	0.20	0.25
1	0.15	0.19	0.29	0.46
2	0.14	0.16	0.22	0.45
3	0.19	0.35	-	-

4.5 Effects of increasing variability

Another way to analyse the results, is to study how the salt wedge evolves when the degree of heterogeneity (σ_Y^2) increases (Fig. 10). The toe penetration in the 2D models is smaller than in the 3D models, especially when the variance increases.

An interesting behaviour can be observed in the isotropic case: in 2D models, the toe penetration decreases when the variance increases, whereas, in 3D the toe penetration increases significantly when the variance increases for the fully isotropic media (Fig. 10a). Intermediate behaviour occurs depending on the magnitude of the correlation length in the direction parallel to the cost. In addition, for statistically anisotropic hydraulic conductivity fields, the toe penetration increases when the variance increases in both 2D and 3D settings (Fig. 10e). This complex behaviour is the result, as discussed before, of the combined effect of the effective hydraulic conductivity and dispersion. For the isotropic heterogeneous 2D domain, the effective hydraulic conductivity is equal to the geometric mean of *ln(K)* independently of the value of σ_Y^2. Yet, regardless of dimentionality and isotropic or anisotropic media, increasing the level of heterogeneity increases dispersion. In this case, the position of the toe is controlled by the dispersion processes which increase with increasing σ_Y^2. It is not the case for the 2D or 3D statistically anisotropic media

where the effective hydraulic conductivity increases in the flow direction when σ_Y^2 increases. Figure 10a shows that there is a certain thresholds of the relation between advective and dispersive solute transport for which the toe penetration can increase or decrease, or even remain constant when the *ln(K)* variance increases.

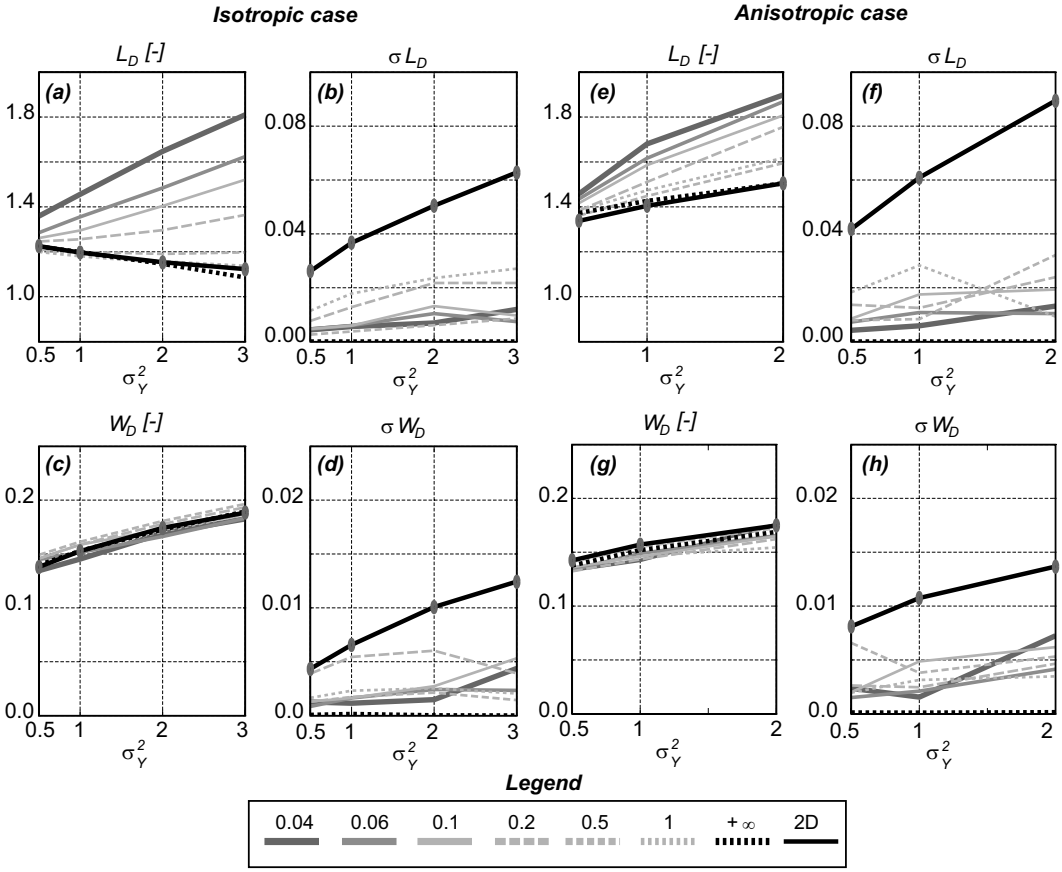

Fig. 10 Evolution of the dimensionless criteria as a function of increasing *ln(K)* variance. Note that 2D results (solid black line) are compared to each 3D model results with increasing l_y from 0.04 (dark gray line) to +∞ (dashed black line).

5. From 2D to 3D

The previous sections have shown that the behaviour of 3D SWI models is generally different from those of 2D models sharing the same statistical parameters of the hydraulic conductivity fields (except of course the correlation length in the direction perpendicular to the section). This shows that forecasts based only on 2D sections may be inaccurate. In the following, we propose a technique to modify the

statistical parameters of the 2D heterogeneous simulations in such a way that we can approximate the results of a 3D analysis which would be more CPU demanding. In addition, the modification of the 2D hydraulic conductivity fields will allows the comparison between 2D and 3D field sharing the same effective directional hydraulic conductivities.

5.1 2D hydraulic conductivity fields transformation

The basic idea of the proposed methodology is to generate a 2D field having the same correlation lengths and effective hydraulic conductivities in the x and z directions than a 3D field. Assuming a multiGaussian random function and assuming that its parameters in 3D are known, it is possible to express the geometric mean μ_g^{2D} and the variance σ^2_{Y2D} of the 2D field from the statistical parameters of the 3D field.

To derive the relation, we first define the correlation lengths of the two fields:

$$\lambda_x^{2D} = \lambda_x^{3D} = \lambda_x\,,\ \lambda_z^{2D} = \lambda_z^{3D} = \lambda_z \text{ and } \lambda_y^{3D} = \lambda_y \tag{18}$$

Using Ababou's (1996) expression (eq. 15) in 2D and 3D, and stating that the 2D and 3D components of the effective conductivity should be identical, one gets a system of 2 equations with 2 unknowns (μ_g^{2D} and σ^2_{Y2D}):

$$\mu_g^{2D}\exp\left(\sigma^2_{Y2D}\left[\frac{1}{2}-\frac{1}{2}\frac{\lambda_h^{2D}}{\lambda_x}\right]\right) = \mu_g^{3D}\exp\left(\sigma^2_{Y3D}\left[\frac{1}{2}-\frac{1}{3}\frac{\lambda_h^{3D}}{\lambda_x}\right]\right) \tag{19}$$

and

$$\mu_g^{2D}\exp\left(\sigma^2_{Y2D}\left[\frac{1}{2}-\frac{1}{2}\frac{\lambda_h^{2D}}{\lambda_z}\right]\right) = \mu_g^{3D}\exp\left(\sigma^2_{Y3D}\left[\frac{1}{2}-\frac{1}{3}\frac{\lambda_h^{3D}}{\lambda_z}\right]\right) \tag{20}$$

μ_g^{3D} and σ^2_{Y3D} are the known mean and variance of the 3D field. λ_h^{2D} and λ_h^{3D} are the harmonic means of the correlation lengths in 2D and 3D:

$$\lambda_h^{2D} = \frac{2\lambda_x\lambda_z}{\lambda_x+\lambda_z},\quad \lambda_h^{3D} = \frac{3\lambda_x\lambda_y\lambda_z}{\lambda_x\lambda_y+\lambda_x\lambda_z+\lambda_y\lambda_z} \tag{21}$$

From (19), an expression of μ_g^{2D} can be obtained and inserted in (20) to get first the relation between the variance of the 2D field and the one of the 3D field and then an expression of the geometric mean of the 2D field:

$$\sigma^2_{Y2D} = \frac{2}{3}\frac{\lambda_h^{3D}}{\lambda_h^{2D}}\sigma^2_{Y3D} \tag{22}$$

$$\mu_g^{2D} = \mu_g^{3D} \exp\left(\sigma_{Y3D}^2 \left[\frac{1}{2} - \frac{1}{3}\frac{\lambda_h^{3D}}{\lambda_h^{2D}}\right]\right) \quad (23)$$

In the case of statistically isotropic media $\lambda_h^{2D} = \lambda_h^{3D}$ and therefore equations (22) and (23) become:

$$\sigma_{Y2D}^2 = \frac{2}{3}\sigma_{Y3D}^2 \quad (24)$$

$$\mu_g^{2D} = \mu_g^{3D} \exp\left(\frac{\sigma_{Y3D}^2}{6}\right) \quad (25)$$

In summary, if one has an estimation of the correlation lengths in 3D and of the first two moments of the permeability distribution, assuming a multi-Gaussian distribution one can use equations (22) and (23) to compute the values μ_g^{2D} and σ^2_{Y2D} that should be used to model an heterogeneous 2D hydraulic conductivity field having the same effective conductivity than the 3D field.

5.2 Numerical test

A numerical evaluation of the transformation was carried out. For each of the cases described earlier in the chapter (isotropic and anisotropic cases described in section 3.1), 100 2D simulations were generated with the parameters of the 3D models (μ_g^{3D} and σ^2_{Y3D}), 100 2D* simulations were generated with transformed parameters (μ_g^{2D} and σ^2_{Y2D}) according to equations (22) and (23). In total, 49 3D hydraulic conductivity fields are compared separately with 49 × 100 2D simulations.

The comparison is made in terms of absolute error (*ae*) of the relative concentrations over the whole domain, such as:

$$ae(i,j) = \left|\overline{C_D^{3D}(i,j)} - \overline{C_D^{2D}(i,j)}\right| \quad (26)$$

where *i* and *j* are the indices of model cells on the grid, $\overline{C_D^{3D}}$ is the spatial ensemble average in the direction perpendicular to the section on one 3D realisation and $\overline{C_D^{2D}}$ is the ensemble average over 100 2D simulations at node (*i,j*).

The obtained results are in agreement with those obtained in the previous sections. The 2D transformed fields (Figs. 11b and 12b) reproduce much better the mean concentrations computed in 3D than the 2D untransformed fields (Figs. 11a and 12a) for all the values of variances that have been tested. However, the uncertainty on the position of the isoline $C^{0.5}{}_D$ seems to be systematically slightly

larger for the transformed 2D fields than for the 3D models (Figs 11c and 12c); in any case the 2D estimations of uncertainty on $C^{0.5}{}_D$ are systematically bounding the 3D ones. Similarly the relative errors on L_D are reduced very significantly when comparing the 2D transformed fields with the 2D original fields (compare Figs. 9 and 13). Before the 2D transformation, the relative error on the saltwater penetration could reach 38 % for a variance of 3. By transforming the 2D field, the error is reduced in general to less than 5 %. The width of the mixing is however not better reproduced when considering the transformed fields. It is worth noting that errors due to the ergodicity limitation may partly explain the misfit between 2D* and 3D predictions for larger *ly* correlations lengths (l_y>0.12).

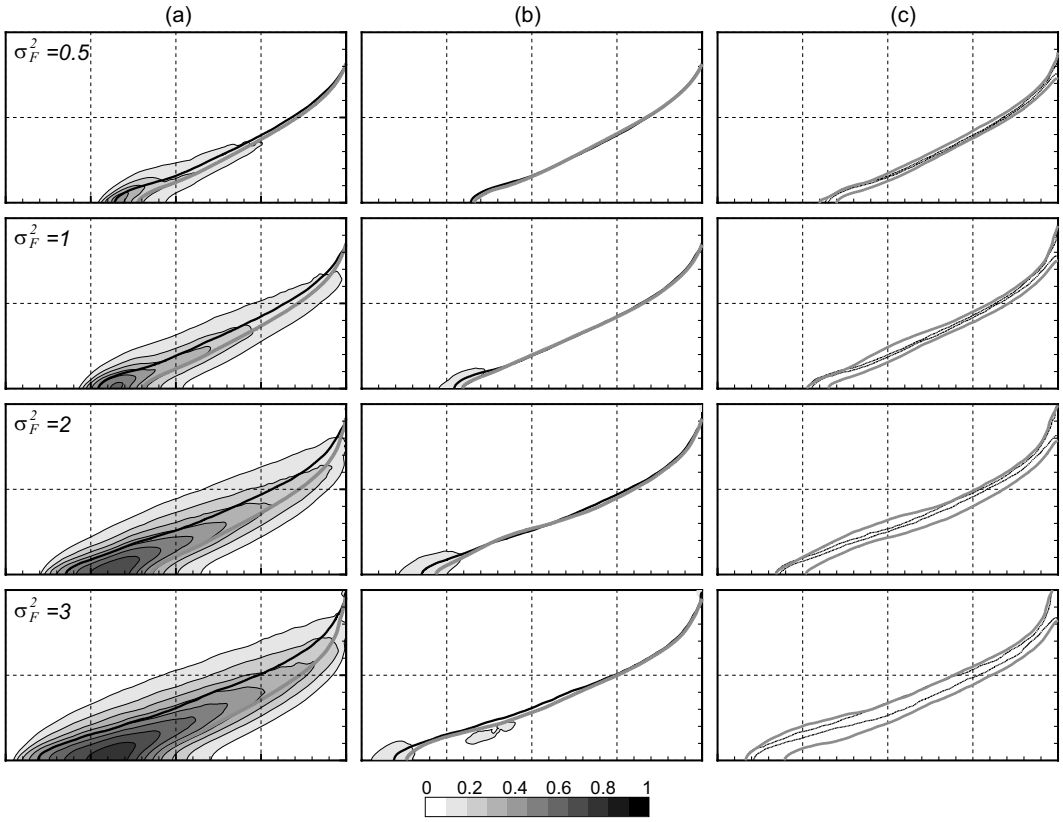

Fig. 11 Comparison between 2D, 2D* and 3D isotropic cases (l_x=l_y=l_z=0.04) for different level of *ln(K)* variances. (a) 3D spatial average concentration $C^{0.5}{}_D$ (solid black line), 2D ensemble average concentration $C^{0.5}{}_D$ before correction (gray lines) and the absolute error (*ae*) in background. (b) Same as (a) but after transformation of the 2D hydraulic conductivity field (2D*). (c) 95% Confidence interval (mean $\pm$ 2 standard deviation) of the relative salt concentration $C^{0.5}{}_D$ of 3D (black lines) and 2D* (gray lines).

It has been shown in the previous sections (4.3 and 4.4) that the differences between 2D and 3D simulations were mainly due to a larger effective hydraulic conductivity in the main flow direction in the 3D models as compared to the 2D ones (both sharing identical statistics of the hydraulic conductivity fields). In addition, more variability of the velocity field in 2D models yielded more dispersion and thus reduced the magnitude of the density driven forces. This results in a shorter toe penetration and larger width of the mixing zone (rotation of the saltwater wedge) in 2D. The proposed transformation allows reducing the differences between the 2D and the 3D forecasts because not only it allows increasing the effective hydraulic conductivity in the main flow direction, but it also reduces the variability of a 2D field when comparing the 2D untransformed and transformed fields.

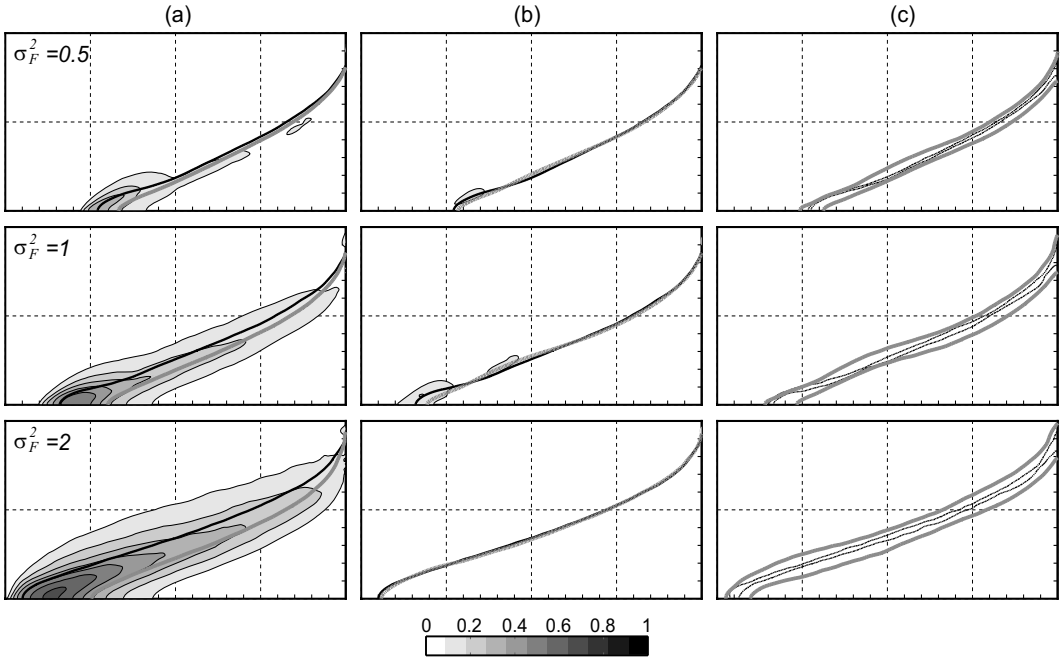

Fig. 12 Comparison between 2D, 2D* and 3D anisotropic cases (l_x=0.12, l_y=l_z=0.04) for different levels of *ln(K)* variances. (a) 3D ensemble spatial average concentration $C^{0.5}{}_D$ (solid black line), 2D ensemble average concentration $C^{0.5}{}_D$ before correction (gray lines) and the absolute error (*ae*) in background. (b) Same as (a) but after transformation of the 2D hydraulic conductivity filed (2D*). (c) 95% Confidence interval (mean $\pm$ 2 standard deviation) of the relative salt concentration $C^{0.5}{}_D$ of 3D (black lines) and 2D* (gray lines).

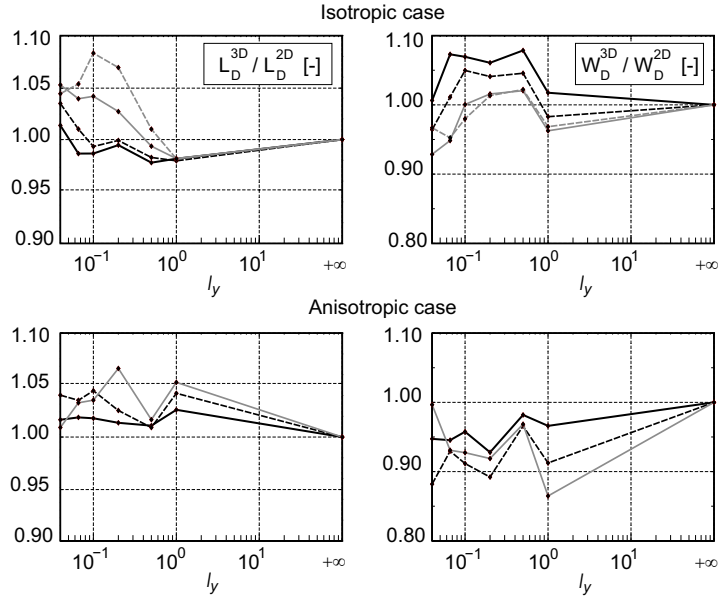

Fig. 13 Dimensionless norms comparison between 2D and 3D for different level on *ln(K)* variance (solid black line for σ_Y^2=0.5, dashed black line for σ_Y^2=1, solid gray line for σ_Y^2=2 and dashed gray line for σ_Y^2=3).

To conclude this section, an important advantage of the proposed transformation is that it may allow to estimate the uncertainty on the position of the interface for a 3D problem by running 2D Monte Carlo simulations in 2D. This can save considerable CPU time (Table 6).

Table 6 Comparison between 2D and 3D CPU time requirements

Model Configuration	Number of nodes	Seconds of CPU time	Relative CPU time
Two-dimensional	33'153 (257 x 129)	180	1.00
Three-dimensional	4'276'737 (257 x 129 x 129)	135000	750.00

6. Summary and conclusions

The study of the effects of heterogeneity of hydraulic conductivity and the effects of dimensionality revealed that modelling seawater intrusion in 2D heterogeneous media may be very different from modelling it in 3D heterogeneous ones sharing the same statistics of hydraulic conductivity distribution. Depending on heterogeneity characteristics, especially dimensionality, correlation lengths ratios and extent, as well as the degree of variance of the hydraulic conductivity distribution, the behaviour of saltwater wedge is variable and rather complex.

In 2D, our results are in agreement with previous studies (Abarca, 2006; 2007a) and showed that the toe penetration is highly controlled by the horizontal hydraulic conductivity and both horizontal and vertical dispersivities. The width of the mixing zone is mainly controlled by dispersion. In this study, it has been demonstrated that the same parameters (i.e. horizontal hydraulic conductivity and both horizontal and vertical dispersivities) are controlling the behaviour of the saltwater wedge for both 2D and 3D configurations. When the effective horizontal hydraulic conductivity increases, toe penetration length increases too. However, in the 2D isotropic cases, an increase of the dispersivities due to an increase of hydraulic conductivity distribution variance resulted in a backward movement of the saltwater wedge. This was partly explained by the fact that dispersion acts against density-driven forces. An interesting result of this study with regard to the particular case of isotropic media is that there is a critical ratio between advection and dispersion processes for which the toe moves forward or backward, or even remains constant when the heterogeneity level increases. For the 2D and 3D anisotropic cases, both the toe penetration length and the width of the mixing zone increase when σ_Y. increases.

The comparison between SWI in heterogeneous and homogenous models sharing the same effective hydraulic conductivities showed that the 2D heterogeneity is affecting more strongly the SWI processes than the 3D heterogeneity. This was observed when comparing the uncertainties related to the concentration distributions resulting from 2D and 3D heterogeneous models predictions, but also when increasing σ_Y. At the same time, the uncertainty is the largest for the toe and outflow areas where both dispersivities are the most affecting solute transport. This is in agreement with the Held et al. (2005) study. For weakly heterogeneous media (σ_Y<1), the effective hydraulic conductivity together with local values of dispersivities can be adequate to model the SWI phenomenon in an equivalent homogenous 2D medium (Held et al., 2005). Yet, for strongly heterogeneous media, we showed that using local values of dispersivities can be inaccurate. However, we could not propose an adequate model to estimate the effective dispersivities with respect to the setting adopted in this study.

Another interesting finding is that it is possible to transform a 2D hydraulic conductivity field in such a way that it can reproduce more accurate 3D SWI predictions. It has been shown that dispersivities are larger in 2D fields than in 3D ones because of higher variability in the velocities (especially the vertical one), while higher effective hydraulic conductivities are in 3D models sharing the same statistics. Transforming the geometric mean (increasing it) and the variance

(decreasing it) of the hydraulic conductivity distribution of a 2D field allows to reduce the differences between 2D and 3D configurations. Yet, reducing the 3rd dimension reduces the number of paths that flow and solute can take which affects especially dispersion as highly controlling density-dependent processes.

It is worth noting that increasing the effective hydraulic conductivities of a 2D model so that it behaves like a 3D anisotropic Henry problem will result in a decrease of the dimensionless parameter *a*, comparing viscous to buoyancy forces meaning an increase of density effects and therefore more accurate exemplification of SWI.

Finally, a comparison between the numerical results obtained in the present study with the solutions of existing analytical models (Dagan and Zeitoun, 1998; Naji et al., 1998; Al-Bitar and Ababou, 2005; Abarca et al., 2007a) is of high interest especially from a practical point of view. Appendix C presents some of those solutions and tests them numerically.

References

Ababou, R., 1996. Random Porous Media Flow on Large 3D Grids: Numerics, Performance, and Application to Homogenization. Chap.1 (pp. 1-25), IMA Vol.79 Math. & Appli.: Environmental studies, mathematical, computational & statistical analysis. M. F. Wheeler (ed.), Springer, New-York, 410 pp.

Abarca, E., 2006. Seawater intrusion in complex geological environments, Technical University of Catalonia, Barcelona, Barcelona, 154 pp.

Abarca, E., Carrera, J., Sánchez-Vila, X. and Dentz, M., 2007a. Anisotropic dispersive Henry problem. Advances in Water Resources, 30: 913-926.

Abarca, E., Carrera, J., Sanchez-Vila, X. and Voss, C.I., 2007b. Quasi-horizontal circulation cells in 3D seawater intrusion. Journal of Hydrology, 339(3-4): 118-129.

Al-Bitar, A. and Ababou, R., 2005. Random field approach to seawater intrusion in heterogeneous coastal aquifers: unconditional simulations and statistical analysis. In: Geostatistics for Environmental Applications. Renard P., Demougeot-Renard H., Froidevaux R. Eds. Springer.

Badon-Ghyben, W., 1888. Nota in verband met de voorgenomen putboring nabij Amsterdam [Notes on the probable results of well drilling near Amsterdam] In: Tijdschrift van het Kononklijk Instituut van Ingenieurs The Hague. vol. 9: 8-22.

Bear, J., 1999. Conceptual and mathematical modeling. In: J. Bear, A.H.-D. Cheng, S. Sorek, D. Ouazar and I. Herrera (Editors), Seawater intrusion in coastal aquifers - Concepts, Methods and Practices. Kluwer Academic, Dordrecht, pp. 127-161.

Bear, J., 2005. Sea Water Intrusion Into Coastal Aquifers. Encyclopedia of Hydrological Sciences. John Wiley & Sons.

Brovelli, A., Mao, X. and Barry, D.A., 2007. Numerical modeling of tidal influence on density-dependent contaminant transport. Water Resources Research, 43: W10426.

Burnett, R.D. and Frind, E.O., 1987. Simulation of Contaminant Transport in 3 Dimensions .2. Dimensionality Effects. Water Resources Research, 23(4): 695-705.

Cornaton, F., 2007. Ground Water: A 3-D Ground Water Flow and Transport Finite Element Simulator. Reference Manual, 190 pp. http://www1.unine.ch/chyn/php/softwares.php.

Croucher, A.E. and O'Sullivan, M.J., 1995. The Henry Problem for seawater intrusion. Water Resouces Research, 31(7): 1809-1814.

Dagan, G. and Bear, J., 1968. Solving the problem of local interface upconing in a coastal aquifer by the method of small perturbations. Journal of Hydraulic Research, 6: 15-44.

Dagan, G. and Zeitoun, D.G., 1998. Seawater-freshwater interface in a stratified aquifer of random permeability distribution. Journal of Contaminant Hydrology, 29(3): 185-203.

Darvini, G., Spendolini, L. and Salandin, P., 2002. Saltwater intrusion for finite Peclet numbers in random permeability aquifers, Developments in Water Science. Elsevier, pp. 523-530.

de Marsily, G. et al., 2005. Dealing with spatial heterogeneity. Hydrogeology Journal, 13(1): 161-183.

Dentz, M., Kinzelbach, H., Attinger, S. and Kinzelbach, W., 2000. Temporal behavior of a solute cloud in a heterogeneous porous medium 1. Point-like injection. Water Resources Research, 36(12): 3591-3604.

Diersch, H.-J.G. and Kolditz, O., 2002. Variable-density flow and transport in porous media: approaches and challenges. Advances in Water Resources, 25: 899–944.

Fetter, C.W., 1972. Position of Saline Water Interface beneath Oceanic Islands. Water Resources Research, 8(5): 1307-&.

Gelhar, L.W., 1986. Stochastic Subsurface Hydrology from Theory to Applications. Water Resources Research, 22(9): S135-S145.

Gelhar, L.W., 1993. Stochastic Subsurface Hydrology. Prentice-Hall, Upper Saddle River, N. J., 385 pp.

Gelhar, L.W. and Axness, C.L., 1983. 3-Dimensional Stochastic-Analysis of Macrodispersion in Aquifers. Water Resources Research, 19(1): 161-180.

Glover, R.E., 1959. The Pattern of Fresh-Water Flow in a Coastal Aquifer. Journal of Geophysical Research, 64(4): 457-459.

Held, R., Attinger, S. and Kinzelbach, W., 2005. Homogenization and effective parameters for the Henry problem in heterogeneous formations. Water Resouces Research, 41(W11420): 1-14.

Henry, H.R., 1964. Effects of dispersion on salt encroachment in coastal aquifers. Geological Survey, Water-Supply Paper 1613-C.

Herzberg, A., 1901. Die Wasserversorgung einiger Nordseebader (the water supply of parts of the North Sea coast in Germany). Journal fuer Gasbeleuchtung und Verwandete Beleuchtungsarten sowie fuer Wasserversorgung, 44: 815-819, and 45: 824-844.

Huyakorn, P., Wu, Y.S. and Park, N.S., 1996. Multiphase approach to the numerical solution of a sharp interface saltwater intrusion problem. Water Resouces Research, 32(1): 93-102.

Matheron, G., 1967. Éléments pour une théorie des milieux poreux. Masson & Cie, Paris, 166 pp.

Matheron, G., 1973. The intrinsic random functions and their applications. Advances in Applied Probability, 5: 439-468.

Pohll, G.M., Warwick, J.J. and Benson, D., 2000. On the errors associated with two-dimensional stochastic solute transport models. Transport in Porous Media, 40(3): 281-293.

Reilly, T.E. and Goodman, A.S., 1985. Quantitative-Analysis of Saltwater Fresh-Water Relationships in Groundwater Systems - a Historical-Perspective. Journal of Hydrology, 80(1-2): 125-160.

Renard, P. and deMarsily, G., 1997. Calculating equivalent permeability: A review. Advances in Water Resources, 20(5-6): 253-278.

Sanchez-Vila, X., Guadagnini, A. and Carrera, J., 2006. Representative hydraulic conductivities in saturated groundwater flow. Reviews of Geophysics, 44(3).

Schwarz, C., 1999. Dichteabhängige strömungen in homogenen und heterogenen porösen medie, Swiss Federal Institute of Technology, Zurich, Zurich.

Shapiro, A.M. and Cvetkovic, V.D., 1990. A Comparison of 2-Dimensional and 3-Dimensional Stochastic-Models of Regional Solute Movement. Transport in Porous Media, 5(1): 1-25.

Simmons, C.T., Fenstemaker, T.R. and Sharp, J.M., 2001. Variable-density groundwater flow and solute transport in heterogeneous porous media:

approaches, resolutions and future challenges. Journal of Contaminant Hydrology, 52(1-4): 245-275.

Simpson, M.J. and Clement, T.P., 2004. Improving the worthiness of the Henry problem as a benchmark for density-dependent groundwater flow models. Water Resources Research, 40(1).

Strack, O.D.L., 1976. Single-Potential Solution for Regional Interface Problems in Coastal Aquifers. Water Resources Research, 12(6): 1165-1174.

Tompson, A.F.B., Ababou, R. and Gelhar, L.W., 1989. Implementation of the 3-Dimensional Turning Bands Random Field Generator. Water Resources Research, 25(10): 2227-2243.

Voss, C.I. and Souza, W.R., 1987. Variable density flow and transport simulation of regional aquifers containing a narrow freshwater-saltwater transition zone. Water Resouces Research, 23(10): 1851–1866.

Welty, C. and Gelhar, L.W., 1991. Stochastic-Analysis of the Effects of Fluid Density and Viscosity Variability on Macrodispersion in Heterogeneous Porous-Media. Water Resources Research, 27(8): 2061-2075.

Welty, C., Kane, A.C. and Kauffman, L.J., 2003. Stochastic analysis of transverse dispersion in density-coupled transport in aquifers. Water Resources Research, 39(6).

Chapter 3

Status of the Korba groundwater resources (Tunisia): Observations and 3D modelling of seawater intrusion*

Abstract This chapter focuses on a case study of seawater intrusion in the Korba aquifer located in the east of the Cape Bon peninsula, Tunisia. The main objective is to quantify the components of the regional groundwater mass balance. Firstly, the chapter presents a review of the previous studies on the site as well as a detailed description of the regional hydrogeological settings and the status of the groundwater resources in 2004. Secondly, a 3D density-dependent flow and solute transport model is developed. This part starts with an estimation of model input parameters based on the existing data and recent field experiments, including electrical resistivity tomography. After, the spatial distribution of the pumping rates distribution was estimated using a multivariate linear regression model combining secondary variables, including aquifer properties and distributed data from remote sensing analysis. The gathered knowledge was then used to build and to calibrate a 3D transient model of 44 years time period (1960-2004). The numerical model was used further to discuss some issues on the management of the regional groundwater resources. The calibration of the 3D model has been achieved in a time dependent, iterative and semi-automatic fashion. Simulations results showed that the current over-exploitation (outputs/inputs) of the Korba aquifer is about 135%. In addition, the model allowed to estimate the time lapse needed to turn back the initial head and slat distributions (before exploitation starts) to about 150 years.

* This chapter is based on the paper:
Kerrou J., Renard P. and Tarhouni J. (2008) Status of the Korba groundwater resources (Tunisia): Observations and 3D modelling of seawater intrusion. Submitted to Journal of Hydrology

1. Introduction

The Korba coastal plain is located in the east of the Cape Bon peninsula in north-eastern Tunisia (Fig. 1). It encompasses an area of around 40 km length and 10 km width, bounded by the Mediterranean Sea along the eastern border. The study area is characterised by a semiarid climate with an average annual precipitation of 420 mm (INM 2001). The difference in precipitation, as compared to the rest of Tunisia, where the average annual precipitation is around 220 mm (INM 2001) is significant. That is one of the reasons why the Cape Bon was always one of the most productive agricultural areas in Tunisia. This, together with the population growth in the country: from 3.78 Mio. inhabitants in 1956 to 9.91 Mio. in 2004 (INS 2004), and the developing economy, has greatly increased the demand of freshwater. Since 1960, groundwater has become a major resource of freshwater in the Cape Bon area and has been solicited mainly for agricultural purposes. The exploitation of the Korba aquifer has increased linearly from 270 wells pumping 4 Mm^3 in 1962 (Ennabli 1980) to more than 8 000 wells pumping 50 Mm^3 in 1985 (DGRE 1985). This increase resulted in a regional depletion of the groundwater table and the consequent salinization caused by seawater intrusion in the Korba aquifer (Tarhouni et al. 1996).

These problems are common to a large number of costal aquifers worldwide (Bear et al. 1999; Custodio 2002; Cheng and Ouazar 2003; Konikow and Kendy 2005). The depletion of the groundwater table in the Korba aquifer was first observed in the early 70's. Yet, the salinization by seawater intrusion was not recognized as a serious threat for local groundwater resources until the mid-80's. This situation has motivated numerous studies in the Korba aquifer.

Ennabli (1980) presented a detailed description of the regional geology and the main aquifers as well as the state of the groundwater resources in 1977. With the existing data at that time, Ennabli developed a first conceptual model of the aquifer system. A 2D numerical model allowed Ennabli (1980) to estimate the areal recharge in the range of 5-8 % of the average annual precipitation (21-34 mm/year), a transmissivity ranging from $5 \cdot 10^{-5}$ to 10^{-2} m^2/s and an average porosity of 0.12. This value, together with an estimated seasonal head variation of 0.88 m (Ennabli 1980), allowed a first estimation of the groundwater regulatory reserve. Tarhouni et al. (1996) used a geochemical approach to determine the origin of aquifer salinization and showed that seawater intrusion is the main source of salt pollution. Khlaifi (1998) described the state of the resource in 1996 and showed that there is a piezometric depression of 5 m below mean sea level around Diar El Hojjej in the

central part of the aquifer (Fig. 1) and the salinization of wells up to 1.5 km inland (up to 7 g/l). This resulted in the abandonment of hundreds of wells close to the sea. Paniconi et al. (2001) elaborated a 3D numerical model of the status of the Korba aquifer in the late 90's. The authors showed the ability of the CODESA-3D code (Gambolati et al. 1999) to handle regional scale seawater intrusion settings and the validity of using numerical models to investigate different groundwater management scenarios. However, the scenarios investigated by Paniconi et al. (2001) did not match expected groundwater mass balances, especially with regard to pumping rates.

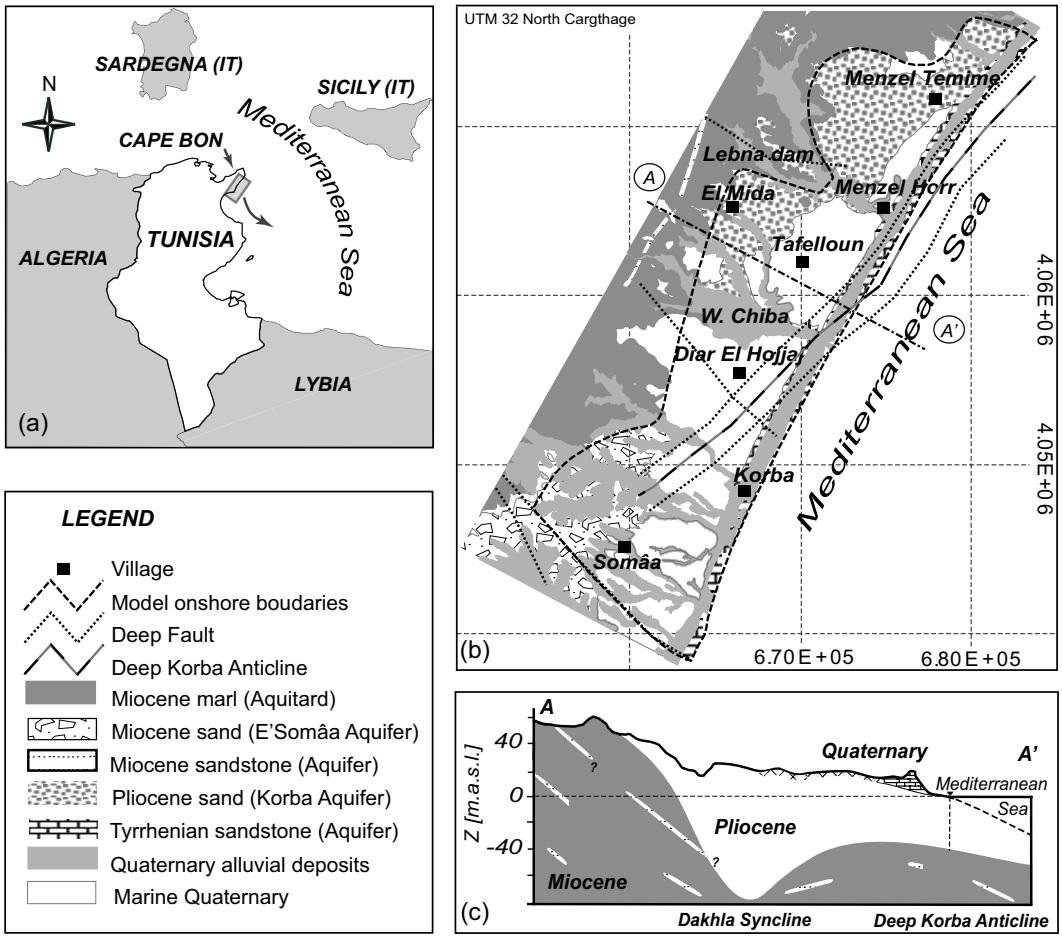

Fig. 1 (a) Location of the Korba aquifer (b) geological setting (square size is 10 x10 km) (c) simplified cross-section.

In addition to lack of sufficient data describing the hydraulic properties of the Korba aquifer, a particular difficulty encountered in the estimation of the mass balance is due to the scarcity of data and the large uncertainty on the pumping rates of thousands of private wells in the region. In 2000, the local water management authorities inventoried more than 9 000 wells pumping altogether around 50 Mm^3/year (DGRE 2000). Most of these wells are located in very small private farms and are traditionally dug and equipped with oil motor pumps. None of those wells is equipped with a flowmeter and no survey has ever been made to exhaustively estimate the pumping rates. To make things worse, the local authorities use an administrative delimitation of the regional aquifers which does not correspond to their physical extent. Indeed, a good knowledge of the withdrawn volumes of groundwater is crucial to understand the dynamics of the aquifer, to further model seawater intrusion and to address optimal management scenarios.

A major issue in the Korba plain is how much groundwater can be exploited in a sustainable way, thus preventing seawater intrusion. Despite the governmental efforts to develop alternative sources of freshwater (construction of dams, water by-passes from the north of the country, distribution of efficient irrigation systems, reuse of treated waste water and artificial recharge of the aquifer), farmers still need to exploit the groundwater resources.

This chapter describes a quantitative study of seawater intrusion in the Korba coastal aquifer. The main objectives of this work are: i) to describe a recent state of the regional groundwater system by analyzing the existing data and data from recent field investigations; ii) to apply different methods to estimate the freshwater mass balance components, with special focus on the abstraction volumes; iii) to use the gained knowledge to elaborate a transient 3D density-dependent flow and transport model to gather better understanding of the aquifer dynamics.

This chapter is organized as follows. Existing knowledge of the Korba aquifer is presented in section 2. The 3D numerical model development is described in section 3. Section 3.1 summarizes the estimation of flow and transport parameters from existing data and field experiments, including vertical salinity and electrical resistivity tomography logging. Then, an analysis of the spatial and temporal distribution of areal recharge by infiltration of precipitation using the daily Thornthwaite and Mather method is presented over a time span of 44 years (Section 3.1.3). To estimate the pumping rates over the whole aquifer, a regression model is developed from a stack of plausible explanatory exhaustive variables describing the state of the aquifer, its properties as well as data from remote sensing analysis (Section 3.1.4).The conceptual model of the Korba aquifer is presented in Section

3.2. Details of a 3D density-dependent flow and salt transport are summarized in Section 3.3. Calibration of the above-mentioned model is described in Section 3.4. Sections 4 and 5 present and discuss respectively the results of the simulations of groundwater mass balance and head and salt concentrations distributions. This chapter ends with a set of conclusions and recommendations with regard to the management of the regional groundwater resources.

2. The Korba aquifer system

The data sets used in this study were provided mainly by the Institut National Agronomique de Tunisie (INAT) and the local groundwater management authority (CRDA Nabeul). Data were compiled in a geographic information system (GIS). Data sets include: rainfall, potential evapotranspiration, soil distribution map, land cover maps from 1996, geographical information (ephemeral streams, salt lakes, etc.), geological logs, transmissivity values estimated from pumping tests, piezometric levels, and Total Dissolved Solids measurements. In order to complete the data set and for describing a recent state of the Korba aquifer, additional field investigations were carried out in August 2004. These include well leveling, water table depth measurements and vertical salinity logs at selected wells.

2.1 Geological setting

The inland lateral extension of the Korba aquifer follows the outcropping geological boundaries (Fig. 1). The geology of the Cape Bon peninsula and its structural evolution is described by Ennabli (1980) and Bensalem (1992; 1995). Three main geological units of marine Quaternary, Pliocene and late Miocene ages constitute the Korba aquifer system (Fig. 1b). The Tyrrhenian Quaternary forms a 1.2 km wide strip parallel to the coastline all along the study area (Figs. 1b and 1c). It is made of arenitic limestones overlying conglomeratic units (Oueslati 1994) with a total thickness ranging between 10 to 50 m.

The second unit, which represents the main aquifer, was formed during the Pliocene by marine deposits in the Dakhla synclinal north of Korba city (Fig 1c). The Dakhla syncline was formed during the Atlasic folding phase. It presents a north-east to south-west axis and is bounded by the Djebel Sidi Abderrahmane (639 m) anticline to the west and by the deep Korba anticline to the east (Figs. 1b and 1c). The lithology of the Pliocene formation is dominantly yellow sand with clay and sandstone intercalations. Laterally, the facies changes southward to more differentiated clay, sand and sandstone layers. The thickness of the Pliocene

formation is about 80 m in the central part of the area, reaches 250 m offshore, and decreasing towards the west (Fig. 1b). Note however that the thickness of the Pliocene sands in the north of Korba city is still unknown. Yet, it is believed to be small. Since the regression of the Pliocene sea, during the Quaternary and until today, the central part of the area was filled with alluvial material (Fig. 1b) deposited by wadi Chiba (wadi: dry stream except during periods of rainfall) and its effluents (Ennabli 1980).

The third unit, called "The Somâa sands", is of late Miocene age and found only to the south of the study area (Bensalem 1998). This unit is mainly composed by thick fine sand layers of continental origin including conglomeratic levels and clay lenses. To the south of the area, the thickness of the Somâa formation might exceed 400 m. Data from offshore oil wells allowed a better characterization of the aquifer system bellow the Mediterranean Sea. These data showed that the Pliocene and Somâa formations extend 2 to 5 km offshore where they thicken.

The geological aquifer units overly (with an angular discordance) mid-Miocene marls which form the base of the system (Figs. 1c). This aquitard may contain lenticular sandstone and clay-sandstone bars of variable thickness and depth but often separated by thick layers of impervious marls for a total thickness of 1 200 m (Abbes and Polak 1981).

2.2 Regional hydrogeology

The Korba aquifer can be divided in two hydrogeological units: the Plio-Quaternary and the late Miocene units. Northern and southern aquifer limits were delineated from flow streamlines almost perpendicular to the sea (Figs. 2b and 2d). A south-east to north-west oriented deep fault (Fig. 1b) helps to delineate the contour of the southern limit. Marine and continental deposits are laterally connected, the late Miocene aquifer feeds the Pliocene unit upstream. Yet, their hydraulic properties are significantly different. The Plio-Quaternary unit is the most productive one. It is characterized by the highest hydraulic conductivities, ranging from 10^{-6} to 10^{-3} m/s while hydraulic conductivities at the Somâa formation are smaller (Ennabli 1980). More precisely, the Tyrrhenian sandstones are believed to form the most permeable unit, followed by the central part of the Pliocene (alluvial deposits), the Pliocene, the Somâa and, finally, the early Miocene formations. These differences can be observed on the hydraulic gradients (Fig. 2) which are ranging from 0.007 in the north to 0.014 in the south (in summer 2004). Ennabli (1980) proposed an average porosity of 0.12 for the whole aquifer system.

The Plio-Quaternary unit represents a typical unconfined coastal aquifer structure especially when it is outcropping (Fig. 1b) but might also be locally semi-confined due to less permeable lenses of large lateral extent. The Somâa unit in the southern part of the system is unconfined in the upstream area but confined close to the coastline where artesian wells existed until the mid 90's. Another difference between the northern and the southern parts of the aquifer is that the groundwater table is shallower in the Plio-Quaternary unit than in the Somâa making traditional implantation of wells easier.

In the following, the water balance of the Korba aquifer is presented starting with the inputs. The recharge of the aquifer by infiltration of precipitation is estimated to be less than 10 % of the 420 mm/year average annual rainfall (Ennabli 1980; Paniconi et al. 2001). The integration of this value over the area of interest (400 km^2) yields 17 Mm^3/year. Additional recharge from wadis and topographic depressions is also expected. Note however that the most important wadis in the region, Chiba, M'laabi and Lebna (Fig. 2a) were dammed upstream in 1963, 1964 and 1984, respectively. Other wadis such as Korba (Fig. 2a), which drain a watershed of 85 km^2, have an average annual runoff of 3.7 Mm^3/year (Hichri 2003). Nazoumou (2002) estimated the infiltration from wadis in an arid area in the centre of Tunisia to 30% of the annual runoff. According to that study, around 1.1 Mm^3/year will percolate from wadi Korba to the aquifer, 0.6 Mm^3/year from wadi Daroufa, 0.8 Mm^3/year from wadi Abids and 0.6 Mm^3/year from wadi El Malah (Fig. 2a). Artificial recharge in the region of Diar El Hojjej (Fig. 1) by direct infiltration of surface water from dams or from the Medjerda Cape-Bon canal started in 1999 but never exceeded 1 Mm^3/year (CRDA 2002). Other sources of recharge are irrigation return flow (believed to be important) and the lateral recharge by leakage (or through faults) from the underlying Miocene with sandstone are not yet evaluated.

On the other side, groundwater abstraction represents a major output. Indeed, the exploitation of the Korba aquifer began in the 60's mainly for irrigation purposes, and reached 43 Mm^3/year in the 80's. In 2000, the total groundwater exploitation was estimated to about 50 Mm^3 with more than 9000 active wells (DGRE 2000). It is worth noting that the number of wells is proportional to the number of farms. Regional groundwater is heavily exploited despite the efforts of the government to mobilize most of the regional surface water and to transport water from the north of the country via the Medjerda Cape-Bon canal. Moreover, in the beginning of the 90's, the government encouraged the farmers to adopt drip

irrigation systems by contributing to 60% of the cost of the installation in order to reduce water consumption. The result was that irrigated surfaces increased at the cost of the same water consumption. The sebkhas (salt lakes) forming a 5 km^2 strip all along the coastline, are suspected to be a groundwater discharge areas. Other outputs like submarine groundwater discharge (SGD) are not yet evaluated.

The above-mentioned incoming magnitudes allow estimating the total recharge in steady state and in the absence of pumping (before 1960). This is of the order of 25 Mm^3/year, which represents mostly the SGD. The total abstraction nowadays represents about twice the amount of recharge. Even without a precise estimation of the other components of the groundwater mass balance, it is self-evident that current overexploitation results in a depletion of the water table and a reduction of the SDG, which leads to an increase of seawater intrusion.

2.3 Piezometry and seawater intrusion characterization

Three piezometric maps and salinity data are available (Ennabli 1980; Khlaifi 1998; Paniconi et al. 2001). Figure 2 displays the evolution of the piezometric level in the Korba aquifer from 1962 to 2004 as well as the hydrographic network (Fig. 2a) and local dams according to their construction period. The piezometric maps of 1962 and 1977 (Figs. 2a and 2b) show that the hydraulic heads in the Korba aquifer were lowered below sea level after 1977 (most likely a few years later, in the 80's when aquifer exploitation reached 43 Mm^3). A visual comparison of figure 2a and 2b shows that damming wadi Chiba in 1963 caused a decrease of the groundwater table downstream due to a reduction of recharge by its effluents. In addition to the perturbation of surface water regime, the growth of groundwater abstraction during the 80's (51.5 Mm^3 in 1985) especially near the cost, lead to the apparition in 1996 of a concentric depression of 5 m below (Fig. 2c) sea level in the region of Diar El-Hojjej. This means that the hydraulic gradients were reversed mainly toward the central part of the aquifer leading to an acceleration of seawater intrusion. Indeed, hundreds of wells close to the cost were salinized and then abandoned despite the action of the government forbidding new wells in the area and distributing surface water. Years after, the depression of Diar El-Hojjej was attenuated and even disappeared, however, pumping migrated northward and led to the apparition of a critical depression of 12 m below sea level in 2004 (Fig. 2d). As opposed to the Chiba dam, the Lebna dam (constructed in 1984) had a positive effect on the aquifer recharge (compare Figs, 2b and 2d). Figure 2 also shows that the interaction between wadis and the aquifer has been perturbed. Using an average porosity of

0.12 (Ennabli 1980) and the depletion of heads from 1962 to 2004, it is possible to estimate that the total volume of groundwater stored in the central part of the Korba aquifer was reduced by 100 Mm^3.

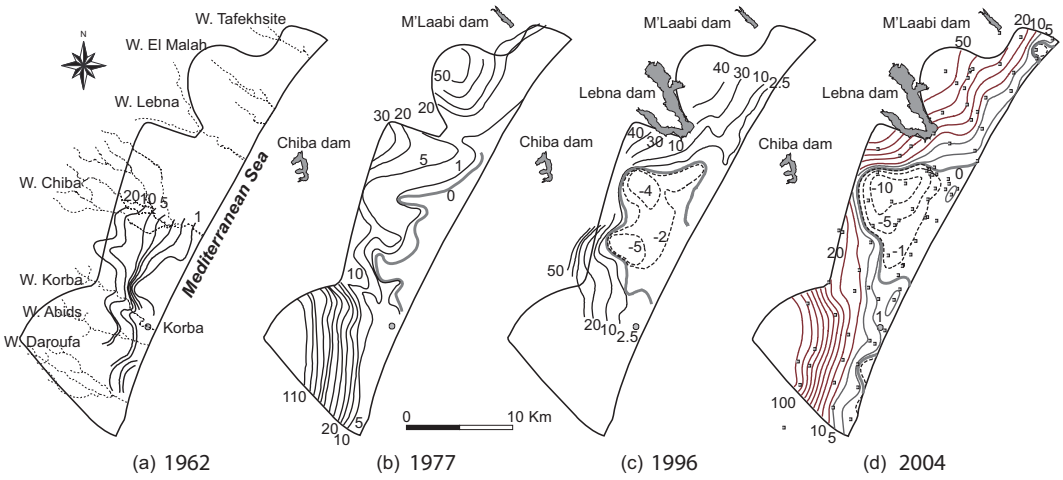

Fig. 2 Piezometric evolution: (a) 1962 from Ennabli (1980); (b) 1977 from Ennabli (1980); (c) December 1996 from Paniconi et al. (2001) and (d) August 2004. The 0 sea reference iso-contour is represented by the thick gray line. The hydrological network is depicted by dotted lines and the dams by gray polygons (Chiba built in 1963; M'Laabi built in 1964 and Lebna built in 1986).

Obviously, the salinity distribution in the Korba aquifer is correlated with the piezometric evolution. The vertical salinity profiles measured in August 2004 allowed to delineate a 3D distribution of salt concentrations in the aquifer by ordinary kriging (Fig. 3a). This facilitates a qualitative description of the state of the resource. These data also permit to describe the evolution of the seawater intrusion by comparing them with data from 1996 (Figs. 3b and 3c). The 3D map of the electrical conductivity displays a wide mixing zone which is clearly affecting the region of Diar El-Hojjej in the central part of the aquifer. The same figure also shows vertical saltwater up-coning near points 3 and 4 (Fig. 3a). In 2004, the well IRH N° 11186 (n° 4 in Fig. 3), at 1.55 km inland presented Total Dissolved Solid (TDS) values ranging between 7 and 25 g/l, confirming the inland seawater encroachment. Based on data from 1996 and 2004 at points 4 and 5 separated by around 1 km, and considering a 0.5 relative concentration, a minimum seawater intrusion velocity in the Korba aquifer is approximately 100 m/year.

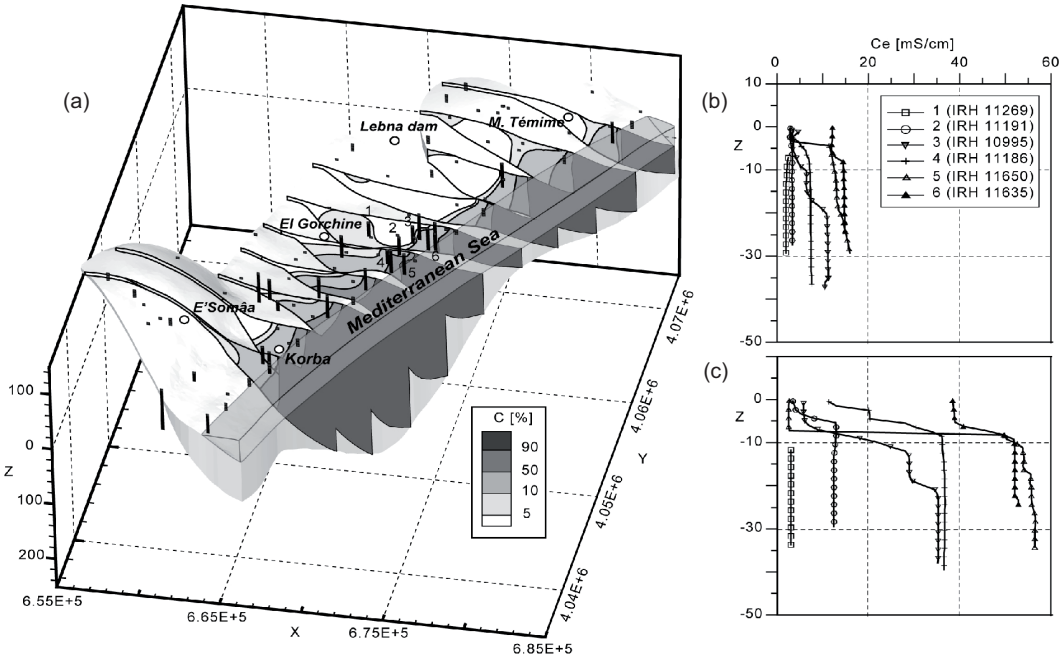

Fig. 3 Salinity description: (a) three-dimensional kriging of 854 data (August 2004 vertical logs and surface measures in black squares); (b) Vertical salinity logs in December 1996; (c) vertical salinity logs in August 2004.

Another feature arising from the 3D salinity map is the effect of the Lebna dam which allowed to maintain high heads and low salinity of groundwater in its surroundings, due to the large volumes infiltrated into the aquifer. In the same figure, it can also be seen that salt recycling plays a role in the salinization of the aquifer (Milnes and Renard 2004) far from the sea (see around Gorshine and upstream in Fig. 3a). Grava (2005) showed that there is a strong correlation between nitrate (NO_3) and chloride (Cl^-) concentrations meaning that irrigation return flow is accelerating the salinization of the aquifer.

3. The Korba aquifer numerical model development

In view of existing data and prior studies, there are still many unknowns about the behaviour of the Korba aquifer. Moreover, the components of the regional groundwater mass balance remain uncertain or unknown. Developing a new 3D numerical model will help to integrate all existing knowledge and data on the Korba aquifer, for a better understanding of its dynamics, and eventual use as a solid basis for the design of management policies. This section is organized as follows. First,

the ingredients for building a conceptual model are presented. Next, the conceptual model is detailed (Section 3.2). Details on the numerical model are presented in Section 3.3. Finally, the model calibration procedure is summarized in section 3.4.

3.1 Model parameters

3.1.1 Aquifer geometry

The geometry of the reservoir is rather well known. Data from different sources (the work by Ennabli (1980), recent borehole lithostratigraphic logs and oil well logs) were combined to delineate the main aquifer formations and were used to interpolate by ordinary kriging the bedrock topography (Figs. 1, 8 and 9). In addition, a digital elevation model (DEM) was interpolated by ordinary kriging high resolution data provided by the Tunisian Institute of Topography. The DEM was combined with the piezometric map of 1962 to build a hypothetical distribution of hydraulic heads in 1960. The latter was used as the top layer of the numerical model and for the calibration of the steady state regime. Both the bedrock and the steady state head maps allowed to compute a map of the saturated aquifer thickness, and, therefore, of the aquifer geometry. This is not only important for the groundwater flow (e.g., for the integration of the hydraulic conductivities) but also for transport simulations to accurately estimate groundwater volumes. The resulting average saturated thickness is estimated to be about 40 m.

3.1.2 Flow and transport parameters

In addition to the qualitative classification of the permeabilities described in section 2.2, transmissivity data from 53 (short term) pumping tests were provided by the local water management authority. These arise from conventional interpretation (i.e., assuming a homogenous medium) of drawdown data. Transmissivity data, unequally distributed over the aquifer, were first classified by formation and then transformed in terms of hydraulic conductivities using the whole saturated thickness of the aquifer for fully penetrating wells and the length of the screen for the others. This resulted in 16 permeability data for the Pliocene formation and 37 for the Somâa one.

The geometric mean hydraulic conductivity and the variance of the natural logarithm of Pliocene permeabilities are 8.9 10^{-5} m/s and 0.67, respectively, and 1.1 10^{-5} m/s and 1.6 for the Somâa sands. Those data show that the Somâa formation is more heterogeneous than the Pliocene one. At the same time, average values of hydraulic conductivities as well as their variance are probably biased because wells

were most probably drilled in the highest transmissivity zones. Yet, the interesting point is that permeabilities of Pliocene sands are (in average) one order of magnitude larger than those of Somâa sands. These estimates will be used as initial guesses for the calibration of the model.

With regard to transport parameters, there are no tracer test data to allow estimation of local dispersivities. However, high resolution electrical resistivity tomography (ERT) was used to estimate the porosity of the Pliocene formation. The relationship between bulk resistivity of a fully saturated porous medium (ρ_r [Ohm·m]), its porosity (ϕ [-]) and the resistivity of the fluid within the pores (ρ_w [Ohm·m]) is expressed by Archie's law (Archie 1942) :

$$\rho_r = a\rho_w\phi^{-m} = F\rho_w \qquad (1)$$

where *m* and *a* are dimensionless material-dependent empirical factors; *m* is known as the cementation index; and *F* is Humble formula (Winsauer et al. 1952)

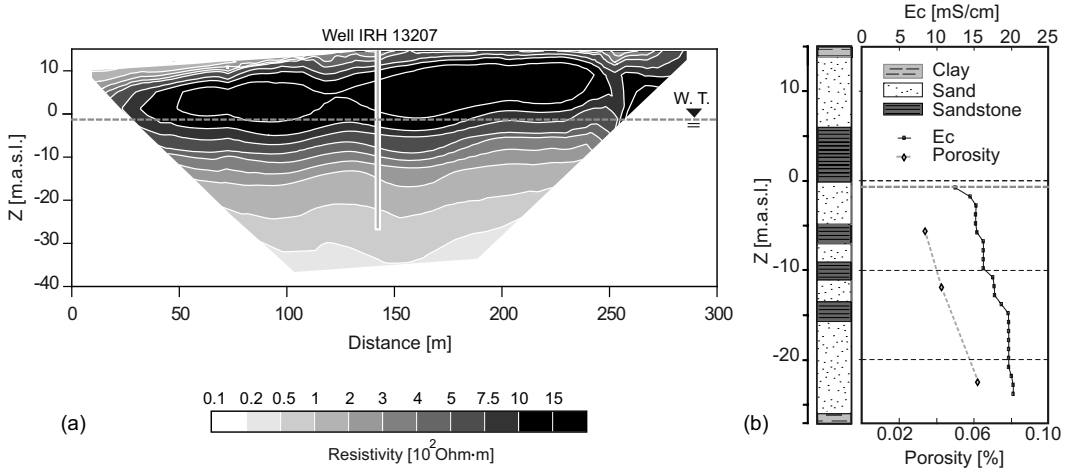

Fig. 4 (a) Inverted resistivity profile and location of the well and of the groundwater table (W.T.); (b) Point 4 (IRH 13207) borehole data showing the local lithologies and the vertical salinity and porosity distributions calculated using equation 1.

Eight ERT profiles of 3 to 5 m electrode spacing investigating a depth of 30 to 50 m (~1/6 of the total horizontal length) were carried out in the Pliocene area. Near each profile, there is a well where groundwater salinity was measured to estimate ρ_w. Figure 4 shows an example of an ERT profile with the corresponding borehole lithology and salinity profiles used for porosity estimation. ERT profile of point 4 shows the geological setting close to the sea with dry arenitic limestone of

resistivities ranging between 10^3 and $1.5 \cdot 10^3$ Ohm·m on top of a saturated sand of 100 - 500 Ohm·m. Those offer a good contrast with the low resistivities (1 - 50 Ohm·m) of the clayey bedrock saturated with saline water. Results of applying equation (1) assuming Humble formula (Winsauer et al. 1952) for unconsolidated formations: $F = 0.81\phi^{-2}$ are displayed in table 1 and show that the porosity of the Pliocene formation is ranging between 4 and 25 %. It is worthwhile noting that, except for the point 4, only values at the level of the groundwater table were used for calculating the porosity. Therefore, only a portion of the material is accounted for in the calculation.

Table 1 Measured resistivities and porosity values estimate by Archie's law, being a=0.81 and m=2.

ID	X	Y	ZVAL	Bulk-media resistivity [Ohms m]	Pore water conductivity [mS/cm]	Porosity [%] for a=0.81, m=2
1	673727.4	4071595.6	54.21	44.09	2.85	25
2	675403.9	4068851.7	12.72	54.17	2.7	24
3	673500.6	4070869.3	47.49	56.12	2.65	23
4	670454.7	4058971.2	15.00	416.26	13	4
5	665274.2	4062304.4	30.67	74.24	2.65	20
6	669843.6	4059709.3	16.73	65.02	5.29	15
7	675400.0	4071945.7	38.79	75.19	2.57	20
8	669694.8	4060084.5	20.00	62.9	5.00	16

3.1.3 Areal recharge

Evaluation of effective recharge is challenging in arid and semi-arid regions. Scanlon et al. (1997) pointed out the wide variability of some published values under similar climatic conditions. In addition, in such an intensively irrigated plain as in Korka, irrigation return flow might be an important component of the groundwater mass balance. The study area is characterised by a semi-arid climate with an average precipitation deficit (precipitation minus pan evaporation) of around 650 mm/year. Generally, 75% of the 420 mm/year average annual rainfall fall is concentrated during the wet season (from September to March). Ennabli (1980) estimated the effective recharge rate to be ranging between 5 and 8 % of the regional average annual rainfall. Paniconi et al. (2001) estimated the effective recharge to be less than 10 % of the average annual rainfall.

In this study, aquifer recharge was estimated using two different but complementary methods. The first method is based on the relationship between the effective recharge and the soil distribution in the area. The second method consists of the calibration of the recharge using a numerical groundwater model (Section 3.4). The following is a description of the first approach. The spatio-temporal analysis of the effective recharge by infiltration of precipitation was achieved using a geographic information system (GIS) database (including detailed soil and land cover maps as well as daily rainfall and pan evaporation data over 44 years) and the "daily" Thornthwaite and Mather method as described in Steenhuis and Van Der Molen (1986).

The regional soil distribution map (Mami and Aloui 1982) was discretized into 328000 cells of 100 by 100 m. Three types of soil were defined: Fine (F), Medium (M) or Coarse size (G) material. Each of these can have five possible thickness values: 40, 60, 80, 100 or 120 cm. This information on soil type distribution and thicknesses is of prime importance for the estimation of the soil water balance. To estimate the latter, one additionally needs the specific field capacity for each type of soil and climatic data. For the field capacity of each soil type, a sensitivity analysis was performed assuming three possible values for each one (%): 5, 6.5 and 9 for the type G; 7, 8.5 and 11 for the type M; and 9, 10.5 and 13 for the type F. Note that for urban areas (U type) higher values (Fig. 5a) were used (15, 17.5 and 21 %). Using soil type, its thickness and the corresponding specific field capacity, one can integrate a relative soil class field capacity. This was used together with the daily rainfall and pan evaporation, to calculate the soil water balance, finally yielding the effective recharge. Average values were used during data gap periods. Figure 5a shows the values of the relative field capacity for each soil type. It is worth noting that surface runoff was neglected because of the flat topography and the dominance of cultivated areas.

Figure 5b shows the resulting recharge in terms of annual rainfall percentage. Indeed, minimal values of field capacity and soil thickness lead to the maximal recharge scenario with up to 25 % of the annual rain. In the following, we only consider the minimal recharge scenario. The recharge at the Korba aquifer is ranging in average between 8 % and 30 % of the annual rainfall depending especially on the frequency and the intensity of the rainy events during the year. However, below an annual rainfall of 200 mm (Fig. 5c), no recharge will occurs or it will be negligible, as was the case during the period of 1985-1988 (Fig. 5b). Such long drought periods may favour seawater intrusion.

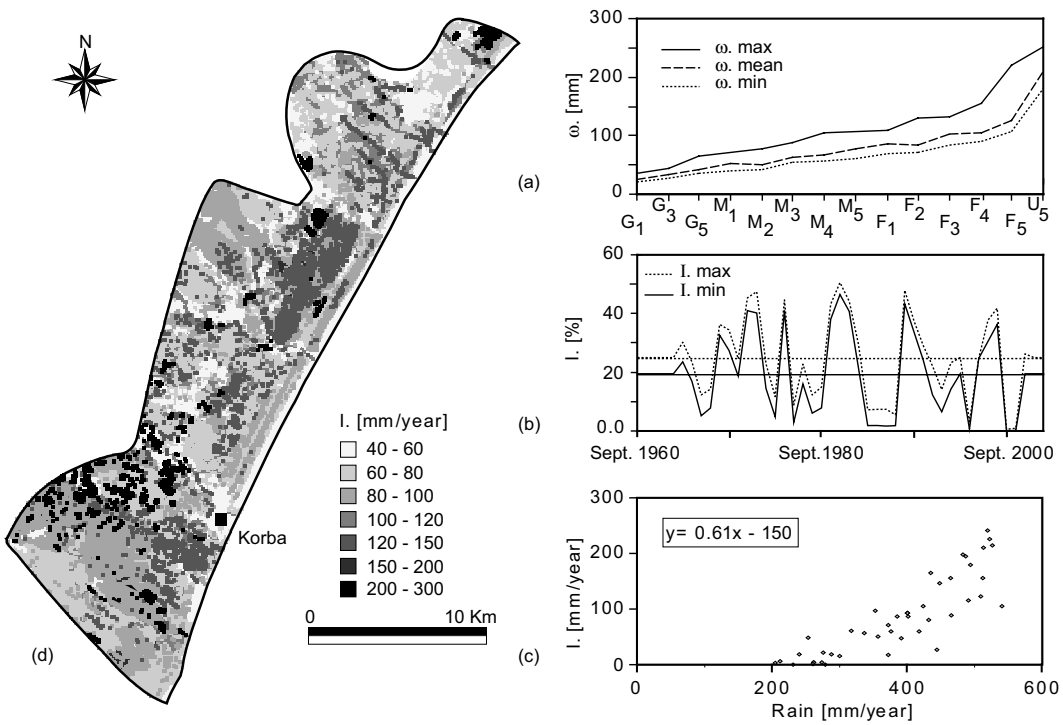

Fig. 5 Spatio-temporal analysis of the recharge at the Korba aquifer by infiltration of precipitation: (a) specific field capacity (*w*) of each soil type (the letter corresponds to soil type: Fine, Medium, and Coarse. The subscripts 1-5 correspond to the thickness of the soil (40, 60, 80, 100 and 120 cm), example: G_1: G type with 40 cm thickness; (b) The percentage of the annual rain that percolates to the aquifer (min, max) (c) Correlation plot between predicted recharge and annual rainfall; (d) spatial distribution of the recharge data.

An important result of recharge analysis was the spatial variation of the recharge rate which may vary by one order of magnitude (Fig. 5d). 90 % of the recharge takes place during the wet season and the inter-annual variation of the recharge might be more than 2.5 times the average value (Fig. 5b). These estimated values of recharge are surprisingly high when compared to those in previous studies. This is partly explained by the method (Thornthwaite and Mather) and the temporal discretization used (daily or monthly). This may lead to a systematic under-estimation of recharge is case of monthly time step because of the dominance of the evaporation in such semi-arid contexts.

Irrigation return flow was also estimated using the abovementioned data, and additionally using data from land cover analysis of 1998 and a detailed irrigation calendar. The irrigated volumes were added to the rain and the same method was

applied. The amount of irrigation water which percolates to the aquifer might increase the total recharge by 8 Mm^3 (in average) per year, which represents 16 % of irrigation water (assuming 50 Mm^3). Note that the analysis of return flow irrigation was made for just 10 years (1993-2003) assuming a constant land cover distribution.

The above estimated average annual recharge will be used as an initial guess for the inverse modelling of the steady state flow (Section 3.4). Its variation rates will be used for the transient simulation using a simplified zonation according to geological criteria which also control aquifer recharge.

3.1.4 Sink terms

The sebkhas (salt lakes) delineate a 5 km^2 fringe all along the coastline and are believed to be groundwater discharge areas. Appling the empirical formula of Coundrain et al. (1998) and considering 0.5 to 1.5 m depth of the water table gives a 0.8 Mm^3/year discharge in average. Thus, this value is negligible. Other sink terms like submarine groundwater discharge are not evaluated. In the following, we focus on the estimation of the pumping rates which are the key to understand the aquifer dynamics, to model seawater intrusion, and to investigate optimal groundwater management strategies.

3.1.4.1 Data for the estimation of pumping rates

Different types and sources of data were used to estimate a map of extraction rates. First, global estimates of the total annual extraction (Q_{annual}) are regularly made by the local administration (CRDA Nabeul). This calculation is based on average seasonal head variation and estimated aquifer porosity. As such, it is not very precise. Eight such values are available starting from1962. According to these records, pumping started in the sixties and increased regularly up to the mid-eighties. Since then, the exploitation rates oscillate around 50 Mm^3/year. The stabilization can be explained, on the one hand, by the change from flood irrigation to drip-irrigation and, on the other hand, by the construction of a network of surface water supply for irrigation in some parts of the study area. The uncertainty around these estimated groundwater abstraction volumes had never been evaluated.

Then, a thorough survey of pumping rates was conducted in 1996 jointly by the Institut National Agronomique de Tunisie and the CRDA Nabeul. During this survey, 432 sites were visited. Farmers were interviewed and the instantaneous discharge rates were measured. From the declaration of the farmers with regard to water usage, the type of crops they grew and the measured pumping rates, an annual

value of the pumping rates for the well *i* was estimated at selected wells. These are located in the central part of the aquifer (Fig. 7a). This data set constitutes the best source of information for evaluating the spatial variability of pumping rates and their relation with background variables. Thus, they are considered as reference values even when they (certainly) also contain some uncertainty.

The main assumption while estimating the pumping rates distribution is that extraction correlates with exhaustive secondary information available over the whole domain. For example, it is reasonable to think that the pumping rates distribution is related to the density of wells and proportional to the transmissivity of the aquifer, etc. The location of shallow and deep wells in 1996 was provided by the CRDA. From that data set, the density of wells was calculated over a regular grid of 300 x 300 m^2 resolution (Fig. 7a). The pumping rates estimated by the exhaustive survey in the central part of the aquifer were integrated as hard data on the same regular grid. Other variables were directly available and some had to be computed a priori. In particular, the next section presents how crop evapotranspiration and its spatial distribution were obtained using energy balance calculation on satellite images.

3.1.4.2 Mapping crop evaporation by remote sensing analysis

Remote sensing can be extremely efficient to acquire spatially distributed data for modeling (Becker 2006; Brunner et al. 2007; Hendricks Franssen et al. 2008). Considering the problem of the estimation of the pumping rates, one technique consists of estimating the crop evaporation from energy balance computations (Bastiaanssen et al. 1998a; Bastiaanssen et al. 1998b; Roerink et al. 2000; Anderson and Kustas 2008) and use that estimation to derive pumping rates from the water mass balance.

For this purpose, the Simplified Surface Energy Balance Index (S-SEBI) algorithm (Roerink et al. 2000) and the equation of Penman-Montheith (Allen et al. 1998) were used (Käser 2004). 23 cloud-free satellite images NOAA AVHRR (Advanced Very High Resolution Radiometer) were selected between the 14th of February 2000 and the 15th of September 2000. Each image has a 1.1 km^2 resolution. The data set also includes air temperature and relative humidity measured on the site by 2 meteorological stations. First, the 5 band images were processed to calculate surface reflectance (ground albedo) and surface temperature which are two constitutive parameters for the S-SEBI algorithm. It assumes that the atmospheric conditions are constant over the image and the area reflects sufficiently wet and dry pixels. This was the case in the eastern part of the Cape Bon images. Then, the

instantaneous evaporative fraction was calculated for each pixel on the basis of the expression of ground albedo versus surface temperature as described in Roerink et al. (2000). Second, using air temperature and relative humidity maps, the daily net radiation was calculated, which in turn was used to compute the daily evapotranspiration as described in Parodi (2002). The daily evapotranspiration allowed estimating the crop reflectance coefficient using the reference evapotranspiration ET_0, calculated by the Penman-Montheith equation, and provided by the Tunisian Institute of Meteorology. The crop reflectance coefficient was then averaged for each month and used with the reference evapotranspiration to calculate seasonal evapotranspiration ET_r over the whole aquifer.

To estimate the pumping rates, the basic assumption is that the difference of ET_r between not irrigated and irrigated areas represents the water that has been added by irrigation and can be subdivided into a surface water and pumped groundwater (Fig. 6b).

The estimated values of evapotranspiration are 45 mm/month in July and 57 mm/month in August for the non irrigated area and 62 and 71 mm/month for the same months respectively, in the irrigated area. Figure 6a shows the crop evaporation of 25 June 2000. The mean difference in ET_r is therefore 14.5 mm/month. Assuming that the pumping rates are constant all along the year over the 168.5 km^2 of irrigated area and knowing that the amount of surface water used for irrigation was 9 Mm^3 (CRDA 2002), the pumping volume for the year 2000 is estimated to be around 18 Mm^3.

This value is much smaller than the estimate of 50 Mm^3/year provided by the local authority and therefore seems to be underestimated (even if 8 Mm^3/year of irrigation return flow are added). This might be explained by the low resolution of the used satellite images (1.1 km^2) which leads to an underestimation of the crop reflectance coefficient. The resolution problem is related to the fact that farmers have very small fields. The surface of 72 % of the farms is less then 5 ha (CRDA 2002), and use mixed multilevel agriculture in the same plot. This introduces a high variability within the pixels of the satellite images. Another source of error could be an inadequate calibration due to a lack of reference ground data. But, even if the absolute value of the estimated evaporation does not seem sufficiently reliable, it is reasonable to think that the method allows to identify regions with higher evapotranspiration and, therefore, higher pumping rates.

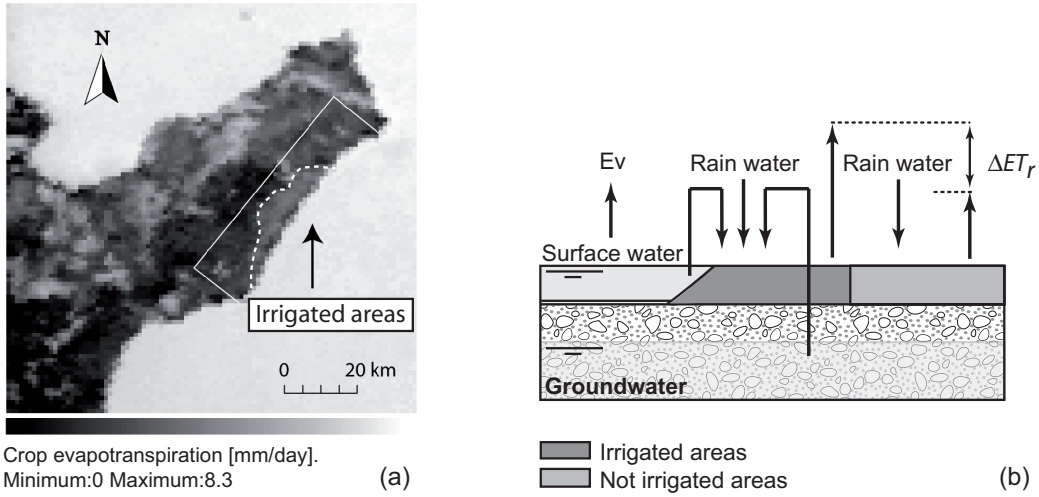

Fig. 6 (a) Crop evapotranspiration for the date of 25 June 2000 modified after Käser (2004). The irrigated area delimited with a dashed white line is also shown. (b) Sketch of the model for estimating pumping rates.

3.1.4.3 Multi-linear regression model for the pumping rates

Pumping rates are assumed to be partly correlated with secondary information available over the whole domain. For example, groundwater abstraction is assumed to be related to the amount of crop evapotranspiration and its spatial distribution calculated using remote sensing analysis. In addition, pumping rates are expected to be correlated with parameters such as: transmissivity (high transmissivity allows high discharge) or depth of the water table (shallow depth facilitates groundwater abstraction). The pumping rates might also be related to other parameters such as: 1) the salinity of the groundwater: if the salinity increases, the groundwater will no longer be suited for irrigation; thus, pumping will decrease or eventually, stop; 2) the elevation of the topography: at higher elevation the water table is deeper which makes traditional well digging more difficult and therefore less pumping is expected; 3) the distance to the sea: far inland the water is less saline; 4) the seasonal piezometric head variation in 1996 indicates the areas with larger stress 5) the piezometric depletion since 1960 indicates the most exploited areas in the long term.

Overall, eight parameters were selected as potential secondary information (Fig. 7b). These are: aquifer transmissivity (T), summer 2000 crop evapotranspiration (ET_r), December 1996 electrical conductivity (Ce), 1996 seasonal head variation

(Dh_{96}), average 1996 water table depth (WT_d), 1960-2004 historical piezometric decline (Dh_h), distance to the sea (D_s), and digital elevation model (Z). For each of these parameters, a distribution map was either already available or it was constructed by ordinary kriging.

Pumping rates measurements at 432 wells (within the dashed polygon in Fig. 7a) were used as hard data to estimate the coefficients of a linear multivariate regression model. In a first step, the pairwise correlations between the selected parameters and measured pumping rates were analyzed (Fig. 7c). Some correlations are weak, as for instance the correlation between the pumping rates and the distance to the sea or the altitude, but some others are statistically significant (with the transmissivity and with the average seasonal head variation). There was also a clear trend between the pumping rates and crop evapotranspiration of 2000 despite the time lag. In a second step, a multi-linear model was estimated by standard linear least squares. The correlation coefficient values obtained by regression reveal that the agreement between interpolated and measured pumping rates is poor (Fig. 7d). Yet, results of the linear regression model are taken simply as initial guesses for the numerical model (Section 3.3 and 3.4). These will be updated by model calibration in such a way that a good agreement with available (head and salt concentration) calibration data is achieved.

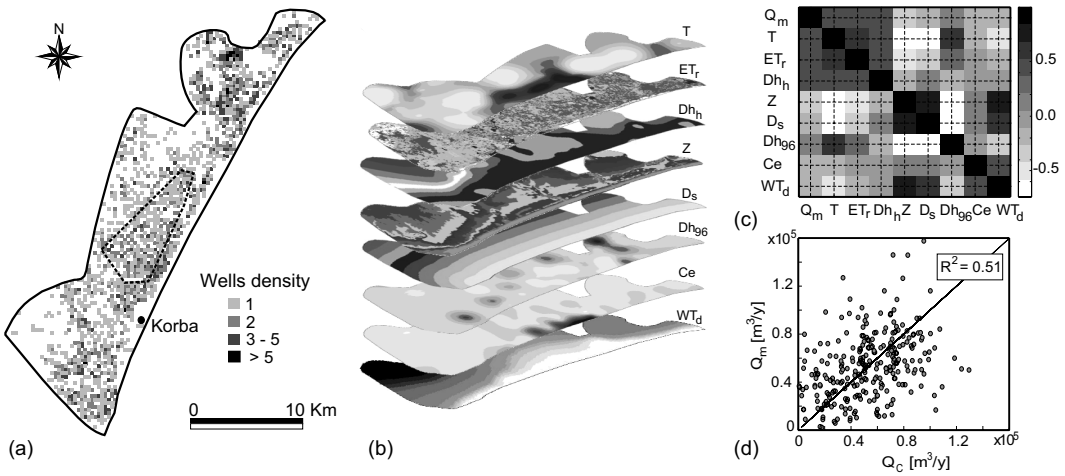

Fig. 7 (a) Well density and area of the exhaustive pumping rate survey (dashed line polygon). Wells are grouped into 1491 clusters on a regular grid of 300 by 300 m cell size. (b) Eight maps with the secondary information. (c) Correlation matrix. (d) Scatter plot of estimated (Q_c) versus measured (Q_m) pumping rates.

3.2 Synthesis and conceptual model

Prior analysis of aforementioned data allows one to elaborate a conceptual model depicting the dynamics of the Korba aquifer (Fig. 8). This is the foundation of any subsequent numerical modelling endeavor (Carrera 2005). The key points and assumptions in the conceptual model adopted here are listed below:

- Northern and southern limits match groundwater flow streamlines. Western limit depicts the contact with the Early Miocene marls. Eastern limit matches the seashore.
- Five geological units are considered (Figs. 8 and 9): the Tyrrhenian Quaternary (Q1); the marine Pliocene (P1) considered as the main aquifer; alluvial Pliocene in the central part of the domain (P2); Late Miocene (the Somâa sands) in the southern part of the aquifer (M2); and the early Miocene (M1).
- Hydraulic parameters are considered homogenous in each of the aforementioned units considering the qualitative description (Section 2.2) and available data (Sections 3.1.2)
- The main groundwater mass balance inputs are areal recharge estimated to be about 20 % of the average annual rainfall and vary in space and time. Lateral recharge and recharge from wadis are also considered.

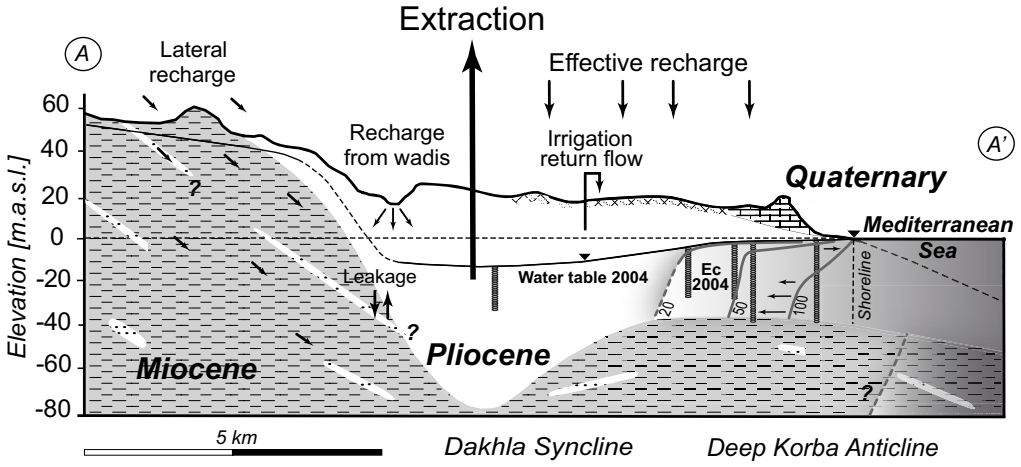

Fig. 8 Simplified geological cross-section (localization in fig. 1) of the Korba aquifer system sketching the conceptual model based on up-to-date geological and hydrodynamic data. The aquifer surface and bedrock topography are shown as well as August 2004 water table and the percentage of seawater electrical conductivity (the maps are constructed by kriging). Note that dashed line iso-contours are hypothetical.

- Groundwater abstraction is assumed to be started in the 60's and increased linearly until the 80's. Since the 80's, the total abstraction volumes are assumed to fluctuate around 50 Mm3/year (as described in Section 3.13).
- Figure 8 shows that the mixing zone is very wide in the Korba aquifer, in the order of several kilometers (about 1.5 km between the 0.25 and 0.75 iso-concentration contours in the central part of the aquifer) with almost vertical salt iso-concentrations. It is obvious that, in this case, a sharp interface conceptual model will lead to misleading results. Therefore, it is necessary to account for dispersion-diffusion processes.
- Given the variability of flow and concentrations patterns, a 2D numerical model will yield local predictions only. However, a 3D model will be suited to account for lateral changes of the hydrodynamic parameters of the aquifer as well as the forcing terms.

3.3 The 3D Numerical model

The 3D numerical model (Fig. 9) was built using Feflow (Diersch 1996). The model domain was discretized in 877 249 prismatic finite elements and 467 760 nodes (Fig. 9). The mesh is refined within the main aquifer layer (Pliocene formation) with element sizes ranging from 150 to 200 m. Near the shoreline element sizes is ranging between 50 and 100 m. Vertically, the mesh is divided into 19 layers of 5 m thickness in average. The mesh setup involved a pre-processing of GIS data of different kinds: points (wells and piezometers), polygons and lines (geological, wadis, etc.) and raster maps (geological layers, surface, top and bottom topography, etc). According to the local geology data and soil distribution, the area is divided into 10 sub-domains (called zones) in which the model parameters are calibrated separately (Fig. 9). This increases the degrees of freedom of the model but allows, first, a more realistic representation of the aquifer geometry and, second, a better fit of available observations.

Modelling is performed in two steps. First, a steady state flow model is used to estimate hydraulic conductivities and recharge, and get suitable initial conditions (heads and concentrations) for the transient model. The latter is performed in a second step and allows to estimate storativity. Steady state boundary conditions are a prescribed constant lateral inflow at most of the length of the western boundary and a prescribed head on the seafloor (Fig. 9). The seaside boundary extends 3.5 km (arbitrarily fixed) offshore to avoid unrealistic boundary effects. For the transient simulation from 1960 to 2004 time period, lateral fluxes were attributed to model

recharge from the Lebna dam (from 1986), and the increasing discharge rates in the wells. Based on the eight estimates of total exploitation volumes and under the assumption that pumping started in 1960 and increased linearly up to 1980, a suitable time function is adopted at the majority of wells (e.g. well Q240 in Fig. 10b). Since pumping was greatly reduced north of Korba in the early 90's (dashed line polygon in Fig. 10a) due to the high salinity, a second time-dependent function was built for the wells located in that region (e.g. well Q361 in Fig. 10b). Note that pumps are simulated at 10 m depth in average. The recharge of the aquifer by infiltration of precipitation (on the top layer of the model) varies in time (yearly) as shown in figure 5b. A total number of 1 498 time-dependent functions (1491 for the well clusters, 6 for the areal recharge and 1 for the lateral flux) are considered for the transient simulations.

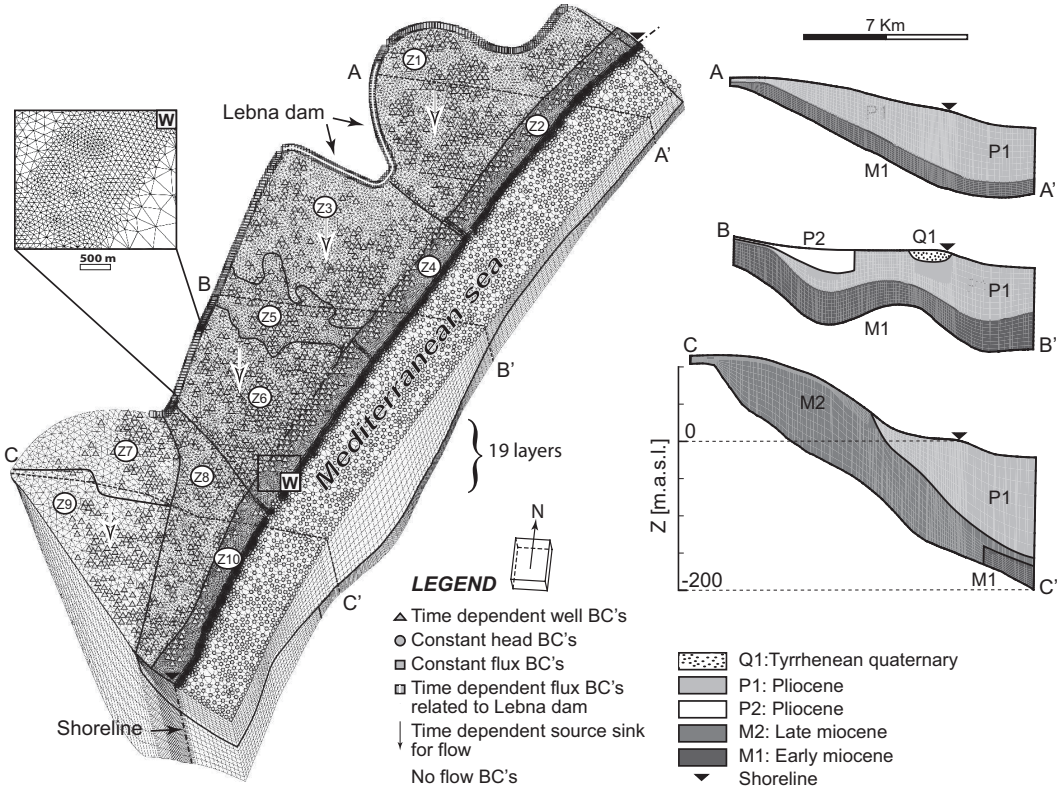

Fig. 9 The Korba aquifer 3D numerical model and three flow material cross-sections (W: zoom window). Note that wells are attributed at the third slice and lateral fluxes are integrated on the thickness of the Pliocene only. The zonation (Z1-Z10) used for inverse calibration is also showed.

With regard to transport boundary conditions, a maximum relative seawater concentration of 1 [-] was assigned at the seafloor to inward seawater fluxes only (water enters the aquifer with seawater concentration but leaves with aquifer concentration).

3.4 Model calibration

The calibration of the 3D model to fit field observations has been achieved in a time dependent, iterative and semi-automatic fashion using PEST (Doherty 1998) coupled to Feflow. The basic idea of the PEST algorithm is the minimization of an objective function defined by the squared weighted sum of residuals (calculated minus observed heads). Model parameters to be calibrated were the geometric mean of the hydraulic conductivity of each formation, the spatial distribution of recharge and the lateral flux. Conditioning dataset for the steady-state calibration is that of 1960, presumably representing natural conditions. To run PEST safely, some constraints (spatial and numeric) have to be fixed. Based on a stratigraphic qualitative analysis, the Tyrrhenian sandstone was defined as the most permeable unit, followed by the Pliocene, the Somâa and the early Miocene formations. However, for recharge, the estimated average values plus and minus standard deviation, were fixed as tolerance interval. Note however that for all parameters the calibration was carried out using 10 subdivisions of the domain to account for the local geology (Fig. 9).

PEST is then used to calibrate the storage compressibility using 1753 time-dependent measured heads as control data (including monthly data during 20-years in six wells and 6-months data during 10-years in 21 wells history). If the resulting heads do not match sufficiently well the observed heads in 2004, then first, both permeabilities and areal recharge are recalibrated in steady state by adapting their ranges (minimum and maximum admitted values for the inverse calibration). If this is still not sufficient, pumping rates estimated by the linear regression model are modified locally (especially near Korba city) and rescaled to fit the transient estimations given by the authorities and finally PEST is restarted again until convergence.

With regard to the transport calibration, tests were made by trial and error to get adequate horizontal and transversal dispersion coefficients (constant in space). Values were chosen sufficiently large to avoid a competition with numerical dispersion in the largest elements. Then, the porosities were calibrated, also manually by trial and error with respect to local lithologies to reproduce as well as

possible the 26 vertical profiles of salinity measured in 2004 as well as 80 shallow local salinity values.

4. Simulations results

The model was calibrated to reproduce the long-term depletion of groundwater levels and seawater encroachment by considering inter-annual variability of the recharge (Fig. 5b) and increasing pumping rates (Fig. 10b). In 1985 and 2004, the total estimated exploitation volumes were 50 and 47 Mm^3/year respectively, with an average pumping rate on a single grid cell of 3.37 10^4 m^3/year and 3.15 10^4 m^3/year. The map of calibrated pumping rates (Fig. 10) shows that the pumping rates at the west of Korba are the smallest. This is related to the low transmissivities in that area of the aquifer.

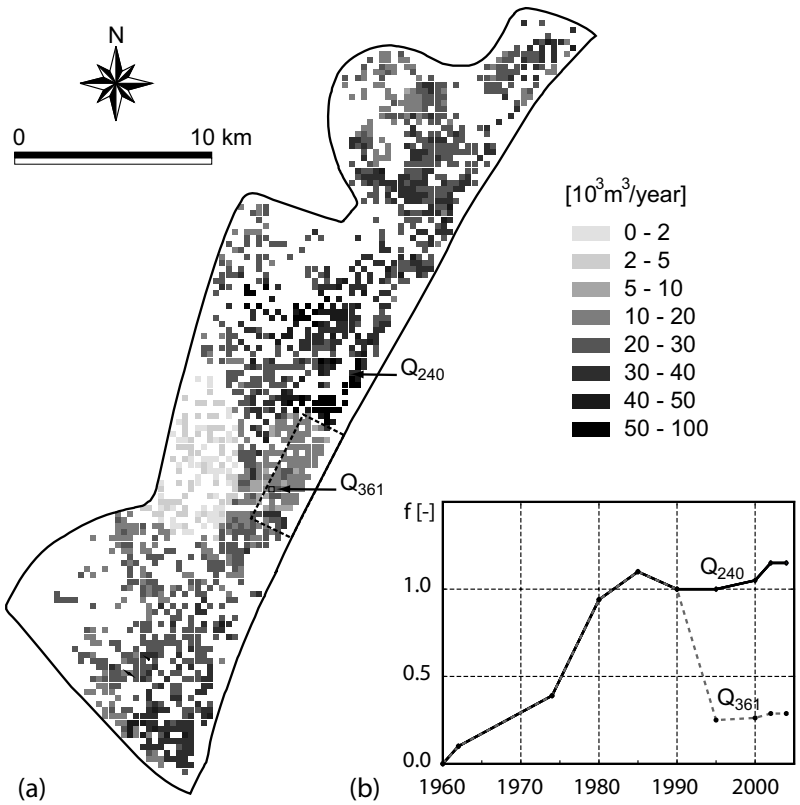

Fig. 10 (a) Average pumping rates (Q 1996) with the area (delineated with dashed line) where pumping are reduced in the 90's (b) Time-dependent evolution functions f [-] for both wells (solid black line for Q_{240} and gray dashed line for Q_{361}) with 1996 extracted volumes as reference.

Figure 11 shows the quality of the fit between observed and calculated heads and concentrations for the transient model. Root mean square errors of 6.2 [m] for heads ($-12 < H_{obs} < 120$ m) and 6.69 [g/l] for salt concentrations ($0.5 < C_{obs} < 36$ g/l) were obtained, indicating an acceptable calibration. A better fit could certainly be obtained by considering a heterogeneous hydraulic conductivity field, but the sensitivity analysis showed that it is difficult to get a better calibration with the conceptual model used. The calibrated parameters are shown in table 2.

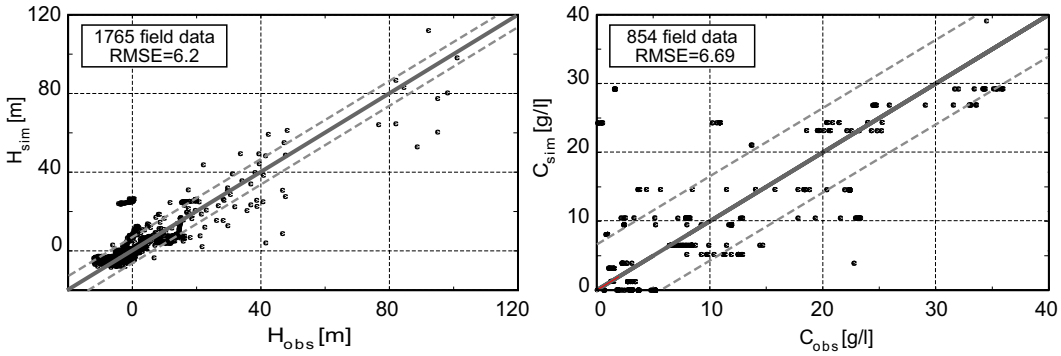

Fig. 11 Scatter plot showing the fits between the observed and calculated: (a) heads [m] and (b) salt concentrations [g/l]. Note that for heads, 1765 measured data were used and 854 data of august 2004 for concentrations.

Figure 12 shows the simulated heads and relative concentrations of salt. They are in agreement with field observations (compare Figs. 2d and 12a and Figs. 3a and 12b and Figs. 8 and 12c) and reproduce the main hydraulic features of the aquifer including the highest gradients in the Somâa aquifer and groundwater table depression in the centre of the aquifer. In addition, the model allowed to reproduce the shape of the mixing zone, its time evolution and its extent in 2004 (Figs. 12bc and 14). Very often, in miscible salt transport models, the 0.5 relative seawater concentration is used to characterize the extension and the geometry of the saltwater wedge in analogy to sharp interface models. Yet, with such a wide mixing zone as the one in the Korba aquifer, it is misleading to use the 0.5 concentrations to characterize seawater intrusion. At the same time, using very low seawater concentrations (e.g. 1 %) can also be misleading because of boundaries but also numerical effects. In this study, we consider the 0.25 and 0.75 relative concentrations to define the width of the mixing zone and the 0.25 to define its extent within the aquifer. Obviously, saltwater wedge movement landward started in 1979 almost simultaneously with the decrease of the water table below sea level

(Fig. 14). Most probably, migration of pumping wells inland as salinity increased above a certain threshold (as happened in the 1990's), led to further inland propagation of the saltwater wedge. The combination of reversed flow direction (hydraulic gradients) due to the depression of the water table below sea level and saltwater up-coning determined the velocity and the geometry of saltwater wedge in the Korba aquifer. In such a case, both horizontal and vertical dispersivities increase proportionally to increasing directional velocities. The latter processes might explain the widening of the saltwater wedge at the same time as it is advancing (Fig. 14). From figure 14, the velocity of the saltwater wedge might be estimated to be around 100 m/year considering the 0.25 concentration and 1.3 km width of the mixing zone in 2004 which represent 4 times the width of the mixing zone prior to seawater wedge encroachment. Figure 14 also shows that the velocity of the 0.25 iso-concentration accelerated in response to the decrease of the water table caused by increasing pumping stresses. However, at the same time as the velocity of the 0.25 iso-concentration increases, there is a slight decrease in the velocity of the higher iso-concentrations. This is normal, because salt spreading opposes density effects.

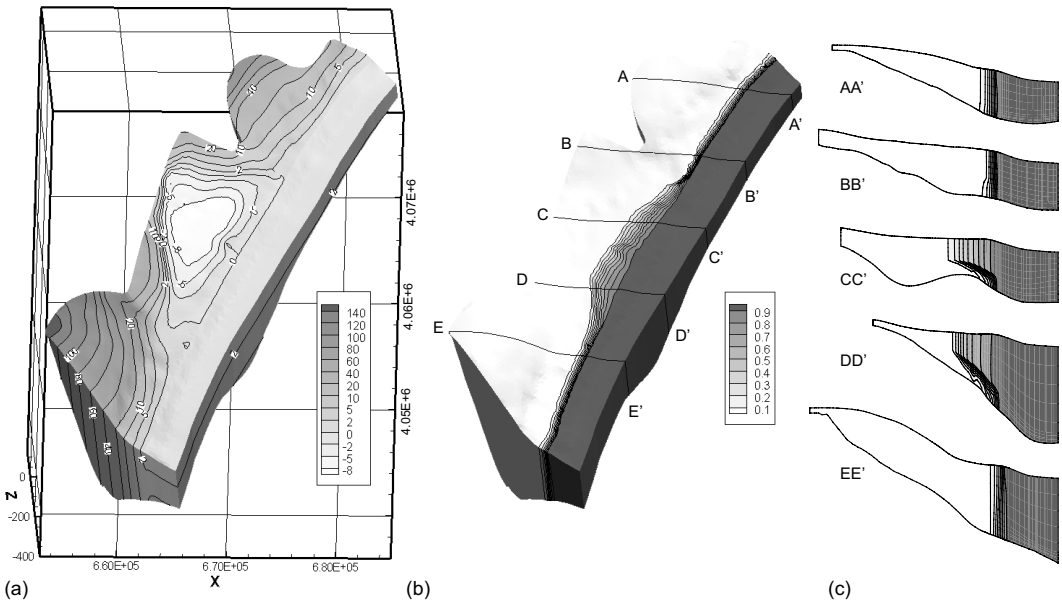

Fig. 12 (a) Three dimensional views of simulated (a) water table elevation [m.a.s.l.] (b) relative salt concentration [-] distribution (c) cross-sections.

With regard to the groundwater mass balance (Fig. 13), the mean areal recharge of the aquifer was estimated by model calibration to 29.7 Mm^3/year (89 mm/year)

which is in agreement with the values obtained by the daily Thornthwaite Mather method (Fig. 9). Note however that on a major part of the aquifer (all zones except Z1 and Z9), areal recharge represents 12 % of the annual average rainfall. Results show that infiltration is higher in the northern and southern parts of the aquifer where the main aquifers are outcropping (Z1 and Z9 in Fig. 9 and Table 2). The Lateral recharge from the adjacent and deep aquifers as well as from the Lebna dam was estimated to be 7.5 Mm^3/year in 2004. The overexploitation induced an additional 7 Mm^3/year seawater inflow into the aquifer as compared to using steady state budget, while it caused a reduction of the submarine groundwater discharge of 16 Mm^3/year.

Table 2 Hydraulic proprieties. First deterministic proprieties are listed. Next, calibrated model parameters (according to figure 9).

Parameter	**Value**
Seawater density [kg/m^3]	$1.025\ 10^3$
Freshwater density [kg/m^3]	$1.00\ 10^3$
Fluid viscosity [kg/m·s]	10^{-3}
Maximum relative concentration [-]	1
Average annual recharge [mm]	
Z1	164
Z2, Z4 & Z10	73
Z3, Z5 & Z6	43.8
Z7	45.6
Z8	54.7
Z9	119
Hydraulic conductivity (isotropic) [m/s]:	
Q1;P1;P2;M1;M2	$2{\cdot}10^{-4}$; $1{\cdot}10^{-4}$; $5{\cdot}10^{-5}$; $6{\cdot}10^{-6}$; $1{\cdot}10^{-7}$
Storage compressibility [1/m] :	
Q1&P1;P2;M1;M2	$5{\cdot}10^{-3}$; $3{\cdot}10^{-3}$; $6{\cdot}10^{-4}$; $1{\cdot}10^{-4}$
Porosity [%] :	
Q1&P1;P2&M1;M2	10; 8; 5
Longitudinal dispersivity [m]	400
Transverse dispersivity [m]	40
Molecular diffusion [m^2/s]	10^{-8}

It is interesting to note that a transient simulation considering an average recharge constant over 44 years resulted almost in the same head and salt distributions as the simulation with time-dependent recharge and a 4 years drought

period (e.g. 1985-1989) as shown in figure 13. This reflects the low diffusivity of the aquifer, especially the Pliocene formation which is around 1.6 10^{-2} m^2/s.

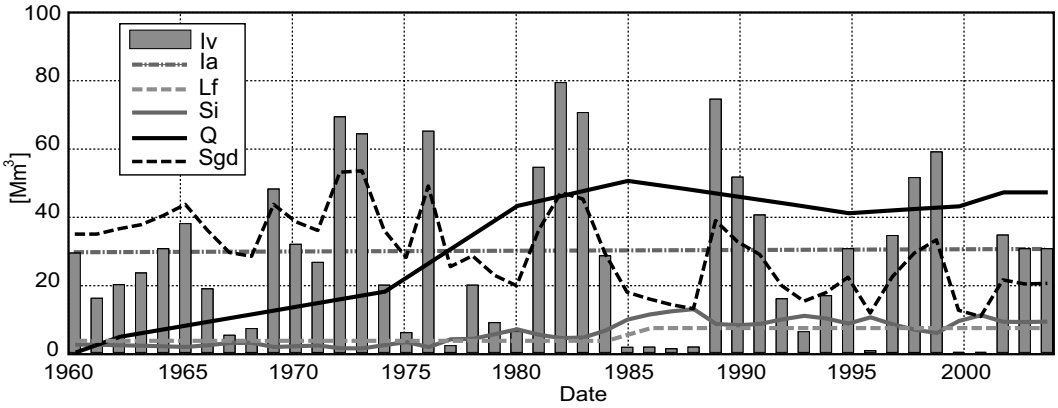

Fig. 13 Time Evolution (1960-2004) of water budget in the Korba aquifer: *Iv*: time dependent recharge, *Ia*: average annual recharge, *Lf*: Lateral recharge with recharge from Lebna dam stating from 1986, *Si*: seawater fluxes entering the system, *Q*: pumping, *Sgd*: submarine groundwater discharge.

Another way to evaluate the current situation of seawater intrusion in the Korba aquifer is the prediction of its evolution in response to pumping rates variations or even to a complete stop. The idea is to use the calibrated numerical model to evaluate the time lapse needed to turn back to the initial (steady state) head and salt concentration distributions. To this end, a simulation was conducted from 2004 to 2200 by keeping the same boundary conditions and aquifer recharge as in 2004 and turning off the pumping in the whole aquifer. A set of fictitious observation points, with regular spacing, forming a line of 3 km perpendicular to the sea, were placed near the bottom of the Pliocene formation in the central part of the aquifer.

Figure 14 shows that the landward movement of the seawater wedge will persist another 10 years after turning off pumps. This is not surprising, because hydraulic gradients will take the same time to be reversed before groundwater restarts to flow towards the sea. The same figure also shows that the maximum width of the mixing zone is reached when saltwater started to recede with the same trends (velocity) for higher and lower iso-concentration. The 0.5 seawater iso-concentrations will spend 80 years to turn back its initial position, however 0.25 iso-concentration will spend about 1.5 century; that for the unrealistic hypothesis of turning off pumping over the whole aquifer in 2004. Of course, these predictions are highly conditioned by the assumed boundary and initial conditions as well as hypothesis simplifying the conceptual model. However, it has been demonstrated that the shape of aquifer

bottom is an affecting parameter of salt wedge penetration and geometry (Abarca et al. 2007). The bottom of the Korba aquifer is characterised by a landward slope of about 1-3° (Fig. 8). The latter configuration is believed to favor saltwater intrusion due to driven forces, while it is believed to oppose saltwater wedge recede seaward. Overall, the predictions made show that there is a long time lag that has to be taken into account to evaluate the effects of current regional groundwater resources depletion.

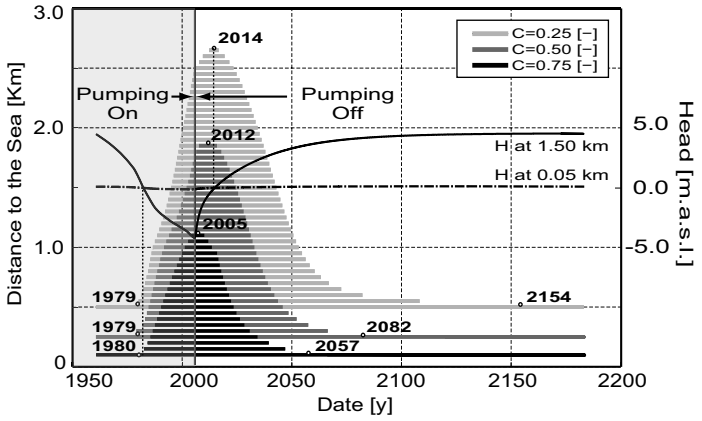

Fig. 14 Simulated seawater intrusion velocity from 1960 to 2004 considering actual pumping rates and the response of the aquifer to a hypothetical complete stop of pumping from 2004-2048.

5. Discussion and conclusions

In order to address the current extent of seawater intrusion in the Korba aquifer, a large-scale three-dimensional numerical model of density-dependent flow and miscible solute transport was developed and reasonably well calibrated in a time dependent, iterative and semi-automatic way. However, some of the limitations of the model are partly explained by the hypotheses that have been made which are mainly related to the available dataset. Assuming the same time dependency of the pumping rates in the majority of wells is one limitation of the model. Yet, results showed that some expected compensation effects due to the large density of wells, especially close to the sea, alleviate that effect. Assuming heterogeneity of the hydraulic conductivity field is believed to result in a better calibration of the model. Also, accounting for salt recycling is expected to result in an improvement of the calibration of the transport parameters. One limitation of the calibration procedure adopted is the non-uniqueness of the inverse problem. To ensure a reliable calibration (especially for transient calibration), the iteration between calibration in

steady state and calibration in transient regime was constrained by the minimum amount of recharge.

Overall, the 3D model allowed accounting for the actual geometry of the aquifer but also the lateral variability of its physical properties as well as pumping and recharge for a precise prediction of seawater intrusion in the Korba aquifer. It is obvious that the assumed boundary and initial conditions highly condition the calibrated model parameters and therefore its outputs. Nevertheless, the regional flow features and their time evolution, the geometry of the mixing zone as well as the velocity of saltwater wedge were estimated by field investigations but also reasonably well reproduced by means of the calibrated 3D numerical groundwater model. Results showed that the situation in the central part of the Korba aquifer is critical. The aquifer is exploited at 135 % (pumping/recharge). The calibrated pumping rates in the northern (north Lebna dam), central (between Lebna dam and Korba) and southern part of the Korba aquifer in 2004 are 13 Mm^3/year, 22 Mm^3/year, and 12 Mm^3/year, respectively; while the total recharge (areal and lateral) is 13 Mm^3/year, 10 Mm^3/year, and 14 Mm^3/year, respectively. It is worth noting that the idea of pumping rates equivalent to the recharge rates is a misleading concept as discussed in Bredehoeft (2002). Some decisions have to be taken to avoid further saltwater contamination, especially in the northern and southern part of the aquifer. A sustainable groundwater management scheme in the Korba aquifer could be established based on the 3D groundwater model developed in this study. An optimization study for the pumping rates as well as for the observation network is also recommended. Most importantly, the same methodology that has been used for the estimation of the pumping rates might also be applied to other environments and other variables. It can also be applied to estimate other model parameters by combining other auxiliary data. Natural recharge for instance, may be estimated by combining secondary information like soil and geological maps, head and rain measurements as well as distributed data from remote sensing analysis in a statistical framework. Furthermore, more sophisticated statistical tools like principal components analysis (PCA) can also be used to infer estimation of the variable of interest from indirect data.

Finally, it is reasonable to point out the uncertainties which are affecting the spatial distributions of direct recharge and pumping rates as well as the uncertainty associated with the hydrodynamic parameters of the aquifer (e.g. hydraulic conductivity, porosity). How do those uncertainties affect model predictions? Analyzing this uncertainty in a stochastic framework can be of great interest for the sustainable management of the groundwater resources in the Korba aquifer.

References

Abarca E, Carrera J, Sanchez-Vila X, Voss CI (2007) Quast-horizontal circulation cells in 3D seawater intrusion. Journal of Hydrology 339: 118-129

Abbes A, Polak M (1981) La formation Saouaf dans les synclinaux de la Dakhla (Cap-Bon) et de Saouaf (Tunisie nord orientale). Notes Services Géologiques de Tunisie 46: 99-111

Allen RG, Pereira LS, Raes D, Smith M (1998) Crop Evapotranspiration—Guidelines for Computing Crop Water Requirements, FAO Irrigation and drainage paper 56. Rome, Italy: Food and Agriculture Organization of the United Nations. ISBN 92-5-104219-5.

Anderson M, Kustas W (2008) Thermal Remote Sensing of Drought and Evapotranspiration. EOS, Transactions, American Geophysical Union 89: 233-240

Archie GE (1942) The electrical resistivity log as an aid in determining some reservoir characteristics. Transactions of the American Institute of Mining and Metallurgical Engineers 146: 54-61

Bastiaanssen WGM, Menenti M, Feddes RA, Holtslag AAM (1998a) A remote sensing surface energy balance algorithm for land (SEBAL) - 1. Formulation. Journal of Hydrology 213: 198-212

Bastiaanssen WGM, Pelgrum H, Wang J, Ma Y, Moreno JF, Roerink GJ, van der Wal T (1998b) A remote sensing surface energy balance algorithm for land (SEBAL) - 2. Validation. Journal of Hydrology 213: 213-229

Bates BC, Z.W. Kundzewicz, S. Wu and J.P. Palutikof, Eds. (2008) Climate Change and Water. Technical Paper of the Intergovernmental Panel on Climate Change, IPCC Secretariat, Geneva, 210 pp.

Bear J, Cheng AH-D, Sorek S, Ouazar D, Herrera I (1999) Seawater intrusion in coastal aquifers- concepts, methods and practices. Kluwer academic publishers, Dordrecht

Becker MW (2006) Potential for satellite remote sensing of ground water. Ground Water 44: 306-318

Bensalem H (1992) Contribution à l'étude de la Géologie du Cap Bon: Stratigraphie, tectonique et sédimentologie. Thèse de Doctorat, Faculté des Sciences de Tunis

Bensalem H (1995) Evolution de la Penisule du Cap Bon (Tunisie nord-orientale) au cours du Neogene. Notes du Service Geologique de Tunisie 61: 73-84

Bensalem H (1998) Les formationes post Saouaf des environs de Nabeul (cap Bon) et leur equivalents off shore et en Tunisie sud atlasique. Notes du Service Geologique de Tunisie 64: 123-128

Bredehoeft JD (2002) The water budget myth revisited: Why hydrogeologists model. Ground Water 40: 340-345

Brunner P, Franssen HJH, Kgotlhang L, Bauer-Gottwein P, Kinzelbach W (2007) How can remote sensing contribute in groundwater modeling? Hydrogeology Journal 15: 5-18

Cheng AH-D, Ouazar D (2003) Coastal Aquifer Management: Monitoring, Modeling, and Case Studies. Lewis Publishers

Coudrain-Ribstein A, Pratx B, Talbi A, Jusserand C (1998) Is the evaporation from phreatic aquifers in arid zones independent of the soil characteristics? Comptes Rendus De L Academie Des Sciences Serie Ii Fascicule a-Sciences De La Terre Et Des Planetes 326: 159-165

CRDA (2002) Rapport d'activités Commissariat Régional au Développement Agricole de Nabeul, Ministère de l'agriculture et des ressources hydrauliques,Tunisie

Custodio E (2002) Aquifer overexploitation: what does it mean? Hydrogeology Journal 10: 254-277

DGRE (1985) Rapport d'exploitation des nappes phréatiques de l'année 1985. Direction Générale des Ressources en Eau, Ministère de l'agriculture et des ressources hydrauliques,Tunisie

DGRE (2000) Rapport d'exploitation des nappes phréatiques de l'année 2000. Direction Générale des Ressources en Eau, Ministère de l'agriculture et des ressources hydrauliques,Tunisie

Diersch HG (1996) Interactive, Graphics-Based Finite Element Simulation System FEFLOW For Modeling Groundwater Flow, Contaminant Mass and Heat Transport. WASY Institute for Water Resource Planning and System Research Ltd, Berlin, Germany

Doherty J (1998) PEST-Model Independent Parameter Estimation, Watermark Numerical Computing, Brisbane, Australia

Ennabli M (1980) Etude hydrogéologique des aquifers du nord-est de la Tunisie pour une gestion intégrée des ressources en eau. Thèse de Doctorat d'État, Université de Nice

Gambolati G, Putti M, Paniconi C (1999) Three-dimensional model of coupled density-dependent flow and miscible transport in groundwater. In: Bear et al (eds) Seawater intrusion in coastal aquifers: concepts, methods, and practices. Kluwer academic publishers, Dordrecht, pp 315–362

Grava M (2005) Hydrochemical, Hydrogeological, and Geostatistical analysis of Eastern Cape Bon aquifer (northern Tunisia) Postgraduate thesis, Centre d'hydrogéologie de l'Université de Neuchâtel

Hendricks Franssen JH, Brunner P, Makobo P, Kinzelbach W (2008) Equally likely inverse solutions to a groundwater flow problem including pattern information from remote sensing images. Water Resources Research 44

Hichri H (2003) Annuaire hydro-pluviométrique du Cap Bon. Ministere de l'agriculture, Tunisie, pp. 95

INM (2001) Almanach Institut National de la Météorologie, Tunisie. http://www.meteo.tn

INS (2004) Recensement Général de la Population et de l'Habitat de 2004. Institut National de la Statistique, Tunisie. http://www.ins.nat.tn/

Käser D (2004) Etude hydrogéologique de la côte orientale du Cap Bon (Tunisie). Apports de la télédétection à l'estimation du bilan hydrique. Postgraduate Thesis University of Neuchâtel

Khlaifi I (1998) Contribution à l'étude de l'intrusion marine par un modèle de transport tridimensionnel : interfaçage avec des systèmes d'information géographique. Thèse de master, Institut National Agronomique de Tunisie

Konikow LF, Kendy E (2005) Groundwater depletion: A global problem. Hydrogeology Journal 13: 317-320

Mami A, Aloui T (1982) Carte des ressources en sols de la Tunisie. Feuille de la Goulette. Directions des sols, Ministère de l'Agriculture, Tunisie

Milnes E, Renard P (2004) The problem of salt recycling and seawater intrusion in coastal irrigated plains: an example from the Kiti aquifer (Southern Cyprus). Journal of Hydrology 288: 327-343

Nazoumou Y (2002) Impact des barrages sur la recharge des nappes en zone aride : Etude par modélisation numérique sur le cas de Kairouan (Tunisie centrale). . Ph.D., Ecole Nationale d'Ingénieurs de Tunis

Oueslati A (1994) Les côtes de la Tunisie. Recherche sur leur évolution au Quaternaire. Imprimerie officielle de la Republique Tunisienne, Tunis

Paniconi C, Khlaifi I, Lecca G, Giacomelli A, Tarhouni J (2001) Modeling and analysis of seawater intrusion in the coastal aquifer of eastern Cap-Bon, Tunisia. Transport in Porous Media 43: 3-28

Parodi GN (2002) AHVRR Hydrological Analysis System. Algorithms and theory - Version 1.3

Roerink GJ, Su Z, Menenti M (2000) S-SEBI: A simple remote sensing algorithm to estimate the surface energy balance. Physics and Chemistry of the Earth Part B-Hydrology Oceans and Atmosphere 25: 147-157

Scanlon BR, Tyler SW, Wierenga PJ (1997) Hydrologic issues in arid, unsaturated systems and implications for contaminant transport. Reviews of Geophysics 35: 461-490

Steenhuis TS, Vandermolen WH (1986) The Thornthwaite-Mather Procedure as a Simple Engineering Method to Predict Recharge. Journal of Hydrology 84: 221-229

Tarhouni J, Jemai S, Walraevens K, Rekaya M (1996) Caracterisation de l'aquifere cotier de Korba au Cap Bon (Tunisie). Progress report 95-96 for AVI-73 EC Project

Winsauer WO, Shearin HM, Masson PH, Williams M (1952) Resistivity of Brine-Saturated Sands in Relation to Pore Geometry. Aapg Bulletin-American Association of Petroleum Geologists 36: 253-277

Chapter 4

Grid-enabled Monte Carlo analysis of the impacts of uncertain discharge rates distribution on seawater intrusion in the Korba aquifer (Tunisia)⋆

Abstract The Korba coastal aquifer, located in the east of the Cape Bon peninsula, Tunisia, suffers heavily from water scarcity and salinization due to seawater intrusion. In 2000, the aquifer was exploited from more than 9000 wells. The problem, no precise information was recorded concerning the current extraction rates, their spatial distribution, or their evolution in time. In this paper, a geostatistical model of the exploitation rates was constructed based on a multi-linear regression model combining incomplete direct data and exhaustive secondary information including aquifer geometry and physical parameters. The impacts of the uncertainty on the spatial distribution of pumping rates uncertainty on seawater intrusion were then evaluated using a 3D density-dependent groundwater flow and solute transport model. To circumvent the large computing time required to run 100 44-years transient models, the simulations were made in a parallel fashion on the Grid infrastructure provided by the Enabling Grid for E-Science in Europe project. Monte Carlo simulations results showed that the uncertainty on the pumping rates led to a zone representing 8.3 % of the aquifer area, where the groundwater heads and salt concentrations were not known with accuracy.

⋆ This chapter is based on the papers:
Kerrou J., Lecca G., Murgia F. and Renard P. (2007) Grid-enabled simulation of the impact of exploitation uncertainty on the seawater intrusion of the Korba aquifer, Tunisia. Regional Impact of Information Society Technologies in Africa. IST-Africa 2007. Mozambique. *Best paper Award*
Kerrou J., Renard P., Lecca G. and Tarhouni J. (2008) A Grid-enabled Monte-Carlo analysis of the impact of uncertain discharge rates distribution on seawater intrusion in the Korba aquifer (Tunisia). Submitted to Journal of Hydrological Sciences

1. Introduction

In 2001, over half the world's population was living within 200 km from the coast and represented as many people as the entire globe inhabitants in 1950 (United Nations Foundation 2008). Such a demographic growth in coastal areas has greatly increased freshwater demand especially for agricultural purposes. Groundwater resources in these areas are therefore intensively exploited despite their extreme vulnerability to seawater intrusion. To provide recommendations to managers, it is important to understand the dynamics of coastal aquifers and to be able to model them. Nowadays, many codes allow modelling seawater intrusion as coupled density-dependent groundwater flow and miscible solute transport (Sorek and Pinder 1999). The validity and the interest of using these numerical models has been extensively demonstrated in numerous research and case studies (Bear et al. 1999; Diersch and Kolditz 2002; Cheng and Ouazar 2003; Milnes and Renard 2004).

Nevertheless, these models are affected by different sources of uncertainty (Carrera 1993). One of the most important is the effect of the uncertainty due to the heterogeneity of the hydraulic conductivities. This problem has been investigated numerically and analytically under different assumptions (Dagan and Zeitoun 1998; Naji et al. 1998; Al-Bitar and Ababou 2005; Abarca 2006). In addition, it is frequent that extraction rates are also highly uncertain. Not having detailed information about extraction rates is a problem encountered in many countries worldwide (Custodio 2002; Konikow and Kendy 2005). In the Korba aquifer (Tunisia), the local water management authority identified more than 9000 active wells in a region covering around 400 km^2. Most of the wells located in very small farms are traditionally dug, shallow, and equipped with oil motor pumps. None of these wells is equipped with a flowmeter and no survey has ever been made to estimate exhaustively their exploitation rate.

In Chapter 3, a multi-linear regression model was built to estimate the pumping rates in the Korba aquifer by combining a series of explanatory exhaustive variables describing the state of the aquifer, its properties, as well as data from remote sensing analysis. The pumping rates estimates were then used to calibrate a 3D density-dependent flow and miscible solute transport model but without accounting for the uncertainty on the estimated pumping rates especially their spatial distribution. Therefore, the main aim of the present work is to study how this uncertainty can be modeled and to investigate what is its impact on seawater intrusion. The approach that is adopted here is to setup a geostatistical model of the pumping rates based on the regression model (Chapter 3) in order to generate a large number of equally

likely simulations. The next step consists in propagating this uncertainty into a realistic 3D density-dependent model by running Monte Carlo simulations.

However running such complex and regional seawater intrusion models on a single PC for a sufficient number of stochastic realizations is often just not feasible. That difficulty can be overcome by using a cluster of computers on which each stochastic realization is executed independently. This is today a common technology but it still remains rather expensive and not all laboratories have access to such an infrastructure, especially hydrogeologists located in countries with low income. This is an issue because these countries are also facing the problem of seawater intrusion and uncertainty with the most dramatic consequences for their economy. Therefore the second aim of the paper is to investigate whether Grid computing could be used to run the Monte Carlo simulations remotely and possibly directly from the countries where the problems occur. Grid computing (Foster and Kesselman 1998) is an emerging technology that allows users to launch computations on a distributed network of computing resources without having to care about the process of making a remote login on a machine, transferring the data back and forth, launching the jobs, etc. All these aspects are handled by a middleware which is a software allowing the user to connect securely to the grid and run the jobs. The Grid takes care of finding a machine that is available, transfer the information, run the job, and send the results back. While that vision is very appealing and extremely well adapted for running Monte Carlo simulations, there are nowadays only a limited number of Grid infrastructures that are running at a large scale. Furthermore, the technology is still in development and not always stable and this is why it is interesting to study whether the exercise can be done or not.

The aims of this chapter are 1) to investigate how to model and propagate the uncertainty on the spatial distribution of the extraction rates to seawater intrusion model outputs, especially head and salt concentration distributions and 2) to test whether it is feasible to use Grid technology to run Monte Carlo simulations. These two questions are addressed by treating the example of the Korba aquifer.

2. Site description

The Korba aquifer is located in the Cape Bon peninsula in Tunisia (Fig. 1). It covers approximately 400 km^2 and has been extensively studied (Ennabli 1980; Tarhouni et al. 1996; Khlaifi 1998; Paniconi et al. 2001; Slama et al. 2008; Kouzana et al. 2009).

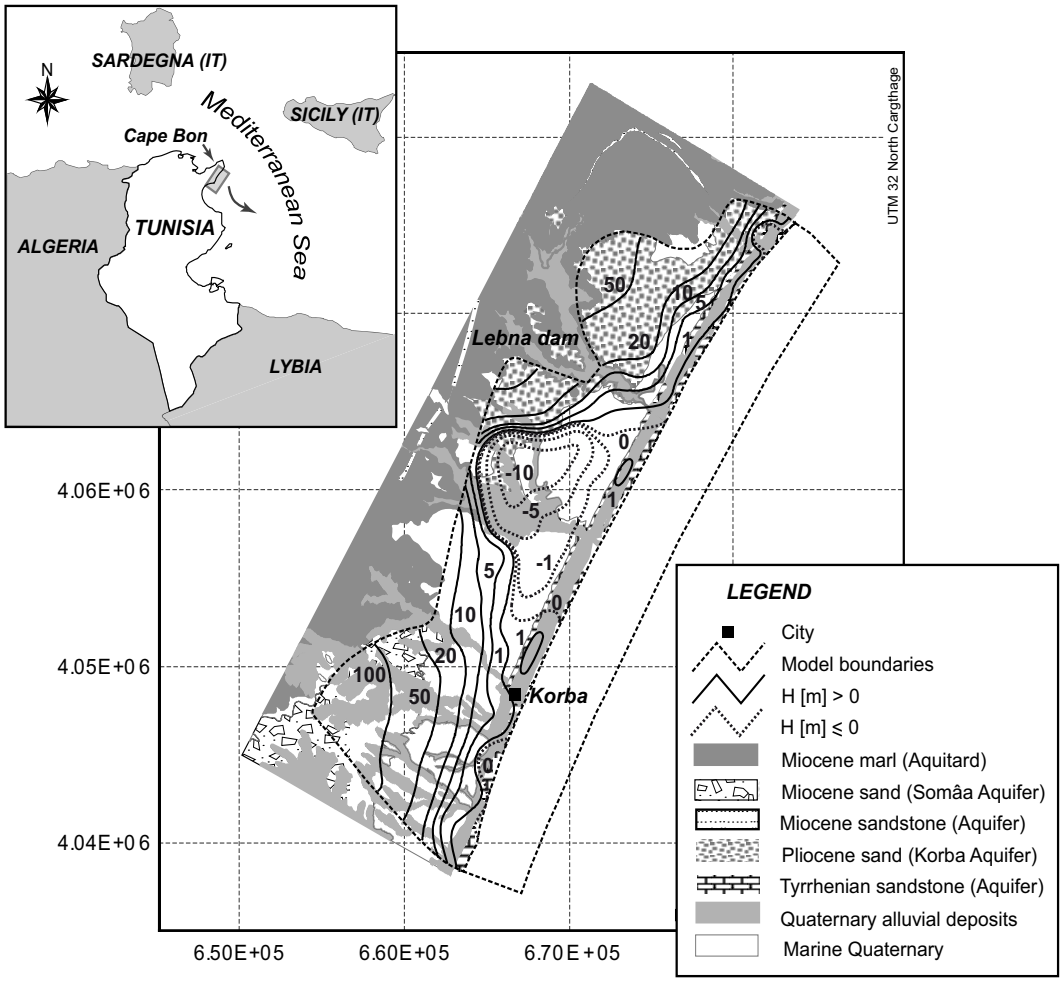

Fig. 1 Location map of the Korba aquifer and geological settings (squares are 10 by 10 km). Hydraulic heads observed in august 2004 are also shown.

Three main geological formations constitute the aquifer system. The first is of Tyrrhenian (Quaternary) age forming approximately a 1.2 km width band parallel to the coast all along the domain. It is constituted mainly by arenitic limestone underlined by a conglomeratic layer (Oueslati 1994). Its thickness varies between 10 and 50 m. The second formation is of Pliocene age and corresponds to marine sediments deposited in the Dakhla syncline in the North of the city of Korba. The dominant lithologies in that formation are yellow sands with alternating clay and sandstone levels. The third formation, called “the sands of Somâa”, is of late Miocene age and is localized only in the South of the study area. It is composed mainly of thick fine sand layers of continental origin including conglomeratic levels

and clay lenses. The Pliocene formation thickness might reach 250 m offshore and decreases toward the West, while the Somâa formation thickness exceeds 400 m (Chapter 3). The aquifer layers are underlined by Miocene marls forming the bedrock of the system (Ennabli 1980). This aquitard contains lenticular sandstone bars of variable thickness and depth often separated by thick layers of almost impervious marls.

The aquifer is essentially unconfined. The Plio-Quaternary units which constitute the largest part of the aquifer (north of Somâa) are the most productive and are characterized by the highest transmissivity. (Chapter 3) estimated the hydraulic conductivity of the Quaternary arenitic limestone to be around 10^{-4} m/s and of 5 10^{-5} m/s for the Pliocene formation and 6 10^{-6} m/s for the Somâa one. The same author estimated the natural recharge of the aquifer by infiltration of precipitation to around 29 Mm^3/y with high variability in space and time, and ranging between 8 % and 30 % of the mean annual rainfall of 420 mm/y. However, the abstraction rates which started in early 60's (Ennabli, 1980) mainly for irrigations purposes were estimated to be ranging around 50 Mm^3 from early 80's to 2004(Chapter 3).

Under natural conditions, groundwater flows towards the sea. However, due to the intense groundwater abstraction, hydraulic gradients are reversed mainly toward the central part of the aquifer leading to enhanced seawater intrusion. In 2004, the piezometric map showed a wide depression in the central part of the aquifer (Fig. 1) where the hydraulic head went down to 12 m under the mean sea level. Vertical salinity profiles in the wells at 2 km from the shoreline showed Total Dissolved Solid (TDS) values ranging between 2 and 15 g/l, confirming the landward seawater encroachment. In Chapter 3, we estimated that the seawater intrusion velocity was on the order of 100 m/y during the last decade and corresponded to around 7 Mm^3/y of saltwater entering to the aquifer.

3. Methodology

3.1 Geostatistical model of the Pumping rates

The geostatistical model of the pumping rates developed for the purposes of the present study is based on the multi-linear regression model built in Chapter 3. For a better understanding of the approach adopted herein, the previous statistical framework is presented briefly. In Chapter 3 we used a set of 432 measured pumping rates (Fig. 2a) as a reference to construct a multi-linear regression model.

The latter combines 8 secondary parameters such as aquifer transmissivity, crop evapotranspiration, seasonal head variation, etc. The regression was then used to estimate the pumping rates over the whole aquifer using the 8 exhaustively mapped variables (Fig. 2a). Even if the correlations between some of the secondary parameters and the pumping rates were statistically significant, others showed weak correlations. The milti-linear regression model fit is not very accurate and an important residual error is clearly visible on the plot of estimated versus measured discharge rates (Fig. 2b).

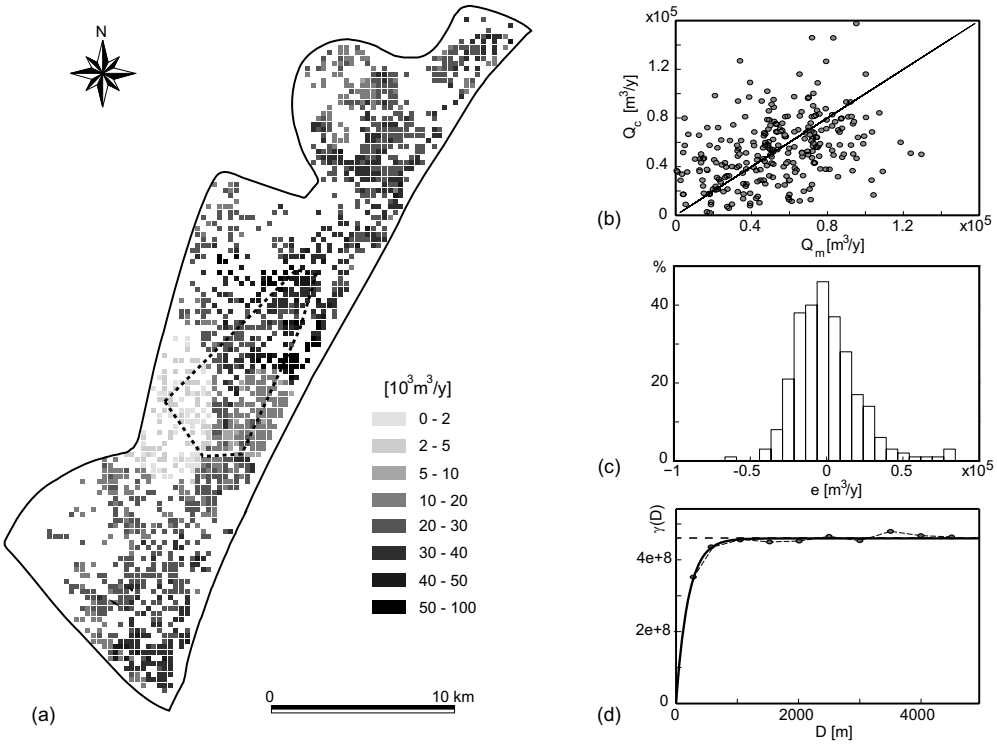

Fig. 2 (a) Average pumping rates map after Chapter 3 with the location of the exhaustive pumping rate survey (dashed line polygon); (b) Scatter plot of estimated Q_c versus measured Q_m pumping rates; (c) histogram of the residual e and (d) experimental (black circle) and model (solid line) variograms of the error.

In this study, the statistics and the spatial distribution of the residuals e between the measured pumping rates and those computed by the multi-linear regression model were analyzed in a geostatistical framework. It was found that the residuals

could be approximated by a Gaussian distribution (Fig. 2c) of zero mean and 2.1 10^4 m^3/y standard deviation. The experimental variogram (Fig. 2d) showed a spatial structure, indicating that the errors correlate over distances reaching up to 700 m. The experimental variogram was then modeled using an exponential model with a range of 700 m (Fig. 2d). In order to allow more spatial continuity of the pumping rates at small scales, it was decided not to use a nugget effect in the model.

Based on the variogram model and the Gaussian distribution, unconditional simulations using the turning band method (Matheron 1973; Tompson et al. 1989) were performed to generate 100 residual maps over the whole domain. The grid used to simulate the residuals is the same as used in Chapter 3 to estimate the average pumping rates map and corresponds to the well density 300 x 300 m resolution grid. Each residual map was added to the average one (estimated by the multi-linear regression) to obtain 100 equally likely realizations of maps of pumping rates all sharing the same total volume.

3.2 The Korba aquifer 3D numerical model

The numerical groundwater model used to propagate the uncertainty on the pumping rates to seawater intrusion forecasts was developed in Chapter 3 and built with ***Groundwater*** simulator (Cornaton 2007). *GroundWater* is a three-dimensional finite element simulator. It solves a broad range of coupled processes, including variably saturated flow, density-dependent flow, heat and thermo-haline transport, as well as groundwater age. The mesh honoring the 3D geometry of the aquifer was discretized into 877'249 prismatic finite elements and 19 layers (Fig. 3) with local refinement in the main aquifer and close to the sea.

The steady-state flow boundary conditions are a prescribed head on the seafloor and constant lateral inflow on the northern part of the Pliocene. The seaside boundary extends 3.5 km offshore (arbitrary fixed) to avoid unrealistic boundaries effects. In transient regime, additional lateral fluxes were attributed to account for recharge from the Lebna dam and an increasing discharge rates in the wells. The recharge of the aquifer by infiltration of precipitation (on the top layer) was estimated from 1960 to 2004, by the daily Thornthwaite-Mather method (Steenhuis and Vandermolen 1986), using the regional soil distribution (100 by 100 m grid) with relative field capacities, daily rainfall and pan evaporation data. It is worth noting that 1498 time-dependent functions (1491 for the well clusters, 6 for the areal recharge and 1 for the lateral recharge) were implemented in the model. With regard

to transport boundary conditions, a maximum relative seawater concentration of 1 [-] was assigned at the seafloor only to inward seawater fluxes (water enters the aquifer with seawater concentration but exits with the aquifer's concentration). The calibration of the 3D model against field observations has been achieved in a time-dependent, iterative and semi automatic fashion using PEST (Doherty 1998) for flow and by trial and error for transport. The overall calibration of the model is considered sufficient to use the model for predicting uncertainty on head and salt concentration distributions within the Korba aquifer.

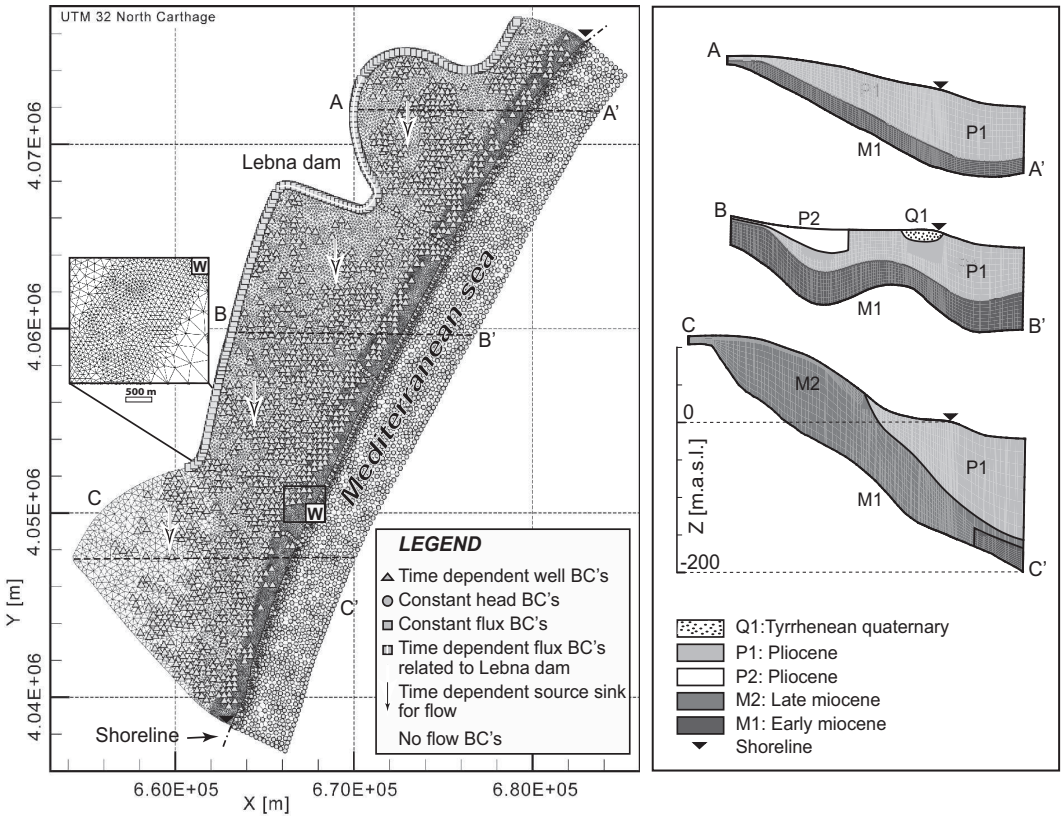

Fig. 3 The Korba aquifer 3D numerical model, modified after Chapter 3. Note that wells were attributed at around 10 m from model surface and the lateral fluxes were integrated over the Pliocene thickness. Element sizes ranging from 150 to 200 m in the main aquifer and ranging between 50 and 100 m near the shoreline. Vertically, the mesh is divided into 19 layers with 5 m thickness in average.

3.3 Monte Carlo simulations and Grid computing

A standard Monte Carlo method was used. For each realization, the numerical model was run (in transient regime for 44 years) by changing only the discharge rates. The resulting outputs are postprocessed to obtain ensemble statistics and probability maps of heads and concentrations. Each single simulation required more than 14 hours of computing time (on a linux AMD Opteron 64 bit machine). To circumvent the large computing time required to complete a sufficient number of simulations, the numerical simulations were run concurrently on the Grid infrastructure developed by the European EGEE project (http://www.eu-egee.org). The EGEE platform consists of over than 68,000 CPUs in addition to about 20 Petabytes of storage. EGEE grid includes more than 120 partners in 48 countries organized in 13 geographically dispersed collaboration groups (virtual organizations) focused on their specific research areas. A particularly interesting aspect offered by this emerging technology is that non-European partners, e.g. Tunisian academic researchers and water managers, can run, via a web portal, their groundwater simulations on the same Grid platform via the EGEE companion project EUMEDGRID (http://www.eumedgrid.org). Note that Monte Carlo simulations were carried out using both ***CODESA3D*** (Gambolati et al. 1999) and ***GroundWater*** (Cornaton 2007) for comparison and validation.

4. Results

4.1 Discharge rates

The ensemble average of the 100 pumping rate realizations was almost similar to the regression estimation of Chapter 3. Figure 4 shows two example realizations. In 1985 and 2004, the total estimated exploitation volumes are 50 and 47 Mm^3/y respectively. The 100 simulated pumping rate maps have all the same total abstraction volumes as the average simulated residual is null. The magnitude of absolute residuals, which is randomly distributed for each simulation in all wells, is 31.25 and 29.3 Mm^3 in 1985 and 2004, respectively. It corresponds to 62.5 % of the total abstraction volume. At each point the groundwater abstraction can be highly variable through the 100 simulations as shown for two candidate wells (240 and 361) in figures 4c and 4d. The median value of the ratio Q_{max}/Q_{min} is 6.5, and it depends on the well location. The average pumping rate on a single grid cell is 3.15 10^4 m^3/y in 2004. Figure 4e shows the time evolution of the pumping rates from 1960 to 2004 which is the same as in Chapter 3.

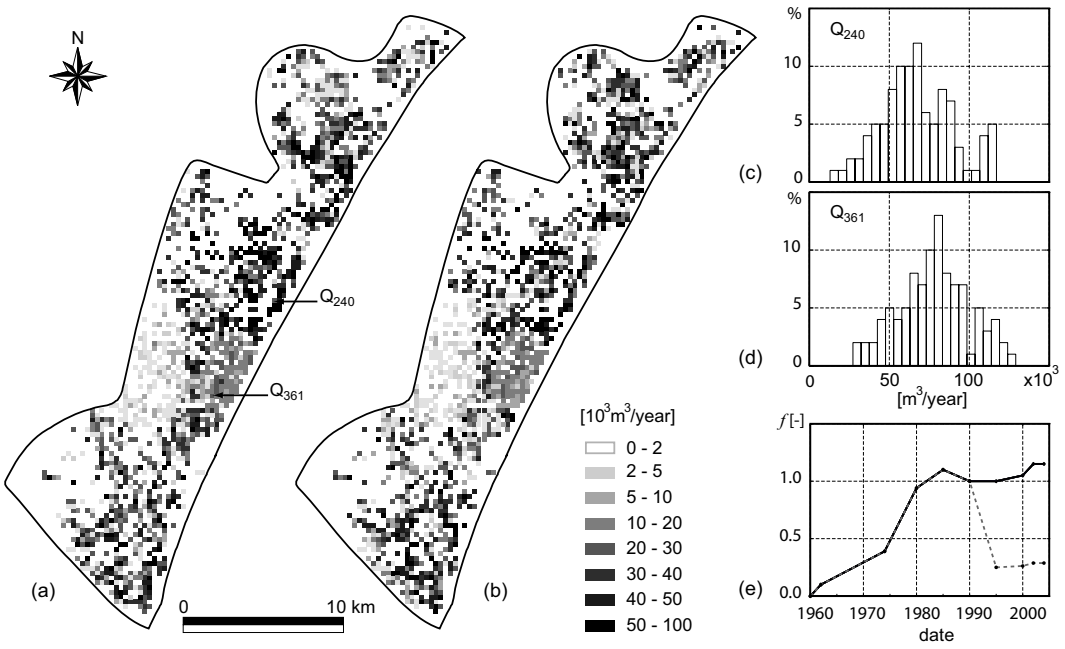

Fig. 4 (a) and (b) Two example maps of the pumping rates (Q_c 1996); (c) and (d) Histogram of pumping rates for two wells (240, 361). (e) Time-dependent evolution functions for both wells (solid black line for Q_{240} and gray dashed line for Q_{361}) with 1996 volumes as reference.

4.2 Grid Computing

The simulations were executed on the EGEE infrastructure. Each simulations was launched separately with the help of Unix shell scripts which execute different tasks (e.g. naming, decompressing, copying files) and a JDL file (Job Description Language) describing all input and output files (of the simulator) and the requirements for the job, launching the job (using gLite commands) on the grid, monitor the job, and transfer back the results. Three technical difficulties were encountered during that procedure. First the middleware was not stable. It was necessary to adapt regularly the shell scripts. Second a significant number of jobs (between 20 and 30 %) were not executed because of reliability problems in the infrastructure. Third, transferring the files was time consuming, but this could have been optimized by running the post-processing as well on the Grid instead of doing it locally after having transferred back all the files. This experience has shown that it is still more difficult to run Monte Carlo simulations on a Grid infrastructure than running it on a local cluster, but it could be done with success.

4.3 Monte Carlo simulations

First of all, the ensemble average head and concentration distributions (Figs. 5ab) are in agreement with the conceptual model of the aquifer as well as the observed head in 2004 (compare Fig. 1 and Fig. 5a). Ensemble average maps show very well the large depression in the central zone of the aquifer and the consequent seawater intrusion.

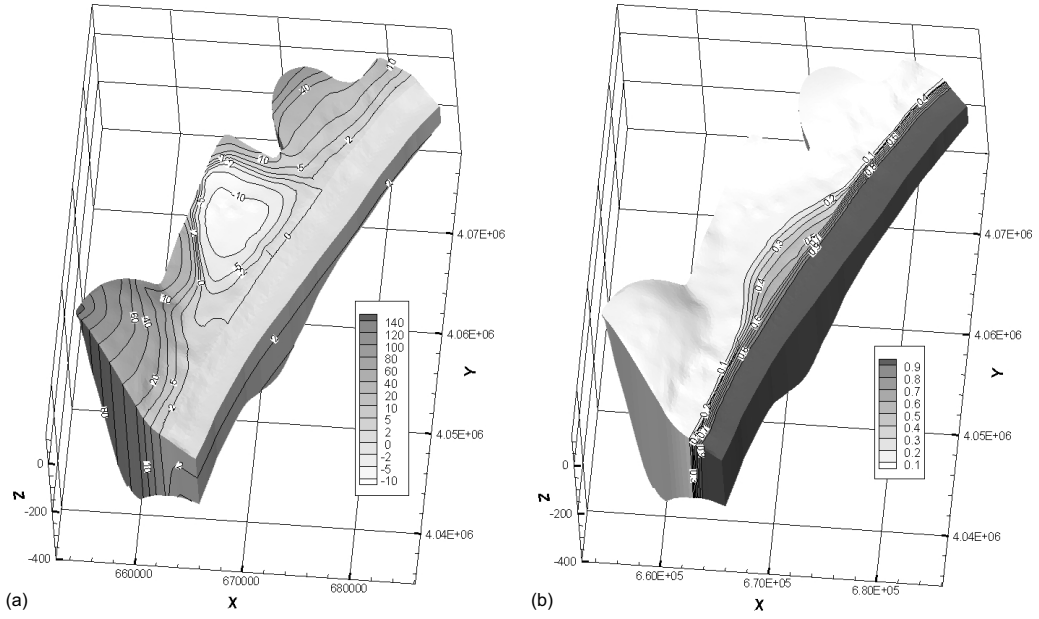

Fig. 5 Ensemble average (a) head [m] (b) relative concentration [%] maps for the 100 realizations.

However, it is important to notice that the map of ensemble average heads over 100 simulations is different from the map of heads calculated using the average pumping. The same occurs for concentration. This is normal and due to the nonlinearity of the flow and transport equations as it was studied for example by Delhomme (1979). It is worth noting that ensemble averages of head and concentration distributions are more robust prediction as compared to the solutions resulting from using average pumping. Note that model parameters were not calibrated for each simulation of the pumping rates.

In addition to ensemble averages, the probability distribution functions of heads and concentrations at any point and the probability maps for exceeding a certain concentration or head threshold were calculated. Figure 6 shows the histograms of

heads and concentrations in two arbitrary wells (360 and 240). The histograms reflect the effects of uncertain pumping rates on heads and concentration and also show that small concentrations are more uncertain (compare 6c and 6d). The same figure also shows that higher pumping rates (in average) led to higher uncertainty (compare Figs. 4c and 4d and Figs 6c and 6d). Figure 7 shows the probability map of exceeding a relative concentration of 0.1 (Fig. 7a) and the probability map of the water table to fall below the mean sea level (Fig. 7b). These maps are graphically not very different from the maps that one could build based on a direct geostatistical interpolation of heads or concentrations. Making such an analysis would allow to map the heads and concentrations and evaluate the uncertainty related to the lack of head or concentration data. However, making such maps may not be easy because neither the heads, nor the concentrations are stationary in space and time. The geostatistical analysis would then need to be rather sophisticated, furthermore such a study would not account for the physics of the process. The maps shown in Figures 5 and 7 have a different meaning. They represent the uncertainty in heads and concentrations resulting from an evaluation of the uncertainty on the discharge rates. They are interesting because they all respect the basic physics used in the 3D density-dependent flow and solute transport model. Because other uncertainties were not accounted for, they also represent a lower bound of the uncertainty.

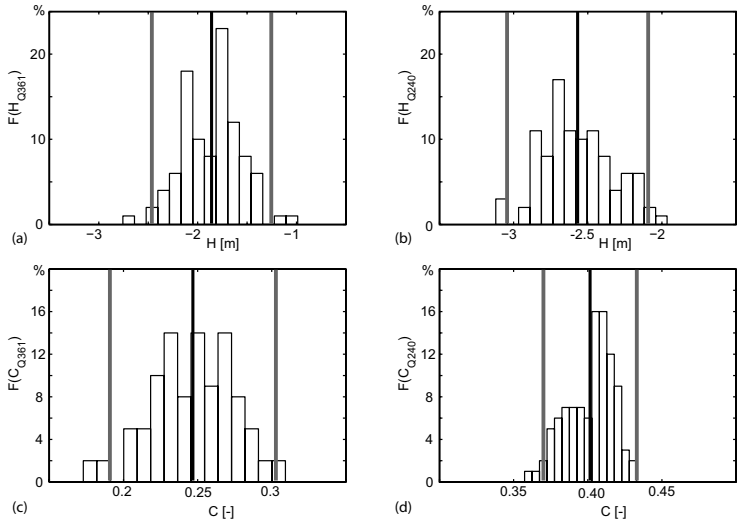

Fig. 6 Histograms of H [m] (a) and (b) and C [-] (c) and (d) in the wells Q_{361} and Q_{240} respectively. Note that ensemble average (black line) and ensemble average plus and minus 2 ensemble standard deviations (gray lines) are also shown.

Analyzing more precisely the results, one can extract the regions where the probabilities are intermediate. They correspond to the maximum uncertainty. For example, in 2004 the area delimited by the 0.05-0.95 isoprobability contours of exceeding the 0.1 relative concentration (UC) covers a fraction of about 4% of the total onshore area of the aquifer. This means that the uncertainty on the spatial exploitation rates distribution leads to a rather small uncertain area in which the seawater intrusion may or may not be encountered.

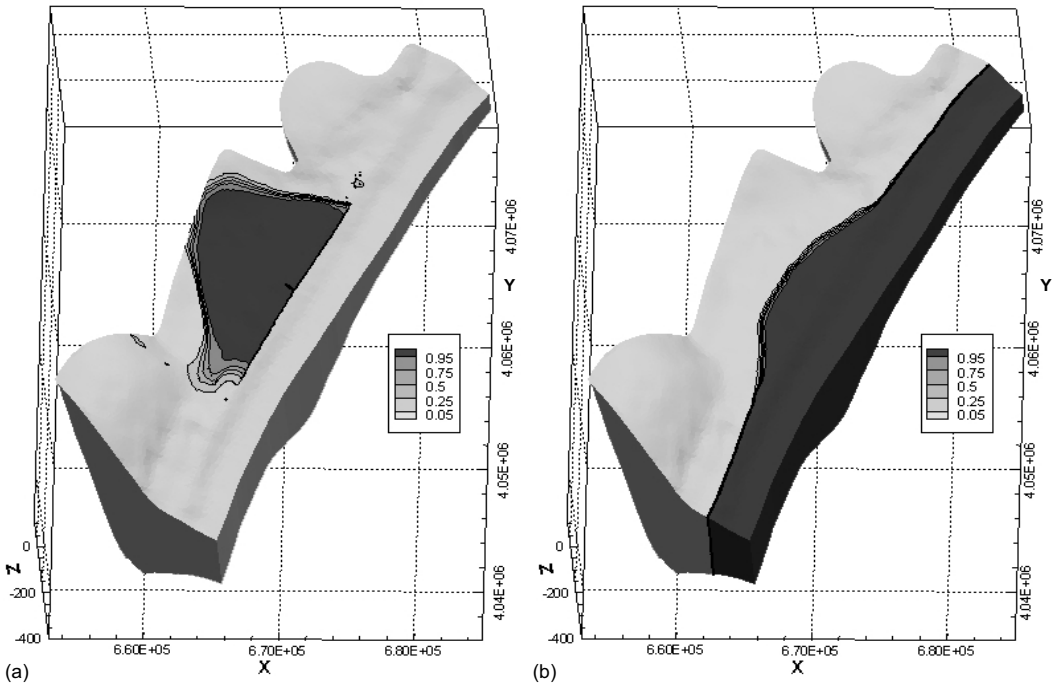

Fig. 7 Probability map for a point (a) to be under the mean sea level and (b) to exceed the 0.1 relative salt concentration. Both maps show 0.95, 0.5 and 0.05 isoprobability contours.

Another way of looking at the problem is to estimate the area in which it is not known precisely whether the groundwater levels are below sea level. For that purpose, one can compute the area delimited by the 0.05-0.95 probability contours of being below the mean sea level (UH). It was found that it is about 8% of the area of the aquifer. Geographically, Figures 7a and 7b show that the large uncertainties on heads and concentrations are located around the piezometric depression in the central part of the aquifer and at the front of the advancing seawater.

The analysis of the temporal evolution of the uncertainty indicators (Fig. 8) reveals a different behavior for heads and concentrations (UH and UC). Initially, there is no uncertainty because all realizations start from the same initial state (i.e. no pumping). Then the uncertainty on heads rises rapidly with increasing discharge, it never decreases even when the discharge decreases. The uncertainty on concentrations rises as well regularly but at a smaller rate. This is explained by two factors. On one side, the flow equation reacts faster than the transport equation. On the other side, the two processes are not affecting the same domain: the seawater intrusion occurs only on a strip along the coast while the piezometric map reacts everywhere in the domain. Using the same normalization constant (area of the aquifer) for both processes is arbitrary.

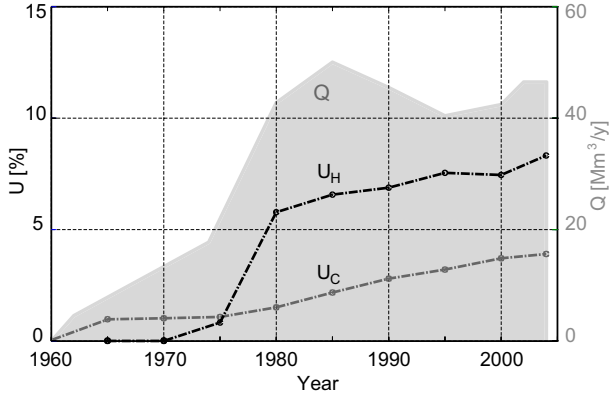

Fig. 8 Time evolution of the uncertainty: Q (gray polygon) is total estimated exploitation volumes [Mm^3], U_H (thin black line) is the ratio (%) between the uncertain area with respect to the probability to fall below sea level and the onshore aquifer area, U_C (thick black line) is the ratio (%) between the uncertain area with respect to the probability to exceed 0.1 relative concentration and the onshore aquifer area.

5. Discussion and conclusions

The aims of the present work were to investigate how to evaluate the uncertainty associated with the spatial distribution of the pumping rates in the Korba aquifer and to test whether grid computing could be used for the Monte Carlo analysis. For that purpose, a geostatistical analysis of the spatial distribution of pumping rates coupled with Monte Carlo simulations were deployed on the distributed computing infrastructure provided by the EGEE Grid platform.

Surprisingly, it was found that the uncertainties on model predictions were small. The hydraulic head uncertainties were larger than the salt concentration uncertainties. There are several interpretations for such moderate level of predicted uncertainty. First, all the other aquifer parameters were kept constant to separate the effect of the uncertainty associated with the spatial distribution of the pumping rates from the effect of the uncertainty associated with other model parameters. Furthermore, the variogram model used to simulate the correction terms, and therefore the variability between the simulations, has a small range as compared to the extent of the model. As a consequence, in spite of the fact that two neighbor wells might have very different pumping rates in the same simulation, this may be compensated by the redistribution of the pumping rates between different simulations. However, even if the area delimited by the isolines 0.05 and 0.95 of the probability of exceeding the 0.1 relative salt concentrations is small with respect to the extent of the aquifer, it still covers more than 1300 ha and represents high potential losses in agricultural production resulting in a high socio-economical impact on the local population. Furthermore, this area is expected to continue to increase due to the time-shift between the evolution of the uncertain area and the evolution of the pumping rates (Fig. 8).

In terms of grid computing, the experience showed that it was more difficult to handle Monte Carlo simulations on the EGEE infrastructure than on a regular cluster. This was mainly due to the fact that the technology was still in development during our tests and that we faced instability problems both with the middleware and the infrastructure. However, the grid could be used remotely to launch simulations from different locations in Europe (Sardinia and Switzerland). With the rapid advances in Grid technology, it is expected that the reliability and stability issues will soon be overcome and that the technology will rapidly become completely transparent for the user. It is clear that this will provide a formidable opportunity for countries or researchers having limited access to local computing resources.

References

Abarca E (2006) Seawater intrusion in complex geological environments. PhD Thesis, Technical University of Catalonia, Barcelona

Al-Bitar A, Ababou R (2005) Random field approach to seawater intrusion in heterogeneous coastal aquifers: unconditional simulations and statistical analysis. In: Geostatistics for Environmental Applications Renard P, Demougeot-Renard H, Froidevaux R Eds Springer

Bear J, Cheng AHD, Sorek S, Ouazar D, Herrera I (1999) Seawater intrusion in coastal aquifers- concepts, methods and practices. Kluwer academic publishers, Dordrecht

Carrera J (1993) An Overview of Uncertainties in Modeling Groundwater Solute Transport. Journal of Contaminant Hydrology 13: 23-48

Cheng AHD, Ouazar D (2003) Coastal Aquifer Management: Monitoring, Modeling, and Case Studies. Lewis Publishers

Cornaton F (2007) Ground Water: A 3-D Ground Water Flow and Transport Finite Element Simulator. Reference Manual, 190 pp http://www1uninech/chyn/php/softwaresphp

Custodio E (2002) Aquifer overexploitation: what does it mean? Hydrogeology Journal 10: 254-277

Dagan G, Zeitoun DG (1998) Seawater-freshwater interface in a stratified aquifer of random permeability distribution. Journal of Contaminant Hydrology 29: 185-203

Delhomme JP (1979) Spatial Variability and Uncertainty in Groundwater-Flow Parameters - Geostatistical Approach. Water Resources Research 15: 269-280

Diersch H-JG, Kolditz O (2002) Variable-density flow and transport in porous media: approaches and challenges. Advances in Water Resources 25: 899–944

Doherty J (1998) PEST-Model Independent Parameter Estimation, Watermark Numerical Computing, Brisbane, Australia

Ennabli M (1980) Etude hydrogéologique des aquifers du nord-est de la Tunisie pour une gestion intégrée des ressources en eau. Thèse de Doctorat d'État, Université de Nice

Foster I, Kesselman C (1998) Computational Grids. In: Foster I, Kesselman C (eds) The Grid: blueprint for a new computing infrastructure. Morgan Kaufmann Publishers, Inc, San Francisco

Gambolati G, Putti M, Paniconi C (1999) Three-dimensional model of coupled density-dependent flow and miscible transport in groundwater. In: Bear et al (eds) Seawater intrusion in coastal aquifers: concepts, methods, and practices. Kluwer academic publishers, Dordrecht, pp 315–362

Khlaifi I (1998) Contribution à l'étude de l'intrusion marine par un modèle de transport tridimensionnel : interfaçage avec des systèmes d'information géographique. Thèse de master, Institut National Agronomique de Tunisie

Konikow LF, Kendy E (2005) Groundwater depletion: A global problem. Hydrogeology Journal 13: 317-320

Kouzana L, Ben Mammou A, Sfar Felfoul M (2009) Seawater intrusion and associated processes: case of the Korba aquifer (Cap-Bon, Tunisia). Comptes Rendus Geosceinces

Matheron G (1973) The intrinsic random functions and their applications. Advances in Applied Probability 5: 439-468

Milnes E, Renard P (2004) The problem of salt recycling and seawater intrusion in coastal irrigated plains: an example from the Kiti aquifer (Southern Cyprus). Journal of Hydrology 288: 327-343

Naji A, Cheng AHD, Ouazar D (1998) Analytical stochastic solutions of saltwater/freshwater interface in coastal aquifers. Stochastic Hydrology and Hydraulics 12: 413-430

Oueslati A (1994) Les côtes de la Tunisie. Recherche sur leur évolution au Quaternaire. Imprimerie officielle de la Republique Tunisienne, Tunis

Paniconi C, Khlaifi I, Lecca G, Giacomelli A, Tarhouni J (2001) Modeling and analysis of seawater intrusion in the coastal aquifer of eastern Cap-Bon, Tunisia. Transport in Porous Media 43: 3-28

Slama F, Milnes E, Bouhlila R (2008) Calibrating unsaturated model parameters using Electrical Resistivity Tomography imaging. In: Refsgaard J.C. KK, Haarder E. and Nygaard E. (ed) Calibration and Reliability in Groundwater Modelling: Credibility of Modelling. IAHS Publication 320: 148-153

Sorek S, Pinder GF (1999) Survey of computer codes and case histories. In: Bear J et al (ed) Seawater intrusion in coastal aquifers: concepts, methods, and practices. Kluwer Academic Publishers, Dordrecht, pp 399–461

Steenhuis TS, Vandermolen WH (1986) The Thornthwaite-Mather Procedure as a Simple Engineering Method to Predict Recharge. Journal of Hydrology 84: 221-229

Tarhouni J, Jemai S, Walraevens K, Rekaya M (1996) Caracterisation de l'aquifere cotier de Korba au Cap Bon (Tunisie). Progress report 95-96 for AVI-73 EC Project

Tompson AFB, Ababou R, Gelhar LW (1989) Implementation of the 3-Dimensional Turning Bands Random Field Generator. Water Resources Research 25: 2227-2243

United Nations Foundation (2008) UN Atlas of the Oceans. http://www.oceansatlas.org/

Chapter 5

Stochastic forecasts of seawater intrusion in the Korba aquifer (Tunisia) towards a sustainable groundwater management*

Abstract This Chapter is concerned with numerical groundwater modelling considering heterogeneous and uncertain hydraulic parameters. It describes how uncertainties on model inputs can be modelled and propagated to long term forecasts of flow and solute transport model. Theses general objectives are addressed through the case study of the Korba coastal aquifer (Tunisia). The stochastic framework presented in this work consisted firstly in modelling two sources of uncertainty. A geostatistical model of the exploitation rates was previously constructed based on linear regression model combining incomplete direct data and exhaustive secondary information including aquifer geometry and physical parameters. A geostatistical model of the hydraulic conductivity within the aquifer was built by combining lithological information and a limited number of hydraulic tests. Secondly, the effects of both uncertainties on 3D density-dependent transient model were analyzed separately and then jointly. Most important, the forecasts of the impacts of two different management scenarios on seawater intrusion in 2048 were performed in a stochastic framework and accounting for uncertainties on the input parameters as well as eventual changes on the boundary conditions of the Korba aquifer. Both uncertainties led to a zone representing 12 % of the aquifer area, where the groundwater heads and salt concentrations were not known with accuracy. Moreover, long term forecasts showed that most probably, the Korba aquifer is potentially subject to important future losses in the agricultural sector.

* This chapter is based on the paper:
Kerrou J., Renard P., Cornaton F. and Perrochet P. (2008) Stochastic forecasts of seawater intrusion in the Korba aquifer (Tunisia) towards a sustainable groundwater management. Submitted to Advances in Water Resources

1. Introduction

Numerical models are frequently used to assess seawater intrusion problems (Galeati et al. 1992; Iribar et al. 1997; Yakirevich et al. 1998; Bear et al. 1999; Paniconi et al. 2001; Sadeg and Karahanoglu 2001; Aharmouch et al. 2002; Arfib et al. 2002; Milnes and Renard 2004) and to design optimal groundwater resources management schemes (Cheng et al. 2000; Mantoglou et al. 2004; Abarca et al. 2006; Alcolea et al. 2008). With the increasing debate on climate change and its potential impacts on groundwater resources worldwide (Eckhardt and Ulbrich 2003; Holman 2006; Scibek and Allen 2006; Bates 2008), groundwater models are more and more used for investigating the response of coastal aquifers to potential sea level rise, or changes in recharge (Sherif and Singh 1999; Essink 2001; Ranjan et al. 2006).

Nevertheless, the modelling of seawater intrusion in coastal aquifers remains a challenge (Diersch and Kolditz 2002). Solving density-dependent flow and solute transport equations requires numerical methods that are very sensitive to space and time discretization. These issues are even more critical when the heterogeneity of the aquifer has to be accounted for. The difficulties are usually reduced by simplifying the problem (reducing problem dimension, assuming homogenous model parameters, assuming a sharp interface, etc.), but even under these simplifications, seawater intrusion models still often imply considerable computing efforts. In addition, the lack of data to estimate model inputs and their distributions in space and time, necessary for a reasonable calibration, leads to uncertain model predictions. In general, the resulting uncertainties justify the need of stochastic models as a tool to help decision makers (Renard 2007). This is illustrated for example by the work of Hassan et al. (2001) and Pohlmann et al. (2002) who evaluated the uncertainty on the transport of radionuclides in a coastal site in Alaska. Using a homogeneous model and Latin Hypercube sampling, they showed that the ratio between recharge and hydraulic conductivity was the parameter most affecting the uncertainty.

In this study, we are interested in the Korba region located in Tunisia (Fig. 1), where seawater intrusion is progressively invading the coastal aquifer. Although the invasion is relatively slow as compared to the lowering of the water levels, it is threatening the agricultural production. Previous calculations have shown that it would require about a century to recover the natural state if all the groundwater exploitation could be stopped now (Chapter 3). While this is not a possible management solution, the main aim of this part of the work is to provide forecasts regarding the possible evolution of the aquifer in the next 40 years if the groundwater abstraction is pursued as usual or if the water management authorities impose a drastic reduction to the farmers.

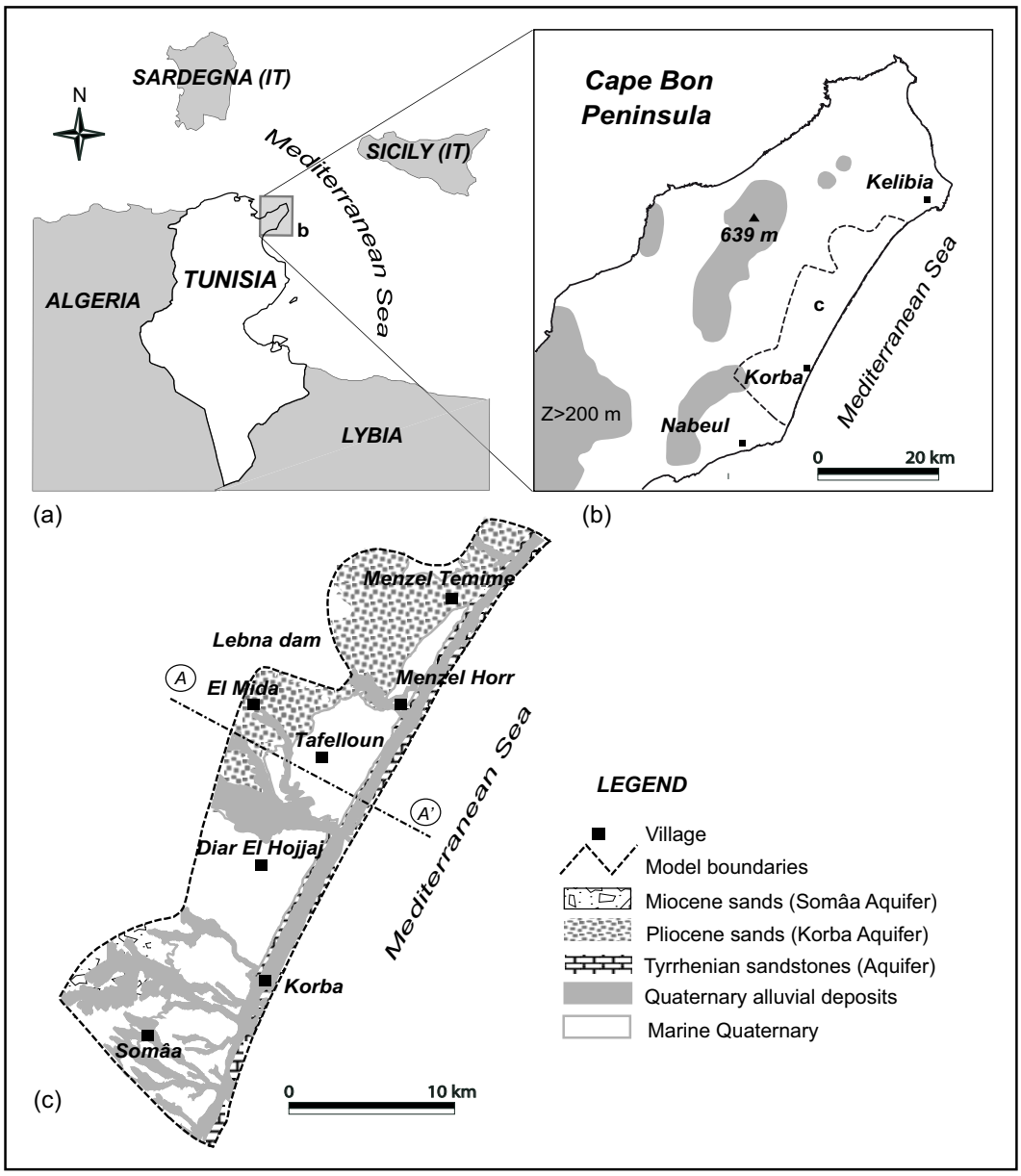

Fig. 1 Location map of (a) Cape Bon north-eastern Tunisia and (b) Korba aquifer; (c) geological setting (AA' cross-section is shown in Fig. 2).

The scenarios account for a plausible evolution of the climatic conditions in the region. Because the system is imperfectly known, a stochastic approach has been chosen. In particular, the uncertainty on the spatial distribution of the pumping rates and the uncertainty due to the heterogeneity of the aquifer are considered. The model of the pumping rate distribution has been developed in Chapter 3. The model

describing the spatial heterogeneity of the hydraulic conductivity has been constructed by combining lithological information and a limited number of hydraulic tests. The lack of sufficient information did not allow to infer a precise geostatistical model and this is why uncertainty on the parameters of the geostatistical model was included as well in the analysis. The combined and separated effects of the two sources of uncertainty (extraction rates and hydraulic conductivity) are compared. From a practical point of view, despite the uncertainties that were analyzed, the computations showed that the aquifer deterioration that has been monitored in the past decades will continue even if groundwater abstraction is massively reduced.

2. The Korba aquifer system

The Korba aquifer system is located in the east of the Cape Bon peninsula in north Tunisia. It is about 40 km long and 10 km wide, bounded by the Mediterranean Sea on the eastern side (Fig. 1). As a major source of freshwater, the aquifer is intensively exploited mainly for irrigation purposes. Its exploitation started in the early 60's and has been estimated to be ranging around 50 Mm^3/y during the last decades. From the early 1980's to 2004 pumping has taken place from more than 9000 wells (DGRE 2000). Aquifer recharge mainly takes place by infiltration of precipitation which is highly variable in space and time. It is ranging between 8 % and 30 % of the 420 mm/y average annual rainfall, which represents 29 Mm^3/y in average (Chapter 3). Such unevenness between inputs and extractions led to seawater encroachment in the Korba aquifer, contaminating groundwater as far as 2 km inland in 2004. That situation has motivated numerous studies (Tarhouni et al. 1996; Khlaifi 1998; Paniconi et al. 2001; Slama et al. 2008; Kouzana et al. 2009).

The main aquifer formation is of Pliocene age and mainly consists of yellow sand with alternating clay and sandstone layers (Ennabli 1980). The thickness of the Pliocene formation is about 80 m in the central part of the area, reaching 250 m offshore and decreasing towards the west (Figs. 1 and 2). This formation is overlayed by Tyrrhenian Quaternary rocks which forms a 1.2 km wide strip parallel to the coastline all along the study area (Figs. 1 and 2), and is mainly composed of arenitic limestone and conglomeratic units (Oueslati 1994).

In the south of the study area, the late Miocene formation, called the Somâa sands, represents the second aquifer formation in importance. It is mainly composed of thick fine sand layers of continental origin including conglomeratic levels and clay lenses for a total thickness of 400 m. Figure 2 displays the conceptual model of

the Korba aquifer which was used to establish a 3D numerical transient model of density-dependent flow and solute transport.

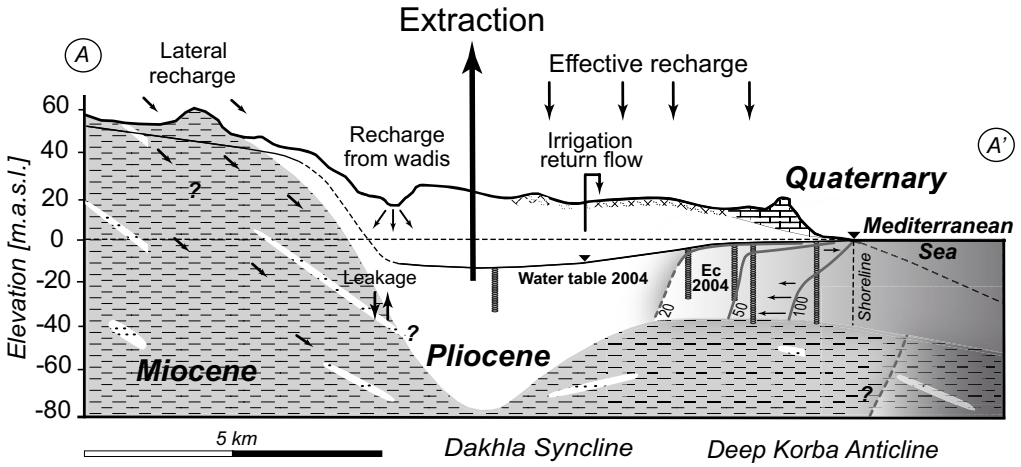

Fig. 2 Simplified geological cross-section (localization in Fig. 1) of the Korba aquifer system illustrating the conceptual model based on up-to-date geologic and hydrodynamic data. The maps (interpolated by kriging) of aquifer surface and bedrock topography, August 2004 water table as well as the percentage of seawater electrical conductivity are also shown (Chapter 3).

3. The 3D deterministic numerical model

For the purposes of this study, a high-resolution 3D numerical model of density-dependent flow and solute transport in the Korba aquifer was elaborated with the *Groundwater* code (Cornaton 2007). To honour the high well-density and to account for the heterogeneity of the hydraulic conductivity, the 3D mesh was discretized into 1.616 million prismatic finite elements (0.842 million nodes) with 36 layers. The mesh displays local horizontal refinement especially close to the sea and vertically in the main aquifer (Pliocene) with an average layer thickness of 3 m. The boundary conditions (BCs) and model parameters were obtained by calibration as previously discussed in Chapter 3.

Steady-state BCs consists of prescribed head on the seafloor and constant lateral inflow along the northern limit of the Pliocene formation. The seaside boundary extends 3.5 km (arbitrarily fixed) offshore to avoid unrealistic boundary effects.

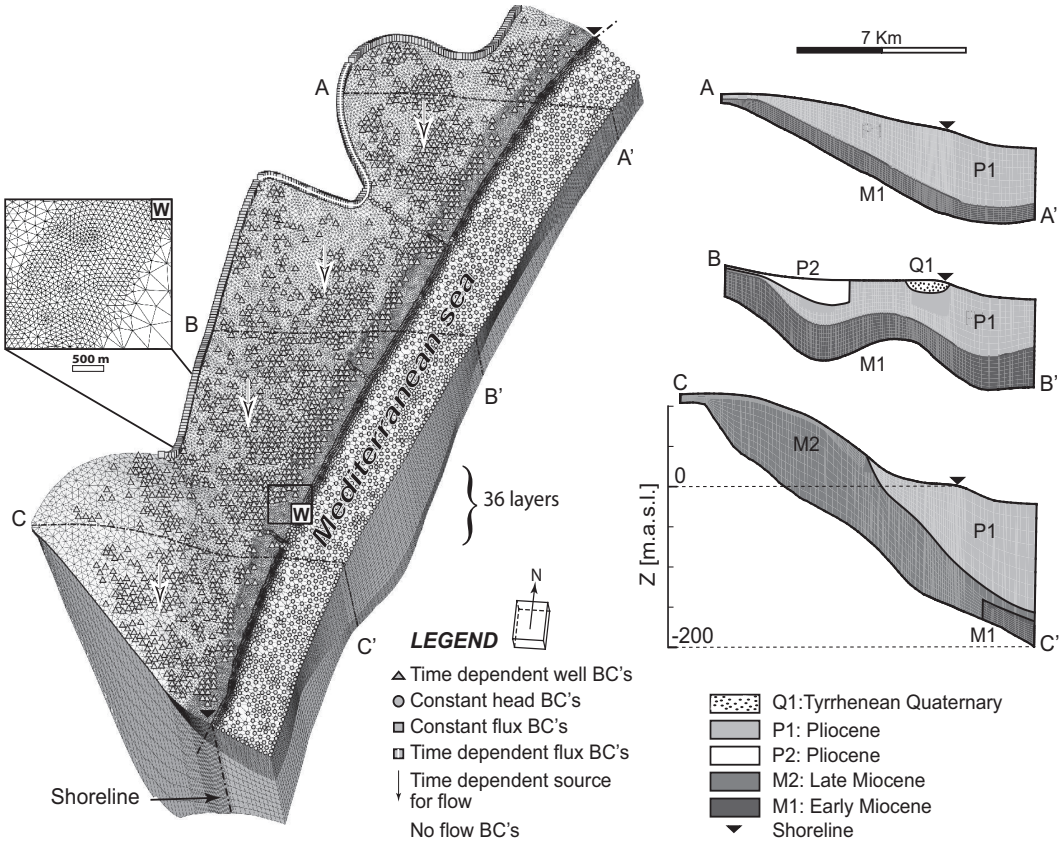

Fig. 3 The Korba aquifer 3D numerical model and three flow material cross-sections. Note that wells are attributed at the third slice and lateral fluxes are integrated on the thickness of the Pliocene only (modified after Chapter 3).

For the 44 years of transient-state simulation (1960-2004), time-dependent lateral fluxes as well as increasing discharge rates in the wells were considered. Space and time-dependent sources for flow were attributed on the top layer of the model to simulate recharge by infiltration of precipitation, estimated to be around 29 Mm^3/y in average. As transport boundary conditions, a maximum relative seawater concentration of 1 [-] was assigned on the seafloor with the constraint to be attributed to inward seawater fluxes only (water enters the aquifer with seawater concentration but exits with the aquifer concentration). Note that for both transient simulations of flow and solute transport, steady-state solutions were used as initial conditions. Calibrated flow and transport parameters are displayed in table 1.

Table 1 Model parameters

Parameter	Value
Seawater density [kg/m^3]	1.025 10^3
Freshwater density [kg/m^3]	1.000 10^3
Fluid viscosity [kg/m·s]	1.000 10^{-3}
Maximum relative concentration [-]	1
Average annual recharge [mm]	89
Hydraulic conductivity isotropic) [m/s]:	
Q1;P1;P2;M1;M2	2 10^{-4} ; 1 10^{-4}; 5 10^{-5}; 6 10^{-6}; 1 10^{-7}
Storage compressibility [1/m] :	
Q1&P2;P1;M1;M2	5 10^{-3}; 3 10^{-3}; 6 10^{-4}; 1 10^{-4}
Porosity [%] :	
Q1&P1;P2&M1;M2	10; 8; 5
Longitudinal dispersivity [m]	400
Transverse dispersivity [m]	40
Molecular diffusion [m^2/s]	10^{-8}

4. Uncertainty modelling

4.1 Pumping rates

The stochastic model of the spatial distribution of the pumping rates has been described in detail in Chapter 3, therefore we will only recall the main assumptions and principles underlying that model in this section. First, a limited number of reliable pumping rate measurements available in the central part of the aquifer were used to calibrate a multivariate linear regression model combining 8 secondary variables including aquifer transmissivity, crop evapotranspiration, seasonal head variation, etc. This allowed to compute a map of estimated pumping rates. The map has been corrected in the regions where no direct data were available based on field knowledge and based on the calibration of the groundwater flow model Chapter 3. In the central part of the aquifer where measurements of flow rates were available, it appeared that the residuals between the estimated map and the measurements were spatially correlated. This allowed to infer a geostatistical model and to generate 100 equally likely unconditional simulations of the residuals. It was assumed that the statistics of the residuals are stationary over the whole aquifer. Each of the residual

maps was then added to the average map , leading to 100 pumping rate maps all sharing the same total extraction rate as the residuals have a zero mean (Fig. 4). The temporal variation of the pumping rates is modelled by rescaling the maps by two time-dependent functions (Fig. 4e) as described in Chapter 3.

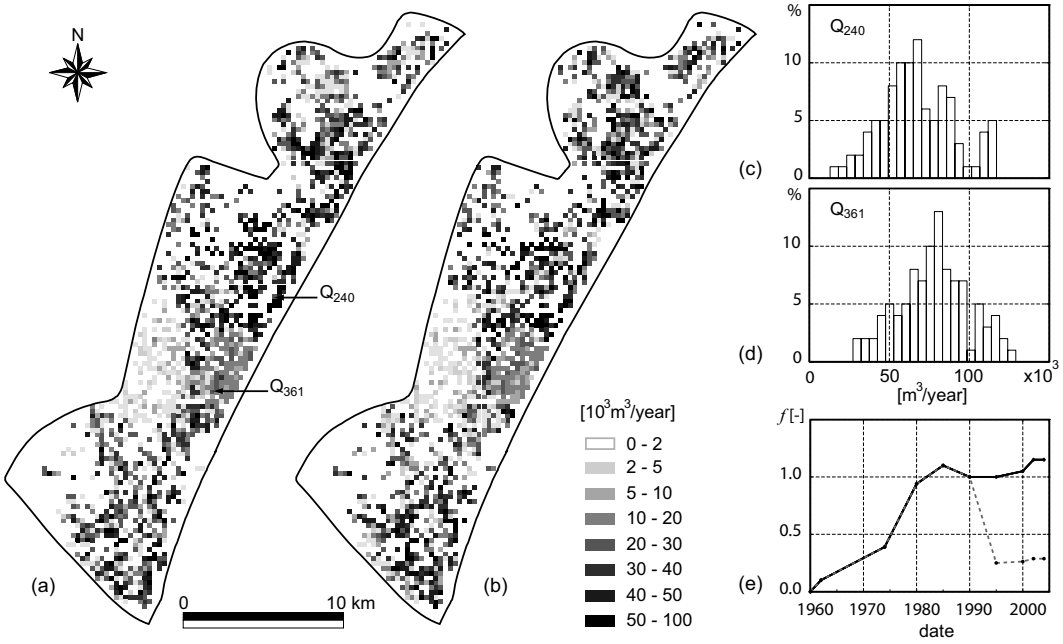

Fig. 4 (a) and (b) Two examples of the pumping rate maps (Q 1996); (c) and (d) Histograms of pumping rates for two wells (240, 361); (e) Time-dependent evolution functions f [-] for both wells (solid black line for Q_{240} and gray dashed line for Q_{361}) with 1996 volume as reference.

4.2 Hydraulic conductivities

The characterization of the heterogeneity was focused on the Pliocene formation because it represents the main aquifer. Two datasets were used. The first consists of 15 hydraulic conductivity data estimated from slug tests completed in the Pliocene formation. The slug tests were carried out by rapidly submerging a sufficiently heavy waterproof metallic cylinder into piezometers after installing pressure data loggers. The target was to create significant instantaneous drawdown and recovery in the order of one meter. Pressure data for both drawdown and recovery were then processed and interpreted mainly using Cooper et al. (1967) and Hvorslev (1951) models. As compared to pumping tests, which provide large-scale averages of hydraulic conductivities, slug tests allow a better characterisation of the small-scale heterogeneity. The hydraulic conductivity estimated from the slug tests varied

between 1.3 10^{-4} m/s and 7 10^{-7} m/s with a variance $\sigma^2_{ln(k)}$=1.5. In addition, the calibration of the 3D model have led to a value of 5 10^{-5} m/s for the average isotropic hydraulic conductivity of the Pliocene formation (Chapter 3). The second data set consists of 36 lithostratigraphical logs located mainly in the central part of the aquifer (Fig. 5) and provided by the regional water management authority (CRDA Nabeul). Those data describe the vertical distribution of the lithotypes within the Pliocene formation.

The procedure used to build the 3D fields of hydraulic conductivity is not standard. It was conceived to combine the available data in a simple manner and provide realistic 3D fields even if the inference of a proper geostatistical model could not be done due to the lack of sufficient data. First, the 36 geological logs were analysed qualitatively with respect to the lithotypes granulometry. Then, the lithostratigraphical data were assigned to three main lithotypes: sand, sandstone and clay with a resolution of 1 m (Figs. 5ab). The computation of the experimental variograms in 3D of each lithofacies did not show any clear spatial correlation. It was therefore decided to convert all lithotype data into hydraulic conductivity values in order to model them directly. To do so, a Gaussian distribution of the hydraulic conductivities was assumed. Its variance was estimated from the slug test data, and its mean was computed according to the following consideration. Since the horizontal hydraulic conductivity highly controls the seawater wedge penetration (Abarca et al. 2007), Ababou's formula (1995) was used to estimate the geometric mean μ_g of the hydraulic conductivity distribution by solving an auxiliary inverse problem, such that the effective horizontal hydraulic conductivity of the heterogeneous fields will correspond to the homogeneous value obtained by calibration ($K_{eff} = 5\ 10^{-5}$ m/s).

$$\mu_g = K_{eff}^{xx} \exp\left[\sigma^2_{\ln k}\left(-\frac{1}{2} + \frac{\lambda_y \lambda_z}{\lambda_x \lambda_z + \lambda_x \lambda_y + \lambda_y \lambda_z}\right)\right] \qquad (1)$$

where λ_x, λ_y and λ_z are the correlation length in the principal directions of anisotropy. Using a log-normal distribution of parameters μ_g = 2.38 10^{-5} m/s and $\sigma^2_{ln(k)}$=1.5, values of hydraulic conductivity were generated independently. These values were then sorted. The smaller values were attributed randomly to the less permeable lithofacies, the intermediate values were attributed to the sandstone, and the most permeable values were attributed to the sand. This allowed simulating the vertical variations of hydraulic conductivity for each geological log (Fig. 5b).

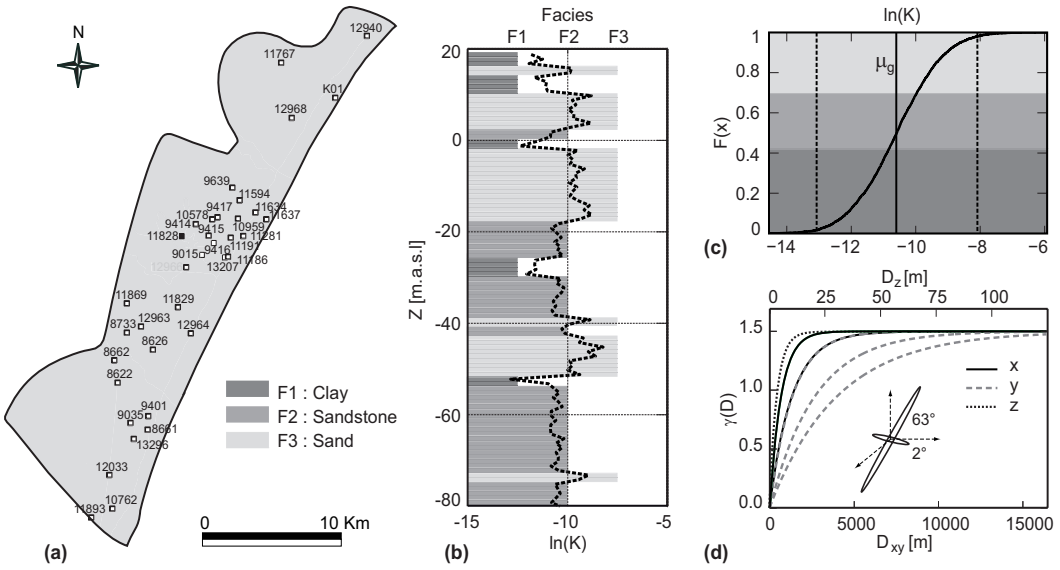

Fig. 5 Geostatistical model of hydraulic conductivities. (a) boreholes location (b) one example of a lithostratigraphical log with random *ln(K)* values simulated with respect to the facies type (c) CDF of the Gaussian *ln(K)* distribution (d) directional variograms, note that six scenarios were considered (see table 2).

In addition, the Pliocene sedimentation in the Korba plain is known to be slightly dipping toward the sea (1 to 5°) and made of elongated bars parallel to the sea as described for example in Allen and Allen (1990). It is expected that the length of these bars is between 2 and 12 km, that they have a width between 2 and 4 km, and a thickness of a few meters. The computation of experimental variograms on the hydraulic conductivities generated as described above confirmed that these orders of magnitude were reasonable as they showed horizontal correlation lengths in the order of 2-4 kilometres and a few meters in the vertical direction. Furthermore, the data showed a geometric anisotropy in the horizontal plane with correlation lengths parallel to the coast about 2 times larger than in the direction perpendicular to the coast. Because the variograms are not based directly on actual measurements, the correlation length cannot be estimated accurately. This parameter uncertainty was therefore taken into account by considering several possible combinations of the correlation lengths in the different directions (Table 2, and Fig. 5d).

Table 2. Values of the different sets of correlation lengths used to simulate the hydraulic conductivity fields.

Set number:	1	2	3	4	5	6
Range perpendicular to the coast [km]	2	2	2	4	4	4
Range parallel to the coast [km]	4	8	12	4	8	12
Vertical range [m]	10	10	10	10	10	10

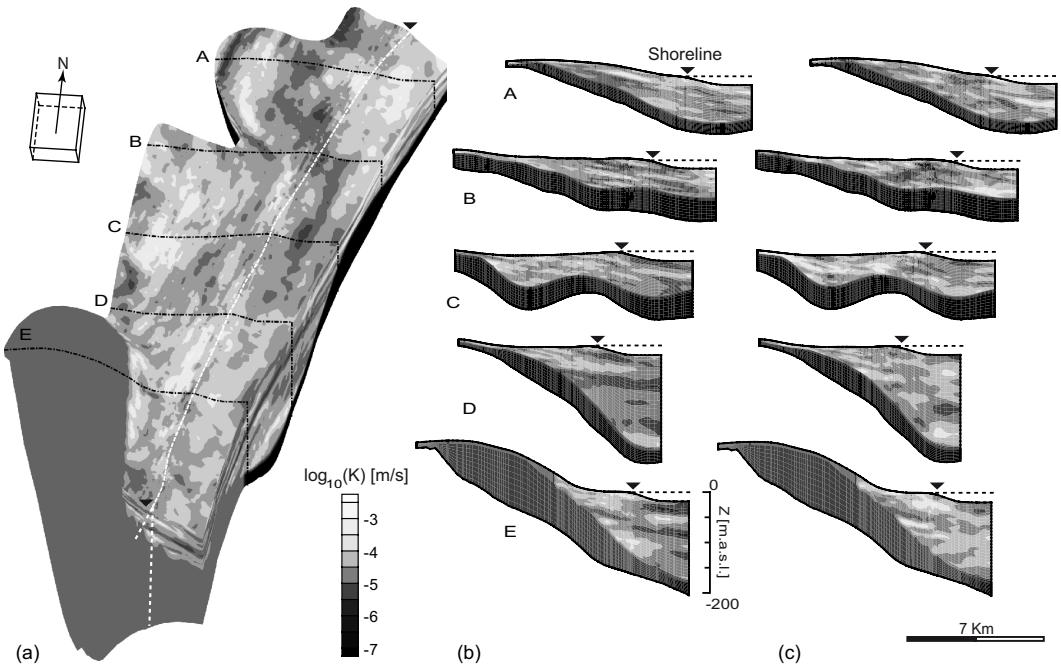

Fig. 6 (a) 3D view of the decimal logarithm of hydraulic conductivity field with vertical cross sections for two combinations of directional correlation lengths [m] (b) λ_x=4000, λ_y=12000 and λ_z=10; (c) for λ_x=2000, λ_y=4000 and λ_z=10.

Assuming a spherical variogram model, the turning band method (Matheron 1973; Tompson et al. 1989) was used to generate 8 simulations for each combinations of the possible ranges in the different directions (shown in Table 2). All simulations were conditioned to the 4423 hydraulic conductivity data simulated along the 36 geological logs. In total, 48 hydraulic conductivity fields were generated. The simulations were performed using a 200 x 200 x 3 m grid.

5. Interaction between uncertainty sources

Before investigating the impact of the uncertainty on the possible long-term evolution of the Korba aquifer, we investigated how the two sources of uncertainty interact. This was done by running 3 sets of Monte Carlo transient simulations for the period 1960-2004. In the first set we considered only uncertain discharge rates, while in the second set we considered only uncertain hydraulic conductivity fields, and in the last set we considered the joint uncertainties.

For the first set, the hydraulic conductivity field was kept equal to the one obtained by calibration (Table 1). For the second set, the extraction rate field was the simulated distribution that gave a response which was the closest to the ensemble average (in terms of concentrations and heads) in the first set of simulations. For the third set, all the combinations between six simulations of pumping rates and six simulations of the hydraulic conductivity fields were used. The six fields of pumping rate and of hydraulic conductivity were sampled in such a way that they correspond to regular probability intervals covering the cumulative density functions of the maximum drawdown computed for the first and second set of Monte Carlo simulations.

For all the simulations, the initial head and salt distributions were previously computed in steady-state so that they were physically consistent with the hydraulic conductivity field used in the corresponding realization. All other flow and transport parameters as well as time-dependent boundary conditions remained unchanged. For each simulation, the *GroundWater* finite-element code (Cornaton 2007) was used to solve the density-dependent flow and solute transport problem. Each single simulation required more than 55 hours of computing time on a linux AMD Opteron 64 bit machine. To circumvent the large computing time required to achieve the uncertainty analysis, Monte Carlo simulations were executed concurrently on a 64 processor Linux cluster. The resulting outputs were then postprocessed to obtain ensemble statistics.

Globally, all the simulations for the three sets and their respective ensemble averages display the main features observed in the measurements collected in 2004: the central depression, higher levels on the southern and northern part of the aquifer, and a penetration of the salt-wedge of about 2.5 km inland in the central part (Figs. 7 and 8). These similarities result from the use of hydraulic conductivity fields sharing the same effective values and pumping rate distributions sharing the same means. Looking more in detail, the head and salt distributions are smoother for the scenarios considering uncertain pumping rates than those considering heterogeneous hydraulic

conductivity (Fig. 7). This reflects the spatial variability of the flow velocities due to the heterogeneity. As expected, the ensemble average maps of heads and concentrations (Fig. 8) are different from the maps computed using the average pumping rates and the homogeneous permeability field. This is classical and due to the nonlinearity of the flow and transport equations (Delhomme 1979). However, it should be concluded here that ensemble averages of head and concentration distributions are more robust predictions as compared to the solutions resulting from using average inputs. It is worth noting that the convergence of ensemble statistics of the heads and concentrations in the wells Q_{240} and Q_{361}, and the maximum drawdown as well as the entering seawater flux over the whole aquifer was checked and accepted with faster convergence of the averages than the variances.

To quantify the uncertainty, iso-probability maps corresponding to the probability of a piezometric head below the mean sea level and iso-probability maps corresponding to the probability of a relative concentration greater than 0.1 were computed (Fig. 8) for the three sets of simulations. The uncertain areas correspond to intermediate probabilities. Thus, two global indicators were computed: U_H [-] represents the area [km^2] delineated by the 0.05 and 0.95 iso-probabilty of being below sea level normalized by the onshore extension of the aquifer (*AA*=328 km^2); similarly U_C represents the percentage of the extension of the aquifer where the probability of exceeding a relative concentration of 0.1 is between 0.05 and 0.95. These uncertainty norms might also be defined as:

$$U_H^{source\_of\_uncertainty}[-] = Area(0.05 \le P(H < 0) \le 0.95)/AA \qquad (2)$$

and

$$U_C^{source\_of\_uncertainty}[-] = Area(0.05 \le P(C > 0.1) \le 0.95)/AA \qquad (3)$$

The results of this analysis are the following:

- Overall, in all cases the uncertainties in 2004 are lower than 10% (Figure 9). This is less than what was expected intuitively.
- The uncertainty on the concentration is controlled mainly be the uncertainty on the hydraulic conductivity field ($U^{QK}{}_C \approx U^K{}_C$, Figure 9).
- The uncertainty on heads increases rapidly in response to increasing pumping rates while the uncertainty on concentration has a steady growth (Figure 9). This is explained by the faster response of the flow equation as compared to the transport equation. In addition, the magnitudes of the two uncertainties are different because of the different extensions of the domain affected by the process: the seawater intrusion occurs only on a strip along the coast while the piezometric map reacts everywhere in the domain.

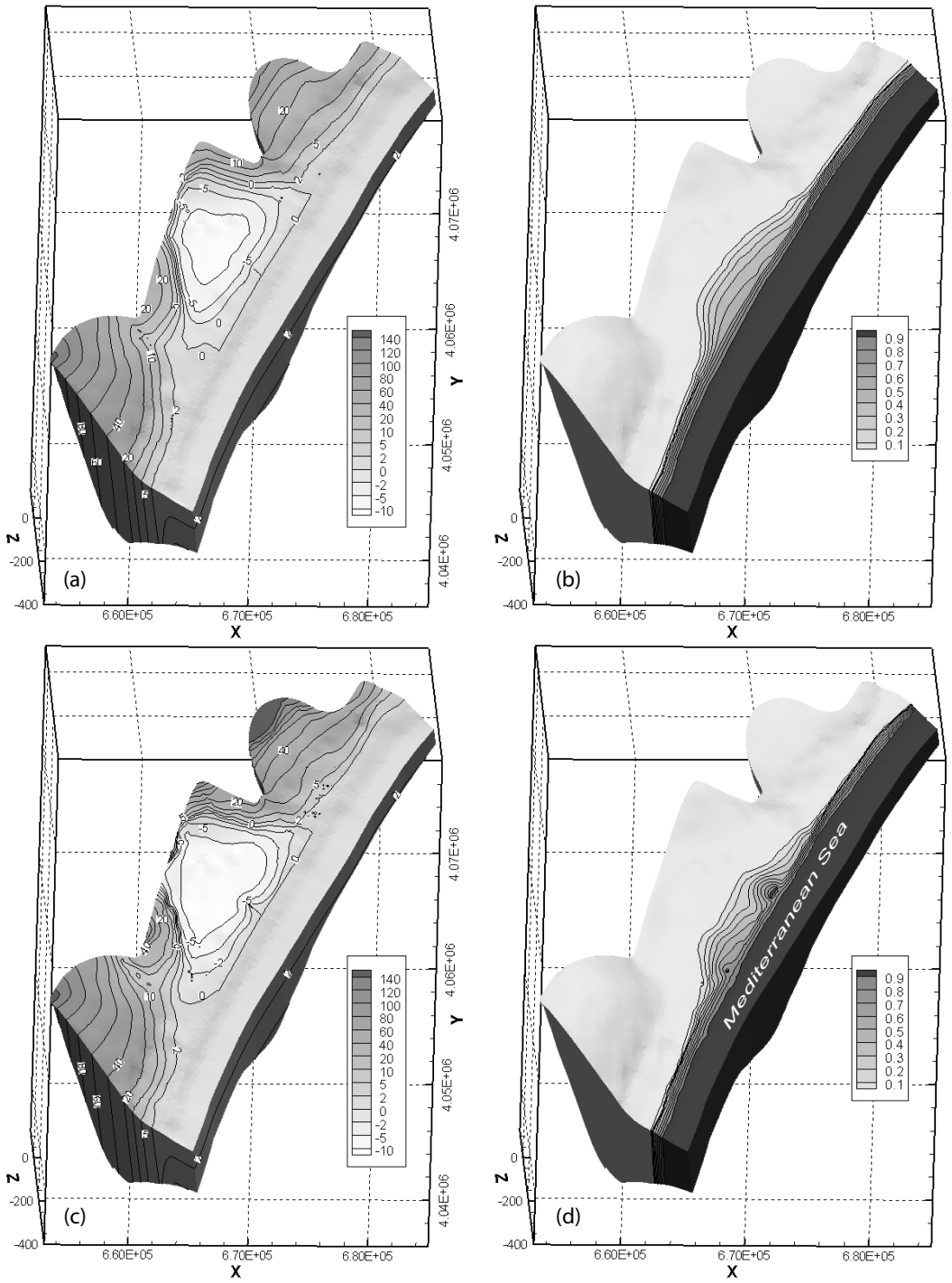

Fig. 7 Examples of simulated heads [m] (a) and (c) and relative concentrations [-] (b) and (d) for variable pumping rate (a) and (b) and heterogeneous hydraulic conductivity field (c) and (d).

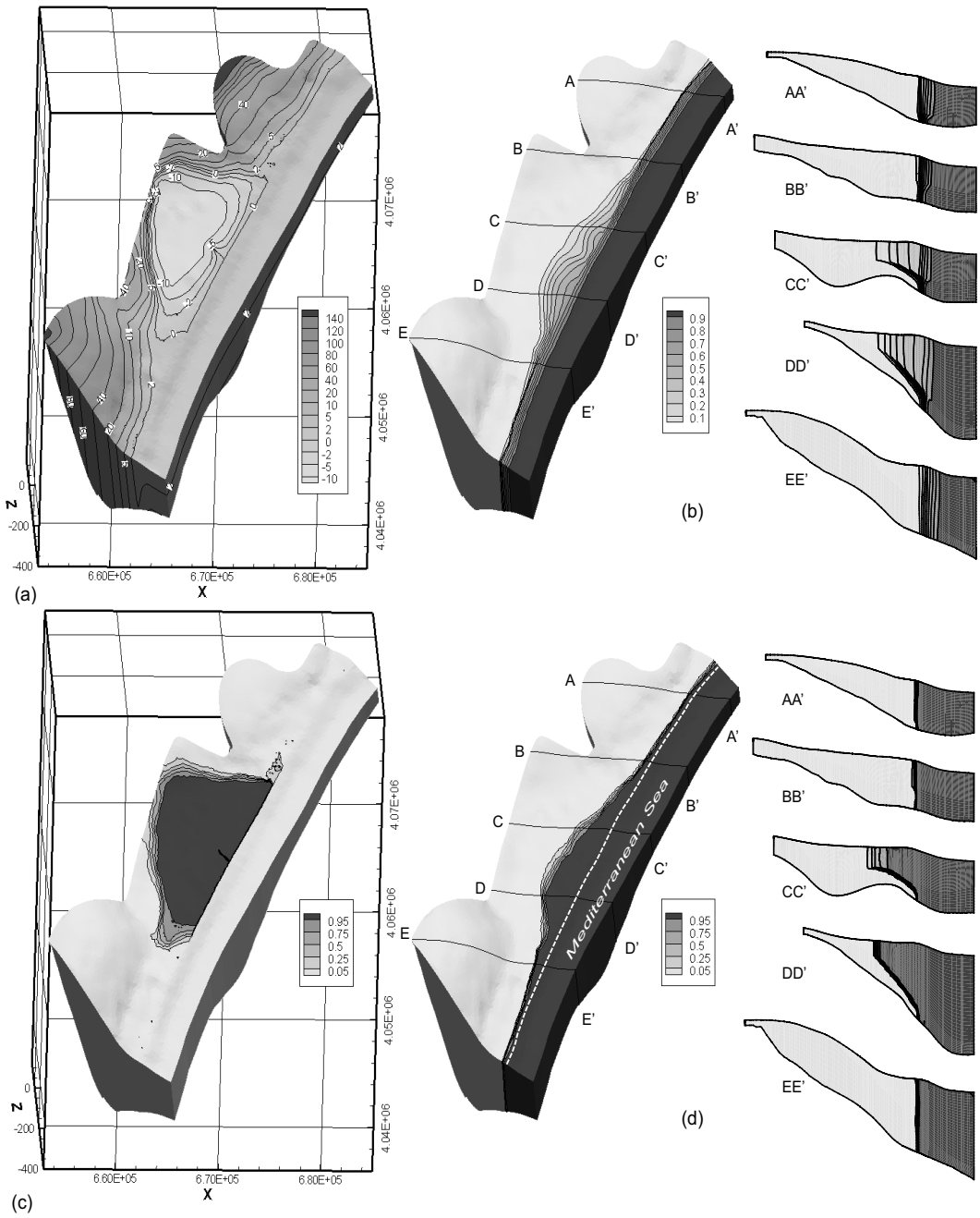

Fig. 8 2004 Ensemble averages for the joint uncertainty on pumping rates and hydraulic conductivity: (a) head [m], (b) relative concentration [-]. 2004 Probability map for a point: (c) to be under the mean sea level and (d) to exceed the 0.1 relative salt concentration.

- The uncertainty on the heads due to the uncertainty on the pumping rates and to the uncertainty on hydraulic conductivity is of the same order of magnitude ($U^{Q}_{H} \approx U^{K}_{H}$, Figure 9) but the joint effect is smaller than the sum of the two effects ($U^{QK}_{H} < U^{K}_{H} + U^{Q}_{H}$, Figure 9).
- Because the system is highly non-linear, and with transient boundary conditions, the different sources of uncertainty can become dominant at different time steps. For example, $U^{Q}_{H} < U^{K}_{H}$ in 1985 and $U^{K}_{H} < U^{Q}_{H}$ in 2000 (Figure 9). Therefore, one cannot assume that one source of uncertainty will always be the main one.

Additional comparisons of the local probability density functions obtained under the three sets of Monte Carlo simulations indicate that there is not a simple way to decouple and simplify the analysis of the uncertainty. This will lead us, in the next section, to consider only the case of joint uncertainty.

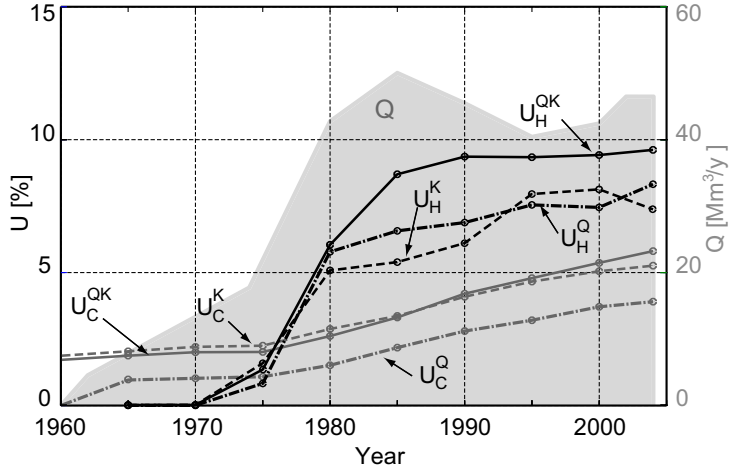

Fig. 9 Progression of the uncertainties during the simulated period: Q (gray background) are the total estimated exploitation volumes [Mm^3/y], U^{QK}_{H} and U^{QK}_{C} (solid black and gray lines) for the scenario of combined uncertainties, U^{K}_{H} and U^{K}_{C} (dashed black and gray lines) for the scenario of uncertain hydraulic conductivity field and U^{Q}_{H} and U^{Q}_{C} (dash-point black and gray lines) for the scenario of uncertain pumping rates.

6. Forecasts of seawater intrusion from 2004 to 2048

6.1 Definition of the scenarios

According to the Tunisian Institute of Statistics (2007), the Tunisian population will grow from 9.93 millions inhabitants in 2004 to 12.74 millions in 2034. This

demographic growth will increase freshwater stress, especially on groundwater, over the whole country. At the same time, most of the global climate change models (Bates 2008) predict decreasing precipitation and increasing temperatures in the Mediterranean region for the next century which will affect the hydrological cycle in many countries. In Tunisia, a reduction of 20 to 25 % of the annual average precipitation is expected for 2050 (Ragab and Prudhomme 2002), which means that the precipitation in the study area will decrease from 420 mm/y to 336-315 mm/y. Consequently, the natural recharge of the aquifer is expected to be reduced by around 20 % in 2050 both for the direct infiltration and for the recharge from the underlying aquifers. In addition, the Mediterranean will most probably rise at a rate of about 2.5 mm/year for the next century (Mangiarotti 2003; Ranjan et al. 2006; Bates 2008). However, this phenomenon is expected to have a limited impact in the Cape Bon (11 cm rise in 2048).

In order to forecast the response of the Korba aquifer to a reduction of the natural recharge and to different management scenarios, long-term stochastic forecasts were carried out. Two scenarios were considered:

- **Scenario 1**: the recharge is reduced linearly and progressively so that the recharge in 2048 will be 24 Mm3/y, which represents 20 % less than the recharge in 2004. The pumping rates of 2004 (47 Mm3/y) are kept constant until 2048. This would be a continuation of the 2004 state of exploitation. Note that it remained constant since the late 1980's (Figure 9). Because this rate of exploitation corresponds to the continuation of a clear over-exploitation of the system - the total extraction estimated in 2004 corresponds to about 135 % of the recharge - this scenario is considered as the worst case scenario.

- **Scenario 2**: the recharge is reduced linearly as for the scenario 1 but the pumping rates as well are reduced linearly to reach the amount of recharge expected in 2048. This represents a progressive reduction of the pumping rates by 50 %.

The sea level rise was considered less dangerous than the other threats and was not accounted for. Considering these two scenarios, Monte Carlo simulations were continued from 2004 to 2048 with the scenario of uncertain pumping rates and uncertain hydraulic conductivity field. For reasons of consistency with reality, a concentration threshold was attributed to constrain pumping wells: pumps are deactivated if the concentration of pumped water exceeds 0.2 relative concentration, and restarted for a concentration less than 0.1

6.2 Results

Figures 10 and 11 show the ensemble averages of hydraulic heads and relative salt concentration as well as the probability maps for the first and the second scenarios. Those statistics were calculated from 36 Monte Carlo simulations for each scenario.

In addition to the uncertainty norms U^H and U^C defined above and in order to evaluate the consequences of each scenario, the area of the aquifer $S^{C>0.1}$ where the relative salt concentrations exceed 0.1 was calculated and normalized by the onshore surface of the aquifer. Similarly, the normalized area of the aquifer where heads are below sea level $S^{H<0}$ was calculated too. These areas where computed for all the simulations in order to obtain their statistical distributions. The results are summarized in Table 3.

Table 3 Summary of the stochastic modelling and forecasts results.

		State in 2004			Forecast in 2048	
		Uncert. Q	**Uncert. K**	**Joint Uncert.**	**Scenario 1**	**Scenario 2**
$S^{H<0}$ [%]	***P=0.95***	27.8	29.8	28.0	21.9	4.1
	P=0.5	32.0	33.2	32.8	29.7	11.6
	P=0.05	36.1	37.4	37.7	40.7	18.8
$S^{C>0.1}$ [%]	***P=0.95***	23.8	21.2	20.7	33.5	30.2
	P=0.5	25.8	23.7	23.4	37.5	33.7
	P=0.05	27.7	26.5	26.5	41.3	37.1
U_C [%]		3.9	5.3	5.8	7.8	6.9
U_H [%]		8.3	7.6	9.6	18.8	14.6

If we first compare the forecasts in 2048 for both scenarios with the state of the aquifer estimated in 2004, we find that in all cases the surface affected by seawater intrusion will increase significantly to reach between 30 and 41% of the aquifer while it is estimated to cover between 20 to 26.5 % of the aquifer in 2004 (Table 3). The estimated uncertainty will also rise in both cases. It is worth noting that due to the constrains of concentrations in wells (Q=0 if C>0.2), 189 wells were turned off and the total pumping in 2048 was reduced by 7 %.

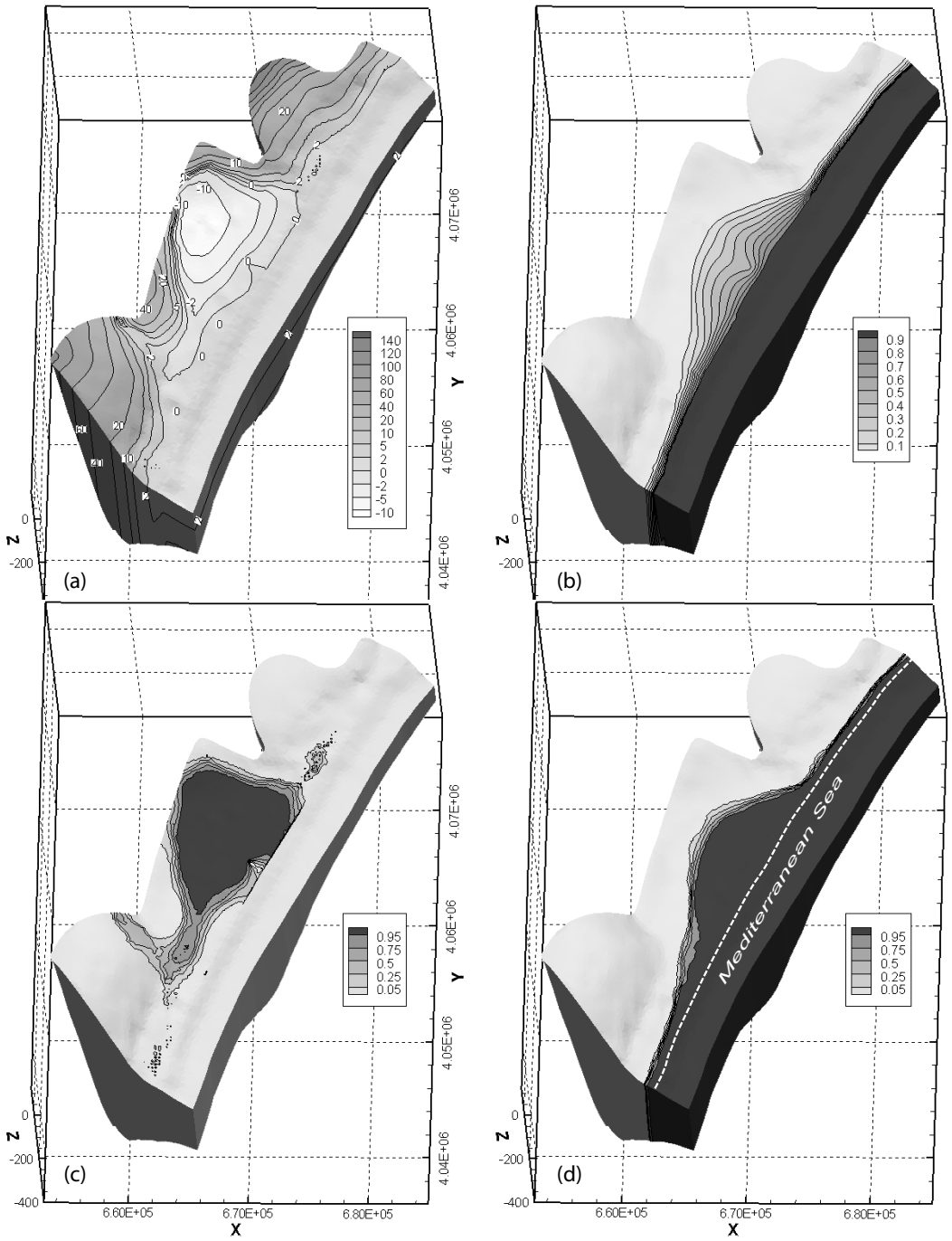

Fig. 10 2048 Scenario 1 forecasts: Ensemble averages: (a) head [m] (b) relative concentration [-] maps for the 36 realizations; Probability map for a point (c) to be under the mean sea level and (d) to exceed the 0.1 relative salt concentration.

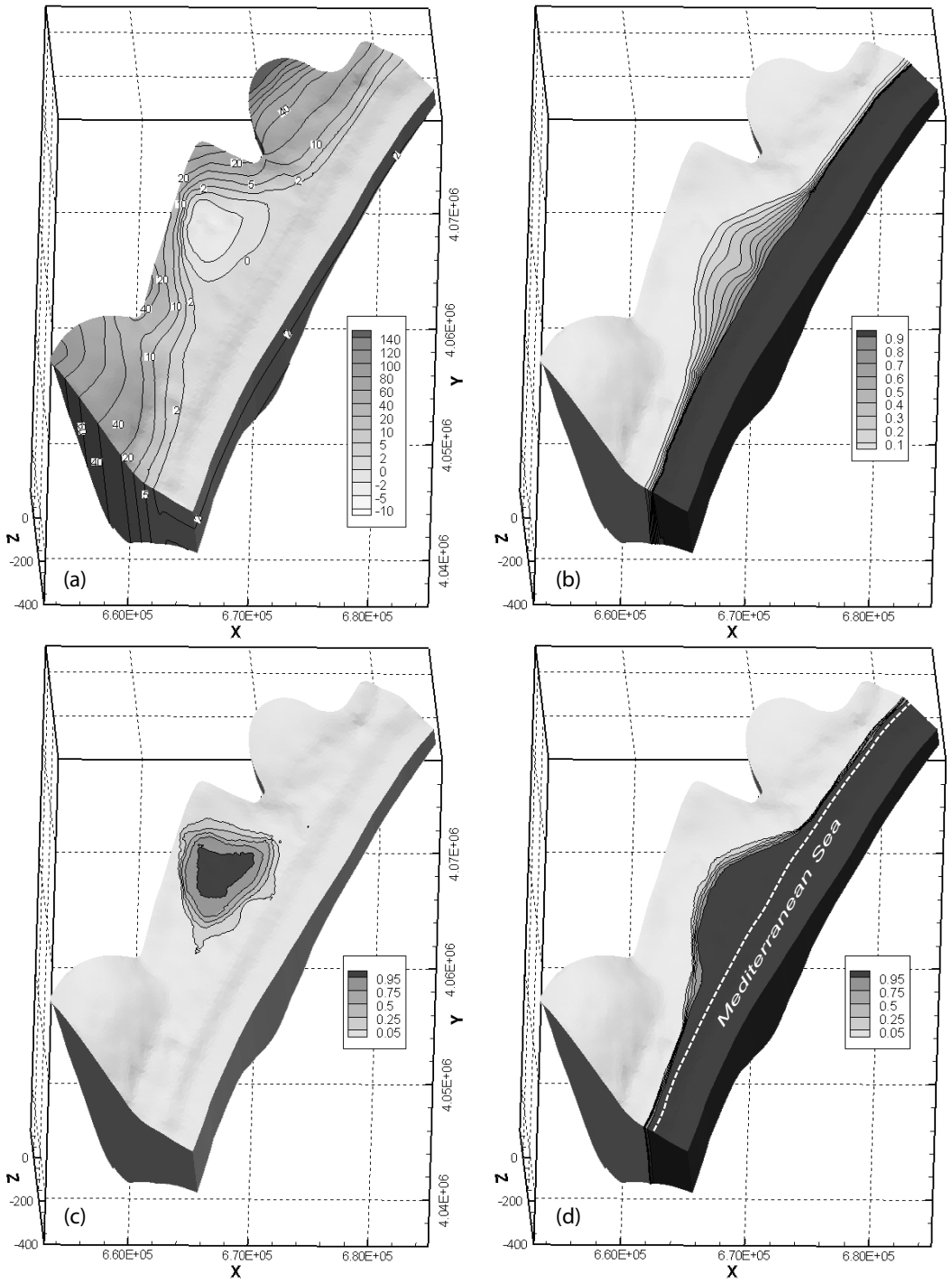

Fig. 11 2048 Scenario 2 forecasts: Ensemble averages (a) head [m] (b) relative concentration [-] maps for the 36 realizations; Probability map for a point (c) to be under the mean sea level and (d) to exceed the 0.1 relative salt concentration.

When comparing the forecasts made for the two scenarios, the results show that reducing progressively the pumping rates over the whole aquifer by 50 % until 2048 will affect more the heads than the salt concentration distribution. The area $S^{H<0}$, where heads are below sea level will be reduced significantly from 29.7 % to 11.6 % (at a probability level of 0.5), while the area $S^{C>0.1}$ will be reduced only from 37.5 to 33.7 % (same probability level). This is expected for two reasons. First, as long as the hydraulic gradients will still be oriented landward (Fig. 11 a), the salt wedge will continue to penetrate further inland even if the piezometric depression is smaller. Furthermore, dispersion is not a reversible phenomenon. Consequently, the time scale required to clean up naturally a coastal aquifer that was invaded by seawater intrusion are usually much longer than the time scale required for the invasion. This was shown in the work in Chapter 3 where the time required for the 0.25 iso-concentration to recede back to its natural state was estimated to be more than a century after the complete stop of 45 years of pumping. The reduction of the pumping rates by half until 2048 will therefore reduce the saltwater intrusion velocity but will not stop it. Most probably (P=0.95), an additional 3000 ha (9.5 % of the surface of the aquifer) will be affected by higher concentrations (C>0.1) as compared to the situation in 2004. Those computations show that the time-lag involved in seawater intrusion and recession is very important to be considered for planning groundwater and land use.

7. Summary and conclusions

This study investigated how the uncertainties on the spatial distribution of pumping rates and hydraulic conductivities affect the knowledge of the current state and evolution of the Korba aquifer in Tunisia. The methodology included a stochastic model for the pumping rates and one for the hydraulic conductivity. The propagation of these uncertainties to heads and concentrations in the aquifer was carried out by Monte Carlo simulations using a 3D numerical model of density-dependent flow and solute transport. For the setup of the geostatistical model of hydraulic conductivities, a multiGaussian distribution with geometric anisotropy was assumed. The stochastic model of the pumping rates was based on a multivariate linear regression and a geostatistical model of the residuals. The two sources of uncertainty were evaluated separately and jointly in order to investigate how they interact. The stochastic model was then used to forecast the head and salt concentration distributions in 2048 for two management scenarios.

It was found that the uncertainty on the hydraulic conductivity distribution had more impact on the transport predictions than the uncertainty on the spatial distribution of the discharge rates. Both sources of uncertainty affected similarly the flow predictions but slight differences could be seen when looking at the time evolution of those uncertainties. Similarly, the uncertainties on flow and transport predictions behave differently as a function of time. The uncertainty on heads react generally faster and show stronger responses than those on concentrations when the pumping rates evolve. The combined effects of the two sources of uncertainty had more impact on the flow predictions than on the transport predictions.

From a practical point of view, the results showed that if the pumping rates remain at their 2004 level and if recharge is reduced by 20 % due to climate change, then there is a high probability (P=0.95) that at least 12.8 % of the surface of the aquifer will be additionally contaminated in 2048. Reducing the pumping rates progressively by 50% until 2048 will not result in a recession of the saltwater wedge; instead an additional 9.5 % (3000 ha) of the surface of the aquifer will be contaminated in 2048 especially in the central part of the aquifer. The Korba area is therefore potentially subjected to important future losses in the agricultural sector. Furthermore, the situation will continue to deteriorate after 2048 in this scenario.

One way to avoid the progressive deterioration of the groundwater quality that will affect the aquifer for tens of years and to reach a possible sustainable situation would be to re-allocate the groundwater extraction to ensure the complete recovery of the central depression. Indeed, the northern and southern parts of the aquifer are still showing high piezometric levels and could be exploited more intensively. The different projects related to artificial recharge currently implemented in the region have a positive impact at a local scale but are an order of magnitude too small to have a significant influence on the central depression. This is why we think that a feasible approach would be to increase the extraction in the north and the south and to reduce it in the center. Water transfer from the different parts and usage of surface water from the dams could be used to compensate the problems due to reduced extraction in the central part. The maximum amounts that could be exploited in each part of the aquifer can be estimated by an optimization study based on the model described in this study. More generally, the use of uncertainty assessments in water resources management goes beyond natural science (Refsgaard and Henriksen 2004). Therefore, it is hoped that the stochastic model elaborated in the present study will be used in conjunction with cost analysis for supporting long-term policy analysis and strategic decision making for integrated and sustainable development in the Korba region.

References

Ababou R (1995) Random porous media flow on large 3-D grids : numerics, performance and application to homogenization. In M F Wheeler (Ed), IMA Volumes in Mathematics and its Applications "Environmental studies : mathematical, computational and statistical analysis", Springer-Verlag New York Publishers, pp 1-25

Abarca E, Carrera J, Sánchez-Vila X, Dentz M (2007) Anisotropic dispersive Henry problem. Advances in Water Resources 30: 913-926. doi:doi:10.1016/j.advwatres.2006.08.005

Abarca E, Vazquez-Sune E, Carrera J, Capino B, Gamez D, Batlle F (2006) Optimal design of measures to correct seawater intrusion. Water Resources Research 42

Aharmouch A, Larabi A, Hilali M (2002) A 3D model for groundwater flow and seawater intrusion interface: Application to the Martil coastal aquifer system. Developments in Water Science 47: 539-546

Alcolea A, Renard P, Mariethoz G, Bertone F (2008) Reducing the impact of a desalination plant using stochastic modeling and optimization techniques. Submitted to Journal of Hydrology

Allen PA, Allen JR (1990) Basin Analysis: Principles & Applications. Blackwell Science

Arfib B, de Marsily G, Ganoulis J (2002) Coastal karst springs in the Mediterranean basin: study of the mechanisms of saline pollution at the Almyros spring (Crete), observations and modelling. Bulletin De La Societe Geologique De France 173: 245-253

Bates BC, Z.W. Kundzewicz, S. Wu and J.P. Palutikof, Eds. (2008) Climate Change and Water. Technical Paper of the Intergovernmental Panel on Climate Change, IPCC Secretariat, Geneva, 210 pp.

Bear J, Cheng AHD, Sorek S, Ouazar D, Herrera I (1999) Seawater intrusion in coastal aquifers- concepts, methods and practices. Kluwer academic publishers, Dordrecht

Cheng AHD, Halhal D, Naji A, Ouazar D (2000) Pumping optimization in saltwater-intruded coastal aquifers. Water Resources Research 36: 2155-2165

Cooper HH, Bredehoe.Jd, Papadopu.Is (1967) Response of a Finite-Diameter Well to an Instantaneous Charge of Water. Water Resources Research 3: 263-&

Cornaton F (2007) Ground Water: A 3-D Ground Water Flow and Transport Finite Element Simulator. Reference Manual, 190 pp http://www1uninech/chyn/php/softwaresphp

Delhomme JP (1979) Spatial Variability and Uncertainty in Groundwater-Flow Parameters - Geostatistical Approach. Water Resources Research 15: 269-280

DGRE (2000) Rapport d'exploitation des nappes phréatiques de l'année 2000. Direction Générale des Ressources en Eau, Ministère de l'agriculture et des ressources hydrauliques,Tunisie

Diersch H-JG, Kolditz O (2002) Variable-density flow and transport in porous media: approaches and challenges. Advances in Water Resources 25: 899–944

Eckhardt K, Ulbrich U (2003) Potential impacts of climate change on groundwater recharge and streamflow in a central European low mountain range. Journal of Hydrology 284: 244-252

Ennabli M (1980) Etude hydrogéologique des aquifers du nord-est de la Tunisie pour une gestion intégrée des ressources en eau. Thèse de Doctorat d'État, Université de Nice

Essink G (2001) Salt water intrusion in a three-dimensional groundwater system in the Netherlands: A numerical study. Transport in Porous Media 43: 137-158

Galeati G, Gambolati G, Neuman SP (1992) Coupled and Partially Coupled Eulerian-Lagrangian Model of Fresh-Water-Seawater Mixing. Water Resources Research 28: 149-165

Hassan A, Pohlmann K, Chapman J (2001) Uncertainty analysis of radionuclide transport in a fractured coastal aquifer with geothermal effects. Transport in Porous Media 43: 107-136

Holman IP (2006) Climate change impacts on groundwater recharge-uncertainty, shortcomings, and the way forward? Hydrogeology Journal 14: 637-647

Hvorslev MJ (1951) Time Lag and Soil Permeability in Ground-Water Observations, Bull. No. 36, Waterways Exper. Sta. Corps of Engrs, U.S. Army, Vicksburg, Mississippi, pp. 1-50.

INS (2007) Prévisions sur l'évolution de la Population 2004-2034. Institut National de la Statistique, Tunisie. http://www.ins.nat.tn/

Iribar V, Carrera J, Custodio E, Medina A (1997) Inverse modelling of seawater intrusion in the Llobregat delta deep aquifer. Journal of Hydrology 198: 226-244

Khlaifi I (1998) Contribution à l'étude de l'intrusion marine par un modèle de transport tridimensionnel : interfaçage avec des systèmes d'information géographique. Thèse de master, Institut National Agronomique de Tunisie

Kouzana L, Ben Mammou A, Sfar Felfoul M (2009) Seawater intrusion and associated processes: case of the Korba aquifer (Cap-Bon, Tunisia). Comptes Rendus Geosceinces

Mangiarotti S (2003) Les variations basse fréquence du niveau de la mer Méditerranée au cours de la deuxième moitié du XXe siècle par altimétrie spatiale et marégraphie. Thèse de doctorat, Université de Toulouse III – Paul Sabatier

Mantoglou A, Papantoniou M, Giannoulopoulos P (2004) Management of coastal aquifers based on nonlinear optimization and evolutionary algorithms. Journal of Hydrology 297: 209-228

Matheron G (1973) The intrinsic random functions and their applications. Advances in Applied Probability 5: 439-468

Milnes E, Renard P (2004) The problem of salt recycling and seawater intrusion in coastal irrigated plains: an example from the Kiti aquifer (Southern Cyprus). Journal of Hydrology 288: 327-343

Oueslati A (1994) Les côtes de la Tunisie. Recherche sur leur évolution au Quaternaire. Imprimerie officielle de la Republique Tunisienne, Tunis

Paniconi C, Khlaifi I, Lecca G, Giacomelli A, Tarhouni J (2001) Modeling and analysis of seawater intrusion in the coastal aquifer of eastern Cap-Bon, Tunisia. Transport in Porous Media 43: 3-28

Pohlmann KF, Hassan AE, Chapman JB (2002) Modeling density-driven flow and radionuclide transport at an underground nuclear test: Uncertainty analysis and effect of parameter correlation. Water Resources Research 38

Ragab R, Prudhomme C (2002) Climate change and water resources management in arid and semi-arid regions: Prospective and challenges for the 21st century. Biosystems Engineering 81: 3-34

Ranjan P, Kazama S, Sawamoto M (2006) Effects of climate change on coastal fresh groundwater resources. Global Environmental Change 16: 388-399

Refsgaard JC, Henriksen HJ (2004) Modelling guidelines - terminology and guiding principles. Advances in Water Resources 27: 71-82

Renard P (2007) Stochastic hydrogeology: What professionals really need? Ground Water 45: 531-541

Sadeg SA, Karahanoglu N (2001) Numerical assessment of seawater intrusion in the Tripoli region, Libya. Environmental Geology 40: 1151-1168

Scibek J, Allen DM (2006) Modeled impacts of predicted climate change on recharge and groundwater levels. Water Resources Research 42

Sherif MM, Singh VP (1999) Effect of climate change on sea water intrusion in coastal aquifers. Hydrological Processes 13: 1277-1287

Slama F, Milnes E, Bouhlila R (2008) Calibrating unsaturated model parameters using Electrical Resistivity Tomography imaging. In: Refsgaard J.C. KK, Haarder E. and Nygaard E. (ed) Calibration and Reliability in Groundwater Modelling: Credibility of Modelling. IAHS Publication 320: 148-153

Tarhouni J, Jemai S, Walraevens K, Rekaya M (1996) Caracterisation de l'aquifere cotier de Korba au Cap Bon (Tunisie). Progress report 95-96 for AVI-73 EC Project

Tompson AFB, Ababou R, Gelhar LW (1989) Implementation of the 3-Dimensional Turning Bands Random Field Generator. Water Resources Research 25: 2227-2243

Yakirevich A, Melloul A, Sorek S, Shaath S, Borisov V (1998) Simulation of seawater intrusion into the Khan Yunis area of the Gaza Strip coastal aquifer. Hydrogeology Journal 6: 549-559

Chapter 6

Issues in characterizing heterogeneity and connectivity in non-multiGaussian media*

Abstract The performances of kriging, stochastic simulations and sequential self-calibration inversion are assessed when characterizing a non-multiGaussian synthetic 2D braided channel aquifer. The comparison is based on a series of criteria such as the reproduction of the original reference transmissivity or head fields, but also in terms of accuracy of flow and transport (capture zone) forecasts when the flow conditions are modified. We observe that the errors remain large even for a dense data network. In addition some unexpected behaviours are observed when large transmissivity datasets are used. In particular, we observe an increase of the bias with the number of transmissivity data and an increasing uncertainty with the number of head data. This is interpreted as a consequence of the use of an inadequate multiGaussian stochastic model that is not able to reproduce the connectivity of the original field.

1. Introduction

Groundwater flow and transport are controlled by physical properties that are characterized by a high degree of heterogeneity and by scales of variation that span several orders of magnitude. A major difficulty is that this heterogeneity, whose knowledge is fundamental for modelling relevant environmental problems (e.g.

* This chapter is based on the papers:
Kerrou J., Renard P., Hendricks-Franssen H.J. and Lunati I. (2008) Issues in characterizing connectivity and heterogeneity in non-multi-Gaussian media. Advances in Water Resources, 31(1), pp 147-159. Doi:10.1016/j.advwatres.2007.07.002
Kerrou J., Renard P., Hendricks-Franssen H.J. and Lunati I. (2006) A synthetic study of the worth of transmissivity and head data to delineate groundwater protection zones in alluvial aquifers. In Calibration and Reliability in Groundwater Modelling: From Uncertainty to Decision Making. M.F.P. Bierkens, J.C. Gehrels, and K. Kovar (eds), IAHS Publication 304, pp 220-226, 2006. ISBN 1901502589

protection zone design, contaminant migration prediction, aquifer remediation, seawater intrusion), has to be inferred on the basis of sparse measurements. In the past decades, a large number of techniques has been developed with the aim of characterizing the spatial variability of aquifer parameters and their uncertainty (Koltermann and Gorelick, 1996; de Marsily et al., 2005; Renard et al., 2005).

Generally speaking, the characterization of the heterogeneity can be addressed based on direct observations of the *physical parameters* (direct methods) or on observations of the *state variables* of the system (inverse methods).

Direct methods infer the distribution of the physical parameters (transmissivity, porosity, etc.) from the local information about the parameters themselves. Note, however, that this information is often obtained by solving an inverse problem involving the state variables (e.g. pumping tests) but their interpretation is local and provides parameter values that become the input of the characterization methods. Additional direct information about the characteristics and the position of geological facies can be provided by geophysical observations. Among the most widely employed direct interpolation techniques are kriging and stochastic multiGaussian simulations. They both are two-point geostatistical methods that proved efficient in a wide variety of applications in hydrogeology but also in other fields such as mining, or petroleum engineering (Delhomme, 1979; Journel and Deutsch, 1993; Caers, 2005).

In practice, however, direct methods are seldom used alone because they do not account for the global information on state variables (e.g. hydraulic head or concentration) and lead to groundwater models that do not reproduce the observed values of those state variables. Instead, this information is taken into account by inverse methods, which characterize the physical parameters from measurements of the state variables.

Inverse modelling has been a topic of intense research and developments (de Marsily et al., 1999; Hu et al., 2001; Hendricks-Franssen et al., 2003; Alcolea et al., 2006; Caers, 2007). As argued in a recent review by Carrera et al. (2005), most methods do not differ from each other in essence, but they may differ with respect to the computational details. Among the inverse techniques, the Monte-Carlo approach, in which multiple equally likely realisations of aquifer properties are conditioned to hydraulic head and concentration data, allows estimating uncertainty. Inverse methods have been applied successfully in a wide range of problems (Capilla et al., 1998; Zimmerman et al., 1998; Lavenue and de Marsily, 2001; Larocque et al., 2003).

Since both direct and inverse methods rely on measurements acquired at few discrete locations, some hypotheses have to be made on the parameters statistics in order to infer the continuum distributions. Most two-point geostatistical techniques illustrated in the previous sections are based on the assumption that the physical parameters follow a multiGaussian distribution, which is analytically simple and fully characterized by a mean and covariance function. Numerical testing is usually performed by applying the characterization techniques to synthetic fields that also feature multiGaussian statistics. The results demonstrate the accuracy and the consistency of the methods. While remaining in the multiGaussian framework, few studies have shown how uncertainty can be reduced by increasing the number of transmissivity, head or concentration data (Wen et al., 1996; Hendricks-Franssen et al., 2003).

MultiGaussian fields maximise entropy (disorder), and in return, minimize the spatial continuity of the extreme values, thus, a loss of connectivity (Journel and Deutsch, 1993). This feature has a high impact on flow and transport as shown by a number of numerical investigations (Sánchez-Vila et al., 1996; Wen et al., 1996; Gómez-Hernández and Wen, 1998; Zinn and Harvey, 2003). While these studies were limited to the context of direct techniques, they all showed that the selection of a multiGaussian model might be consequential on flow and transport simulations. Both direct and inverse techniques are available to handle non-multiGaussian media. Examples of direct techniques include the sequential indicator simulation method (Gómez-Hernández and Srivastava, 1990), truncated pluriGaussian simulations (Armstrong et al., 2003), or multiple-point statistics (Strebelle, 2002). Examples of inverse methods that are able to handle non-multiGaussian media are the conditional probabilities method (Capilla et al., 1999), a combination of truncated pluriGaussian simulation and the gradual deformation approach (Hu et al., 2001), the inverse modelling of multimodal hydraulic conductivity distributions with the representer method (Janssen et al., 2006), or the probability perturbation method combined with multiple-point statistics (Caers and Hoffman, 2006) among others.

Although it is known already now for more than a decade that multiGaussian models have severe limitations, and although alternative methods exist, most groundwater hydrology studies adopt a multiGaussian model, often also because data are not available to infer a non-multiGaussian model. Therefore, this study explores what happens if a multiGaussian model is adopted for a non-multiGaussian medium, a situation that is most probably very common in practice. In particular, we do not only investigate the implications of a wrong random function model in direct studies, but also in inverse problems.

In summary, the goal of the present study is to investigate and compare the reliability of direct and inverse multiGaussian techniques when applied to characterize fields that are not multiGaussian and exhibit preferential flow paths. A main question of interest in this study was to what extend hydraulic head data, used in inverse modelling, are able to correct the consequences of the wrong assumption of a multiGaussian random function model. Two situations may occur: either the inverse conditioning is able to detect non-multiGaussian structures and would alleviate the problems associated with a wrong random function (multiGaussian), or the discrepancy between the model and the reality would still lead to inaccurate predictions. In the latter case, checking the multiGaussianity assumption for a particular case study would be extremely important; moreover, the groundwater community would be encouraged to further develop and adopt methods based on different statistics.

After creating a 2D synthetic reality, our methodology mimics the procedure that would be followed during a practical case study. We start constructing a synthetic transmissivity field such that it possibly represents a real aquifer characterized by long-correlation structures such as channels and lenses (section 2.1). A reference head field, which mimics natural flow conditions, is obtained by simulating the flow on this transmissivity field (section 2.2). The transmissivity and the head fields are sampled in order to obtain a series of datasets with an increasing number of data points, which represent synthetic experimental data to be used as input for the aquifer characterization (section 3.1). At this point, we first analyse the datasets in order to infer the statistics required for the characterization step and compute histograms and variograms (section 3.2). Then, for each dataset, we reconstruct three transmissivity fields by applying three multiGaussian characterization techniques, i.e. kriging, stochastic direct simulations and self-calibrated sequential simulations (sections 3.3 and 3.4). The performance of the characterization techniques is evaluated both in terms of reproduction of the real transmissivity field and reproduction of the initial flow situation (section 4.1). Most important, the inferred transmissivity fields are used to make predictions on different flow scenarios. In particular, we consider the response of the aquifer to the construction of a well. Forecasts in terms of total fluxes through the domain, head in the pumping well, and protection-zone extension around the pumping well are considered (sections 4.2-4.3). The reliability of the techniques is estimated as a function of the number of transmissivity and head data used to condition the transmissivity fields.

2. Synthetic reality

2.1 Transmissivity field

The study is conducted on a synthetic transmissivity (*T*) field, which consists of channels and lenses displaying internal heterogeneity (Fig. 1a–1c). It is built from an aerial photograph displaying braided channels in the Ohau River, New Zealand (Mosley, 1982). According to the classification of natural rivers from Rosgen (1994), the architecture displayed on this photograph belongs to the "*type D: braided channels*". This kind of sedimentary environment can be regarded as the ancestor of our synthetic aquifer.

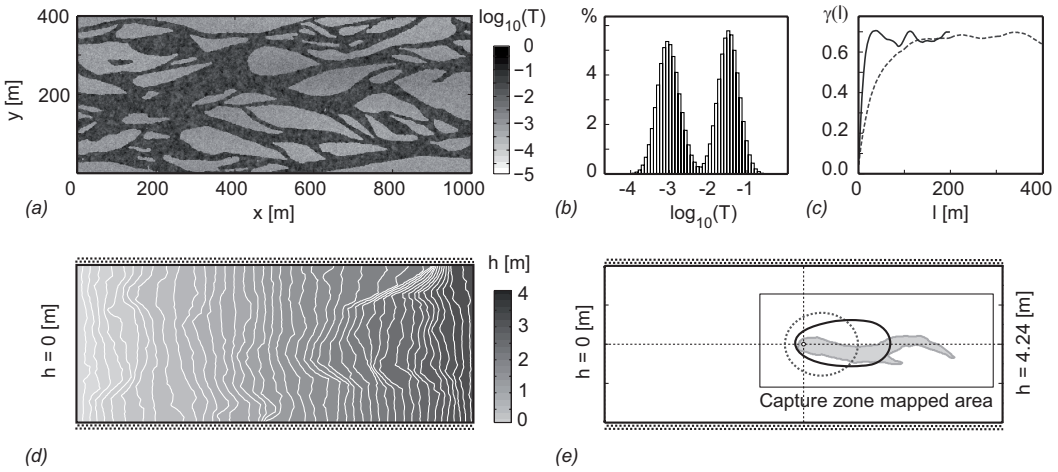

Fig. 1 (a) The synthetic transmissivity field, (b) histogram of the log decimal of the transmissivities, (c) *x* (dashed line) and *y* (solid line) directional variograms, (d) head field and boundary conditions for the uniform steady flow situation, (e) 10-days capture zone under the radial steady flow conditions (gray shape) and the mapped area; the 10-days capture zone calculated using the analytical solution of Bear and Jacobs (1965) on the basis of the geometric mean (dashed line) and using the equivalent transmissivity (solid line).

The Ohau aerial photograph is digitized and used at its real scale so that the size of the channels and lenses is realistic. The image size is 1000 m by 400 m and discretized into 1 m by 1 m cells. Two multiGaussian unconditional simulations are separately generated to populate the channels and the lenses with natural logarithm of transmissivity (*T*) values. The first simulation describes the *T* distribution in the channels and has an exponential variogram with a short correlation range (3 m). The

second simulation describes the lenses and has a nested variogram that includes one isotropic exponential model with a 3 m range, plus a cubic anisotropic model with a long range in the *x* direction (600 m) and a shorter one in the *y* direction (300 m). Note that the mean and the variance of the two distributions were chosen such that the values are realistic for such a geological environment. The long-range correlation is used to mimic a regional trend in the deposition of fine sediments. This leads to a bimodal, non-multiGaussian, anisotropic transmissivity field with about 50% of the surface occupied by channels (highly permeable coarse material) and 50% occupied by lenses (poorly permeable fine material).

The decimal logarithm of *T* has a mean of -2.3 and a variance of 0.67, which corresponds to $\sigma^2_{ln(T)}$=3.6 (note that the variance is computed considering the *T* field as a whole, regardless to its bimodal nature). The overall integral scale was estimated to be 27 m in the *x* direction (approximately 2.7 % of the length of the domain) and 8 m in the *y* direction (2 % of the domain width) by integrating numerically the correlation function calculated from the reference *T* field.

2.2 Reference flow

A reference 2D flow field, which mimics natural flow conditions, is obtained by prescribing the hydraulic heads on the eastern and western boundaries, and imposing no-flow conditions on the northern and the southern boundaries (Fig. 1d). It is assumed that the aquifer is confined and there is no recharge (no source term). The flow problem on the reference transmissivity field is solved with the Feflow code (Diersch, 1996) and a head distribution is obtained that reflects the flux variations generated by the permeability contrast between the channels and the lenses (Fig. 1d). The reference head field will be sampled to provide the input data for the inverse characterization technique.

3. Characterization procedure

The characterization procedure consists in applying independently or successively different techniques. The starting point is the sampling of the transmissivity field to obtain the data for computing the experimental histogram and variogram. In addition, either the data are interpolated by kriging, or a set of stochastic simulations conditional to transmissivity measurements is generated. These stochastic simulations can be additionally conditioned to hydraulic-head data obtained by sampling the reference flow field. Finally, we consider the case in

which an exhaustive knowledge on the geology is available (i.e. channel location and structure are exactly known).

3.1 Sampling the transmissivity and head fields

To simulate the aquifer characterization procedure in a real case study, the reference transmissivity field and the head field are sampled at random locations in order to mimic field measurements. For each variable three datasets consisting of 21, 250, and 1000 measurements are obtained. (Note that transmissivity and heads are sampled at identical locations). Figures 2c and 2f show the sample locations (circles) of the 21 and 250 datasets, respectively (1000-dataset locations are not shown because they are too dense). The transmissivity and the head datasets represent error-free local data. The mean distance between the samples is 89 m, 26 m, and 12 m, respectively. In order to avoid unit-dependent indicators and include the integral scale in our reasoning, the mean distance is normalized by the integral scale in the x direction. The corresponding dimensionless mean distances, d, are 3.5, 1, and 0.47 for 21, 250, and 1000 samples, respectively. In other words, the three datasets represent measurements whose mean spacing ranges from three times to half the integral scale. Note that the reference image is anisotropic and that the integral scale in the y direction is much smaller, even smaller than the mean distance between the samples in the 1000-measurement case. The statistics of the decimal *log*-transmissivity of the three datasets used are presented in Table 1.

3.2 Experimental variograms

The three transmissivity datasets (25, 250 and 1000 T samples) are analysed separately in a geostatistical framework. The 250 and 1000 T samples clearly exhibit a bimodal histogram (Figs. 2d and 2g). Before analysing the spatial correlation, the $log_{10}T$ values are transformed into a normal variable N via a Gaussian transformation since the simulation algorithms require to work with normal distributed variables. Note that, after comparison with the normal score transform, the Hermite polynomials decomposition was selected to compute the Gaussian transform as it provided a slightly better histogram reproduction for the direct and back transform. Then, the assumption of bi-Gaussianity of the normal variable N is tested and cannot be rejected, even if this may be surprising since the transmissivity data are clearly not bi-Gaussian. After analysing the anisotropy of the variogram maps of the transformed data, directional experimental variograms are calculated and modelled for each dataset in both x and y directions (Figs. 2b, 2e and 2h). Note

that the experimental variogram of the 21 *T* samples did not show any anisotropy, thus an isotropic exponential model is used in this case. The variogram of 1000 *T* showed a nested structure, which is modelled by one exponential and one spherical model. Cross validation is performed to test whether the fitted variogram models are acceptable. Note that no nugget effect is considered since data are known to be error free. Furthermore, the absence of nugget effects allows a higher degree of control on the *T* field during the inverse calibration.

Table 1 Samples statistics and adjusted variograms, *N* represents the Gaussian transform of $log_{10}(T)$

Number of *T* sample	21	250	1000
Average distance between samples	89	26	12
Dimensionless distance *d* [-]	3.5	1	0.47
Mean log_{10}(T [m^2/s])	-2.06	-2.28	-2.23
Minimum log_{10}(T [m^2/s])	-3.31	-3.86	-3.82
Maximum log_{10}(T [m^2/s])	-1.03	-0.82	-0.37
Std. log_{10}(T [m^2/s])	0.77	0.82	0.82
N variogram type	Exp.	Exp.	Exp. + Sph.
Nugget effect	0	0	0
Variogram sill	0.98	0.99	0.77 + 0.23
Variogram range along *x* [m]	89	85	35 & 185
Variogram range along *y* [m]	89	15	25 & 35

3.3 Kriging and conditional simulations

First, ordinary kriging of the *N* normally distributed values is applied to each transmissivity dataset (21, 250, 1000 *T* samples) with the corresponding modelled variogram. The *T* fields (Figs. 2c, 2f and 2i) are obtained by back-transforming the kriged *N* field in two steps.

First, *N* is back transformed into $log_{10}(T)$ with the inverse Gaussian transform (Hermite polynomials) based on the histogram of the data, then we take the decimal power of this field to obtain the transmissivity. Note that the last part of the back transform is often corrected to avoid the bias that it induces in the value of the arithmetic mean of *T*, but for 2D aquifers we should be more concerned with the bias in the geometric mean of *T* rather than in the arithmetic mean because the later controls the mean flow through the system. Taking the decimal power preserves the geometric mean, therefore this is what we did. Then, 100 conditional stochastic

simulations of the normally distributed *N* values are generated for each dataset using the Turning Band Method and back transformed into *T* fields. The upper row of Figure 3 shows examples of the resulting *T*-field simulations (the lower row shows how these fields are improved by inverse modelling). In the end, the geometric means of the simulations, of the kriging and of each dataset have been compared and are very similar.

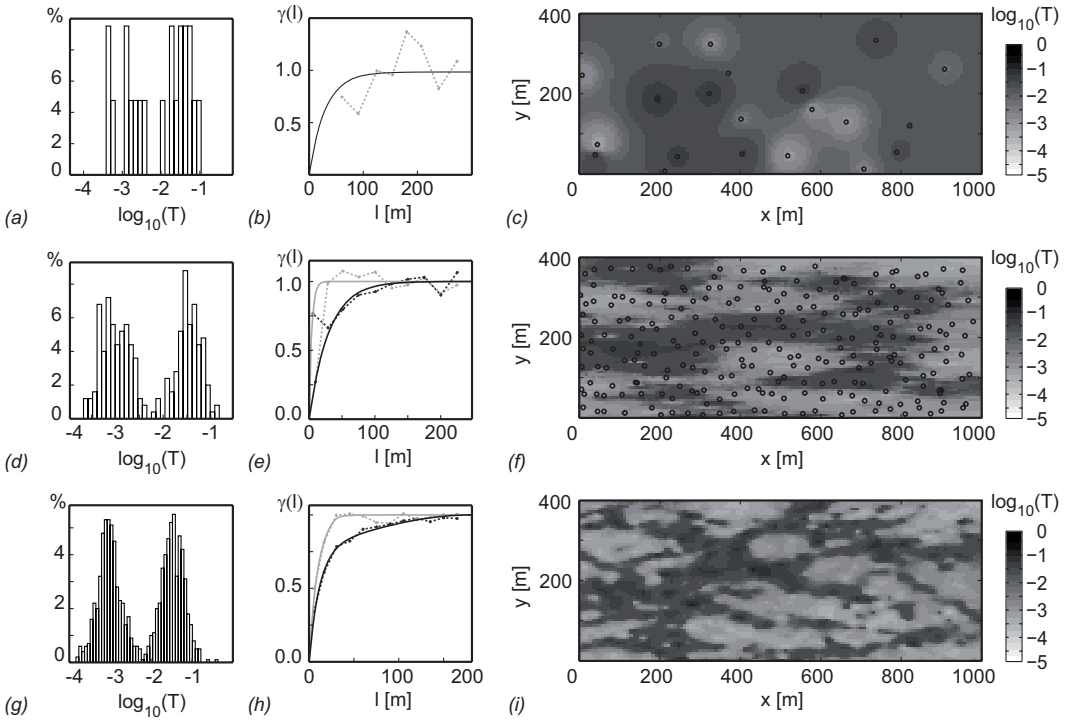

Fig. 2 *T* fields estimation steps for 21 *T* (a, b and c), 250 *T* (d, e and f), and 1000 *T* data (g, *h* and i): (a, d, and g) histogram of the *T* data, (b, e and h) experimental (dashed line) and model (solid line) variograms of the *N* Gaussian transform of the decimal log of the *T* data in both *x* (black line) and *y* (gray line) directions except for 21 *T* which was isotropic, (c, f and i) kriged maps and *T* samples locations except for 1000 *T* because of its high density.

3.4 Inverse modelling

The three sets of stochastic simulations of *log*-transmissivity can, in addition, be conditioned to the hydraulic-head data by means of the sequential self-calibration method as implemented in the INVERTO code (Hendricks-Franssen, 2001.). Six pairs of data are considered with an increasing number of transmissivity (T) and head (h) samples, i.e. (21T,21h), (21T,250h), (21T,1000h), (250T,250h) (250T,

1000h), (1000T,1000h). Note that the number of conditioning head data is always at least as large as the number of transmissivity data. For each pair, 100 equally likely inverse realisations are generated that are conditioned both to the transmissivity and hydraulic-head data.

During the inversion, the variogram estimated from the data (section 3.2), is used as a model to interpolate the perturbations optimised at the master blocks. Two master blocks are laid out per correlation length, and the position of the master blocks is modified during the inverse conditioning. The lower raw of Figure 3 shows examples of the resulting transmissivity fields.

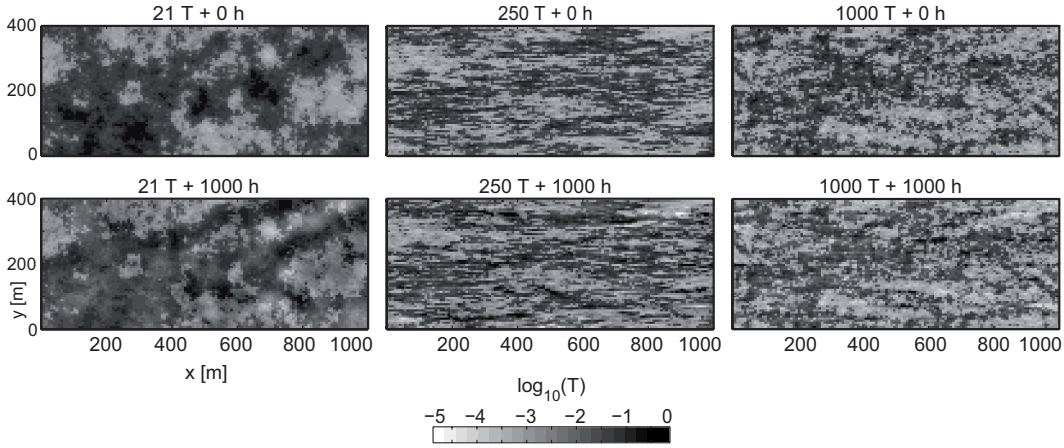

Fig. 3 Simulations conditioned only to the *T* values (upper maps), and the same simulations conditioned to *T* and *h* measurements according to the map title.

3.5 Characterization with exhaustive geological conditioning

In addition to the multiGaussian characterization presented in the previous sections, a test was conducted to estimate the efficiency of the characterization methods when the location of the channels would be exhaustively known. This is clearly unrealistic but it constitutes an end member that allows investigating what is the best estimate that can be obtained if one would know the position of the channels. We considered only the dataset with 21 *T* samples, but in addition we have a binary map that indicates if a pixel is within a channel or not. The 21 *T* samples are then divided in two groups, according to their locations in a channel or in a lens, and they are analysed and modelled separately. Note that, due to the lack of data, the two variograms are very weakly constrained. The resulting models are spherical with a range of 85 m for the channels data and 190 m for the lenses. Following the

procedure presented above, Turning Band simulations are used to separately populate the channels and the lenses and generate 100 *T* fields.

Finally, these fields are processed with INVERTO (Hendricks-Franssen, 2001.) to produce 100 equally likely realisations conditional to 21 transmissivity data, 250 hydraulic-head data, and to the exhaustive geological information. In the inverse conditioning, each geological unit is separately perturbed. This means that perturbations in lenses do not affect the hydraulic conductivities in channels and vice versa. Both in the lenses and the channels 100 master blocks each are placed. In that case, INVERTO uses the geological knowledge to optimize the local values of the transmissivity by having different variograms for the different facies.

4. Numerical results

In order to evaluate the reliability of the characterization techniques, the estimated *T* fields and the simulated *h* fields are compared with the corresponding reference fields. Note that the two techniques provide different kind of results: the estimated *T* field is unique and aims at providing a locally accurate map, the simulations aim at reproducing the variogram. Consequently, their comparison may be theoretically questionable, but we argue that it has a practical relevance and this is why we perform it. Moreover, since we want to assess the ability of predicting the behaviour of the aquifer under different flow scenarios, the estimated transmissivity fields are used to forecast the system response when a pumping well is located in the middle of the domain.

4.1 Reproduction of the reference T and h fields

The kriged *T* fields and some examples of simulations conditional to transmissivity and head data are shown in Figures 2 and 3. By visual comparison with the reference transmissivity field (Fig. 1) it is evident that a large number of samples is required to start recovering the channel structure. Even in these cases, the simulated images are quite different from the reference.

To quantify this discrepancy and assess the accuracy both in terms of reproduction of the *log*-transmissivity and hydraulic-head fields, we introduce the average absolute error,

$$\varepsilon(X) = \frac{1}{n}\sum_{i=1}^{n}\left|\overline{X}_{s,i} - X_{ref,i}\right|, \qquad (1)$$

and the average ensemble standard deviation,

$$\varepsilon_\sigma(X) = \frac{1}{n}\sum_{i=1}^{n}\sigma_{X_i}\ , \qquad (2)$$

where n is the number of grid cells, i a grid cell index, X the variable considered (decimal *log*-transmissivity or steady-state hydraulic head), the overbar indicates ensemble average, $\sigma_{X_i} = \left[\overline{(X_{s,i}^2)} - (\overline{X}_{s,i})^2\right]^{1/2}$ is the ensemble standard deviation of X at a given node, the subscript s refers to the realisations, and the subscript *ref* to the reference (synthetic) values.

Table 2 presents calculated average absolute error ε and average ensemble standard deviation ε_σ for transmissivity and head fields of all the combinations of T and h data. From the results presented in Table 2, one can observe that, in general, conditioning improves the characterisation of the *log*-transmissivity and hydraulic-head fields, and reduces the ensemble variance as expected. However, the reduction is smaller than observed in similar multiGaussian studies (Hendricks-Franssen, 2001.). It is noteworthy to indicate that the uncertainty reduction for the *logT* and *h* estimation ($\varepsilon_\sigma(Y)$ and $\varepsilon_\sigma(h)$) are in most cases smaller than the improvement in the characterisation of the *log*-transmissivity field ($\varepsilon(Y)$) and the hydraulic head field ($\varepsilon(h)$), unlike the studies with a multiGaussian model for *log*-transmissivity (Hendricks-Franssen, 2001.).

Table 2 Performance measures for the generated ensembles, conditioned to different amounts of data. The absolute average error ε and average ensemble standard deviation ε_σ are expressed in percent of the values calculated for 21 *T*.

Conditioning data	$\varepsilon(Y)$	$\varepsilon_\sigma(Y)$	$\varepsilon(h)$	$\varepsilon_\sigma(h)$
T=21	100.0	100.0	100.0	100.0
T=21, H=21	98.9	90.1	41.9	19.5
T=21, H=250	94.3	80.9	13.2	8.1
T=21, H=250,	48.0	54.4	7.2	4.5
T=21, H=1000	92.9	74.9	9.2	6.1
T=250, H=250	79.5	106.7	11.0	7.4
T=250, H=1000	79.4	106.0	8.7	6.5
T=1000, H=1000	64.9	87.0	10.0	5.7

Note that, in spite of using a wrong *logT* model in the inverse conditioning and in spite of a somewhat limited improvement in the characterisation of the *logT* field, the characterisation of the hydraulic head field improves spectacularly. Overall, the inverse modelling improves the characterisation of hydraulic-head and *log*-transmissivity fields and reduces uncertainty, but compared with multiGaussian cases using the correct random function model the improvements tend to be smaller. Note that in case of 1000 head samples no clear trend can be observed when the number of *T* samples is increased from 21 to 250 and 1000.

As expected, knowing the geology (the position of channels and lenses) considerably improves both the characterisation of the *log*-transmissivity field and the reproduction of the heads.

4.2 Forecasting the flow: fluxes and heads

In this section, the transmissivity fields obtained from the characterization procedures are used to predict the system behaviour under a different flow scenario, i.e. when a pumping well is added in the middle of the domain. The boundary conditions are identical as for the reference flow, but an additional pumping well with a constant flow rate of 700 m^3/d is added in the middle of the domain (x=500 m, y=200 m).

Two criteria are used to evaluate the performance of the *T* estimated fields: the accuracy in estimating the outflux at the western boundary (Q_{out}) and the well-bore head (H_w). Figure 4 shows the histograms of Q_{out} and H_w for some of the considered cases. The vertical lines represent the reference value calculated with the reference *T* field, the ensemble average from the simulations, and the value calculated with the kriged field. Note that heads and fluxes estimated with the kriged field are different from those obtained by the ensemble averages of the simulations. This is due to the fact that even if the flow equations are linear for heads, they are not linear in terms of hydraulic conductivities. However, none of these two estimations can be said more accurate than the other.

Without conditioning to head data, we observe a reduction of the uncertainty on the forecasted heads or fluxes when the number of *T* data increases (compare Figs. 4a, 4i and 4m or Figs. 4b, 4j and 4n). It is instructive to compare the results provided by an exhaustive geological knowledge with those provided by conditioning to 1000 transmissivity data (Figs 4e-f and 4m-n, respectively).

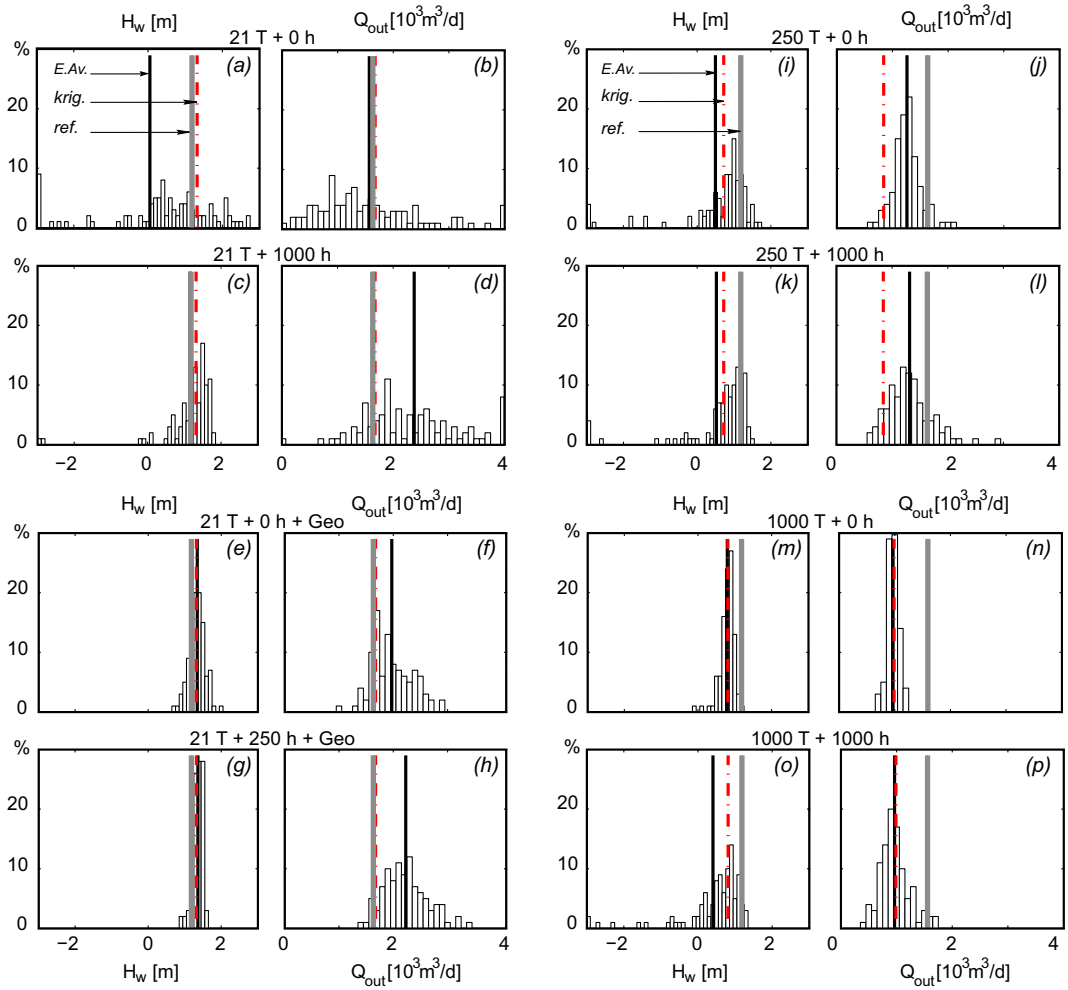

Fig. 4 Histograms of the final head in the well (a,e,i and m) for the simulations conditioned only with *T*; (c,g,k and o) the same plus 1000 head data according to the title. The integral out flux (b,f,j and n) for the simulations conditioned only with *T*; (d,h,l and p) the same plus 1000 head data according to the title. For each set of the 100 simulations: the thick gray line represents the reference field values (ref.); the solid thin line represents the ensemble average of the simulations (E.Av.), the dash-points line represents the kriged values (krig.).

As expected, the information on the position of channels and lenses truly improves the knowledge of the system, as proved by the reduction of both errors and uncertainty. In the case of 1000 *T* data, instead, the uncertainty reduces, but the error does not, as can be observed in Figure 4n, where the histogram of the forecast out-fluxes does not contain the reference value. The uncertainty has reduced but the

forecasts are incorrect. This clearly shows the risk of conditioning to many *T* data with a wrong statistical model. The systematically smaller fluxes indicate that the connectivity is lower than in the reference field.

Adding head data generally has a positive impact but does not necessarily reduce the uncertainty. When the number of *T* data is small, conditioning with head data reduces uncertainty (compare Figs 4a and 4c for example). It was surprising to observe that when the number of *T* data is very large, conditioning on heads increases the uncertainty (Figs 4n and 4p). However, it has to be observed that this effect is such that the forecast histograms always include the reference values. In other words, it seems that if too many points are conditioned to transmissivity, information on the hydraulic heads is not able to substantially affect the flux ensemble average, but it improves the correctness of the prediction by increasing the uncertainty. This result will be addressed in more detail in the discussion.

4.3 Capture zone forecast and performance analysis

As a last comparison between the characterisation methods, we assess the accuracy of the different *T* fields in forecasting the 10-days capture zone of the pumping well, which is delineated by simulating advective-dispersive transport. We assume a constant porosity equal to 0.3, whereas the longitudinal and transversal dispersivities are small and equal to 2 and 0.2 m, respectively. This yields an advection-dominated transport. The capture zones are calculated by solving the Kolmogorov backward equation (Uffink, 1989; Mariethoz et al., 2006). The mean-life expectancy is calculated with the GroundWater finite element code (Cornaton, 2003) and the 10-days capture zone is defined as the region around the well where the mean-life expectancies are less than 10 days (Fig. 1e). Note that the shape of the capture zone is strongly controlled by the local transmissivity distribution in the vicinity of the well. The reference capture zone is depicted in Figure 1e, together with the capture zones calculated by means of the analytical solution of Bear and Jacobs (1965) for a purely advective transport of an inert solute. Shown are both results obtained by using the geometric mean of the *T* reference field and the equivalent homogenous transmissivity obtained from the Darcy flux. Note that the 10-days capture zone resulting from the geometric mean reflects the assumed isotropy of the *T* field.

In the direct conditional-simulation approach and in the inverse approach, several simulations have been constructed for a given dataset. In these two cases, the uncertainty is estimated by constructing the probability maps for a point to belong to

the capture zone. These maps are shown in Figure 5. Visual inspection of the results (Fig. 5) reveals that the forecasts can significantly differ from the reference. We note that the reference is not always completely included in the forecasted capture zones. Indeed, the eastern finger of the reference capture zone is predicted neither by kriging, nor by the 0.5 isoprobability contour of the simulations, nor by the geometric mean. The latter leads to a prediction very similar to that obtained with the analytical isotropic solution of Bear and Jacobs (1965). As observed before, the a-priori knowledge of the geology significantly improves the characterization of the *T* fields. If the position of the channels is known, the predicted capture zone is already accurate with a small number of *T* data (21) and even better when additional head data (250) are used for conditioning the transmissivity field.

To quantify the accuracy of the characterization methods, we introduce two error norms for comparing the forecast capture zone, Z, with the reference capture zone, Z_{ref}: the missed area,

$$e_{ma} = \frac{N_p}{B_p + N_p}, \qquad (3)$$

and the unnecessarily protected area,

$$e_{uc} = \frac{P_l}{B_p + P_l}, \qquad (4)$$

where N_p [m^2] is the area of the reference protection zone that is not correctly identified by the forecast, i.e. the area of $Z_{ref} \cap Z$, B_p [m^2] is the area of the reference protection zone that is correctly forecasted, i.e. the area of $Z \setminus Z_{ref}$, P_l [m^2] is the area wrongly forecasted as belonging to the protection zone, i.e. the area of $Z_{ref} \setminus Z$. In other words, e_{ma} is the percentage of the reference that has not been identified, whereas e_{uc} is the percentage of the forecast that is unnecessarily protected.

In addition, an evaluation of the total error is provided by the average squared residual between the forecasted (Z) and the reference well capture zone (Z_{ref}),

$$\varepsilon_s = \frac{1}{100}\sum_{s=1}^{100}\left(\frac{1}{n}\sum_{i=1}^{n}\left(Z_{s,i} - Z_{ref,i}\right)^2\right), \qquad (5)$$

where *s* indicates the simulation, *i* is the grid node and *n* the total number of nodes in the grid. s , resp. ref, is an indicator variable, equal to 1 if the node belongs to Z, resp. Z_{ref}, and 0 if not.

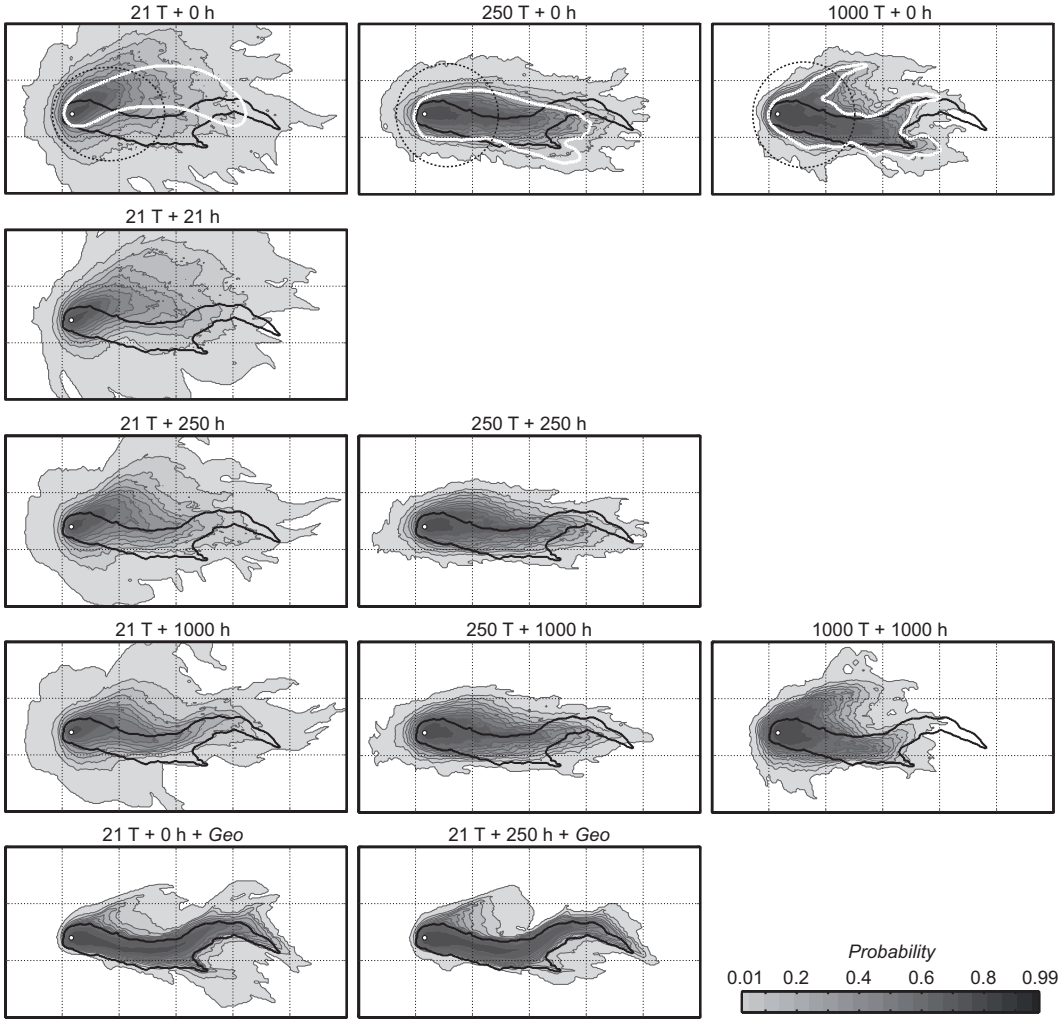

Fig. 5 10-days capture zone probability maps. The black line represents the reference 10-days capture zone. The white line (in the upper maps) represents the zone forecasted by kriging. The gray levels represent the isoprobability contours for all the combinations of *T* and *h* datasets (according to the map title). The dashed line on the upper maps represents the 10-days capture zone for an homogenous field in which *T* is equal to the geometric mean of the *T* samples.

Finally, the uncertainty is quantified by the dimensionless ratio between the uncertain area and the reference protection zone,

$$u = \frac{I}{N_p + B_p}, \qquad (6)$$

where $N_p + B_p$ [m^2] is the area of the reference protection zone, Z_{ref}, and I [m^2] is the area located between the 0.9 and 0.1 isoprobability contours.

The missed area e_{ma} and unnecessarily protected area e_{uc} errors are calculated for different levels of probability threshold (0.2, 0.5 and 0.8) and are summarized in Figure 6. It can be observed that the average squared residual (ε_s) is almost identical for kriging and for the simulations conditioned only on T (Figure 6a) and that ε_s decreases regularly with decreasing d. Adding head data clearly reduces ε_s only when the mean distance d between the sample is large with respect to the integral scale, i.e. when the simulations are conditioned to few T data. The best results are obtained with the geological knowledge.

When kriging is employed, ε_s, the missed area (e_{ma}), and the unnecessarily protected area (e_{uc}) decrease when d decreases (Figs. 6a, and 6c–6f). When d is lower than 1, the errors do not reduce significantly (or stabilize) when new samples are added. In the best cases, the missed area represents around 20% of the reference protection zone and the area unnecessarily protected represents around 45% of the forecasted zone.

When stochastic simulations are employed, the uncertainty area u can be estimated. We find that it varies between 1.5 and 3.5 times the real area of the reference capture zone. Figure 6b shows how u decreases regularly when d decreases and that adding head data reduces the uncertainty very significantly, especially when the distance d between the transmissivity data is large.

The probability maps obtained from stochastic simulations (Fig. 5) are tools to help making decisions. The level of risk can be quantified by the probability threshold P that is employed to define the capture zone. A risk-prone decision maker may for example take a probability threshold of 0.5 while a conservative decision maker may take a probability threshold of 0.8. Figures 6c and 6d show the evolution of the missed area and unnecessarily protected area as a function of d, and of the probability threshold P in the case of simulations conditioned only to T data, while Figures 6e and 6f show the equivalent when 1000 h data are used in addition. These results suggest that the error decreases with d only if the latter is larger than 1. When conditioning to head data, it does not appear clear whether conditioning to more T data improves the characterization. On the contrary, in case 1000 T data are used for conditioning, the unnecessarily protected area is larger than in case only 21 T data are used for conditioning (using in both cases 1000 head data for inverse conditioning). There are also some counterintuitive results that show that when the distance between the sample is small and when a large number of head and

transmissivity data are provided, the errors can be larger than with a smaller number of data (see for example the curves of the unnecessarily protected area e_{uc} on Figure 6f and for a probability threshold of 0.2; e_{uc} decreases when the distance between the samples decreases). This is in contrast with what was observed for the fluxes, where the inverse simulations yield a better histogram than the simulations conditioned only to *T*. In all cases, the most remarkable fact is that errors remain large even with a considerable amount of data.

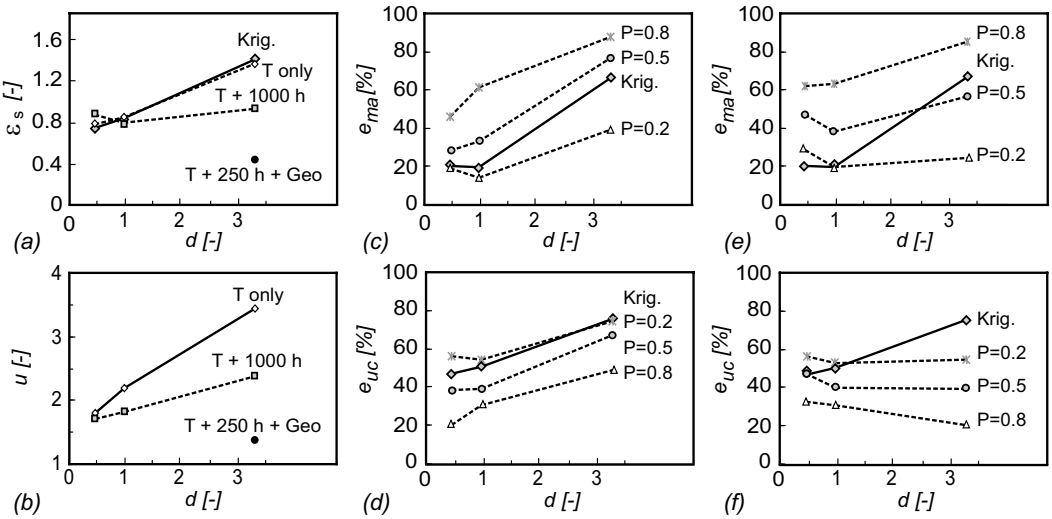

Fig. 6 Results: (a) the averaged squared error between forecasted and reference capture zone vs. mean distance between the samples for the three methods, (b) uncertainty vs. mean distance between the samples, (c) e_{ma} (missed area) for 0.2, 0.5, and 0.8 probability threshold vs. distance between the samples with transmissivity data only, (d) e_{uc} (unnecessarily protected area) for 0.2, 0.5, and 0.8 probability threshold vs. distance between the samples with transmissivity data only, (e) and (f): same as (c) and (d) but 1000 additional head measurements used to condition the *T* fields.

5. Discussion

The numerical simulations presented in this paper consider a 2D aquifer that displays channels and lenses and follows non-multiGaussian statistics. Our approach has been to consider this field, which is supposed to reflect the properties of a realistic aquifer, as “the reality” and try to characterize it on the basis of simulated local measurements of transmissivity and heads. It has to be remarked that we have used a single *T* field as reference (as in a real test case there is only one real aquifer) and the results are therefore influenced by the specific transmissivity arrangement

and location of the well. However, we believe that the difficulties encountered might be faced anytime that the problem of characterizing a channelized aquifer is addressed. Having located the well in the most permeable region reflects the fact that real wells are placed in transmissive regions in order to optimize efficiency. Our assumption is that the *T*-field considered qualitatively illustrates the difficulties encountered with media that exhibit a highly connected network of permeable channels. In practice, vertical averaging of the 3D hydraulic conductivity might filter the complexity of the porous media by yielding a model characterized by smoother contrasts between permeable and less-permeable regions. However, if we accept the picture of the 3D aquifer as having a hydraulic conductivity that displays an interconnected network of permeable channels and isolated poorly permeable lenses, we can expect difficulties similar to those described in this paper. Even more problematic, the smoother 2D data of the transmissivity would tend to additionally hide the extreme values of the hydraulic conductivity, which are expected to play an important role, in particular for transport (e.g. for capture-zone estimation or remediation problems).

Therefore, despite the limitations, we argue that the numerical results presented in the previous section enable some general considerations. Some conclusions are expected, such as the fact that exhaustive geologic knowledge provides most of the necessary information or that samples denser than the integral scale do not significantly improve the characterization. Other conclusions are surprising such as the fact that 1) uncertainty and errors remain very large even in the presence of (unrealistically) many data, 2) conditioning to many *T* data may reduce uncertainty but increase the bias, and 3) conditioning to many *T* data seems to inhibit the inverse conditioning from improving the characterization.

Before going further, we observe that the reduction of uncertainty concomitant with an increased bias that has already been mentioned by Scheibe and Chien (2003). They compare multiGaussian characterization techniques based on real field data. The quality criterion was the reproduction of a measured tracer breakthrough curve. They showed that conditioning to a large number of small scale measurements did not significantly improve the model prediction and could even lead to biased and overly confident predictions. As an additional element of analysis, it was shown in Ababou et al. (1994) based solely on algebraic arguments, that the conditioning and stability of the (Gaussian) kriging system gets worse as local point measurements become more dense particularly in the absence of a nugget effect. Our findings are fully consistent with these results and suggest that problems do not arise

because of measurement errors, but are generated by erroneously applying multiGaussian characterization techniques to non-multiGaussian fields.

Why the multiGaussian assumption prevent providing accurate results when the number of data is large? When the mean distance *d* between the *T* data is small with respect to the integral scale of the reference, the inference of a variogram model is easy and accurate. The histograms are also well defined. Then, the high density of conditioning *T* data leads to a situation in which the variability between the simulations is very small. This can be seen on the histograms of the forecasted water levels in the pumping well or in the histogram of the forecasted outflow rates (Figs. 4m and 4n). The simulated fields are very strongly constrained by the *T* data, by the variogram model, as well as by the multiGaussian assumption used by the simulation technique. Therefore, the inverse technique has very little degrees of freedom. In case of a large amount of conditioning transmissivity data, the hydraulic head data cannot modify the transmissivity field significantly, because the transmissivity data "freeze" the – wrongly postulated – multiGaussian model. Conditioning to head data has only very local impacts and cannot result in significant changes of the large scale structure of the field. This can be seen by comparing the fields before and after inversions in Figure 3. Important changes are observed with 21 *T* data, while little changes are visible with 1000 *T* data. *Appendix D§* presents additional simulations aimed at investigating in more detail the role of transmissivity data in inverse conditioning when a non-multi-Gaussian medium is erroneously modelled as being multi-Gaussian.

These observations and the fact that the error norms did not reduce significantly when increasing the number of *T* conditioning data from 250 to 1000 samples, are in agreement with the findings of Grabow et al. (1993) and van Leeuwen et al. (2000). Grabow et al (1993) showed that the reduction of the number of *T* conditioning data did not increase the error of flow and transport predictions. Van Leeuwen et al. (2000) showed that beyond a certain threshold of conditioning data density the performance did not improve further. Both Grabow et al. (1993) and van Leeuwen et al. (2000) explain their results by the screening effect due to redundancy of data. Note that van Leeuwen et al. (2000) dealt with a reference multiGaussian field originally avoiding the connectivity problem. This redundancy effect is probably accentuated when narrow preferential flow paths exist.

The synthetic field used in this numerical study displays a bimodal distribution with a high connectivity of the large values. There are clear channels that completely cross the domain (Figure 1). The channels are globally oriented along the *x* axis and offer a high connectivity in that direction, but locally their orientation varies and

they are generally not parallel to the *x* axis; and they have a wide range of width along the *y* direction. All this complexity cannot be captured by the variogram, and is smoothed out by the multiGaussian model. Even if the variograms are very well estimated with a large number of *T* data and even if the *T* map produced by kriging shows the locations of most of the main channels (Figure 2i), the kriged map does not reproduce the connectivity because the thin sections of the channels are clogged by low transmissivity values (compare Figs. 2 and 3i).

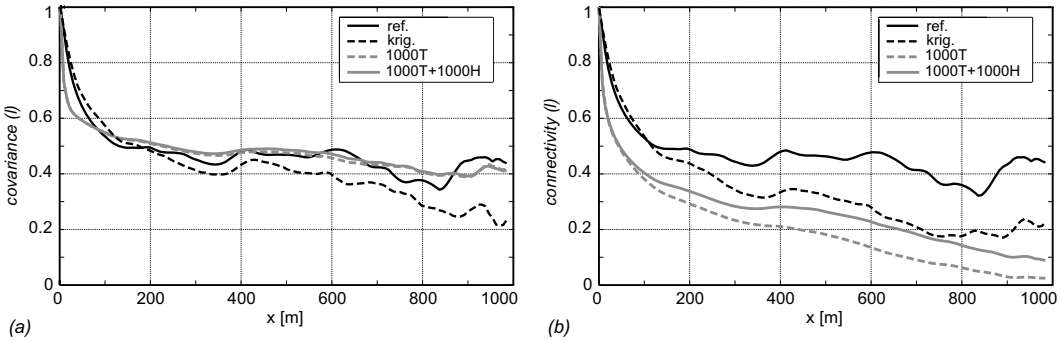

Fig. 7 Directional covariance (a) and connectivity (b) functions along the *x*-axis for 1000 *T* data. The lines corresponding to the simulations are ensemble averages over the 100 simulations (1000T, and 1000T+1000h).

This visual observation is confirmed by the comparison of the connectivity functions of the reference field and of the kriging or the simulated fields (Fig. 7). We remind that the connectivity function represents the probability that a transmissive cell taken randomly in the domain is connected by a continuous path of adjacent cells of similar transmissivity with another transmissive cell located at a certain lag distance (Stauffer and Aharony, 1994). Figure 7 shows that all the characterization methods reasonably reproduce the covariance function of the reference (Fig. 7a), but they systematically underestimate the connectivity of the reference (Fig. 7b). The lack of connectivity of the high values explains the tendency of underestimating the flux through the domain.

6. Conclusion

The goal of this work was to investigate and compare the reliability of direct and inverse multiGaussian techniques when applied to characterize fields that are not multiGaussian and exhibit preferential flow paths. For that purpose, the performances of kriging, stochastic simulations and sequential self-calibration method have been compared, as a function of an increasing number of samples of transmissivity and head data on a synthetic braided alluvial aquifer for predicting flow and transport. Multiple error indicators were used.

We found that up to a certain quantity of data, adding head or transmissivity measurements reduces the errors and the uncertainty. However, a limit is reached: when the density of samples becomes high, we observe unexpected outcomes such as increased bias with an increasing number of *T* data, or increased uncertainty estimation with an increased number of head data. The simulations results suggest that in case a large number of transmissivity data is used for conditioning, the hydraulic head data are less able to correct the consequences of the erroneous multiGaussian model (in terms of the evaluated performance measures). Particularly problematic is the bias with many *T*-data because the simultaneous decrease of the uncertainty may lead to overestimate the reliability of the results. In any case, errors remain important even with a large quantity of data.

These outcomes can be explained by the fact that two-point multiGaussian characterization techniques are unable to capture the correct connectivity, which plays a primary role in dictating flow and transport. Using a multiGaussian model when the reality is not multiGaussian may lead to inaccurate predictions. These results confirm and extend the opinion expressed by Gómez-Hernández and Wen (1999) that modellers must be extremely careful when taking the decision of using a multiGaussian model.

In order to overcome these limitations, it is extremely important to use a stochastic model that allows reproducing the connectivity of the original field. Along that direction, we argue that techniques such as the multiple-point statistics (Journel and Deutsch, 1993; Strebelle, 2002; Feyen and Caers, 2006) may allow that. Moreover, secondary information, such as geophysics, should be used whenever possible to infer the connectivity structures and to constrain the stochastic model.

References

Ababou, R., Bagtzoglou, A.C. and Wood, E.F., 1994. On the Condition Number of Covariance Matrices in Kriging, Estimation, and Simulation of Random-Fields. Mathematical Geology, 26(1): 99-133.

Alcolea, A., Carrera, J. and Medina, A., 2006. Pilot points method incorporating prior information for solving the groundwater flow inverse problem. Advances in Water Resources, 29(11): 1678-1689.

Armstrong, M., Galli, A., Le Loc'h, G., Geffroy, F. and Eschard, R., 2003. Plurigaussian simulations in geosciences. Springer, Berlin, 149 pp.

Bear, J. and Jacobs, M., 1965. On the movement of water bodies injected into aquifers. Journal of Hydrology, 3: 37-57.

Caers, J., 2005. Petroleum geostatistics. Society of Petroleum Engineers.

Caers, J., 2007. Comparing the gradual deformation with the probability perturbation method for solving inverse problems. Mathematical Geology, 39(1): 27-52.

Caers, J. and Hoffman, T., 2006. The probability perturbation method: A new look at Bayesian inverse modeling. Mathematical Geology, 38(1): 81-100.

Capilla, J.E., Gomez-Hernandez, J. and Sahuquillo, A., 1998. Stochastic simulation of transmissivity fields conditional to both transmissivity and piezometric head data - 3. Application to the Culebra Formation at the Waste Isolation Pilot Plan (WIPP), New Mexico, USA. Journal of Hydrology, 207(3-4): 254-269.

Capilla, J.E., Rodrigo, J. and Gomez-Hernandez, J.J., 1999. Simulation of non-Gaussian transmissivity fields honoring piezometric data and integrating soft and secondary information. Mathematical Geology, 31(7): 907-927.

Carrera, J., Alcolea, A., Agustín, M., Hidalgo, J. and Slooten, L.J., 2005. Inverse problem in hydrogeology. Hydrogeology Journal, 13: 206-222. doi:10.1007/s10040-004-0404-7

Cornaton, F., 2003. Deterministic models of groundwater age, life expectancy and transit time distribution in advective-dispersive systems. PhD Thesis, Université de Neuchâtel, Neuchâtel, 144 pp.

de Marsily, G. et al., 2005. Dealing with spatial heterogeneity. Hydrogeology Journal, 13(1): 161-183.

de Marsily, G., Delhomme, J.-P., Delay, F. and Buoro, A., 1999. 40 years of inverse problems in hydrogeology Comptes Rendus de l'Academie des Sciences Series IIA Earth and Planetary Science, 329(2): 73-87. doi:10.1016/S1251-8050(99)80208-0

Delhomme, J.P., 1979. Spatial variability and uncertainty in groundwater flow parameters. Water Resources Research, 15(2): 281-290.

Diersch, H.G., 1996. Interactive, Graphics-Based Finite Element Simulation System FEFLOW For Modeling Groundwater Flow, Contaminant Mass and Heat Transport. WASY Institute for Water Resource Planning and System Research Ltd., Berlin, Germany.

Feyen, L. and Caers, J., 2006. Quantifying geological uncertainty for flow and transport modelling in multi-modal heterogeneous formations. Advances in Water Resources, 29(6): 912-929.

Gómez-Hernández, J.J. and Srivastava, R.M., 1990. Isim3d - an Ansi-C 3-Dimensional Multiple Indicator Conditional Simulation Program. Computers & Geosciences, 16(4): 395-440.

Gómez-Hernández, J.J. and Wen, X.-H., 1998. To be or not to be multi-gaussian? A reflection on stochastic hydrogeology. Advances in Water Resources, 21(1): 47-61.

Grabow, G.L., Mote, C.R., Sanders, W.L., Smoot, J.L. and Yoder, D.C., 1993. Groundwater monitoring network design using minimum well density. Water Science and Technology, 28(3–5): 327–335.

Hendricks-Franssen, H.-J., Gómez-Hernández, J. and Sahuquillo, A., 2003. Coupled inverse modelling of groundwater flow and mass transport and the worth of concentration data. Journal of Hydrology, 281(4): 281-295.

Hendricks-Franssen, H.J., 2001. Inverse stochastic modeling of groundwater flow and mass transport, University of Valencia, 363 pp.

Hendricks Franssen HJ., G.-H.J., Sahuquillo A., Capilla JE., 1999. Joint simulation of transmissivity and storativity fields conditional to hydraulic head data. Advances in Water Resources Research, 23: 1-13.

Hu, L.Y., Le Ravalec, M. and Blanc, G., 2001. Gradual deformation and iterative calibration of truncated Gaussian simulations. Petroleum Geoscience, 7: S25-S30.

Janssen, G.M.C.M., Valstar, J.R. and van der Zee, S.E.A.T.M., 2006. Inverse modeling of multimodal conductivity distributions. Water Resources Research, 42(W03410): doi:10.1029/2005WR004356.

Journel, A.G. and Deutsch, C.V., 1993. Entropy and spatial disorder. Mathematical Geology, 25(3): 329-355.

Koltermann, C.E. and Gorelick, S.M., 1996. Heterogeneity in sedimentary deposits: A review of structure-imitating, process-imitating, and descriptive approaches. Water Resources Research, 32(9): 2617-2658.

Larocque, M., Delay, F. and Banton, O., 2003. A comparison of two stochastic inverse methods in a field-scale application. Ground Water, 41(1): 15-23.

Lavenue, M. and de Marsily, G., 2001. Three-dimensional interference test interpretation in a fractured aquifer using the pilot point inverse method. Water Resources Research, 37(11): 2659-2675.

Mariethoz, G., Renard, P., Cornaton, F. and Jaquet, O., 2006. High resolution stochastic modelling of aquifers, example for a contamination migration problem, Proceedings of the Swiss Geoscience Meeting, Bern, Switzerland, November 24th to 25th.

Mosley, M.P., 1982. Analysis of the effect of changing discharge on channel morphology and instream uses in a braided river, Ohau River, New Zealand. Water Resources Research, 18(4): 800-812.

Renard, P., Gomez-Hernandez, J. and Ezzedine, S., 2005. Characterisation of Porous and Fractured Media. In: M. Anderson (Editor), Encyclopedia of Hydrological Sciences. John Wiley & Sons, Ltd.

Rosgen, D.L., 1994. A classification of naturel rivers. CATENA, 22: 169-199.

Sánchez-Vila, X., Carrera, J. and Girardi, J.P., 1996. Scale effects in transmissivity. Journal of Hydrology, 183(1-2): 1-22.

Scheibe, T.D. and Chien, Y., 2003. An evaluation of conditioning data for solute transport prediction. Ground Water, 41(2): 128-141.

Stauffer, D. and Aharony, A., 1994. Introduction to percolation theory. Taylor and Francis, London.

Strebelle, S., 2002. Sequential simulation drawing structures from training images. PhD Thesis Thesis, Stanford University.

Uffink, G.J.M., 1989. Application of the Kolmogorov's backward equation in random walk simulation of groundwater contaminant transport. In: H.E.

Kobus and W. Kinzelbach (Editors), Contaminant Transport in Groundwater. A.A. Balkema, Rotterdam, The Netherlands.

van Leeuwen, M., Butler, A.P., te Stroet, C.B.M. and Tompkins, J.A., 2000. Stochastic determination of well capture zones conditioned on regular grids of transmissivity measurements. Water Resources Research, 36(4): 949-957.

Wen, X.-H., Gómez-Hernández, J.J., Capilla, J.E. and Sahuquillo, A., 1996. Significance of conditioning to piezometric head data for predictions of mass transport in groundwater modeling. Mathematical Geology, 28(7): 951-968.

Zimmerman, D.A. et al., 1998. A comparison of seven geostatistically based inverse approaches to estimate transmissivities for modeling advective transport by groundwater flow. Water Resources Research, 34(6): 1373-1413.

Zinn, B. and Harvey, C.F., 2003. When good statistical models of aquifer heterogeneity go bad: A comparison of flow, dispersion, and mass transfer in connected and multivariate Gaussian hydraulic conductivity fields. Water Resources Research, 39(3): 1051, doi:10.1029/2001WR001146.

Chapter 7

Concluding comments

Modelling seawater intrusion

Synthetic study

We investigated numerically the effects of different degrees of heterogeneity of hydraulic conductivity and the effects of problem dimensionality on modelling saltwater intrusion with coupled variable-density flow and solute transport in steady-state. The evaluation was made in terms of dimensionless toe penetration and width of the mixing zone and dimensionless inflowing saltwater. Results showed that the impacts of heterogeneity of hydraulic conductivity on seawater intrusion are stronger in two-dimensional media than in three-dimensional ones. Depending on the degree of heterogeneity, those impacts may be variable and rather complex.

Moreover, it was found that using effective hydraulic conductivity is not sufficient to reproduce the mean behaviour of the saltwater wedge in a 2D heterogeneous aquifer with a medium to high *ln(K)* variances. It is therefore suggested that the effective values of the longitudinal and transversal dispersivities should be computed to better represent the system. This is important because it indicates that if one wants to investigate the effect of heterogeneity on a real heterogeneous system (that is naturally three dimensional), it is not possible to simply use a homogenous model without effective dispersivities to obtain a correct model of the seawater intrusion.

Furthermore, we proposed a methodology based on stochastic effective hydraulic conductivities allowing a 2D field transformation so that the 2D solute transport predictions are close to the 3D ones. This transformation is based on the

geometric mean and variance of *ln(K)*, and the correlation lengths of the 3D hydraulic conductivity distribution. The most important gain is saving CPU time.

The Korba coastal aquifer study

Through the case study of the Korba aquifer, we combined data from different sources to characterize the recent status of the aquifer and to estimate the components of the regional groundwater mass balance, especially the effective recharge and the abstraction rates. Using these estimations, we showed the interest of using a 3D numerical model to compile all the knowledge on the site and to reproduce the evolution of the system starting from the equilibrium (steady) state to 2004 in light of the existing reference data, and to predict the response of the aquifer to changes in its boundary conditions. The maximum amounts that could be exploited in the aquifer Korba can be estimated by an optimization study based on the models described in this study considering uncertain inputs.

In addition, we estimated uncertainties related to model parameters, and propagated them to model outputs. Then, we evaluated how those uncertainties are affecting model predictions. The results of the stochastic simulations showed that both uncertainties led to a zone representing 12 % of the aquifer area, where the groundwater heads and salt concentrations are not known with accuracy. Results also showed that reducing the pumping rates progressively by 50% until 2048 will not result in a recession of the saltwater wedge; instead an additional 9.5 % of the surface of the aquifer will be contaminated in 2048.

Characterizing heterogeneity

The main outcomes of the comparison of the reliability of kriging, stochastic simulations and sequential self-calibration method when applied to characterize fields that are not multiGaussian are:

- Up to a certain quantity of data, adding head or transmissivity measurements reduces the errors and the uncertainty on capture zone forecasts;
- When the density of samples becomes high, an increased bias with an increasing number of transmissivity data, and an increased uncertainty estimation with an increased number of head data were observed;
- In the case where a large number of transmissivity data is used for conditioning, the hydraulic head data are less able to correct the consequences of the erroneous multiGaussian model.

These outcomes can be explained by the fact that connectivity, which conditions flow and transport processes, is a property that cannot be captured by standard two-point multiGaussian characterization techniques. These results confirm and extend the opinion expressed by Gómez-Hernández and Wen (1999) that modellers must be extremely careful when taking the decision of using a multiGaussian model. Using a multiGaussian model when the reality is not multiGaussian may lead to inaccurate predictions. To sidestep these limitations:

- Techniques such as the multiple-point statistics (Feyen and Caers 2006; Journel and Zhang 2006; Strebelle 2002) may allow to better reproduce the connectivity features.
- Secondary information, such as geophysics, should be used whenever possible to infer the connectivity structures and to constrain the stochastic model.

Finally, it will be interesting to investigate the dynamics of seawater intrusion in other complex and non-multiGaussian media.

References

Abarca E (2006) Seawater intrusion in complex geological environments. PhD Thesis, Technical University of Catalonia, UPC

Abarca E, Carrera J, Sánchez-Vila X, Dentz M (2007) Anisotropic dispersive Henry problem. Advances in Water Resources 30: 913-926. doi:doi:10.1016/j.advwatres.2006.08.005

Feyen L, Caers J (2006) Quantifying geological uncertainty for flow and transport modelling in multi-modal heterogenesous formations. Advances in Water Resources 29: 912-929

Held R, Attinger S, Kinzelbach W (2005) Homogenization and effective parameters for the Henry problem in heterogeneous formations. Water Resouces Research 41: 1-14. doi:doi:10.1029/2004WR003674

Hendricks Franssen HJ. G-HJ, Sahuquillo A., Capilla JE. (1999) Joint simulation of transmissivity and storativity fields conditional to hydraulic head data. Advances in Water Resources Research 23: 1-13

Journel A, Zhang T (2006) The necessity of a multiple-point prior model. Mathematical Geology 38: 591-610

Strebelle S (2002) Conditional simulation of complex geological structures using multiple-point statistics. Mathematical Geology 34: 1-21

Appendixes

Appendix A

Equivalent hydraulic conductivity

The second method used to calculate the equivalent hydraulic conductivities is called the uniform boundary conditions method. It consists of solving numerically the diffusivity equation with fixed linear constant gradients attributed to the boundaries (faces) parallel to the flow and constant head in the principal flow directions such as:

$$H(x,y,z)=c_1x+c_2y+c_3z+cst. \quad (1)$$

where H is the hydraulic head [m], $\boldsymbol{c_1}$, $\boldsymbol{c_2}$, $\boldsymbol{c_3}$ and *cst.* [-] are fixed (known) constants, and x, y and z are the coordinates system. Solving the linear system below after calculating the fluxes q^x, q^y and q^z using the numerical models yields the full tensor of the hydraulic conductivity.

$$\begin{pmatrix} q^x \\ q^y \\ q^z \end{pmatrix} = -\begin{pmatrix} K_{xx} & K_{xy} & K_{xz} \\ K_{yx} & K_{yy} & K_{yz} \\ K_{zx} & K_{zy} & K_{zz} \end{pmatrix}.\begin{pmatrix} \partial H/\partial x \\ \partial H/\partial y \\ \partial H/\partial z \end{pmatrix} \equiv \begin{pmatrix} K_{xx} & K_{xy} & K_{xz} \\ K_{yx} & K_{yy} & K_{yz} \\ K_{zx} & K_{zy} & K_{zz} \end{pmatrix}.\begin{pmatrix} c_1 \\ c_2 \\ c_3 \end{pmatrix} \quad (2)$$

An advantage of this approach is that it applies for any kind of medium (scale) and heterogeneities. Note however, that with this method, convection due to freshwater/seawater density contrast is not taken into account, Darcy fluxes q [m/s] are calculated for uniform density flow.

In the following, we analyse the evolution of directional hydraulic conductivities as a function of heterogeneity and dimensionality. Effective (Chapter 2, Section 3.2) and equivalent hydraulic conductivities are estimated for both 2D and 3D configurations and shown in Figures 1 (for the isotropic cases) & 2 (for the anisotropic cases).

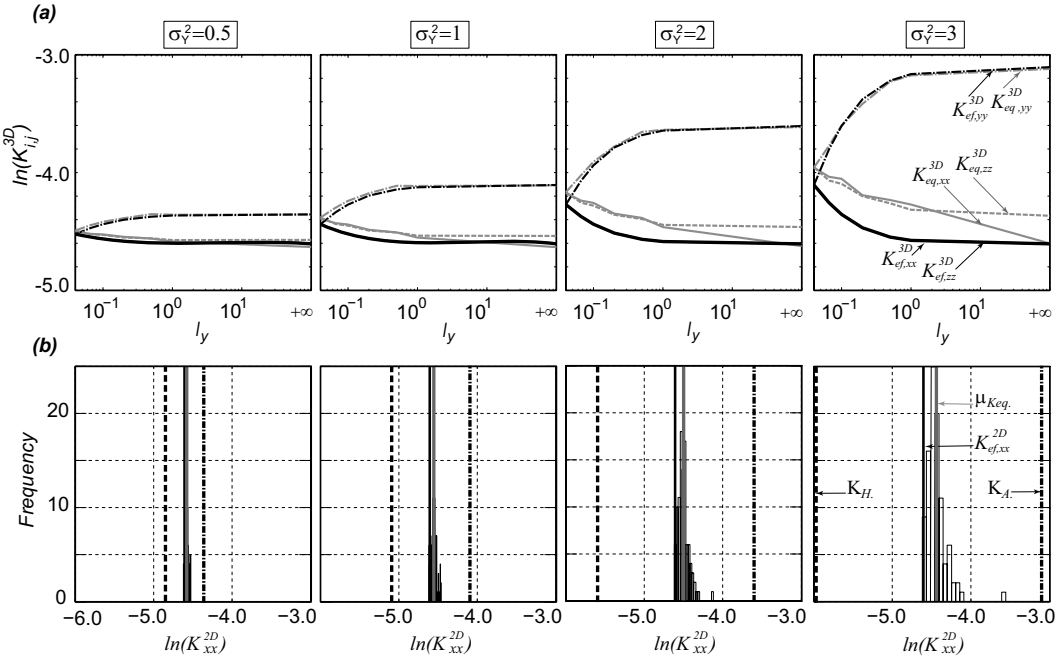

Fig. 1 Effective and equivalent hydraulic conductivity for the isotropic cases. (a) Evolution of the effective and equivalent directional hydraulic conductivities as a function of increasing l_y for four levels of *ln(K)* variance in the 3D models. (b) Effective (black lines) and ensemble average (gray lines) of the equivalent hydraulic conductivity along the *x* direction calculated over 100 2D simulations (histogram in background); the harmonic mean (dashed line) and the arithmetic mean (dashed-point line) hydraulic conductivity of one realisation. Note that the ensemble averaging is made using the geometric mean.

Figures 1 and 2 show that the two methods used resulted in similar values of the effective and equivalent hydraulic conductivities, especially for small variances. However, there is a difference between the estimations of hydraulic conductivities in the *x* and *z* directions (main flow directions) which increases when *ln(K)* variance increases. For a *ln(K*) variance larger than 1, the numerical method overestimates the equivalent directional hydraulic conductivities. As demonstrated by Lachassagne et al. (1990) this trend (overestimation of the effective hydraulic conductivity) is due to the finite elements method (the way of integrating the fluxes between two elements). Note that for the 3D cases, only one realisation was used while the effective hydraulic conductivity is representative of an ensemble average of multiple 3D realisations.

In 2D anisotropic configuration (Figs. 2b and 2c), the numerical estimation of the horizontal hydraulic conductivity (in the flow direction) is more accurate than in the vertical direction. However both estimations are in agreement with the stochastic theory. Indeed, in statistically anisotropic media, the effective hydraulic conductivity

in the horizontal direction (parallel to the flow direction) tends to approach the arithmetic mean which is its upper bound, while it tends to approach the harmonic mean in the vertical direction which is its lower bound.

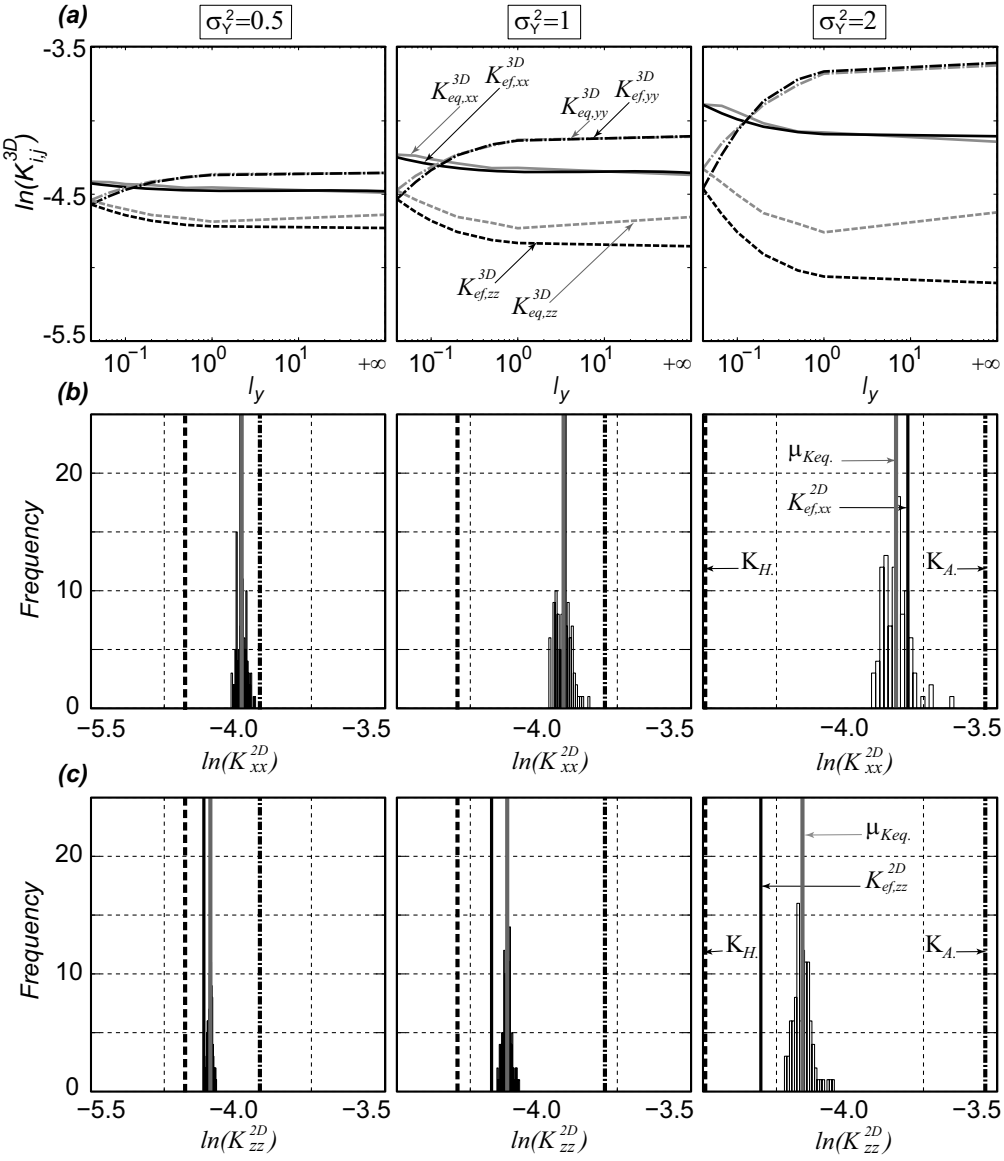

Fig. 2 Effective and equivalent hydraulic conductivity for the anisotropic cases. (a) Evolution of the effective and equivalent directional hydraulic conductivity as a function of increasing l_y for three levels of the *ln(K)* variance in the 3D models. (b) Effective (black lines) and ensemble average (gray lines) of the equivalent hydraulic conductivity along the *x* direction calculated over 100 2D simulations (histogram in background); the harmonic mean (dashed line) and the arithmetic mean (dashed-point line) hydraulic conductivity of one realisation. (c) Same as (b) but in the *y* direction.

In addition, when the *ln(K)* variance increases, $K_{ef,xx}$ and $K_{eq,xx}$ increases while $K_{ef,zz}$ and $K_{eq,zz}$ decreases. The same behaviour is observed in 3D anisotropic configurations (Fig. 2 a). The difference in the estimation of the hydraulic conductivity in the vertical direction can be attributed to the fact that the stochastic solution is a diagonal tensor; however the numerical method gives the full tensor of the hydraulic conductivity. This also relates to the effects of the flow boundary (bounded domain).

Appendix B

3D Anisotropy effects on SWI

The question is: to what extent the horizontal anisotropy of the 3D model affects saltwater intrusion. Firstl, an isotropic 3D hydraulic conductivity fields (with equal directional correlation lengths; $l_x=l_y=l_z$) was generated. Second, the correlation lengths following the *x* and *y* directions (l_x and l_y) were increased respectively in 5 steps until they largely exceed the size of the domain in their respective directions. For each l_x and l_y combination, a 3D model was generated according to the parameters listed in Table 1. Figure 1 shows some of the resultant 36 3D models. Note that $l_z=0.04$ is kept constant and $\mu_Y=\mu_g=0.01$ [m/s] and $\sigma_Y=1$ for all this set.

Table 1 Dimensions and statistics of the hydraulic conductivity fields

Parameter	**Value**
ln(*K* [m/s]) distribution	Gaussian
Geometric mean (*K* [m/s])	0.01
ln(*K* [m/s]) variance	1
Variogram type	Spherical
Cases of range along *x*(l_x) [m]	0.04, 0.1, 0.2, 0.5, 1 & $+\infty$
Cases of range along *y*(l_y) [m]	0.04, 0.1, 0.2, 0.5, 1 & $+\infty$
Range along *z* (l_z) [m]	0.04

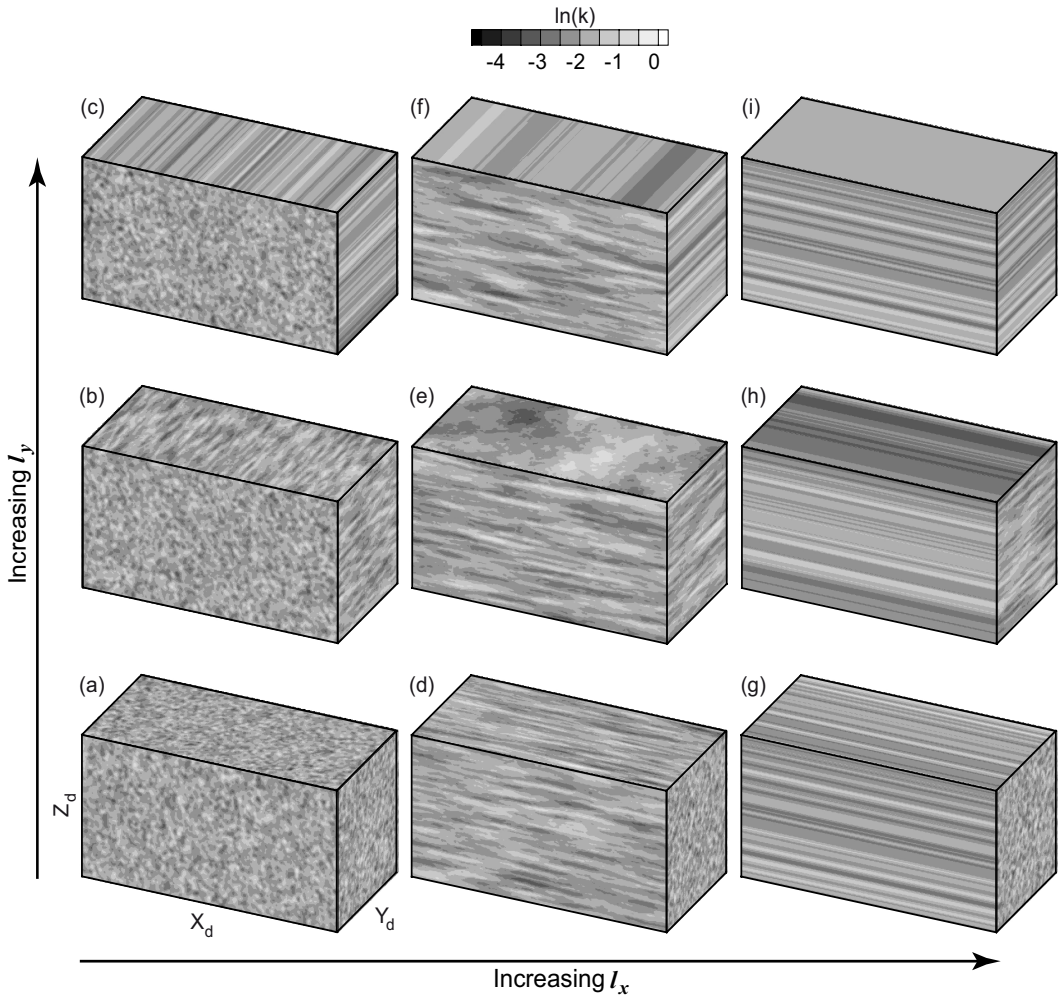

Fig. 1 View of the 3D hydraulic conductivity fields. For all cases l_z=0.04, μg=0.01 and σ_Y=1 are kept constant: (a) l_x=l_y=0.04 (statistically isotropic case); (b) l_x=0.04, l_y=0.5; (c) l_x=0.04, l_y=+∞; (d) l_x=0.5, l_y=0.04; (e) l_x=0.5, l_y=0.5 (f) l_x=0.5, l_y=+∞; (g) l_x=+∞, l_y=0.04; (h) l_x=+∞, l_y=0.5 (i) l_x=+∞, l_y=+∞. Note that (c) is equivalent to the *Abarca et al.* (2006) and *Held et al.* (2005) cases, and (i) is equivalent to the *Dagan and Zeitoun* (1998) case.

Using the analytical model described in chapter 1 (section 3.2) the effective hydraulic conductivities are estimated for all generated 3D cases. The resulting hydraulic conductivity anisotropy ratios are shown in Figure 3. Note that for σ_Y^2 =3, the maximum anisotropy ratio r_{yx} reached 4.8 for the case of l_x=l_z=0.04 and l_y=+∞. and r_{yx}=0.22 for the case of l_x=3*l_z=0.12 and l_y=+∞.

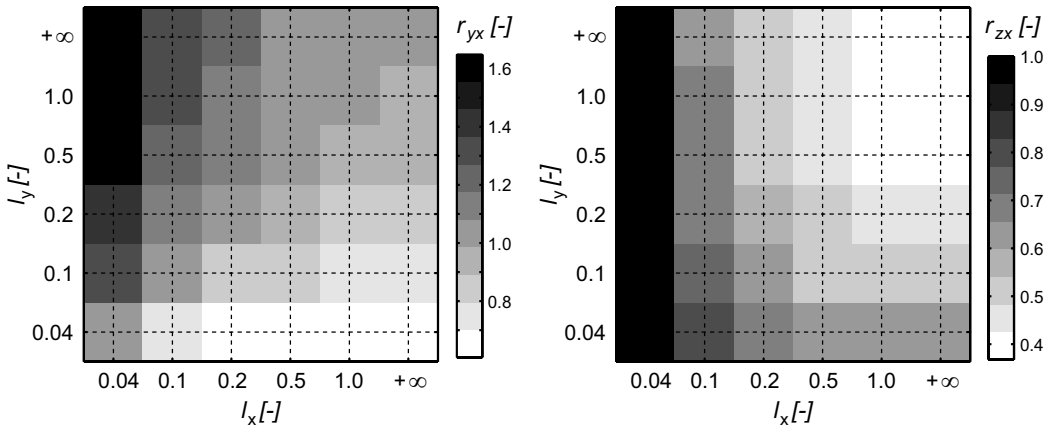

Fig. 2 Horizontal and vertical anisotropiy ratios for all $\boldsymbol{l_x}$ and $\boldsymbol{l_y}$ combinations calculated using the analytical model of *Ababou* (1995) for a *ln(K)* variance of 1. Note that for *ln(k)*=3, r_{yx} exceed 4.8.

Density-dependent flow and salt transport are solved as described in section 3.3 of Chapter 2. Results are shown in figure 3. As expected L_D increases with an increasing l_x (Fig. 3) in both 2D (the upper line corresponding to l_y=+*inf.*) and 3D configurations, and is always larger in 3D than in 2D. However W_D increases with increasing l_x more significantly in 2D models than in 3D ones. Note that for higher correlation lengths, errors due to ergodicity condition loss are expected.

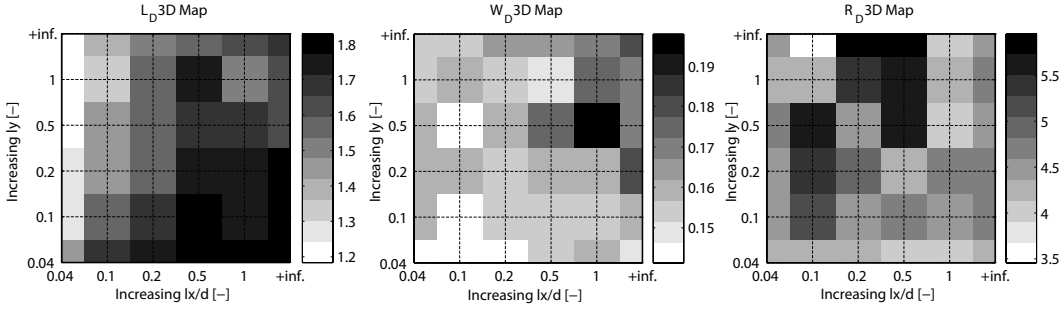

Fig. 3 Evolution of L_D, W_D and R_D as functions of increasing l_x and l_y in a 3D configuration. Note that the results for l_y=+*inf.* (upper line) correspond to 2D configurations.

For this set of simulations, the outputs L_D, W_D and R_D are analysed to determine how much these parameters are correlated to the horizontal or vertical hydraulic conductivity anisotropy. The most evident correlations are shown in Figure 4. Results show that there is a negative correlation between the horizontal anisotropy

ratio (r_{YX}) and the penetration of the saltwater wedge and a negative correlation between the vertical anisotropy ratio (r_{ZX}) and the width of the mixing zone.

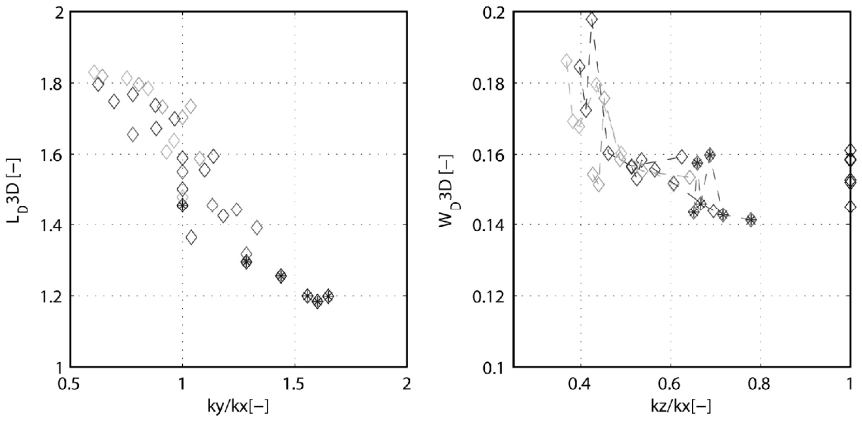

Fig. 4 Effects of 3D anisotropy. (a) Dimensionless toe penetration as a function of r_{YX}, (b) dimensionless width of the mixing zone as a function of r_{ZX}.

Appendix C

Analytical solutions of SWI

In the following we describe and test three existing analytical (including regression) solutions of the position and geometry of the mixing zone. Note that the notations are the same as in Chapter 2.

1. SWI solutions

1.1 Abarca et al. (2007)

The authors used the anisotropic dispersive Henry problem to perform multivariate linear regressions for each of the parameter: L_D and W_D. The resulting best fit of the dimensionless penetration length is:

$$L_D \approx L_{GHD} - (0.136x^{0.724} + 0.69x^{0.362}) \approx L_{GHD} - \left(0.82 \left(\frac{\alpha_G}{a_x^2 \sqrt{r_K}} \right)^{0.4} \right) \quad (1)$$

where $L_{GHD} = \frac{1}{2a_z r_K}$ is a sharp interface based approximation of toe penetration and $x = \frac{\alpha_G}{a_x^2 \sqrt{r_K}}$. The dimensionless width of the mixing zone is: $W_D = 2.7\alpha_G$

1.2 Dagan and Zeitoun (1998)

The authors assessed the effect of a random spatial variability of the permeability on seawater intrusion for the first time. They considered that the permeability is a random function of depth (1D heterogeneity) in a perfectly layered structure. Assuming a sharp interface, they used Darcy's law, mass conservation for each fluid, pressure continuity on the interface and *Dupuit* assumption to derive a simple analytical solution of the statistical moments of the position of the interface between fresh and salt waters in a 2D steady flow of freshwater in a confined aquifer.

The dimensionless average position of the interface $\boldsymbol{L_{GHD}}$ at $\boldsymbol{z=d}$ (distance between the point where the freshwater-saltwater interface intercepts the bottom of the aquifer and seaside boundary $\boldsymbol{L_{GH}}$, normalized by the thickness of the aquifer $\boldsymbol{d}$) is given by (eq. 17 in Dagan and Zeitoun 1998):

$$L_{GHD} = \frac{1}{2\,a_A} \qquad (2)$$

where $a_A = \frac{q_b}{\varepsilon K_A}$ with K_A the arithmetic mean of the permeabilities. Note that in a homogeneous medium with an equivalent hydraulic conductivity which is equal to the arithmetic mean, the interface shape is the *Dupuit* parabola and independent from the hydraulic conductivity variance.

The variance of the horizontal coordinates of the interface is given by (eq. 22 in Dagan and Zeitoun 1998):

$$\sigma^2_{L_{GHD}} = \frac{\sigma^2 I_z^4}{a^2 d^4}\left[\frac{2}{3}\left(\frac{\zeta}{I}\right)^3 - \left(\frac{\zeta}{I}\right)^2 - 2\left(\frac{\zeta}{I}\right)\exp\left(-\frac{\zeta}{I}\right) - 2\exp\left(-\frac{\zeta}{I}\right) + 2\right]$$

for $0<=\zeta<=1$ (3)

where $\sigma^2 = \exp(\sigma_Y^2) - 1$ and I_z is the integral scale of the spatial distribution of the permeabilities.

This solution allows estimating analytically the position of the interface in heterogeneous media and also the uncertainty associated to it. It is important to remark that this solution does not account for an outflow face.

1.3 Naji et al. (1998)

The authors developed another kind of solutions, called stochastic solutions of saltwater-freshwater interface which allow predicting the statistical quantities of mean and standard deviation of the interface position. They showed how it is possible to extend deterministic solutions (e.g., Strack's solution (1976), Glover's solution (1959)) to stochastic counterparts using Taylor's series. Such solutions allow propagating the uncertainty to one or more input parameters to estimate the interface position which is considered uncertain as well. Note that for applying this solution, assumptions such as the homogeneity of the input parameters as well as the uncertainty associated with it have to be made. Moreover, the standard deviation of the input parameters should be very small. The effects of the spatial variability of the input parameter such as the hydraulic conductivity cannot be evaluated using such stochastic solutions. The Following equations are the stochastic version (Naji et al. 1998) of the Glover's deterministic solution for the position of the freshwater-saltwater interface considering uncertain hydraulic conductivity fields:

Glover's deterministic solution $$x = \frac{\zeta^2 - a^2}{2a} \quad (4)$$

Mean position of the interface $$\overline{x} = \frac{\zeta^2 - \overline{a}^2}{2\overline{a}} + \frac{\overline{a}}{2}\left(\frac{\sigma_K^2}{\overline{K}^2}\right) \quad (5)$$

And the variance is: $$\sigma_x^2 = \frac{1}{4}\left(\overline{a}\zeta^2 + \overline{a}\right)^2\left(\frac{\sigma_K^2}{\overline{K}^2}\right) \quad (6)$$

2. Numerical comparison

2.1 Abarca et al. (2007)

In the following we evaluate the performance of the methods of estimation of the toe penetration and the width of the mixing zone described before.

Figure 1 shows that for the homogeneous case, the regression models allow a good estimation of L_D and W_D especially for low the *ln(K)* variances. When *ln(k)* variance increases, the dimensionless toe penetration is over-estimated whereas the width of the mixing zone is under-estimated. This is due to the inadequacy of using local dispersivities values since both (L_D and W_D) parameters are controlled by the geometric mean of the dispersivities.

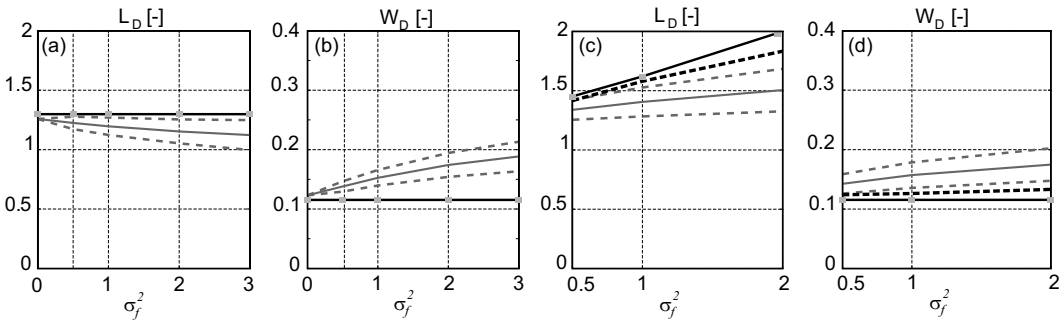

Fig. 1 Dimensionless toe penetration (a and c) and width of the mixing zone (b and d) for isotropic (a and b) and anisotropic (c and d) fields: using Abarca's regression (Solid black line), 2D Monte Carlo simulations ensemble averages (solid gray line) and 95% confidence interval (dashed gray line), and homogeneous medium (dashed black line).

2.2 Dagan and Zeitoun (1998)

For the application of *Dagan's* model, we used the geometric mean hydraulic conductivity $K_G=(K_{xx}*K_{zz})^{1/2}$ instead of the arithmetic mean and a correlation length equal to $I_i=3\lambda_i/8$. Figure 2 shows a comparison between the solution of Dagan et al. (1998) and the ensemble averages of the 2D (coupled density dependent flow and transport) Monte Carlo simulations.

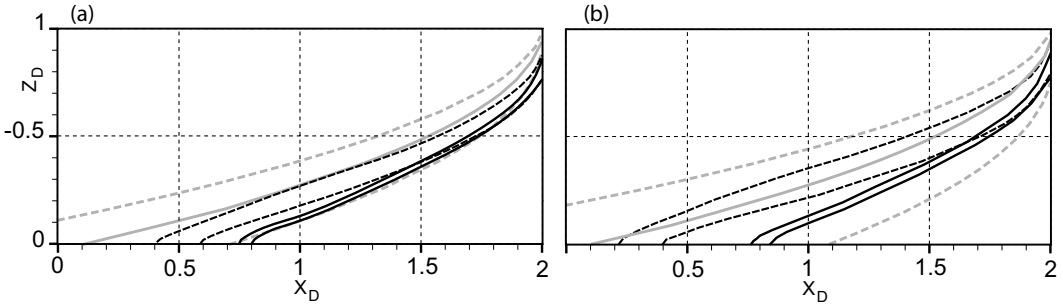

Fig. 2 Comparison between Dagan et al. (1998) Model (average position in solid gray line, 95% confidence interval in dashed gray line) and the ensemble averages of the 2D simulations (95 % confidence interval for isotropic case (l_x= l_z=0.04) in solid black line and for perfectly layered aquifer (l_z=+inf.) in dashed black line) for *ln(K)* variance equal to (a) 0.5 and (b) 1.

Results showed that for small *ln(K)* variances (up to 1), Dagan's solution gives an acceptable estimation of the toe penetration over the upper 80 % on the thickness of the aquifer. For higher variances, uncertainty is over-estimated.

2.3 Naji et al. (1998)

Naji's solution is not adequate because it assumes a weak uncertainty (perturbation) of (homogeneous) hydraulic conductivity. In other words, *K* is a random variable with relatively small variance, and it is spatially constant.

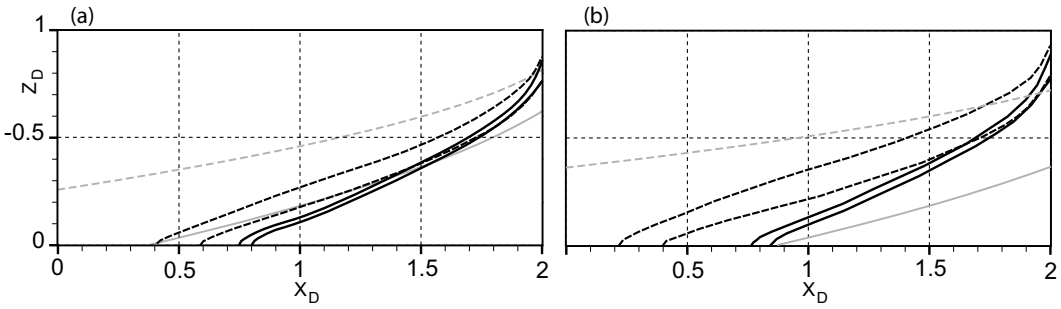

Fig. 3 Naji et al. Model (mean solution in solid gray line and 95% confidence interval in dashed gray line) and the ensemble averages of the 2D simulations (95 % confidence interval for isotropic case (l_x= l_z=0.04) in solid black line and for perfectly layered aquifer (l_z=+inf.) in dashed black line) for σ_Y^2 equal to (a) 0.5 and (b) 1.

References

Abarca E, Carrera J, Sánchez-Vila X, Dentz M (2007) Anisotropic dispersive Henry problem. Advances in Water Resources 30: 913-926. doi:doi:10.1016/j.advwatres.2006.08.005

Dagan G, Zeitoun DG (1998) Seawater-freshwater interface in a stratified aquifer of random permeability distribution. Journal of Contaminant Hydrology 29: 185-203

Glover RE (1959) The Pattern of Fresh-Water Flow in a Coastal Aquifer. Journal of Geophysical Research 64: 457-459

Naji A, Cheng AHD, Ouazar D (1998) Analytical stochastic solutions of saltwater/freshwater interface in coastal aquifers. Stochastic Hydrology and Hydraulics 12: 413-430

Strack ODL (1976) Single-Potential Solution for Regional Interface Problems in Coastal Aquifers. Water Resources Research 12: 1165-1174

Appendix D

Can conditioning to transmissivity data worsen model predictions?⋆

Abstract It is reasonable to think that spatially variable transmissivity fields often follow non-multi-Gaussian statistics. Nevertheless, in groundwater flow and mass transport studies multi-Gaussian models are very popular. This paper investigates the consequences of adopting a wrong Random Function (RF) model. Previous studies have shown that conditioning to hydraulic head data, adopting a multi-Gaussian approach, only very marginally detects connected structures typical for non-multi-Gaussian fields. In addition, several numerical simulations performed have given us a hint that conditioning on a large number of transmissivity data might prevent head conditioning from being effective. We consider non-multi-Gaussian *T* fields (with braided structures) and compare the results obtained by using the *T* data only for computing the variogram with those obtained by additionally conditioning to *T* data (erroneously, a multi-Gaussian RF model is assumed). The preliminary results presented here do not clearly show an improvement when only part of the data is used for *T* conditioning. However, evidence is found that conditioning to *T* data yields a systematic loss of connectivity behind a distance of the order of the variogram range. This fact prevents the inverse problem from identifying elongated capture zones. Conditioning to *h* data, instead, generally yields an increase in connectivity, which is more effective at distances larger than the variogram range, and seems to allow a partial recovery of non-Gaussian structures.

⋆ This appendix is based on the paper:

Kerrou J., Hendricks-Franssen H.J., Renard P. and Lunati I. (2008) How conditioning to transmissivity data can worsen model predictions. In Calibration and Reliability in Groundwater Modelling: Credibility of Modelling. J. C. Refsgaard, K. Kovar, E. Haarder, and E. Nygaard (eds), IAHS Publication 320, pp 299-304, 2008. ISBN 1901502589

1. Introduction

Groundwater protection and aquifer remediation are two examples of activities in which modelling the aquifer response to human activity is important. The first step toward accurate modelling is a reliable characterization of the geological medium. The heterogeneous structure of the aquifer has to be inferred on the basis of data that are available at discrete locations and can consist of transmissivity (T) and head (h) measurements. Groundwater flow and contaminant mass transport predictions are strongly affected by the uncertainty of the transmissivity field. As such, it is important to incorporate transmissivity measurements in flow models, which is achieved by geostatistical simulations. In general, the T fields produced by stochastic characterization are conditioned to the available T data, which are considered the only reliable values of the unknown field. However, many problems are associated with those measurements (e.g. scale dependence, interpretation or measurement errors, abrupt changes within short distances), which make the use of those values difficult.

The characterization of the uncertain of spatially variable transmissivity field can be further improved by conditioning to hydraulic head data by inverse modelling. An important decision to be taken when modelling groundwater flow concerns the multi-Gaussian assumption of the random field (e.g. Gómez-Hernández & Wen, 1998). Since the connectivity of extreme values of transmissivity has a strong impact on contaminant travel time, neglecting the connectivity (as multi-Gaussian models do) can yield a severe underestimation of travel times (e.g. Zinn & Harvey, 2003). Although inverse modelling methods were developed which can handle non-multi-Gaussian fields (e.g. Capilla *et al.*, 1999; Hendricks Franssen & Gómez-Hernández, 2002), it is cumbersome to infer the Random Function (RF) model from sparse observation data. This is one of the reasons why most spatially variable transmissivity fields are modelled as if they were multi-Gaussian, although this is often not the case. Kerrou *et al.* (2008) investigated how such a wrong decision affects the modelling results. They used a synthetic aquifer with marked non-multi-Gaussianity (Fig. 1), and modelled it with multi-Gaussian methods. They also investigated to what extent inverse modelling (conditioning to hydraulic head data) was able to correct the adoption of a wrong RF model. Note that hydraulic head data could detect channels of extreme hydraulic conductivities, even if such channeling was not detected on the basis of transmissivity data and not imposed by the RF model. Indeed, hydraulic head and transmissivity are correlated through the

groundwater flow equation. Kerrou *et al.* (2008) found that hydraulic head data were hardly able to detect such channels, and that connectivity is underestimated even for inverse conditioned realizations. At the same time, they found that transmissivity data might prevent head data from being effective in finding connected channels in inverse conditioning. In case 1000 hydraulic head data were available for inverse conditioning, the results in terms of flow and transport predictions were better (although more uncertain), if 21 transmissivity data were used for conditioning than if 1000 transmissivity data were employed. Figure 2 (after Kerrou *et al.*, 2008) shows how conditioning is able to detect some of the connectivity.

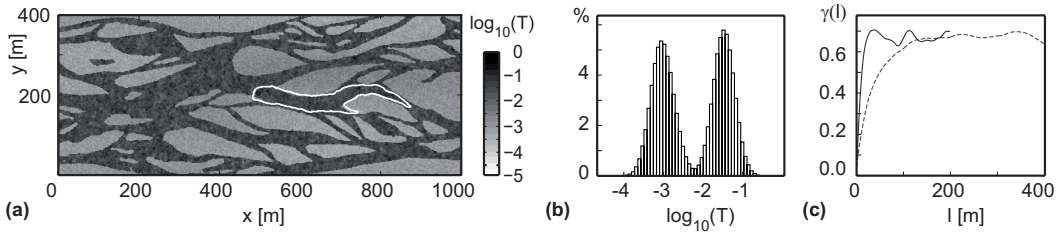

Fig. 1 (a) The synthetic transmissivity field with the 10-days capture zone around the well (small black circle) under steady flow conditions (white contour), (b) histogram of the decimal log of the transmissivities, (c) *x* (dashed line) and *y* (solid line) directional variograms.

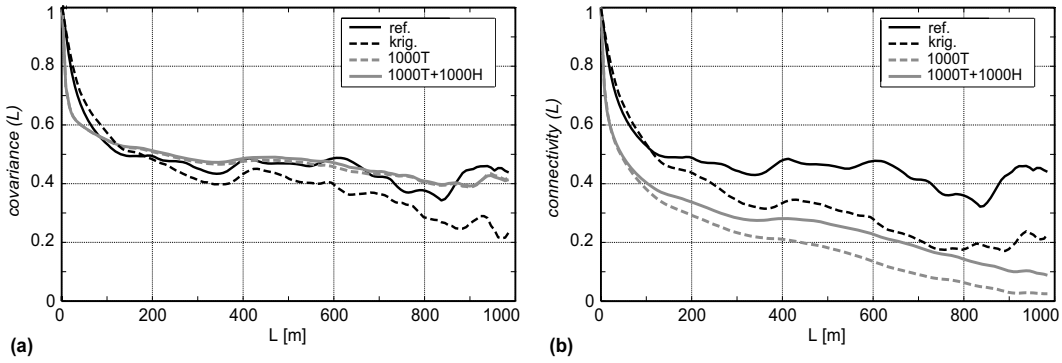

Fig. 2 Directional covariance (a) and connectivity of the high transmissivities higher than the geometric mean (b) functions along the x-axis for 1000 T data. The lines correspond to the ensemble averages over the 100 simulations (1000T, and 1000T+1000h). After Kerrou *et al.* (2008).

This paper presents some additional simulations aimed at investigating in more detail the role of transmissivity data in inverse conditioning when a non-multi-Gaussian medium is erroneously modelled as being multi-Gaussian. The same synthetic reality is used as by Kerrou *et al.* (2008), in order to directly compare the results obtained by Kerrou *et al.* (2008) and these results.

2. Methodology

This study is conducted on a synthetic transmissivity field (*T*) built from an aerial photograph displaying braided channels and lenses in the Ohau River, New Zealand (Mosley, 1982). Two unconditional multi-Gaussian simulations were generated to separately populate with *T* values channels and lenses. This yielded an aquifer whose structure consists of channels and lenses displaying internal heterogeneities (Fig. 1). By imposing constant head boundary conditions on the east (4.24 m) and west (0 m) boundaries and no flow boundary conditions in the north (positive y-axis direction) and south of the reference *T* field (assumed as a confined aquifer), a uniform steady-state flow was calculated.

The synthetic *T* field was sampled to provide data for both direct and inverse characterization methods; also the reference hydraulic head field was sampled for inverse conditioning. The transmissivity data sets consist of 21, 250 and 1000 *T* measurements; the hydraulic head data set consists of 1000 *h* data. These data were used in direct conditioning with the turning bands method and in inverse conditioning with *INVERTO* (Hendricks Franssen, 2001). Some of the simulations were performed without conditioning to transmissivity data, aiming at investigating whether conditioning to transmissivity data prevents head data from revealing non-multi-Gaussian structures. Note that in those cases a variogram model estimated with the help of 250 or 1000 *T* data was adopted. In all cases 100 equally likely realisations were generated. These realisations were used as input for a forecasting problem. Figure 3 shows one of the generated realisations for two of the studied scenarios.

For the forecasting problem, a well was added in the middle of the domain (the boundary conditions being the same as for the reference head field). The 10-days capture zone of the well was calculated by solving the Kolmogorov backward equation with the *GroundWater* finite element code (Cornaton 2007).

3. Results

A large number of comparison measures were calculated, but here we compare the results only on the basis of the well capture zone maps and the measures of connectivity. The other measures, especially the average ensemble absolute error and the average ensemble standard deviation (comparing each set of realizations to the *T* and *h* reference fields), showed in most cases better results when more transmissivity data were used for conditioning. These measures do not indicate that the effect of conditioning to transmissivity data limits the impact of head data.

The 10-days capture zone probability maps calculated for different datasets are shown in Fig. 4. Visual inspection of the capture zone maps indicates that conditioning to *T* data tends to reduce uncertainty. However, the identification of the capture zone is not clearly improved. In particular, it is surprising that probability spreads in the direction transversal to the flow. This is evident when the variogram estimated on the basis of 1000 transmissivity data was used (Fig. 4(d)–(h)).

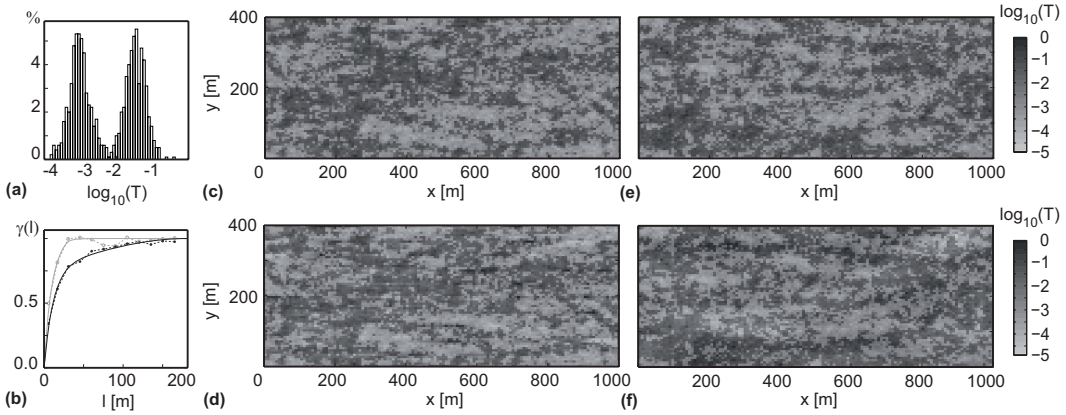

Fig. 3 (a) Histogram of 1000 samples of the decimal log of *T*, (b) *x* (black line) and *y* (grey line) directional variograms; (c) a simulation conditioned to the 1000 *T* data only; (d) the same simulation after conditioning to 1000 *T* and *h* measurements; (e) an unconditional simulation generated using only the variogram of 1000 *T* data; (f) the same unconditional simulation generated using the variogram of 1000 *T* data and conditioning to 1000 *h* measurements.

Conditioning to 21 *T* data yields a probability area that is larger in the *y* direction (compare Fig. 4(d), resp. Fig. 4(e), with Fig. 4(g), resp. Fig. 4(h)), whereas it becomes shorter in the *x* direction and fails to identify the most upstream part of the capture zone. We attribute this to a lack of connectivity typical of multi-Gaussian models: if the connectivity in the flow direction is underestimated, the forecasted capture zone

becomes less elongated and spreads in the transversal direction to satisfy mass balance (the area is solely determined by the well flow rate and must be the same regardless of the specific *T* field). Also the results obtained conditioning to 1000 *T* data can be expressed by this argument. The lack of connectivity makes it more convenient for the well to extract water from the northern channel than from far upstream in the southern channel (compare Fig. 1 and Fig. 4(f)). Therefore, the upstream part of the channel is not captured anymore in any of the realisations, whereas a high probability of flow from the northern channel is erroneously predicted (Fig. 4(f)). Conditioning to *h* data, instead, always helps in finding the elongated channel, as it can be observed by comparing Fig. 4(d), resp. Fig 4(g), with Fig. 4(e), resp. Fig. 4(h). So, a visual inspection of the well capture zones gives hints that transmissivity data make it more difficult to find the parts of the well capture zone which are related to the non-multi-Gaussian properties of the *T* field.

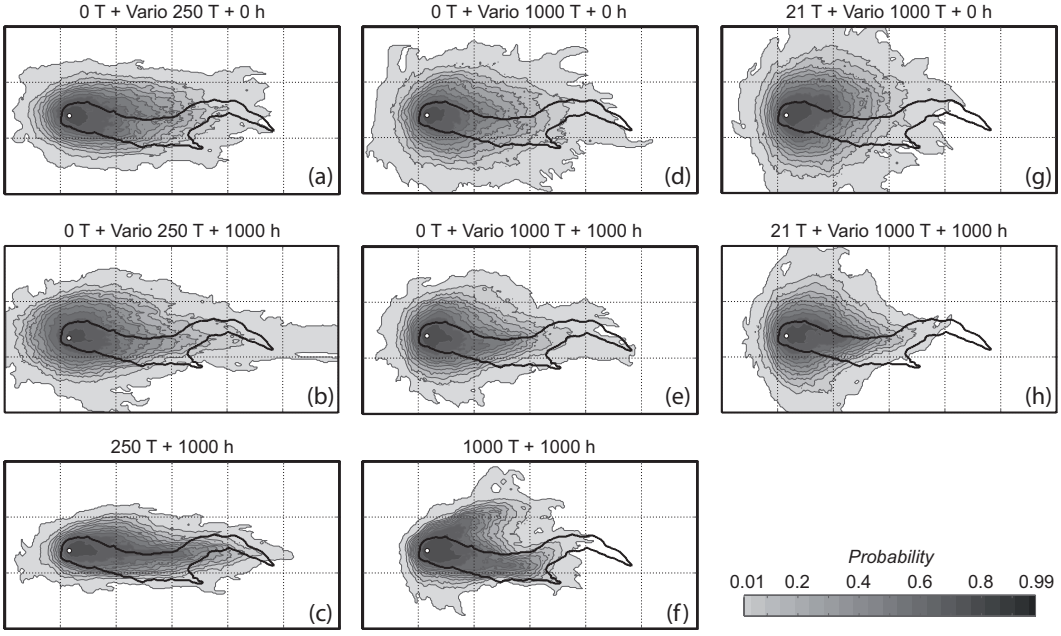

Fig. 4 Probability maps of the 10-days capture zone. The black line represents the reference 10-days capture zone. The grey levels represent the isoprobability contours for all the combinations of *T* and *h* datasets, and variogram models (i.e., estimated on the basis of 250 or 1000 transmissivity data), according to the map title.

To further investigate these aspects, we have calculated the connectivity of the *T* fields (Fig. 5). The multi-Gaussian simulations systematically underestimate the

connectivity of the non-multi-Gaussian reference *T* field. When more conditioning data are used, the characterization of connectivity improves. Although the best results are obtained if both transmissivity and head data are used for conditioning, it is evident that conditioning to head data increases the long-range connectivity. Note that this effect can only be appreciated at distances larger than the variogram range (about 100 m, see Fig. 3).

4. Discussion and conclusions

This paper analysed the role of transmissivity data in inverse conditioning, if a multi-Gaussian model was erroneously adopted. Kerrou *et al.* (2008) found evidence that head data were less able to "correct" the wrong Random Function model for transmissivity in case many transmissivity data were used for conditioning.

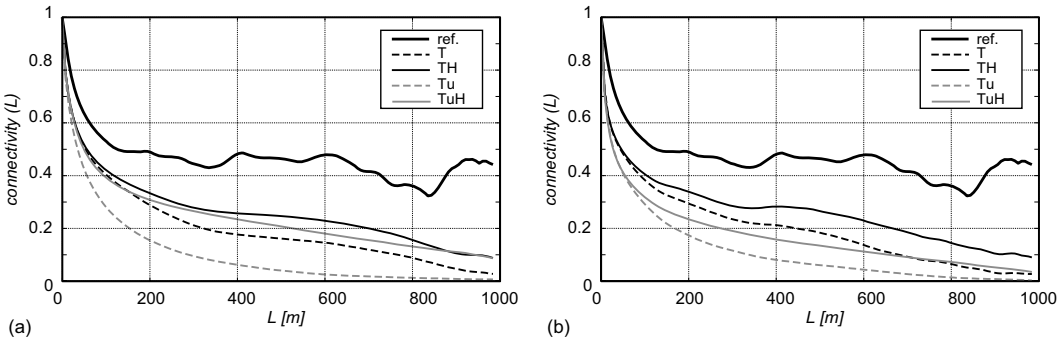

Fig. 5 Connectivity functions (of transmissivities higher than the mean) along the *x*-axis for (a) 250 *T* data and (b) 1000 *T* data. The lines corresponding to the simulations are ensemble averages over the 100 simulations. Index corresponds to: *T* transmissivity data plus their variogram, *Tu* only variogram, *TH* transmissivity and heads, *TuH* only variogram plus heads and *ref* reference field.

This paper points again in that direction, and addresses the question whether using only the head data for conditioning and a small number of transmissivity data (whereas all transmissivity data are used to compute the variogram) can improve the prediction.

The results presented here do not indicate such an improvement, and suggest that it is rather the RF model based on the computed variogram and on the multi-Gaussian assumption which is responsible for unsatisfactory predictions. This is confirmed by the fact that, in general, conditioning to *T* data improves the identification of the capture zone in the vicinity of the well, i.e. within a distance

comparable with the variogram range, but yields a systematic loss of connectivity behind this distance. Conditioning to *h* data, instead, yields an increase in connectivity that is more effective at distances larger than the variogram range. We can suggest that, in general, head data tend to help to detect the elongated channels of the well capture zone, whereas transmissivity data have an opposite impact and yield a less elongated and larger probability map.

In order to assess the impact of conditioning to transmissivity data when a multi-Gaussian model is erroneously applied to a non-multi-Gaussian reality, further investigation are needed. The present work indicated that connectivity plays a primary role and therefore suggested that the wrong RF model is the first source of deterioration for the capture-zone prediction. To circumvent these difficulties, we argue that two solutions may be proposed, one is to use alternative RF models that can handle different connectivity patterns such as the multiple point statistics or to use a multi-Gaussian model but with variograms that would have smaller ranges than the experimental variograms. In that way, the inverse method may have more degrees of freedom and may be able to compensate the inconsistencies between the head data and the stochastic model for the transmissivity field.

References

Capilla, J., Rodrigo, J. & Gómez-Hernández, J.J. (1999) Simulation of non-Gaussian transmissivity fields honouring piezometric data and integrating soft and secondary information. Math. Geology 31(7), 907–927.

Cornaton, F. (2007) GroundWater: A 3-D groundwater flow and transport finite element simulator. Reference manual. http://www1.unine.ch/chyn/php/softwares.php.

Gómez-Hernández, J. J. & Wen, X. -H. (1998) To be or not to be multi-Gaussian? A reflection on stochastic hydrogeology. Adv. Water Resour. 21(1), 47–61.

Hendricks Franssen, H. J. (2001) Inverse stochastic modeling of groundwater flow and mass transport. PhD dissertation Technical University of Valencia, Spain.

Hendricks Franssen, H. J. & Gómez-Hernández, J. J. (2002) 3D Inverse modelling of groundwater flow at a fractured site using a stochastic continuum model with multiple statistical populations. Stoch. Env. Res. & Risk A. 16, 155–174.

Kerrou, J., Renard, P., Hendricks Franssen, H. J. & Lunati, I. (2008) Issues in characterizing heterogeneity and connectivity in non-multi-Gaussian media. Adv. Water Resour. 31(1), 147-159 doi:10.1016/j.advwatres.2007.07.002.

Mosley, M. P. (1982) Analysis of the effect of changing discharge on channel morphology and instream uses in a braided river, Ohau River, New Zealand. Water Resour. Res. 18(4), 800–812.

Zinn, B. & Harvey, C. F. (2003) When good statistical models of aquifer heterogeneity go bad: A comparison of flow, dispersion, and mass transfer in connected and multivariate Gaussian hydraulic conductivity fields Water Resour. Res. 39(3), 1051. doi:10.1029/2001WR001146.